PEOPLE'S DEMOCRATIC REPUBLIC OF ALGERIA

MINISTRY OF HIGHER EDUCATION AND SCIENTIFIC RESEARCH

FERHAT ABBAS UNIVERSITY – SETIF 1

FACULTY OF SCIENCES

DEPARTEMENT OF CHEMISTRY

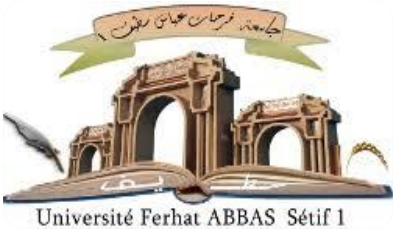

THESIS

Submitted in candidacy for the degree of

LMD DOCTORATE

Section : Chemistry

Option: Physical Chemistry

By : Zaidi Meriem

Titled

Nonlinear Optical Properties of Organometallic Complexes: Contributions from Quantum Chemistry.

In front of the jury:

Pr. AZIZI Amor	**Univ. Ferhat ABBAS Setif 1**	**Chairperson**
Pr. HANNACHI Douniazed	**Univ. Hadj Lakhdar Batna 1**	**Supervisor**
Pr. BELKHIRI Lotfi	**Univ. Mentouri Constantine 1**	**Examiner**
Pr. LAKEHAL Salima	**Univ. Mostefa Ben Boulaid Batna 2**	**Examiner**
Dr. BOURZAMI Riadh	**Univ. Ferhat ABBAS Setif 1**	**Examiner**
Pr. HADDADI Khelifa	**Univ. Ferhat ABBAS Setif 1**	**Examiner**
Pr. CHERMETTE Henry	**Univ. Claude Bernard Lyon 1**	**Guest**
Pr. CHAFAI Nadjib	**Univ. Ferhat ABBAS Setif 1**	**Guest**

Acknowledgment

The completion of this thesis marks the end of a rewarding and transformative journey, and I am deeply grateful to all those who supported me along the way.

The research and results that I am honored to present in this thesis were conducted under the supervision of Professor Douniazed HANNACHI at University Batna 1, who proposed this exciting research topic and supported me with great kindness throughout these years of study. I am deeply thankful for the trust she placed in me, the freedom she gave me in my research, and the invaluable advice she provided during our many scientific discussions. Her professionalism, generosity, and constant availability have been a true source of inspiration.

My heartfelt thanks also go to Professor Henry CHERMETTE at University of Lyon 1, who welcomed me into the ISA laboratory during a two-month research stay. His warm reception, valuable assistance, and expert advice greatly contributed to the advancement of this work. Thank you, Professor CHERMETTE, for the time you devoted to me and for the enriching scientific exchanges that helped strengthen the quality of this thesis.

I wish to express my deep gratitude to the jury members: Pr. Amor AZIZI for agreeing to chair the thesis committee. Pr. Lotfi BELKHIRI, Pr. Salima LAKEHAL, Dr. Riadh BOURZAMI, Pr. Khelifa HADDADI and Pr. Nadjib CHAFAI, for taking the time to evaluate this thesis. I am honored by your presence on the jury.

Special thanks to Dr. Farouk. ZAIDI for his advices, encouragements. I also extend my deep appreciation to Pr. Mouhamed Fahim HAROUN.

To my friends and colleagues, thank you for your encouragement, friendship, and generosity were vital to the completion of this thesis and made these years of research more fulfilling and enjoyable. Thank you for the moments we shared, for your advice, and for your constant support during times of doubt.

Lastly, I express my deepest love and appreciation to my family, whose encouragement, patience, a special thanks to my dear brother, Omar ZAIDI, a member at the Laboratoire de Physique Quantique et Systèmes Dynamiques (LPQSD), for his invaluable assistance. His commitment was of great importance to my work. Thank you for your patience, enthusiasm, and kindness.

Table of Contents

Chapter II

Chapter III

Chapter IV

Chapter V

Figure captions

Chapter II

Chapter III

Chapter IV

Chapter V

Table captions

Chapter III

Chapter IV

Chapter V

Scheme Captions

Chapter I

Chapter II

Chapter IV

List of abbreviations

Abbreviation	Definition
α	Polarizability
β	First Hyperpolarizability
γ	Second Hyperpolarizability
Δα	Polarizability Anisotropy
BOA	Born–Oppenheimer approximation
CI	configuration interaction
CC	coupled cluster theory
DFT	Density Functional Theory
DR	Depolarization Ratio
EFISHG	Electric Field Induced Second Harmonic Generation
FDF	Frequency Dispersion Factor
GGA	Generalized-Gradient Approximation
HK	Hohenberg and Kohn
HOMO	Highest Occupied Molecular Orbital
HRS	Hyper-Rayleigh Scattering
ICT	Intra charge transfer
Ips	Ionization Potentials
KS	Kohn and Sham
LDA	Local Density Approximation
LED	Light Emitting Diode
LMCT	Ligand to metal charge transfer
LSDA	Local Spin Density Approximation
LUMO	Lowest Unoccupied Molecular Orbital
M-GGA	meta-GGA

MLCT	Metal to ligand charge transfer
NLO	Non-Linear Optical
QTAIM	Quantum Theory of Atoms in Molecules
SHG	Second Harmonic Generation
SOS	Sum-Over-States
TD-DFT	Time Dependent Density Functional Theory
THG	Third Harmonic Generation
TM	Transition Metals
vdW	van der Waals
XC	exchange–correlation

General Introduction

General Introduction

At the end of the nineteenth century, physics was dominated by classical mechanics, electromagnetism, and thermodynamics, which were thought to provide a complete description of nature. However, classical physics failed to explain key microscopic phenomena such as black-body radiation, atomic stability, and spectroscopy. These limitations revealed the need for new theories, ultimately leading to the development of quantum mechanics in the early twentieth century.

The application of quantum mechanics to chemistry gave rise to quantum chemistry, a discipline that employs theoretical models and computational methods to study molecular systems. Among its most powerful applications is the study of optical properties, particularly those that arise in nonlinear optical (NLO) materials.

Nonlinear optics is a subdiscipline of optics in which focuses on materials that can strongly interact with the electric field of incident laser radiation and generate nonlinear optical (NLO) responses which have grown significantly in scientific and technological domains [1]–[5]. The strength of light-matter interaction is much more intense than that typically encountered in linear optics. It provides fundamental theories and principles of devices for laser radiation in the visible, ultraviolet and infrared spectral ranges. The origins of modern nonlinear optics are often attributed to the experimental demonstration of second-harmonic generation (SHG) by Franken et al.[6] The pivotal advancement enabling this breakthrough was the invention of the first laser by Maiman and Collins in 1960 [7], [8]. Nonlinear optical materials are compounds capable of exhibiting phenomena such as second-harmonic generation (SHG) and third-harmonic generation (THG). They play a vital role in a wide range of applications, including optical communication, computing, data storage, and laser technology. Additionally, they are crucial in photopharmacology, photoactuators, controlled drug transport and release etc. These phenomena have led to the evolution of new technologies such as ultrafast lasers, [9], [10] nonlinear microscopy [11], and nonlinear optical switching [9], [10], [12]. Furthermore, nonlinear optical materials have great potential applications in different fields such as optoelectronics,[13], [14] photonics [15], optical computing, optical communications [16], [17], holographic imaging and dynamic image processing etc [18], [19].

Within the wide range of NLO-active molecules, organometallic complexes have emerged as particularly promising candidates due to their structural versatility, tunable

electronic properties, and strong charge-transfer capabilities. The incorporation of transition metals into conjugated organic frameworks introduces new pathways for electron delocalization and metal–ligand interactions, both of which are critical for enhancing NLO responses. Complexes based on metallocenes, multidecker sandwich structures[20], [21], and donor–acceptor architectures [22]–[25] demonstrate favorable characteristics such as redox activity, asymmetric charge distribution[26]–[28], introducing diffuse excess electrons [29]–[32], key factors in achieving strong second- and third-order NLO effects.

This thesis is devoted to the investigation of the linear and nonlinear optical (NLO) properties of two distinct classes of materials. The first class comprises two series of metal-doped nanocages, $M@B_{64}Al_{12}N_{12}$ and $M@B_{66}Al_{12}N_{12}$, where M represents a transition metal spanning the series from Sc to Zn. The second class involves multidecker sandwich clusters of the type $\{\mu\text{-}B_2H_2S_2Pd(Cl)_2\}$–$(CoCp)_n$ (n = 2–5). The study emphasizes a comprehensive analysis of their structural, electronic, linear and nonlinear optical characteristics. To achieve this objective, state-of-the-art computational methodologies were employed, with particular reliance on density functional theory (DFT) as the primary framework for electronic structure and optical property calculations.

For clarity and coherence, this thesis is organized into five chapters, each addressing a key aspect of the investigation.

- The first chapter introduces fundamental concepts of quantum mechanics, including the Born–Oppenheimer and Hartree–Fock approximations, which simplify the many-body Schrödinger equation and provide the foundation for understanding complex chemical and physical phenomena. It also presents the basic principles of density functional theory (DFT) and the Hohenberg–Kohn theorems, which form the cornerstone of modern computational approaches.
- The second chapter focuses on the theoretical framework of linear and nonlinear optical phenomena. It describes fundamental parameters such as polarizability and hyperpolarizability, emphasizing their significance in advanced technologies such as optical switching, frequency conversion, and telecommunications. By examining the physical origins of nonlinear optical (NLO) behavior, this chapter establishes the basis for the computational studies presented in later sections.

- The third chapter is devoted to the computational investigation of the second- and third-order nonlinear optical (NLO) responses of $M@B_{66/64}Al_{12}N_{12}$ nanocages. For these systems, a topological analysis was carried out within the framework of the Quantum Theory of Atoms in Molecules (QTAIM), and delocalization indices (DI) were evaluated to gain insights into the nature of chemical bonding. In addition, the optical absorption spectra were analyzed, and both static and dynamic NLO parameters of the doped nanocages were computed. To further elucidate the origin of the NLO response, the sum-over-states (SOS) approach was employed.
- The fourth chapter is dedicated to predicting and tailoring the second-order nonlinear optical (NLO) behavior of a novel series of multidecker sandwich clusters, $\{\mu\text{-}B_2H_2S_2Pd(Cl)_2\}\text{–}(CoCp)_n$ (n = 2–5). In this part, both static and frequency-dependent first- and second-order NLO coefficients are determined, together with a comprehensive examination of their geometric, electronic, and optical attributes.
- The fifth chapter extends the findings of Chapter IV by examining the third-order nonlinear optical responses of multidecker cluster compounds. Particular emphasis is placed on quantifying the fundamental parameters associated with second hyperpolarizability. These results are systematically compared with those obtained for metallocene-based systems, offering a deeper understanding of the correlations between molecular architecture and optical performance.

References

[1] J. Zyss and I. Ledoux, "Nonlinear Optics in Multipolar Media: Theory and Experiments," *Chem. Rev.*, vol. 94, no. 1, pp. 77–105, 1994, doi: 10.1021/cr00025a003.

[2] D. M. Burland, R. D. Miller, and C. A. Walsh, "Second-Order Nonlinearity in Poled-Polymer Systems," *Chem. Rev.*, vol. 94, no. 1, pp. 31–75, 1994, doi: 10.1021/cr00025a002.

[3] T. Verbiest, S. Houbrechts, M. Kauranen, K. Clays, and A. Persoons, "Second-order nonlinear optical materials: Recent advances in chromophore design," *J. Mater. Chem.*, vol. 7, no. 11, pp. 2175–2189, 1997, doi: 10.1039/a703434b.

[4] S. Di Bella, "Second-order nonlinear optical properties of transition metal complexes," *Chem. Soc. Rev.*, vol. 30, no. 6, pp. 355–366, 2001, doi: 10.1039/b100820j.

[5] S. R. Marder, "Organic nonlinear optical materials: Where we have been and where we are going," *Chem. Commun.*, no. 2, pp. 131–134, 2006, doi: 10.1039/b512646k.

[6] P. A. Franken, A. E. Hill, C. W. Peters, and G. Weinreich, "Generation of optical harmonics," *Phys. Rev. Lett.*, vol. 7, no. 4, pp. 118–119, 1961, doi: 10.1103/PhysRevLett.7.118.

[7] T. H. MAIMAN, "Stimulated Optical Radiation in Ruby," *Nature*, vol. 187, pp. 493–494, 1960, doi: org/10.1038/187493a0.

[8] R. J. Collins, D. F. Nelson, A. L. Schawlow, W. Bond, C. G. B. Garrett, and W. Kaiser, "Coherence, narrowing, directionality, and relaxation oscillations in the light emission from ruby," *Phys. Rev. Lett.*, vol. 5, no. 7, pp. 303–305, 1960, doi: 10.1103/PhysRevLett.5.303.

[9] L. T. Cheng, W. Tam, S. R. Marder, A. E. Stiegman, G. Rikken, and C. W. Spangler, "Experimental Investigations of Organic Molecular Nonlinear Optical Polarizabilities. 1. Methods and Results on Benzene and Stilbene Derivatives," *J. Phys. Chem.*, vol. 95, no. 26, pp. 10643–10652, 1991, doi: 10.1021/j100179a027.

[10] K. A. Green, M. P. Cifuentes, M. Samoc, and M. G. Humphrey, "Metal alkynyl complexes as switchable NLO systems," *Coord. Chem. Rev.*, vol. 255, no. 21–22, pp. 2530–2541, 2011, doi: 10.1016/j.ccr.2011.02.021.

[11] J. A. Delaire and K. Nakatani, "Linear and Nonlinear Optical Properties of Photochromic Molecules and Materials," *Chem. Rev.*, vol. 100, no. 5, pp. 1817–1845, 2000, doi: 10.1021/cr980078m.

[12] J. Dang, D. Mei, Y. Wu, and Z. Lin, "A comprehensive survey on nonlinear optical phosphates: Role of multicoordinate groups," *Coord. Chem. Rev.*, vol. 431, p. 213692, 2021, doi: 10.1016/j.ccr.2020.213692.

[13] M. S. Kodikara, R. Stranger, and M. G. Humphrey, "Computational studies of the nonlinear optical properties of organometallic complexes," *Coord. Chem. Rev.*, vol. 375, pp. 389–409, 2018, doi: 10.1016/j.ccr.2018.02.007.

[14] Y. Y. Liang, B. Li, X. Xu, F. Long Gu, and C. Zhu, "A Density Functional Theory Study on Nonlinear Optical Properties of Double Cage Excess Electron Compounds: Theoretically Design M[Cu(Ag)@(NH 3) n](M = Be, Mg and Ca; n = 1–3)," *J. Comput. Chem.*, vol. 40, no. 9, pp. 971–979, 2019, doi: 10.1002/jcc.25371.

[15] N. Baggi *et al.*, "Design of cyclometallated 5-π-delocalized donor-1,3-di(2-pyridyl)benzene platinum(II) complexes with second-order nonlinear optical properties," *Polyhedron*, vol. 140, no. Ii, pp. 74–77, 2018, doi: 10.1016/j.poly.2017.11.051.

[16] C. Andraud, F. Cyril, B. Olivier, H. Chermette, and P. L. Baldeck, "Excitonically Coupled Oligomers and Dendrimers for Two-Photon Absorption," *Adv. Polym. Sci.*, vol. 214, pp. 149–203, 2008, doi: 10.1007/12_2008_158.

[17] Z. R. Khan, M. Shkir, V. Ganesh, S. AlFaify, I. S. Yahia, and H. Y. Zahran, "Linear and Nonlinear Optics of CBD Grown Nanocrystalline F Doped CdS Thin Films for Optoelectronic Applications: An Effect of Thickness," *J. Electron. Mater.*, vol. 47, no. 9, pp. 5386–5395, 2018, doi: 10.1007/s11664-018-6437-9.

[18] K. Iliopoulos, O. Krupka, D. Gindre, and M. Salle, "Reversible Two-Photon Optical Data Storage in Coumarin-Based Copolymers," *J. Am. Chem. Soc.*, vol. 132, pp. 14343–14345, 2010, doi: 10.1021/ja1047285.

[19] M. Homocianu, A. Airinei, C. Hamciuc, and A. M. Ipate, "Nonlinear optical properties (NLO) and metal ions sensing responses of a polymer containing 1,3,4-oxadiazole and bisphenol A units," *J. Mol. Liq.*, vol. 281, pp. 141–149, 2019, doi: 10.1016/j.molliq.2019.02.065.

[20] S. J. Wang, Y. F. Wang, and C. Cai, "Multidecker Sandwich Cluster VnBenn +1 (n = 1, 2, 3, 4) as a Polarizable Bridge for Designing 1D Second-Order NLO Chromophore: Metal-π Sandwich Multilayer Structure as a Particular Charge-Transfer Axis for Constructing Multidimensional NLO Molecules," *J. Phys. Chem. C*, vol. 119, no. 28, pp. 16256–16262, 2015, doi: 10.1021/acs.jpcc.5b04656.

[21] S. J. Wang, Y. F. Wang, and C. Cai, "Multidecker sandwich complexes VnBenn+1 (n = 1, 2, 3) as stronger electron donor relative to ferrocene for designing high-performance organometallic second-order nlo chromophores: Evident layer effect on the first hyperpolarizability and two-dimensional N," *J. Phys. Chem. C*, vol. 119, no. 10, pp. 5589–5595, 2015, doi: 10.1021/jp5123272.

[22] M. Blanchard-Desce, I. Ledoux, J. M. Lehn, J. Malthête, and J. Zyss, "Push-pull polyenes and carotenoids: Synthesis and non-linear optical properties," *J. Chem. Soc., Chem. Commun.*, no. 11, pp. 737–739, 1988, doi: 10.1039/C39880000737.

[23] D. Hannachi *et al.*, "The Effect of Resonance-Assisted Hydrogen Bond on the Second-Order Nonlinear Optical properties of Pyridine Hydrazone Photoswitches: A Quantum Chemistry Investigation," *New J. Chem.*, 2023, doi: 10.1039/D3NJ02848H.

[24] E. Cariati, C. Dragonetti, E. Lucenti, F. Nisic, S. Righetto, and E. Tordin, "An acido-triggered reversible luminescent and nonlinear optical switch based on a substituted styrylpyridine : EFISH measurements as an unusual method to reveal a protonation – deprotonation NLO contrast," *Chem. Commun.*, vol. 50, no. 13, pp. 1608–1610, 2014, doi: 10.1039/c3cc48149b.

[25] F. Ricci, F. Elisei, P. Foggi, A. Marrocchi, A. Spalletti, and B. Carlotti, "Photobehavior and Non − Linear Optical Properties of Push − Pull , Symmetrical and Highly Fluorescent Benzothiadiazole Derivatives," *J. Phys. Chem.*, vol. 120, no. 41, pp. 23726–23739, 2016, doi: 10.1021/acs.jpcc.6b07290.

[26] D. Hannachi, M. F. Haroun, A. Khireddine, and H. Chermette, "Optical and nonlinear optical properties of Ln(Tp)2, where Ln = La,...,Lu and Tp = tris(pyrazolyl)borate: a DFT+TD-DFT study," *New J. Chem.*, vol. 43, p. 14377, 2019, doi: 10.1039/c9nj03232k.

[27] M. Zaidi, D. Hannachi, and H. Chermette, "Correlation between Second Ionization Potential and Nonlinear Optical Properties of Bivalent Transition-Metal Complexes : A Quantum Chemical Study," *Inorg. Chem.*, vol. 60, pp. 6616–6632, 2021.

[28] D. Kamli, D. Hannachi, and H. Chermette, "Bis-TTF-Ge derivatives: promising linear and nonlinear optical properties, a theoretical investigation," *New J. Chem.*, vol. 47, pp. 1234–1246, 2023, doi: 10.1039/d2nj03671a.

[29] A. Ahsin and K. Ayub, "Remarkable electronic and NLO properties of bimetallic superalkali clusters: a DFT study," *J. Nanostructure Chem.*, no. 0123456789, 2021, doi: 10.1007/s40097-021-00429-2.

[30] A. Ahsan and K. Ayub, "Adamanzane based alkaline earthides with excellent nonlinear optical response and ultraviolet transparency," *Opt. Laser Technol.*, vol. 129, no. March, p. 106298, 2020, doi: 10.1016/j.optlastec.2020.106298.

[31] A. Ahsan, S. Sarfaraz, F. Fayyaz, M. Asghar, and K. Ayub, "Enhanced non-linear optical response of calix[4]pyrrole complexant based earthides in the presence of oriented external electric field," *J. Mol. Liq.*, vol. 350, p. 118504, 2022, doi: 10.1016/j.molliq.2022.118504.

[32] A. Ahsan and K. Ayub, "Extremely large nonlinear optical response and excellent electronic stability of true alkaline earthides based on hexaammine complexant," *J. Mol. Liq.*, vol. 297, pp. 36–40, 2020, doi: 10.1016/j.molliq.2019.111899.

Chapter I

Theoretical foundations

I.1. Introduction

Quantum chemistry provides a rigorous theoretical framework for investigating the electronic structure of molecular systems by solving the time-independent Schrödinger equation. Given the complexity of many-electron systems, practical computations rely on fundamental approximations such as the Born–Oppenheimer separation, which decouples nuclear and electronic motion. Core methodologies include Hartree–Fock (HF) theory, post-HF correlation methods (e.g., MP2, CCSD), and density functional theory (DFT), each offering varying balances between accuracy and computational cost. These approaches are implemented using basis sets that approximate molecular orbitals and are essential for achieving reliable results.

In this chapter, the fundamental theoretical concepts and computational strategies underlying these methods are introduced, providing the necessary foundation for exploring molecular properties through quantum chemical models.

I.2. Schrödinger equation

The foundations of quantum chemistry go back to 1926 when the physicist Erwin Schrödinger introduced a key concept within quantum theory, this is now referred to as the Schrödinger equation.

This equation is a fundamental part of quantum mechanics and explains how the quantum state of a physical system changes over time. Essentially, solving this equation enables us to understand atomic and molecular behaviours on a quantum level, which is essential to quantum chemistry. The most common form of this equation, the time-independent Schrödinger equation, is written as [1]:

$$\hat{H}\Psi = E\Psi \tag{I.1}$$

Where:

$\hat{H}$ Represents the Hamiltonian operator of the system under consideration (atom, molecule, solid); it is known and contains terms related to the kinetic energy of the electrons and atomic nuclei, as well as terms describing the Coulomb interaction between electron-nucleus, electron-electron, and nucleus-nucleus. The unknowns to be determined are the wave function Ψ and the energy E.

The Schrödinger equation serves as the foundation for first-principles methods, which seek to determine the energy (E) and wave function (Ψ) of a quantum system without relying on

experimentally adjusted parameters. Quantum computational methods rely on various mathematical frameworks that involve applying the Schrödinger equation while accounting for all interactions between the particles in the systems being studied. However, due to the presence of interaction terms for all pairs of particles in the Hamiltonian operator, the equation can only be solved analytically for a few very simple systems.

For a molecular system, the total Hamiltonian operator $\hat{H}$ is expressed as the sum of the kinetic and potential energy operators of both nuclei and electrons.

$$\hat{H} = \hat{T}_N + \hat{T}_e + \hat{V}_{Ne} + \hat{V}_{ee} + \hat{V}_{NN} \quad \text{(I.2)}$$

where the kinetic energy operators are defined as follows:

$\hat{T}_N = -\sum_{\alpha=1}^{N} \frac{\hbar^2}{2M_\alpha} \Delta_\alpha$ (kinetic energy of the nuclei)

$\hat{T}_e = -\sum_{i=1}^{n} \frac{\hbar^2}{2m_e} \Delta_i$ (kinetic energy of electrons)

and where the Coulomb potential terms are given by:

$\hat{V}_{NN} = \sum_\alpha \sum_{\alpha>\beta} \frac{Z_\alpha Z_\beta e^2}{R_{\alpha\beta}}$ (nuclear-nuclear electrostatic repulsion)

$\hat{V}_{Ne} = -\sum_i \sum_\alpha \frac{Z_\alpha e^2}{r_{i\alpha}}$ (electrostatic attraction electrons nuclei)

$\hat{V}_{ee} = \sum_j \sum_{i>j} \frac{e^2}{r_{ij}}$ (electron-electron electrostatic repulsion)

Where r_{ij} the distance between electrons i and j, e the elementary charge, $r_{i\alpha}$ the distance electron i - nuclei α, Z_α atomic number of nuclei α, $R_{\alpha\beta}$ the distance between nuclei α and β and Δ_i and Δ_α the Laplacian operators associated with the electron i and the nuclei α, respectively.

In quantum chemistry, the primary challenge is to find approximate solutions to the Schrödinger equation in complex many-body systems with multiple electrons and nuclei interacting, with each particle experiencing the collective influence of all others.

I.3. Born Oppenheimer Approximation

The first major simplification is the Born–Oppenheimer approximation (BOA). It exploits the large mass difference between nuclei and electrons to treat their motions separately.

We assume that the nuclei are stationary relative to the fast-moving electrons. This leads to the decomposition:

The Born-Oppenheimer approximation [2] plays a crucial role in electronic structure calculations. It exploits the large mass difference between nuclei and electrons to treat their motions separately. Even for the lightest nucleus, the proton, its mass is about 1836 times greater than that of an electron. As a result, nuclei move much more slowly compared to electrons. This allows, in many cases, the assumption that electrons evolve within an average potential created by fixed nuclei. Under this approximation, the electronic wave function $\Psi_e(\vec{r},\vec{R})$ explicitly depends on the electronic coordinates $\vec{r}$ while being parametrically dependent on the nuclear coordinates $\vec{R}$. Consequently, the total wave function can be expressed as the product of an electronic wave function and a nuclear wave function:

$$\Psi(\vec{r},\vec{R}) = \Psi_n(\vec{R})\Psi_e(\vec{r},\vec{R}) \tag{I.3}$$

The electronic Schrödinger equation becomes:

$$\hat{H}_e\Psi_e(\vec{r},\vec{R}) = E_e\Psi_e(\vec{r},\vec{R}) \tag{I.4}$$

$$\hat{H}_e = \hat{T}_e(\vec{r}) + \hat{V}_{Ne}(\vec{r},\vec{R}) + \hat{V}_{ee}(\vec{r}) + \hat{V}_{NN}(\vec{R}) \tag{I.5}$$

which leads to:

$$\hat{H}_e = -\sum_{i=1}^{n}\frac{1}{2}\Delta_i + \sum_i\sum_\alpha\frac{Z_\alpha}{r_{i\alpha}} + \sum_j\sum_{i>j}\frac{1}{r_{ij}} + \hat{V}_{NN}(\vec{R}) \tag{I.6}$$

This approximation represents a first step toward solving Schrödinger Equation but it remains insufficient on its own.

The electronic Schrödinger generally has no analytical solutions. The main difficulty arises from the electron-electron interaction $\hat{V}_{ee}$, which accounts for all quantum effects between electrons, and the Coulomb repulsion term $\frac{1}{r_{ij}}$, which couples their motion. To simplify the problem, this repulsion can be treated as an average effect, meaning each electron moves within the mean field generated by the others. This approximation forms the foundation of the Hartree-Fock method.

I.4. Hartree Approximation

The Born-Oppenheimer approximation simplifies the electronic problem but fails to resolve the fundamental challenge posed by electron-electron interactions, leading to an N-body problem.

Solving this problem exactly, even for a single electron, remains impossible due to the complexity of these interactions. In 1927, an approximate technique was introduced by Douglas Hartree [3] to calculate wave functions and energy levels in atoms and ions This method is based on the premise that electrons operate independently, lacking any correlations in their movements.

Based on this approximation, the probability of locating an electron at position r_1 within orbital 1 is regarded independent of the probability of another electron being at position r_2. Consequently, the Hamiltonian of the system is then expressed as:

$$H = \sum_{i=1}^{N} h(i) \tag{I.7}$$

where $h(i)$ represents the monoelectronic Hamiltonian.

The associated electronic wave function is constructed as a product of single-electron wave functions, known as the Hartree product [4]:

$$\Psi^{HP} = (x_1; x_2; \dots; x_N) = \left|\varphi_i(x_1)\varphi_j(x_2) \dots \varphi_k(x_N)\right| \tag{I.8}$$

This approximation assumes that each electron moves independently within an average potential generated by all other electrons, ignoring direct electron-electron interactions. In this model, electrons are treated as uncorrelated, meaning their individual wave functions can be represented as a simple product. However, this approach overlooks key quantum mechanical effects, including the Pauli exclusion principle and electron correlation, which results in an overestimation of Coulomb repulsion. Despite these limitations, it provides a foundational framework for more advanced methods, such as Hartree-Fock theory, which introduces spin considerations and enforces the antisymmetry of the wave function when exchanging two electrons, leading to a more accurate solution of the Schrödinger equation.

I.5. Hartree-Fock approximation

The Hartree approximation is an important step in solving the electronic Schrödinger equation, but it doesn't fully align with the core principles of quantum mechanics. In particular, it overlooks the Pauli exclusion principle [5], which requires that the total wave function of a system of electrons must be antisymmetric when any two electrons are exchanged. This means that swapping two electrons in the wave function must introduce a negative sign, reflecting the fundamental nature of fermions.

The initial objective is to obtain an approximate solution to the electronic Schrödinger equation [1]. The Hartree-Fock method, introduced by Fock and Slater in 1930, extends the Hartree approach by incorporating additional quantum mechanical principles. This refinement is achieved by replacing the Hartree wave functions with a Slater determinant [6]. This determinant consists of single-electron functions known as spin orbitals and applies to closed-shell systems, where all electrons are paired. Each spin orbital is the product of a spatial function ϕ_i (orbital), which depends on the electron's spatial coordinates, and a spin function that can take one of two opposite values: α (S)= 1/2 and β (S)= -1/2. In a closed-shell system, the spin density is zero, making the system symmetric with respect to these two spin states. This symmetry allows a pair of electrons to be described using the same spatial orbital ϕ_i.

This describes the configuration in which the polyelectronic determinant for an N electron system comprises N/2 spatial orbitals $\{\varphi_1, \varphi_2, \dots, \varphi_{N/2}\}$. Every spatial orbital appears two times inside the determinant, linked with spin functions of opposite values to ensure that the two corresponding spin orbitals are distinct.

an N×N determinant made from N different spin orbitals that explain single-electron states using both space and spin coordinates. So, the polyelectronic wave function is written as:

$$\Psi(r_1, r_2 \dots, r_N) = \frac{1}{\sqrt{N!}} \begin{vmatrix} \varphi_1(r_1) & \varphi_1(r_2) & \dots & \varphi_1(r_N) \\ \varphi_2(r_1) & \varphi_2(r_2) & \dots & \varphi_2(r_N) \\ \vdots & \vdots & & \vdots \\ \varphi_N(r_1) & \varphi_N(r_2) & \dots & \varphi_N(r_N) \end{vmatrix} \quad \text{(I.9)}$$

The Hartree-Fock model serves as a foundation for further refinements, either by introducing additional approximations, as seen in semi-empirical methods, or by incorporating additional determinants to generate solutions that progressively converge toward the exact solution of the electronic Schrödinger equation.

I.6. Post Hartree-Fork

The Hartree–Fock (HF) approximation provides a good initial approach for solving the electronic Schrödinger equation, but it does not provide electron correlation, the correlating effects of electrons present contemporaneously within the atom beyond the mean-presentation nature. This omission can cause large errors in computed properties, especially total energies, reaction barriers, and spectroscopic properties. Post-Hartree–Fock methods have been devised to introduce correlation effects systematically to improve upon this. A very straightforward example is Møller–Plesset perturbation theory, where the Hamiltonian is split into a zeroth-

order contribution (the HF Hamiltonian) and a perturbation. The energy correction in second-order perturbation theory (MP2) is:

$$E_{MP2} = \sum_{i<j,a<b} \frac{|\langle ij||ab\rangle|^2}{\varepsilon_i+\varepsilon_j-\varepsilon_a-\varepsilon_b} \quad \text{(I.10)}$$

In doing so i, j occupied orbitals a, b virtual orbitals, ε orbital energy and $\langle ij||ab\rangle$ antisymmetric two-electron integral. Another widely used approach is configuration interaction (CI), where the associated wave functions are expressed as linear combinations of Slater determinants:

$$\psi_{CI} = c_0\phi_0 + \sum_{i,a} c_i^a \phi_i^a + \sum_{i<j,a<b} c_{ij}^{ab} \phi_{ij}^{ab} + \cdots \quad \text{(I.11)}$$

ϕ_0 is the HF reference, and ϕ_i^a, ϕ_{ij}^{ab} etc. represent single-excitation and double-excitation configurations. The full CI theory provides exact solutions on a finite basis, but is computationally infeasible outside of small systems due to scaling factors. In contrast, coupled cluster theory (CC) employs an exponential approach to compute the wave functions:

$$\left|\psi_{CC}\right\rangle = e^{\hat{T}}|\phi_0\rangle, \quad \hat{T} = \hat{T}_1 + \hat{T}_2 + \hat{T}_3 + \cdots \quad \text{(I.12)}$$

Where $\hat{T}_n$ represents the excitation operator. The most commonly used approximation is CCSD(T), which contains single and double numbers exactly and treats triple numbers in a perturbative manner. The method is known for its high accuracy and size-wideness and is therefore considered a benchmark for quantum chemical predictions. Overall, post-HF methods, while computationally expensive, are able to model electronic structure with high accuracy and are indispensable in systems where correlations play a dominant role.

I.7. Density Functional Theory (DFT)

A comprehensive examination of the electronic characteristics of a molecular system necessitates consideration of electron correlation effects, especially when transition metals are present. Although Post-Hartree-Fock methods take these effects into account, they tend to be computationally intensive, which restricts the size of the systems that can be analyzed.

Over the past three decades, Density Functional Theory (DFT) has undergone significant advancements for investigating chemical systems, proving to be a formidable alternative to Post-Hartree-Fock methods. Initially created and utilized for solid-state issues, DFT has become increasingly favored in chemical applications due to several important factors:

- This theory includes in its formalism a large part of electronic correlation.

- This approach is relevant to a wide range of systems, such as covalent, ionic, and metallic compounds.
- The study of larger molecular systems is made possible due to its lower demand for computational resources compared to Post-Hartree-Fock methods.
- A more intuitive chemical interpretation of the resulting wave function is facilitated by its single-determinant characteristic.

I.7.1 Framework of Density Functional Theory (DFT)

While Hartree-Fock methods express the system's energy as a functional of its wave function ψ, Density Functional Theory (DFT) instead defines energy as a functional of the electronic density (ρ). One of the key advantages of DFT is its ability to solve the Schrödinger equation using only the observable ρ, which is defined in real space R^3. This replaces the high-dimensional configuration space of 3N variables required for the wave function in Hartree-Fock methods.

However, while this approach avoids the complexity of the many-body problem by relying on the electronic density, the challenge lies in formulating an explicit analytical expression for energy as a functional of (ρ).

Before exploring the fundamental principles of Density Functional Theory, it is essential to define its central quantity: the electronic density (ρ).

I.7.2 The electronic density

Electrons are inseparable and indistinguishable particles. While an individual electron cannot be precisely localized [7], its probability of presence within a given volume element can be estimated, which corresponds to the electronic density (ρ). Rather than being treated as isolated entities, electrons must be considered collectively as an electron cloud, with the electronic density identifying the regions of space where they are most likely to be found.

The electronic density (ρ) is a positive function defined by the three spatial coordinates (x, y, z). It gradually decreases to zero at infinite distance and is worth N - total number of electrons - when integrated over the whole space.

$$\begin{cases} \rho(r \mapsto \infty) = 0 \\ \int \rho(r) dr = N \end{cases} \tag{I.13}$$

The electronic density ρ (r) is, by definition, the probability of finding an electron within a unit volume $d\tau$ at position r. Unlike the wave function ψ, the electronic density is an observable quantity.

Notably, ρ (r) appears to contain sufficient information to describe the system, whereas the wave function ψ holds a far greater amount of information, some of which is not essential for understanding chemical bonding.

These considerations suggest that the electronic density alone is enough to fully determine the properties of an atomic system. This idea has motivated several attempts to develop a quantum formalism based on ρ (r). However, it was Hohenberg and Kohn who formulated an exact theoretical framework (Without any approximations) expressed through two fundamental theorems.

I.8. Hohenberg -Kohn theorems:

Pierre Hohenberg and Walter Kohn established two fundamental theorems in 1964, providing a theoretical foundation for calculating the ground-state electronic energy using the electronic density $\rho(r)$[8].

I.8.1 Theorem 1

In an electronic system described by the Hamiltonian H_{el}, the ground-state energy and wave function are determined by minimizing the corresponding functional $E[\psi]$. In an N electron system, the external potential $v_{ext}(r)$ fully defines the Hamiltonian H_{el}. This implies that if the number of electrons N and the external potential $v_{ext}(r)$ are known, the Hamiltonian can be uniquely determined, granting access to the ground-state energy and wave function. Thus, the external potential defines the essential characteristics of a given system.

The first theorem of Hohenberg and Kohn [8] provides a theoretical justification for the idea that a given electronic density ρ (r) corresponds to a unique external potential $v_{ext}(r)$. Indeed, the external potential is uniquely determined by the electronic density, up to an additive constant. Since ρ (r) also defines the total number of electrons in the system, it follows that the electronic density uniquely determines the wave function and, consequently, all electronic properties of the system.

For a system characterized by a given number of electrons N, nuclear positions (R_α), and nuclear charges (Z_α), the addition of the electronic density ρ (r) allows for the construction of the corresponding Hamiltonian. As a result, the fundamental wave function ψ_f and the ground-state energy E_f can be determined.

$$\rho \Rightarrow \{N, Z_\alpha, R_\alpha\} \Rightarrow H \Rightarrow \psi_f \Rightarrow E_f \tag{I.14}$$

The total energy of the system is thus a functional of the electronic density $\rho(r)$, expressed as $E = E[\psi]$. This expression can be rewritten by explicitly separating the terms that depend on the specific system, such as the number of electrons N and the external potential (N, $v_{ext}(r)$) that is, independent of any parameters specific to a given system.

The system-independent terms are grouped into a functional known as the Hohenberg-Kohn functional. This functional includes the electronic kinetic energy $T_e[\rho]$ and the potential energy arising from electron-electron interactions $V_{e-e}[\rho]$.

I.8.2 Theorem 2:

The configuration that results in the lowest energy corresponds to the ground-state electronic density of a system, which can be mathematically represented as:

$$E[\rho(r)] \geq E_{GS}[\rho_{GS}(r)] \tag{I.15}$$

In this expression, $E[\rho(r)]$ denotes the energy calculated for an arbitrary electronic density $\rho(r)$, while $E_{GS}[\rho_{GS}(r)]$ signifies the minimum energy that the system can achieve, linked to the actual ground-state density $\rho_{GS}(r)$.

While this theorem provides a method to determine the ground-state density and its corresponding energy, it does not provide an explicit formulation for the functional $F[\rho(r)]$ nor a direct approach for solving the many-electron Schrödinger equation.

I.9. Kohn-Sham theorem

In the Kohn-Sham framework [9] of density functional theory (DFT), the exact exchange energy from Hartree-Fock (HF) theory is replaced by a more general exchange-correlation functional. This functional accounts for both exchange and electron correlation effects, the latter being absent in HF theory. The total Kohn-Sham energy is given by:

$$E_{KS}(\rho) = T[\rho(r)] + E_H[\rho(r)] + \int \mathcal{V}_{ext}(r)\rho(\boldsymbol{r})d\boldsymbol{r} + V_{xc}[\rho(r)] \tag{I.16}$$

Where:

$T[\rho(r)]$ is the kinetic energy of non-interactive electrons.

$\mathcal{V}_{ext}(r)$ is the external potential

$E_H[\rho(r)]$ is the Hartree energy

$V_{xc}[\rho(r)]$ is the exchange-correlation potential, expressed as:

$$V_{xc}[\rho(r)] = \frac{\delta E_{xc}(\rho)}{\delta \rho(r)} \tag{I.17}$$

The exchange-correlation energy functional $E_{xc}(\rho)$ consists of four key contributions: exchange, correlation, kinetic, and Coulomb terms. These arise naturally when expressing the total energy of a system in terms of the density operator within the framework of density functional theory (DFT).

In principle, the total energy of the system can be determined using the formal expression for the Kohn-Sham energy functional. However, this remains an unsolved problem due to the unknown exact form of the exchange-correlation potential $V_{xc}[\rho(r)]$. This uncertainty necessitates the development of approximate exchange-correlation functionals to enable practical calculations of electronic structure and total energy [10], [11].

I.10. Exchange-Correlation Approximations in DFT

An accurate treatment of the exchange–correlation (XC) energy, which is defined as all quantum mechanical electron interactions that are not described by the classical Coulomb interaction, is a central challenge in Density Functional Theory (DFT). Since the exact form of the XC functional is not known, approximations to it have been developed at different levels of accuracy and computational cost with a goal of achieving the best possible way. These approximations are typically organized according to "Jacob's Ladder"

I.10.1 Local Density Approximation (LDA)

In order to precisely account for the effects of electron-electron correlation, it is essential to develop an algebraic representation for the exchange-correlation energy E_{xc}. The initial method examined adheres to the Kohn and Sham framework, with the goal of defining a reference system that allows for the most accurate expression of the exchange-correlation functional.

The fundamental concept of the Local Density Approximation (LDA) involves treating the exchange-correlation potential as a localized quantity, determined at a particular point r and only slightly influenced by density fluctuations nearby. Instead of striving to accurately depict the precise exchange-correlation hole, LDA aims to replicate the physical properties of its spherically averaged equivalent.

The LDA, serving as the basis for all contemporary exchange-correlation functionals, can be formally expressed in the following manner:

$$E_{xc}^{LDA}[\rho] = \int \rho(r)\varepsilon_{xc}\big(\rho(r)\big)dr \tag{I.18}$$

This is the functional for which an almost exact form is known. The approximation of $E_{xc}[\rho]$ is based on the uniform electron gas model, where the term $\varepsilon_{xc}\big(\rho(r)\big)$ represents the exchange-correlation energy per particle in a uniform electron gas of density $\rho(r)$. Additionally, $\varepsilon_{xc}\big(\rho(r)\big)$ can be expressed as the sum of an exchange contribution and a correlation contribution:

$$\varepsilon_{xc}\big(\rho(r)\big) = \varepsilon_x\big(\rho(r)\big) + \varepsilon_c\big(\rho(r)\big) \tag{I.19}$$

The exchange term, commonly referred to as "Dirac exchange"[12] and denoted by S (as it was later adopted by Slater), is known in an exact form:

$$\varepsilon_x^S\big(\rho(r)\big) = \frac{-3}{4}\left(\frac{3\rho(r)}{\pi}\right)^{1/3} \tag{I.20}$$

The correlation term $\varepsilon_c\big(\rho(r)\big)$ cannot be expressed in an exact analytical form. The most widely adopted approximation for this term was developed by Vosko, Wilk, and Nusair (VWN) [13]. Their approach is based on an interpolation of highly accurate quantum Monte Carlo calculations performed by Ceperley and Alder [14] for the uniform electron gas.

The fundamental idea behind the Local Density Approximation (LDA) is that the exchange-correlation energy of an inhomogeneous system can be treating each small region as if it were part of a homogeneous electron gas with the same local density. This approximation is reasonable when the density varies slowly, though in practice, this condition is not strictly met. Nevertheless, LDA has proven to be remarkably effective, and its application to atoms and molecules is justified by the success of its numerical implementations.

I.10.2 Local Spin Density Approximation (LSDA)

The LSDA method extends the LDA method to spin-polarized systems, where the electron density is separated into spin-up and spin-down components. The exchange-correlation functional is then given by:

$$E_{xc}^{LSDA}[\rho_\alpha, \rho_\beta] = \int \rho(r)\varepsilon_{xc}\left(\rho_\alpha(r), \rho_\beta(r)\right) dr \quad \text{(I.21)}$$

This approach accounts for the different exchange-correlation contributions from each spin channel and is essential for the analysis of magnetic systems, open-shell molecules, and transition metal complexes, where spin polarization plays a role.

I.10.3 Generalized Gradient Approximation (GGA)

The exchange energy is the primary source of error in LDA, frequently underestimated, whereas the correlation energy is usually overestimated, despite its overall contribution to the total energy being lesser. Notably, these two errors often offset each other. To enhance the precision of DFT calculations, more accurate approximations for the exchange-correlation functional are necessary. Some researchers have suggested improving the density functional by integrating its derivatives to address system inhomogeneities. However, this initial approach performed worse than LDA because it disrupted key physical conditions that gave LDA its reliability. To address this, modifications were introduced to enforce these essential constraints, resulting in the Generalized Gradient Approximation (GGA), which played a key role in the success of DFT.

$$E_{xc}^{GGA}[\rho; \nabla\rho] = \int \varepsilon_{xc}^{GGA}\big(\rho(r), \nabla\rho(r)\big) dr \quad \text{(I.22)}$$

The exchange and correlation contributions are often treated separately:

$$E_{xc}^{GGA}(\rho, \nabla\rho) = E_x^{GGA}(\rho, \nabla\rho) + E_c^{GGA}(\rho, \nabla\rho) \quad \text{(I.23)}$$

Since the main limitation of LDA arises from its treatment of exchange, special attention was given to improving this component:

$$E_x^{GGA}(\rho, \nabla\rho) = E_x^{LDA} - \int F\big(s(r)\big)\rho^{4/3}(r) dr \quad \text{(I.24)}$$

where F is a function of the reduced density gradient:

$$s(r) = \frac{|\vec{\nabla}\rho(r)|}{\rho^{4/3}(r)} \quad \text{(I.25)}$$

Several functionals based on this approximation have been proposed, such as Becke 88 (B88) [15] and Perdew-Wang 86 (PW86) [16]:

***B88*:** The B88 exchange functional is derived from a dimensional analysis of the exchange density.

$$F^{B88}(s) = \frac{\beta s^2}{1+6\beta s \times \sin^{-1}(s)} \quad \text{(I.26)}$$

With $\beta = 0.0042\ a.u.$

The parameter β is empirically determined through a least-squares fit to the exchange energies of six noble gas atoms, ranging from He to Rn.

PW91: The Perdew-Wang functional [17] is a modified version of this approach, designed to satisfy specific scaling conditions.

***PW86*:** This functional is based on an analysis of the gradient expansion of the exchange-correlation hole around its LSDA form.

$$F^{PW86}(s) = \left[1 + 1.296\left(\frac{s}{p}\right)^2 + 14\left(\frac{s}{p}\right)^4 + 0.2\left(\frac{s}{p}\right)^6\right]^{1/15} \quad \text{(I.27)}$$

With: $p = (24\pi^2)^{1/3}$

The Perdew-Burke-Ernzerhof (PBE) functional [18] is a refinement of this approach. Notably, neither PW86 nor PBE rely on empirically fitted parameters.

I.10.4 Meta GGA

With recent progress, a new class of functionals has been developed that depend not only on the electron density and its gradient but also on the Laplacian. These functionals, known as meta-GGA (M-GGA), have shown significant improvements over previous approaches, particularly in predicting properties such as atomization energies [19]. However, they are computationally more demanding, and optimizing the parameters for their construction is a more intricate process [20].

A meta-GGA exchange-correlation functional can be defined according to the expression:

$$E_{xc}^{meta-GGA}[\rho(\vec{r})] \approx \int \varepsilon_{xc}[\rho(\vec{r}), |\nabla\rho(\vec{r})|, \nabla^2\rho_{i\sigma}(\vec{r}), \tau_\sigma(\vec{r})]\rho(\vec{r})d\vec{r} \quad \text{(I.28)}$$

In which the orbital kinetic energy density of the occupied Kohn-Sham orbitals, $\tau_\sigma(\vec{r})$, is written as:

$$\tau_\sigma(\vec{r}) = \frac{1}{2}\sum_i^{occ} \left|\frac{\nabla\varphi_{i\sigma}(\vec{r})}{m_e}\right|^2 \quad \text{(I.29)}$$

The measure of "electronic localization" [15], [21], [22] is provided by the quantity $\tau_\sigma(\vec{r})$, which can help ascertain whether the localized exchange-correlation hole model serves as a suitable approximation for the true exchange-correlation function of the system being analyzed. Certain systems, such as the H_2^+ molecule at significant separations, cannot effectively utilize this localized hole approximation. Additionally, in any type of system, the exchange-correlation holes associated with classical bonds invariably possess a minor nonlocal component. By integrating the orbital kinetic energy density, meta-GGA functionals present an enhancement over the GGA model. Indeed, these meta-GGA functionals significantly decrease the relative errors in calculations of atomization energy, reducing them to approximately 2-3% [23], [24]. Nevertheless, these functionals are still semi-local, relying solely on the density and Kohn-Sham orbitals at a specific point $\vec{r}$ and within an infinitesimal vicinity of that point. Nonlocality can only be explicitly addressed through exchange-correlation functionals referred to as "hybrids. These are named in contrast to the previously discussed functional categories (LDA, GGA, meta-GGA), which are considered "pure" DFT functionals.

The term "hybrid" refers to the combined use of exact exchange energy from the Hartree-Fock model and exchange-correlation energy at the DFT level.

Examples of M-GGA functionals include M06-L [25], B95 [26].

I.10.5 The hybrid functional

The foundation of this functional type involves beginning with the exchange-correlation expression of GGA functionals and incorporating a specific percentage of the true or exact exchange, aligning with Hartree-Fock exchange. This precise proportion of Hartree-Fock exchange is established through a semi-empirical approach.

The findings achieved with this category of functionals indicate that they rank among the top methods for characterizing molecular electronic structures and their related properties. Notable hybrid functionals include those created by Becke, such as:

B3LYP functional is a hybrid exchange-correlation functional by the recipe, mostly used with density functional theory, for the combination, or rather mixing Hartree–Fock exact exchange with Becke's gradient corrected exchange and Lee–Yang–Parr correlation functionals to molecular properties at balanced accuracy [15], [26], [27], it can be written as follows:

$$E_{B3LYP}^{XC} = a_0 E_{LDA}^{X} + (1 - a_0) E_{HF}^{XC} + a_1 \Delta E_{Becke88}^{X} + E_{LDA}^{C} + a_2 (E_{LYP}^{C} - E_{LDA}^{C}) \quad \text{(I.30)}$$

With a_0=0.80, a_1=0.72 and a_2=0.81

B3P86 [15], [26], [28] along with others like ***O3LYP*** [27], [29].

I.10.6 Range-Separated Hybrid Functionals

This class of functionals separate the exchange interaction into a short-range and long-range parts multiplied by an attenuation parameter. This is important for systems in which there are charge-transfer excitations or long-range electron correlation. Examples include:

CAM-B3LYP (Coulomb-Attenuating Method B3LYP) is a long-range corrected functional developed to handle the inaccuracies of the non-Coulomb part of exchange functional at long distances [30].

ωB97X-D is a range-separated hybrid density functional developed to accurately capture long-range charge-transfer interactions and dispersion effects [31], [32].

I.10.7 Meta-hybrid functionals

Meta-hybrid functionals represent new generation of exchange-correlation (XC) functionals used in density functional theory (DFT). They extend the capabilities of generalized gradient approximation (GGA) and hybrid functionals by introducing kinetic energy density as an additional variable, enhancing the accuracy of electronic structure predictions for a broad range of systems.

A typical meta-hybrid GGA functional has the form:

$$E_{XC}^{meta-hybrid}[\rho] = E_X^{GGA}[\rho, \nabla\rho, \tau] + aE_X^{HF} + E_C^{GGA}[\rho, \nabla\rho, \tau] \quad \text{(I.31)}$$

Where:

E_X^{GGA}: GGA exchange

E_C^{GGA}: GGA correlation

E_X^{HF}: exact Hartree-Fock exchange

τ: kinetic energy density

a: HF exchange mixing coefficient

Available meta-hybrid functionals:

M06: Functional (27% HF exchange) by Yan-Truhlar [25], [33]

M06-2X: Functional (54% HF exchange) by Yan-Truhlar [25], [33]

TPSSH: Functional (10% HF exchange) by Tao-Perdew-Staroverov-Scuseria [34], [35]

I.10.8 Dispersion Correction

A major shortcoming of standard DFT is that it treats long-range dispersion or van der Waals (vdW) forces poorly. The critical importance of these forces in the structural stability and properties of molecular assemblies, biological macromolecules, molecular crystals, and supramolecular complexes. Typical locals (LDA) and semi-locals (GGA), plus some hybrids functionals do not explicitly account for these long-range correlations effects, therefore large errors are possible in binding energies, geometries and electronic properties.

I.10.8.1 Grimme's DFT-D3

To overcome the limitations of standard DFT in accounting for long-range van der Waals interactions, various dispersion correction schemes have been introduced. Among these, Grimme's DFT-D3 (Dispersion version 3) has emerged as one of the most reliable and widely used methods due to its high accuracy, computational efficiency, and broad compatibility with different functionals. The DFT-D3 enhances conventional DFT by incorporating empirical dispersion corrections, thereby enabling a more realistic description of weak, non-covalent interactions such as van der Waals forces which are typically underestimated or entirely omitted in traditional DFT calculations.

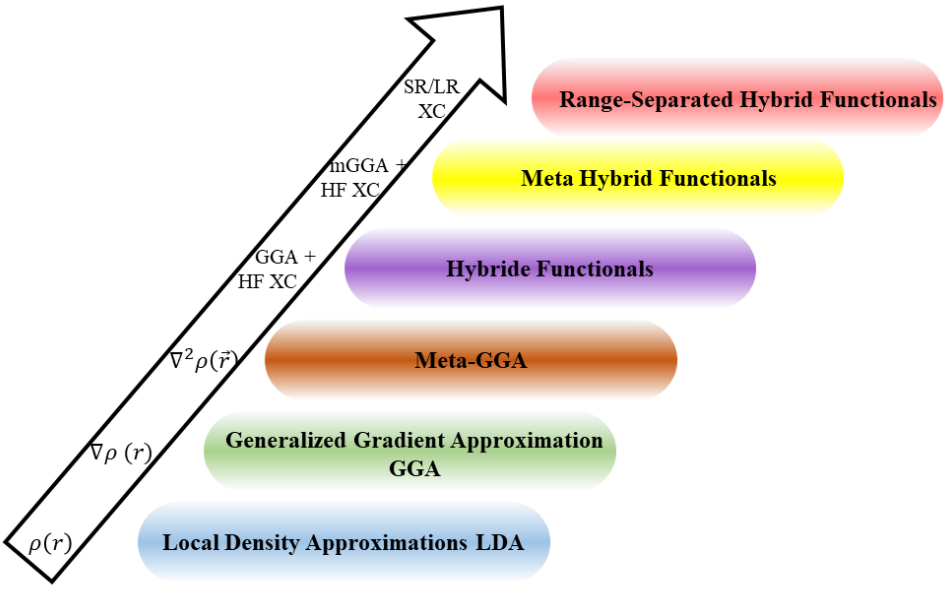

Schema I.1: Jacob's Ladder diagram of Density Functional Approximations

I.11. Conclusion

In this chapter, we delved into the intricate realm of quantum mechanics, examining essential concepts such as the Born-Oppenheimer and Hartree-Fock approximations. These theories provide a simplification of the many-body Schrödinger equation and establish a basis for comprehending complex chemical and physical phenomena.

In addition, we have unveiled the innovative concepts of DFT and the Hohenberg-Kohn theorems, which have fundamentally changed our approach to scientific inquiry. Particularly noteworthy is DFT, which has established itself as a dependable and precise technique embraced by researchers; it has turned theoretical investigation into a virtual coordination laboratory, facilitating remarkable scientific advancements. The importance of these developments in computational science cannot be overstated. They enable scientists to conduct virtual experiments, anticipate real-world results, and investigate conditions and properties that traditional experimental labs cannot access. Furthermore, these developments greatly lower the cost and time required for scientific research, making it more efficient and widely accessible. These theoretical foundations have moved beyond mere abstraction, leading to tangible scientific breakthroughs and technological innovation.

References

[1] E. Schrödinger, “Quantisierung als Eigenwertproblem,” *Ann. Phys.*, vol. 385(13), pp. 437–490, 1926, doi: 10.1007/978-3-662-47059-6_13.

[2] M. Born and R. Oppenheimer, “Born Oppenheimer,” *Ann. Phys.*, no. 20, pp. 457–484, 1927, doi: doi.org/10.1002/andp.19273892002.

[3] A. H. C. Horn, *Essentials of Computational Chemistry, Theories and Models By Christopher J. Cramer. Wiley: Chichester, England. 2002. 562 pp. ISBN 0-471-48551-9 (hardcover). $110. ISBN 0-471-48552-7 (paperback). $45.*, vol. 43, no. 5. 2003. doi: 10.1021/ci010445m.

[4] D. R. Hartree, “The Wave Mechanics of an Atom with a Non-Coulomb Central Field Part I Theory and Methods,” *Math. Proc. Cambridge Philos. Soc.*, vol. 24, no. 1, pp. 89–110, 1928, doi: 10.1017/S0305004100011919.

[5] W. Pauli, “Uber den Zusammenhang des Abschlusses der Elektronen- gruppen im Atom mit der Komplexstruktur der Spektren .,” *Zeitschrift für Phys.*, vol. 31, pp. 765–783, 1925.

[6] J. C. Slater, “PHYSICAL REVIEW,” *Phys. Rev.*, vol. 34, no. 10, pp. 1293–1322, 1929.

[7] V. W. H. Kopenhagen, “Uber den anschaulichen Inhalt der quantentheoretischen Kinematik und Mechanik.,” *Zeitschrift für Phys.*, vol. 43, pp. 172–198, 1927.

[8] W. Hohenberd, P. & Kohn, “Inhomogeneous Electron Gas,” *Phys. Rev.*, vol. 136, pp. B864–B871, 1964, doi: doi.org/10.1103/PhysRev.136.B864.

[9] W. K. AND and L. J. SHAM, “Self-Consistent Equations Including Exchange and Correlation Effects,” *Phys. Rev.*, vol. 140, no. 4A, pp. A1133–A1138, 1965, doi: 10.1103/PhysRev.140.A1133.

[10] B. Ouarda, “Etude des propriétés magnétiques des multicouches métal/oxyde,” 2017.

[11] B. E. Hao Huang, “A Density Functional Theory Study into the Mechanism and Reactivity in Heterogeneous System,” 2021.

[12] J. C. Slater, “A simplification of the Hartree-Fock method,” *Phys. Rev.*, vol. 81, no. 3, pp. 385–390, 1951, doi: 10.1103/PhysRev.81.385.

[13] S. H. Vosko, L. Wilk, and M. Nusair, “Accurate spin-dependent electron liquid

correlation energies for local spin density calculations: a critical analysis," *Can. J. Phys.*, vol. 58, no. 8, pp. 1200–1211, 1980, doi: 10.1139/p80-159.

[14] D. M. Ceperley and B. J. Alder, "Ground state of the electron gas by a stochastic method," *Phys. Rev. Lett.*, vol. 45, no. 7, pp. 566–569, 1980, doi: 10.1103/PhysRevLett.45.566.

[15] A. D. Becke, "Density-fnnctional exchange-energy approximation with correct asymptotic behavior," *Phys. Rev. A*, vol. 38, no. 6, pp. 3098–3100, 1988, doi: 10.1103/PhysRevA.38.3098.

[16] J. P. Perdew and W. Yue, "Accurate and simple density functional for the electronic exchange energy: Generalized gradient approximation," *Phys. Rev. B*, vol. 33, no. 12, pp. 8800–8802, 1986, doi: 10.1103/PhysRevB.33.8800.

[17] J. P. Perdew and Y. Wang, "Accurate and simple analytic representation of the electron-gas correlation energy," *Phys. Rev. B*, vol. 45, no. 23, pp. 13244–13249, 1992, doi: 10.5860/choice.31-4930.

[18] J. P. Perdew, K. Burke, and M. Ernzerhof, "Generalized gradient approximation made simple," *Phys. Rev. Lett.*, vol. 77, no. 18, pp. 3865–3868, 1996, doi: 10.1103/PhysRevLett.77.3865.

[19] F. Sousa, P. A. Fernandes, and M. J. Ramos, "Review article," *J. Phys. Chem. A*, vol. 111, pp. 10439–10452, 2007.

[20] H. Chermette, "La théorie fonctionnelle de la densité en chimie," *L'Act. Chim*, vol. 7, pp. 10–15, 1996.

[21] H. L. Schmider and A. D. Becke, "Chemical content of the kinetic energy density," *J. Mol. Struct. THEOCHEM*, vol. 527, no. 1–3, pp. 51–61, 2000, doi: 10.1016/S0166-1280(00)00477-2.

[22] A. D. Becke and K. E. Edgecombe, "A simple measure of electron localization in atomic and molecular systems," *J. Chem. Phys.*, vol. 92, no. 9, pp. 5397–5403, 1990, doi: 10.1063/1.458517.

[23] S. Kurth, J. P. Perdew, and P. Blaha, "Molecular and solid-state tests of density functional approximations: LSD, GGAs, and Meta-GGAs," *Int. J. Quantum Chem.*, vol. 75, no. 4–5, pp. 889–909, 1999, doi: 10.1002/(SICI)1097-461X(1999)75:4/5<889::AID-

QUA54>3.0.CO;2-8.

[24] C. Adamo, M. Ernzerhof, and G. E. Scuseria, "The meta-GGA functional: Thermochemistry with a kinetic energy density dependent exchange-correlation functional," *J. Chem. Phys.*, vol. 112, no. 6, pp. 2643–2649, 2000, doi: 10.1063/1.480838.

[25] Y. Zhao and D. G. Truhlar, "A new local density functional for main-group thermochemistry, transition metal bonding, thermochemical kinetics, and noncovalent interactions," *J. Chem. Phys.*, vol. 125, no. 19, 2006, doi: 10.1063/1.2370993.

[26] A. D. Becke, "Density-functional thermochemistry. IV. A new dynamical correlation functional and implications for exact-exchange mixing," *J. Chem. Phys.*, vol. 104, no. 3, pp. 1040–1046, 1996, doi: 10.1063/1.470829.

[27] T. Lecklider, "Maintainng a heathy rhythm," *EE Eval. Eng.*, vol. 50, no. 11, pp. 36–39, 2011.

[28] M. G. Trisolini, J. Cromwell, and G. C. Pope, "Conclusions: Planning for Second-Generation Pay for Performance," *Pay Perform. Heal. Care Methods Approaches*, no. June, pp. 341–370, 2011, doi: 10.3768/rtipress.2011.bk.0002.1103.12.

[29] N. E. Schultz, Y. Zhao, and D. G. Truhlar, "Density functional for inorganometallic and organometallic chemistry," *J. Phys. Chem. A*, vol. 109, no. 49, pp. 11127–11143, 2005, doi: 10.1021/jp0539223.

[30] T. Yanai, D. P. Tew, and N. C. Handy, "A new hybrid exchange-correlation functional using the Coulomb-attenuating method (CAM-B3LYP)," *Chem. Phys. Lett.*, vol. 393, no. 1–3, pp. 51–57, 2004, doi: 10.1016/j.cplett.2004.06.011.

[31] J. Da Chai and M. Head-Gordon, "Systematic optimization of long-range corrected hybrid density functionals," *J. Chem. Phys.*, vol. 128, no. 8, 2008, doi: 10.1063/1.2834918.

[32] J. Da Chai and M. Head-Gordon, "Long-range corrected hybrid density functionals with damped atom-atom dispersion corrections," *Phys. Chem. Chem. Phys.*, vol. 10, no. 44, pp. 6615–6620, 2008, doi: 10.1039/b810189b.

[33] Y. Zhao and D. G. Truhlar, "The M06 suite of density functionals for main group thermochemistry, thermochemical kinetics, noncovalent interactions, excited states, and

transition elements: Two new functionals and systematic testing of four M06-class functionals and 12 other function," *Theor. Chem. Acc.*, vol. 120, no. 1–3, pp. 215–241, 2008, doi: 10.1007/s00214-007-0310-x.

[34] J. Tao, J. P. Perdew, V. N. Staroverov, and G. E. Scuseria, "Climbing the density functional ladder: Nonempirical meta–generalized gradient approximation designed for molecules and solids," *Phys. Rev. Lett.*, vol. 91, no. 14, pp. 3–6, 2003, doi: 10.1103/PhysRevLett.91.146401.

[35] V. N. Staroverov, G. E. Scuseria, J. Tao, and J. P. Perdew, "Comparative assessment of a new nonempirical density functional: Molecules and hydrogen-bonded complexes," *J. Chem. Phys.*, vol. 119, no. 23, pp. 12129–12137, 2003, doi: 10.1063/1.1626543.

Chapter II

Theoretical aspects of linear and nonlinear optical phenomena

II.1. Introduction

Since their inception, lasers (with electric fields exceeding 10^4 $V \cdot cm^{-1}$) have enabled the observation of nonlinear optical (NLO) phenomena, where the external field surpasses the Coulomb force acting on atomic electrons. This breakthrough has driven significant advances across physics [1] and chemistry [2].

A core feature of NLO lies in its wavelength dependence, which has spurred the search for active media operating beyond the visible spectrum. Due to limitations in achieving direct emission across all wavelengths, frequency conversion techniques have become essential.

A pivotal experiment by Franken et al. demonstrated second-harmonic generation (SHG) using a ruby laser and quartz crystal [3], laying the foundation for modern NLO research. Since then, interest has grown in organic materials due to their broadband non-resonant response and minimal energy input. SHG and third-harmonic generation (THG) are now central to high-power laser applications. Initially dominated by semiconductors and inorganic crystals (e.g., $LiNbO_3$), the field has expanded to include organic molecular crystals with promising nonlinear efficiency [4], [5], [6], [7]. The interaction between light and NLO materials alters intrinsic properties, enabling electric field coupling and affecting optical parameters such as frequency, phase, and polarization.

This chapter provides a detailed introduction to the fundamental concepts of polarizability and nonlinear susceptibility, followed by an in-depth analysis of wave propagation phenomena in nonlinear media.

II.2. Development History of Nonlinear Optics

The evolution of nonlinear optics (NLO) passed through three main phases: theoretical prediction, applied development, and applied advancement. Two-photon absorption and the Kerr effect were important phenomena predicted before the invention of the laser in 1960; however, verification was nearly impossible without this invention. The foundational phase began with the invention of the laser (1961-1965) and during this period several nonlinear effects like frequency doubling Raman and Brillouin scattering could be observed experimentally. It got formalized into a discipline with Bloembergen's book Nonlinear Optical Phenomena published in 1965 [8]. In mature phase (1965-1984) was characterized by deeper exploration into transient coherent effects, four-wave mixing, optical bistability, solitons, and the development of theoretical models, culminating in Shen's the Principles of Nonlinear Optics

[9]. From 1984 to 2015, the field of nonlinear optics proceeded into an application expanse with several breakthroughs in semiconductor quantum structures [10], [11], organic materials [12], optical limiting [13]–[15], photorefractive effects [16], quantum optics [17], photonic crystals [18], and plasmonic technologies [19]. During this period nonlinear optics became a main driver for new advances in laser science, information processing, communication, and materials technology.

II.3. Polarizations and Susceptibilities

II.3.1. Induced Polarization by an Electromagnetic Field: Linear Approximation

The propagation of light in a transparent medium is dictated by its dielectric properties, while its interaction with an electromagnetic field at the microscopic scale is characterized by the induced polarization:

$$p = \alpha E \tag{II.1}$$

It characterizes the charge displacement and is linearly dependent on the applied electric field. When the field oscillates at a specific frequency, the induced polarization exhibits oscillations at the same frequency.

(Here, α denotes the linear polarizability, and E represents the applied electric field).

At the macroscopic scale, the polarization P of the medium is given by:

$$P = -Nex = \varepsilon_0 \chi^{(1)} E \tag{II.2}$$

where N represents the density of polarizable units in the medium (in this case, electrons), e is the elementary charge of the electron, x denotes the charge displacement induced by the field, and $\chi^{(1)}$ is the linear (first-order) susceptibility of the material.

The first-order susceptibility $\chi^{(1)}$ can be estimated using the classical model of linear polarizability, in which electrons are bound to atoms through a harmonic potential. In this model, the restoring force F acting on the electron is a linear function of its displacement x from the nucleus, expressed as ($F = kx$). Additionally, the applied electric field E exerts a force on the electron. Solving the equation of motion for the electron allows for the determination of x, and consequently, the evaluation of $\chi^{(1)}$.

At both the microscopic and macroscopic scales, the polarization of a medium is not necessarily uniform in all directions. For instance, if an external electric field E is applied along the x-axis

of a molecule, the resulting perturbation will influence the electronic distribution not only along x but also in the transverse directions y and z. Since the electric field can be applied along three mutually orthogonal directions, a complete description of polarizability requires nine independent components. This makes polarizability a tensor quantity, which can be represented as a 3×3 matrix. Consequently, it is more appropriate to express the induced polarization in the following form:

$$P_i(\omega) = \sum_j \alpha_{ij}(\omega) E_j(\omega) \tag{II.3}$$

where the indices $i,\ j$ correspond to the Cartesian axes $x,\ y$ of the reference frame associated with the molecule subjected to the electric field E.

The polarizability tensor α is presented as:

$$\alpha = \begin{pmatrix} \alpha_{xx} & \alpha_{xy} & \alpha_{xz} \\ \alpha_{yx} & \alpha_{yy} & \alpha_{yz} \\ \alpha_{zx} & \alpha_{zy} & \alpha_{zz} \end{pmatrix} \tag{II.4}$$

Isotropic polarizability (average value):

$$\bar{\alpha} = \frac{1}{3}(\alpha_{xx} + \alpha_{yy} + \alpha_{zz}) \tag{II.5}$$

Anisotropy of polarizability:

$$\Delta\alpha = \sqrt{\frac{1}{2}\left[\left(\alpha_{xx} - \alpha_{yy}\right)^2 + \left(\alpha_{yy} - \alpha_{zz}\right)^2 + (\alpha_{zz} - \alpha_{xx})^2\right] + 3\left(\alpha_{xy}^2 + \alpha_{yz}^2 + \alpha_{zx}^2\right)} \tag{II.6}$$

Polarization anisotropy is also evident at the macroscopic scale, where the induced polarization is expressed as:

$$P_i(\omega) = \varepsilon_0 \sum_j \chi_{ij}^{(1)}(\omega) E_j(\omega) \tag{II.7}$$

As a result, in optically anisotropic materials, the refractive index varies depending on the direction of propagation.

The permittivity tensor $[\varepsilon]$ (or the first-order susceptibility tensor $\chi^{(1)}$) can be diagonalized, yielding eigenvalues $\varepsilon_x, \varepsilon_y, \varepsilon_z$, which correspond to the principal dielectric axes of the material, denoted as X, Y, Z. Consequently, the refractive index of the medium depends on both the propagation direction and the polarization of the incident wave.

Specifically, when a wave propagates within a dielectric plane (*XY*, *YZ*, or *ZX*), its polarization consists of two components: a perpendicular component to the plane, for which the refractive

index remains independent of the propagation direction this is referred to as an ordinary wave and a parallel component to the plane, for which the refractive index varies with the propagation direction. This is known as an extraordinary wave. These anisotropic refractive index properties, combined with their frequency dispersion, play a crucial role in optimizing the efficiency of nonlinear interactions, particularly through phase-matching techniques.

II.3.2. Microscopic and Macroscopic Nonlinearities

At the microscopic level, the interaction of light with matter is described by the induced dipole moment μ of a molecule in an external electric field E. This dipole moment can be expanded in a power series with respect to the applied field:

$$\mu_i = \mu_i^{(0)} + \sum_j \alpha_{ij} E_j + \sum_{jk} \beta_{ijk} E_j E_k + \sum_{jkl} \gamma_{ijkl} E_j E_k E_l + \cdots \quad \text{(II.8)}$$

Where:

$\mu^{(0)}$ is the permanent dipole moment.

α is the linear polarizability tensor.

β is the first hyperpolarizability tensor (second-order NLO).

γ is the second hyperpolarizability tensor (third-order NLO).

The intrinsic nonlinear optical response of a single unit, like a molecule, bond, or chromophore, is characterized by these molecular tensors. The values of β and γ are significantly affected by the symmetries and electronic structure of the molecule.

The polarization P, which appears in Maxwell's equations and governs light propagation through the medium, is the sum of the microscopic dipole moments per unit volume:

$$P = N\left(\sum_j \alpha_{ij} E_j + \sum_{jk} \beta_{ijk} E_j E_k + \sum_{jkl} \gamma_{ijkl} E_j E_k E_l + \cdots\right) \quad \text{(II.9)}$$

Where: N is the number density of polarizable units.

and the corresponding macroscopic polarization is given by:

$$\vec{P} = P_0 + \varepsilon_0\{\chi^{(1)}\vec{E} + \chi^{(2)}\vec{E}\vec{E} + \chi^{(3)}\vec{E}\vec{E}\vec{E} + \cdots\} \quad \text{(II.10)}$$

where ε_0 is the vacuum permittivity, $\chi^{(1)}$the linear susceptibility which is directly linked to the linear refractive index n_0, $\chi^{(2)}$ and $\chi^{(3)}$respectively the second and third order nonlinear susceptibilities and E the electric field. $\chi^{(2)}$ and $\chi^{(3)}$ nonlinear optical susceptibilities are

tensors of the third and the fourth rank and contain 27 and 81 components, respectively. The susceptibilities display several forms of symmetry that are crucial in nonlinear optics: permutation symmetry, time-reversal symmetry, and spatial symmetry. While time-reversal and permutation symmetries are intrinsic characteristics of the susceptibilities, the spatial symmetry of the susceptibility tensors indicates the structural properties of the nonlinear medium. A broader symmetry principle known as overall permutation symmetry is used as an approximation when all optical fields involved in the susceptibility equations (both excitations and responses) are significantly distant from any transition, a concept initially proposed by Kleiman [20].

The first hyperpolarizability tensor β:

$$\beta = \begin{pmatrix} \beta_{xxx} & \beta_{xxy} & \beta_{xxz} & \beta_{xyx} & \beta_{xyy} & \beta_{xyz} & \beta_{xzx} & \beta_{xzy} & \beta_{xzz} \\ \beta_{yxx} & \beta_{yxy} & \beta_{yxz} & \beta_{yyx} & \beta_{yyy} & \beta_{yyz} & \beta_{yzx} & \beta_{yzy} & \beta_{yzz} \\ \beta_{zxx} & \beta_{zxy} & \beta_{zxz} & \beta_{zyx} & \beta_{zyy} & \beta_{zyz} & \beta_{zzx} & \beta_{zzy} & \beta_{zzz} \end{pmatrix} \quad \text{(II.11)}$$

The second hyperpolarizability tensor γ:

$$\gamma = \begin{pmatrix} \gamma_{xxxx} & \gamma_{xxxy} & \gamma_{xxxz} & \gamma_{xxyx} & \gamma_{xxyy} & \gamma_{xxyz} & \gamma_{xxzx} & \gamma_{xxzy} & \gamma_{xxzz} \\ \gamma_{yxxx} & \gamma_{yxxy} & \gamma_{yxxz} & \gamma_{yxyx} & \gamma_{yxyy} & \gamma_{yxyz} & \gamma_{yxzx} & \gamma_{yxzy} & \gamma_{yxzz} \\ \gamma_{zxxx} & \gamma_{zxxy} & \gamma_{zxxz} & \gamma_{zxyx} & \gamma_{zxyy} & \gamma_{zxyz} & \gamma_{zxzx} & \gamma_{zxzy} & \gamma_{zxzz} \\ \gamma_{xyxx} & \gamma_{xyxy} & \gamma_{xyxz} & \gamma_{xyyx} & \gamma_{xyyy} & \gamma_{xyyz} & \gamma_{xyzx} & \gamma_{xyzy} & \gamma_{xyzz} \\ \gamma_{yyxx} & \gamma_{yyxy} & \gamma_{yyxz} & \gamma_{yyyx} & \gamma_{yyyy} & \gamma_{yyyz} & \gamma_{yyzx} & \gamma_{yyzy} & \gamma_{yyzz} \\ \gamma_{zyxx} & \gamma_{zyxy} & \gamma_{zyxz} & \gamma_{zyyx} & \gamma_{zyyy} & \gamma_{zyyz} & \gamma_{zyzx} & \gamma_{zyzy} & \gamma_{zyzz} \\ \gamma_{xzxx} & \gamma_{xzxy} & \gamma_{xzxz} & \gamma_{xzyx} & \gamma_{xzyy} & \gamma_{xzyz} & \gamma_{xzzx} & \gamma_{xzzy} & \gamma_{xzzz} \\ \gamma_{yzxx} & \gamma_{yzxy} & \gamma_{yzxz} & \gamma_{yzyx} & \gamma_{yzyy} & \gamma_{yzyz} & \gamma_{yzzx} & \gamma_{yzzy} & \gamma_{yzzz} \\ \gamma_{zzxx} & \gamma_{zzxy} & \gamma_{zzxz} & \gamma_{zzyx} & \gamma_{zzyy} & \gamma_{zzyz} & \gamma_{zzzx} & \gamma_{zzzy} & \gamma_{zzzz} \end{pmatrix} \quad \text{(II.12)}$$

In centrosymmetric materials, all components of the $\chi^{(2)}$ tensor are zero, resulting in the absence of second-order nonlinear optical effects as well as first-order electro-optical effects in glasses; thus, alternative methods must be employed to disrupt the centrosymmetry of these materials.

II.4. Applications of Nonlinear Optics

From the present perspective, the applications of nonlinear optics primarily span three key areas: laser technology, information and communication systems, and advanced materials science.

II.4.1. Application in Laser Technology

- **New Laser Device**

Building on the principles of nonlinear optics, researchers have developed different new sorts of laser equipment, including the ultrashort pulse lasers, tunable lasers (in both wavelength and power), the stimulated Raman laser, the nonlinear fiber laser, the soliton laser, the terahertz laser, the nanoscale laser etc. Nonlinear optics also plays a crucial role in enhancing laser performance by enabling mode selection, power stabilization, and precise measurement of laser parameters.

- **Laser Pulse Compression**

Q-switching and mode-locking are key techniques rooted in nonlinear optical principles, enabling the generation of ultrashort laser pulses. These methods allow for the compression of laser pulse durations, producing pulses in the picosecond, femtosecond, and even attosecond range, which are essential for high-precision applications in science and technology.

- **Laser Frequency Conversion**

Nonlinear optical techniques such as frequency doubling, sum and difference frequency generation, parametric amplification and oscillation, third-harmonic generation, four-wave mixing, and various forms of stimulated scattering enable a wide range of laser frequency conversions.

- **Laser Transportation**

A key application of nonlinear optics in adaptive optical technology is optical phase conjugation, which is used to correct wavefront distortions. This technique is particularly valuable for compensating beam distortions during laser propagation through the atmosphere and is also applied in addressing beam distortion challenges in laser-driven nuclear fusion systems.

- **Laser Protection**

Nonlinear optics play a key role in military applications, particularly in protection against laser-based threats such as blinding weapons that use intense laser pulses to damage human eyes or sensitive photodetectors. Nonlinear optical limiters, which automatically reduce transmission at high light intensities, offer significant advantages over linear optical limiters due to their dynamic response and effectiveness over a wider range of laser intensities.

II.4.2. Application in Information Technology

- **Optical Communication**

Modern optical communication systems including fiber-optic and free-space optical communication rely heavily on nonlinear optical technologies. Key components such as semiconductor lasers, Raman optical amplifiers, optical modulators, self-focusing lenses, optical switches, wavelength converters, optical delay lines, add-drop multiplexers, and optical cross-connects all utilize nonlinear optical effects. Furthermore, advanced communication methods such as coherent optical communication, optical soliton communication, optical chaos communication, optical quantum communication, and future all-optical communication are all associated with nonlinear optics.

- **Optical Computing**

Digital optical information processing represents a promising direction for the future of information technology. Core components of next-generation optical computing such as all-optical computers, optical logic gates, 3D two-photon optical storage, optical amplifiers and all-optical switches, are fundamentally based on the principles of nonlinear optics.

- **Optical Sensing**

Distributed fiber sensors utilizing Raman and Brillouin scattering represent an emerging class of fiber-optic sensing technology. To enable fully optical sensing networks (Internet of Things) nonlinear fiber gratings are crucial for developing all-optical switches. Additionally, nonlinear optics plays a vital role in laser-based remote sensing technologies.

II.4.3. Application in Material Technology

- **High Resolution Spectrum Analysis**

By harnessing nonlinear optical effects such as stimulated Raman scattering, four-wave mixing, second-harmonic generation, and two-photon absorption triggered by ultrafast laser pulses, scientists have developed high-resolution nonlinear spectroscopic techniques. These methods offer both high spatial and temporal resolution and are widely used to study atomic and molecular structures, energy level fine structures, changes in physical and chemical clusters, and biological cell activity. When combined with near-field optical microscopy, this technology evolves into near-field spectroscopic imaging, enabling detailed analysis of nanoscale structural changes, material luminescence behavior, and chemical reaction processes.

- **Micromachining of Material**

High-precision laser direct writing, based on multiphoton absorption (like two-photon absorption) and multiphoton ionization, has become a valuable technique for fabricating nanomaterials and engineering nanoscale structures. To enhance the luminous ef fi ciency of solid light-emitting devices (LED), as well as the light absorption efficiency of solar cells, laser micromachining is an effective approach for creating microstructured patterns on device surfaces.

- **Investigation of New Material**

Nonlinear optical techniques can be applied to study a wide range of advanced materials, including low-dimensional systems such as surfaces, interfaces, and clusters; quantum-confined structures like quantum wells, quantum wires, and quantum dots; 1D, 2D, and 3D photonic crystals; surface plasmon polariton materials; nanoscale structures such as nanospheres, nanocavities, and nanotubes; materials with negative refractive indices; chiral materials; and even biological cells. These methods are also essential for measuring the nonlinear optical properties of these novel materials.

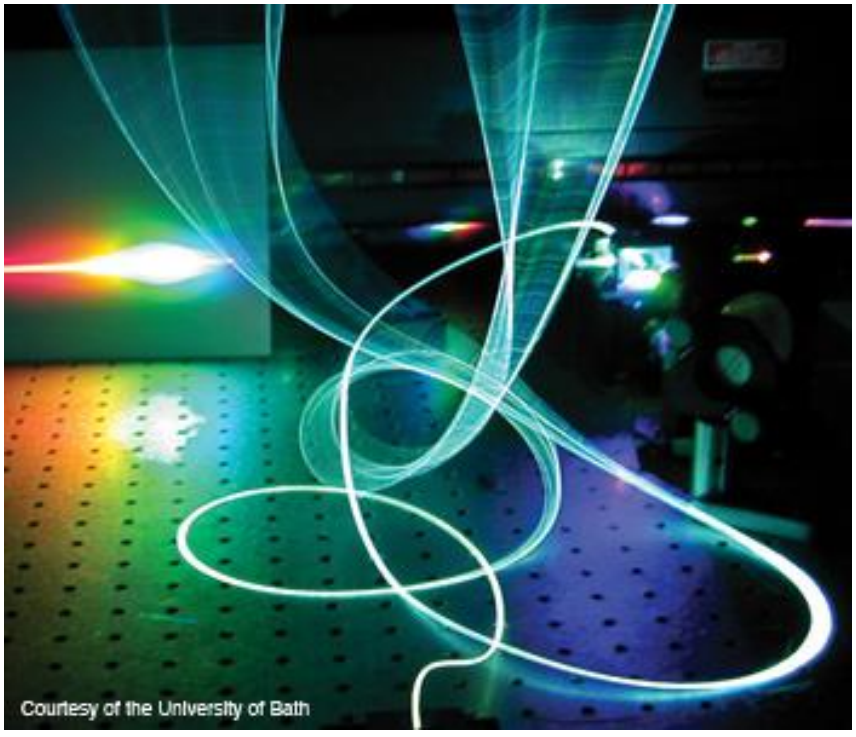

Figure.II.1: Nonlinear Optical Application in Laser Technology [21]

II.5. Nonlinear Optical Processes Classification

Nonlinear optical materials are classified according to their main type of nonlinear response: ***(a) Second-order (quadratic, χ^2) materials*** require noncentrosymmetric structures and enable key processes such as second harmonic generation (**SHG**), sum/difference frequency generation (**SFG/DFG**), optical rectification and electro-optic effects, making them indispensable for frequency conversion and high-speed optical modulators (e.g. $LiNbO_3$, KTP). ***(b) Third-order materials (cubic, χ^3)***, even when present in isotropic systems (e.g. glasses, liquids), exhibit third-harmonic generation (**THG**), four-wave mixing (**FWM**), self-phase modulation (**SPM**), optical Kerr effect and optical bistability. These form the basis for applications in purely optical switching, signal processing and nonlinear spectroscopy (e.g. silicon, CS2, nonlinear polymers). The distinction between χ^2 and χ^3 fundamentally determines the choice of materials based on symmetry constraints and the target light-matter interaction.

II.6. Computational Discovery of NLO Materials

The discovery and optimization of materials with enhanced nonlinear optical (NLO) properties have become critical goals in modern materials science. In this context, computational approaches particularly density functional theory (DFT) have emerged as indispensable tools for predicting and rationalizing the NLO response at the molecular and solid-state levels.

These methods enable accurate estimation of key parameters such as polarizability, hyperpolarizability, and electronic transition characteristics prior to synthesis, offering insight into structure–property relationships. By simulating electronic structures and optical responses, computational modeling guides experimental efforts, significantly reducing trial-and-error cycles and minimizing the cost and time associated with material screening.

Moreover, computational predictions help identify promising molecular frameworks and functional groups, evaluate the effects of substitution patterns or conjugation length, and explore the influence of electronic and geometric factors under various conditions. As a result, theoretical calculations have become a cornerstone for the rational design, control, and accelerated discovery of high-performance NLO materials, complementing and enhancing experimental research strategies.

II.6.1. NLO parameters

II.6.1.1. First hyperpolarizability:

The first hyperpolarizability β is a second-order nonlinear optical (NLO) property that describes

the response of a molecular system to an applied electric field beyond the linear regime. It is defined by the following expression:

$$< \beta >= \sqrt[2]{\beta_x^2 + \beta_y^2 + \beta_z^2} \quad \text{(II.13)}$$

The first hyperpolarizability components are expressed as:

$$\beta_x = \beta_{xxx} + \beta_{xyy} + \beta_{xzz} \quad \text{(II.14)}$$

$$\beta_y = \beta_{yyy} + \beta_{xxy} + \beta_{yzz} \quad \text{(II.15)}$$

$$\beta_z = \beta_{zzz} + \beta_{zyy} + \beta_{xxz} \quad \text{(II.16)}$$

Hyper-Rayleigh Scattering (HRS), also known as incoherent second-harmonic scattering, is a powerful experimental method used to determine the first hyperpolarizability (β_{HRS}) of molecules in solution or in isotropic media. It involves the scattering of light at twice the frequency (second harmonic) of the incident laser, arising from the nonlinear optical response of individual molecules, the β_{HRS} can be described as: [22]–[24]

$$\langle \beta_{HRS} \rangle = \sqrt{\{\langle \beta_{ZZZ}^2 \rangle + \langle \beta_{XZZ}^2 \rangle\}} \quad \text{(II.17)}$$

Here, $\langle \beta_{ZZZ}^2 \rangle$ and $\langle \beta_{XZZ}^2 \rangle$ represent the orientationally averaged components of the β tensor, computed using the following relations:

$$\langle \beta_{ZZZ}^2 \rangle = \frac{1}{7}\sum_i^{x,y,z} \beta_{iii}^2 + \frac{4}{35}\sum_{i\neq J}^{x,y,z} \beta_{iiJ}^2 + \frac{2}{35}\sum_{i\neq J}^{x,y,z} \beta_{iii}\,\beta_{ijj} + \frac{4}{35}\sum_{i\neq J}^{x,y,z} \beta_{jii}\,\beta_{iij} + \frac{4}{35}\sum_{i\neq J}^{x,y,z} \beta_{iii}\,\beta_{jji} + \frac{1}{35}\sum_{i\neq J}^{x,y,z} \beta_{Jii}^2 + \frac{4}{105}\sum_{i\neq J\neq k}^{x,y,z} \beta_{iij}\,\beta_{jkk} + \frac{1}{105}\sum_{i\neq J\neq k}^{x,y,z} \beta_{jii}\,\beta_{jkk} + \frac{4}{105}\sum_{i\neq J\neq k}^{x,y,z} \beta_{iij}\,\beta_{kkj} + \frac{2}{105}\sum_{i\neq J\neq k}^{x,y,z} \beta_{ijk}^2 + \frac{4}{105}\sum_{i\neq J\neq k}^{x,y,z} \beta_{ijk}\,\beta_{jik} \quad \text{(II.18)}$$

$$\langle \beta_{XZZ}^2 \rangle = \frac{1}{35}\sum_i^{x,y,z} \beta_{iii}^2 + \frac{4}{105}\sum_{i\neq J}^{x,y,z} \beta_{iii}\,\beta_{ijj} - \frac{2}{35}\sum_{i\neq J}^{x,y,z} \beta_{iii}\,\beta_{jji} + \frac{8}{105}\sum_{i\neq J}^{x,y,z} \beta_{iiJ}^2 + \frac{3}{35}\sum_{i\neq J}^{x,y,z} \beta_{ijj}^2 - \frac{2}{35}\sum_{i\neq J}^{x,y,z} \beta_{iij}\,\beta_{jii} + \frac{1}{35}\sum_{i\neq J\neq k}^{x,y,z} \beta_{ijj}\,\beta_{ikk} - \frac{2}{105}\sum_{i\neq J\neq k}^{x,y,z} \beta_{iik}\,\beta_{jjk} + \frac{2}{35}\sum_{i\neq J\neq k}^{x,y,z} \beta_{ijk}^2 - \frac{2}{105}\sum_{i\neq J\neq k}^{x,y,z} \beta_{iij}\,\beta_{jkk} - \frac{2}{105}\sum_{i\neq J\neq k}^{x,y,z} \beta_{ijk}\,\beta_{jik} \quad \text{(II.19)}$$

II.6.1.2. Depolarization Ratio in Nonlinear Optics

In nonlinear optics, the depolarization ratio (DR) is a key parameter for studying the symmetry and tensorial properties of the first hyperpolarizability (β). It plays a crucial role in Hyper-Rayleigh Scattering (HRS) and other second-order nonlinear processes, helping researchers analyse molecular anisotropy and validate theoretical models against experimental data.

- **Connection to Hyperpolarizability Tensor Components**

The β tensor can be decomposed into symmetry-adapted contributions, primarily:

- Dipolar (J=1): Aligned with charge asymmetry (e.g., push-pull chromophores).
- Octupolar (J=3): Higher-order symmetry (e.g., symmetric 3D structures).

A low DR suggests dominant dipolar character, while a high DR indicates strong octupolar contributions.

- **Theoretical Calculation of DR**

In quantum chemistry, β is computed using time-dependent density functional theory (TD-DFT) or response theory. The DR is derived by orientationally averaging the tensor components:

$$DR = \frac{\langle \beta_{ZZZ}^2 \rangle}{\langle \beta_{XZZ}^2 \rangle} \quad \text{(II.20)}$$

This approach allows researchers to predict DR values from first principles and compare them with experimental HRS measurements.

Typical depolarization ratio (DR) values are indicative of the underlying symmetry of the first hyperpolarizability (β) tensor in nonlinear optical systems. A DR value of approximately 1.5 is characteristic of octupolar systems (tensor rank $\beta_{j=3}$), reflecting a high degree of symmetry often observed in trigonal or tetrahedral structures. Conversely, a DR close to 5 corresponds to an ideal dipolar system, typically associated with strongly asymmetric charge distributions. In general, DR values exceeding 1.5 suggest a dipolar dominance ($\beta_{j=1}$), where the nonlinear optical response is primarily aligned with the molecular dipole moment

II.6.1.3. Second hyperpolarizability:

The second hyperpolarizability (γ) is a third-order nonlinear optical (NLO) property that describes a system's response to an external electric field beyond the linear and quadratic regimes. It plays a crucial role in phenomena such as third-harmonic generation (THG), the Kerr effect, and two-photon absorption, making it essential for the design and characterization of advanced optoelectronic and photonic materials.

The overall magnitude of γ is calculated to be [25]–[27]:

$$\gamma = \sqrt{\gamma_x^2 + \gamma_y^2 + \gamma_z^2} \quad \text{(II.21)}$$

The average second hyperpolarizability is given by the following expression:

$$< \gamma >= \frac{1}{5}\left[\gamma_{xxxx} + \gamma_{yyyy} + \gamma_{zzzz} + 2\left(\gamma_{xxyy} + \gamma_{yyzz} + \gamma_{xxzz}\right)\right] \quad \text{(II.22)}$$

The *i* components of the second hyperpolarizabilities are defined as follows:

$$\gamma_i = \frac{1}{15}\sum_{j,k}(\gamma_{jjkk} + \gamma_{jkkj} + \gamma_{jkjk}) \qquad i,j = \{x,y,z\} \quad \text{(II.23)}$$

The quadratic nonlinear refractive index $n2$ is a third-order nonlinear optical (NLO) parameter that describes the intensity-dependent change a material's refractive index. the quadratic nonlinear refractive index is one of the most important quantities in nonlinear optics, it is estimated using the second hyperpolarizability coefficients, calculated via the following equation [28]:

$$n_2(cm^2/W) = 8.28 \times 10^{-23}\gamma^{DFWM} \text{ (a.u.)} \qquad \text{(II.24)}$$

The degenerate four-wave mixing (DFWM) nonlinear susceptibility $\gamma^{DFWM}(\omega) = \gamma(-\omega;\ \omega, -\omega, \omega)$, denoted as [29]:

$$\gamma^{DFWM}(-\omega;\ \omega, -\omega, \omega) \approx (1/3)\gamma(-2\omega;\ \omega, \omega, 0) + \gamma(-\omega;\ \omega, 0, 0) \qquad \text{(II.25)}$$

II.7. Electronic transitions

The way electrons move during transition is fundamental to understanding the optical behavior of a molecule or material. These transitions are typically categorized according to the origin and destination of the charge transfer during excitation:

- Ligand-to-Metal Charge Transfer (***LMCT***): Electron density is transferred from ligand orbitals to metal centers.
- Metal-to-Ligand Charge Transfer (***MLCT***): Electron density shifts from metal orbitals to ligand orbitals.
- Ligand-to-Ligand Charge Transfer (***LLCT***): Electron density moves between different ligands, often mediated by the coordination center.
- Intramolecular Charge Transfer (***ICT***): Redistribution of electron density occurs within a single molecule, typically from donor to acceptor moieties.
- Local Excitation (***LE***): Excitation remains localized within a specific part of the molecule, with little or no charge transfer

II.7.1. Charge Transfer Descriptors

The characterization of electronic transitions can be made more precise through hole electron analysis descriptors [30], [31], which provide quantitative measures of both the nature and extent of charge transfer.

To quantify the spatial extent of charge transfer (CT) during electronic excitation, the CT length (D index) calculated as:

$$D\ index = \left[(D_x)^2 + \left(D_y\right)^2 + (D_z)^2\right]^{1/2} \qquad \text{(II.26)}$$

The spatial overlap between hole and electron densities can be quantified by:

$$S_r(r) = \sqrt{\rho^{hole}(r)\rho^{ele}(r)} \quad \text{(II.27)}$$

To characterize the overlapping extent of hole and electron, S_r index is defined as:

$$S_r(\text{index}) = \int S_r(r)dr \equiv \int \sqrt{\rho^{hole}(r)\rho^{ele}(r)}\, dr \quad \text{(II.28)}$$

The charge transfer direction (H_{CT}) can defined as:

$$H_{CT} = |H.u_{CT}| \quad \text{(II.29)}$$

u_{CT} is the unit vector in CT direction and H index displays the width of the average distribution of holes and electrons.

$t\ index$ is used to measure separation degree between the hole and electron in CT direction:

$$t\ index = D\ index - \ H_{CT} \quad \text{(II.30)}$$

The variations of dipole moment of the excited state with respect to the ground state in X, Y and Z directions can be simply calculated as

$\Delta\mu_x = (X_{ele} - X_{hole}),$ $\Delta\mu_y = -(Y_{ele} - Y_{hole}),$ $\Delta\mu_Z = -(Z_{ele} - Z_{hole})$

$$\Delta\mu = \sqrt{\Delta\mu_x^2 + \Delta\mu_x^2 + \Delta\mu_x^2} \quad \text{(II.31)}$$

The charge density difference (CDD) between excited state and ground state can be easily evaluated as

$$\Delta\rho(r) = \ \rho^{ele}(r) - \rho^{hole}(r) \quad \text{(II.32)}$$

To characterize the nature of electronic transitions in molecular systems, we examined the spatial separation of charges during excitation by analyzing hole-electron distributions. The distributions of holes and electrons are defined as follows [30], [32]

$$\rho^{hole}(r) = \sum_{i\to a}(W_i^a)^2\varphi_i(r)\varphi_i(r) + \sum_{i\to a}\sum_{j\neq i\to a} W_i^a W_j^a \varphi_i(r)\varphi_j(r) \quad \text{(II.33)}$$

$$\rho^{ele}(r) = \sum_{i\to a}(W_i^a)^2\varphi_a(r)\varphi_a(r) + \sum_{i\to a}\sum_{i\to b\neq a} W_i^a W_i^b \varphi_a(r)\varphi_b(r) \quad \text{(II.34)}$$

Where φ is the orbital wave function, W is the coefficient of excitation, *i* and *j* are the occupied orbital label, *a* and *b* are the virtual orbital label.

In our work, the crucial excited state wavefunctions have been obtained by natural transition orbitals (NTOs) in terms of "excited particle" to "empty hole" of the electronic transition density matrix. The CT indices have been determined with the MULTIWFN program. [30]

II.8. Quantum Theory of Atoms in Molecules (QTAIM)

The Quantum Theory of Atoms in Molecules (QTAIM), postulated by Richard F. W. Bader [33], is a powerful in the sense that it can provide a very detailed way of looking at and interpreting the electronic structure of any molecule. At the heart of QTAIM lies the concept of the electron density distribution, which describes how electrons are arranged in space within a molecular system.

In this approach, an atom is defined not by arbitrary boundaries such as a nucleus and its surrounding electron cloud, but by regions of space—known as atomic basins—that are uniquely determined by the topology of the electron density. Within this framework, important features of molecular structure and bonding are revealed through the analysis of critical points, which are specific locations where the gradient of the electron density goes to zero. These points are classified according to the curvature of the density:

- Nuclear Critical Points (NCPs), located at atomic nuclei and characterized by local maxima in electron density.
- Bond Critical Points (BCPs), situated along bond paths where the density exhibits a saddle point.
- Ring Critical Points (RCPs), associated with ring structures, and Cage Critical Points (CCPs), found in cage-like, three-dimensional molecular frameworks.

Additional important properties can be derived from electron density. The Laplacian of electron density allows insight into regions of electron concentration (where the Laplacian is negative) and electron depletion (where it is positive). Similarly, energy density analysis allows for a deeper understanding of the kinetic and potential energy distribution within a molecule, providing valuable information about chemical bonding and reactivity.

Using these principles, QTAIM establishes a rigorous and widely applicable framework for relating electron density to chemical structure and bonding, making it an indispensable tool in modern theoretical and computational chemistry.

II.8.1. Characterization of Bonding Interactions

II.8.1.1. Closed-Shell Interactions

Closed shell interactions mostly occur as observed in ionic bonding, van der Waals forces, and hydrogen bonding. The major characteristic of these interactions is weakness or lack of substantial sharing of electron density between the atoms involved.

II.8.1.2. Open-Shell Interactions

Open-shell interactions mostly emerge in systems that have unpaired electrons. These interactions are mostly associated with covalent bonding particularly in the case of radicals, transition metal complexes, and paramagnetic species.

II.8.1.3. Intermediate Interactions

Intermediate interactions are those that lie in between the two extremums of closed-shell (ionic or weakly interacting) and open-shell (covalent) bonding. They mostly occur in polar covalent bonds, weakly coordinated complexes, or systems possessing both ionic and covalent characteristics.

II.8.2. Bond Classification Through Topological and Energetic Parameters

The classification of bonding interactions can be rigorously established by analyzing the electron density (ρ) and its Laplacian ($\nabla^2\rho$) at Bond Critical Points (BCPs). Low electron density ($\rho < 0.1$) with a positive Laplacian ($\nabla^2\rho > 0$) is typically associated with closed-shell interactions, such as ionic bonds. In contrast, high electron density ($\rho > 0.1$) combined with a negative Laplacian ($\nabla^2\rho < 0$) is characteristic of open-shell, covalent interactions.

Espinosa and co-workers [34] introduced the ratio $|V|/G$, where V represents the potential energy density and G the kinetic energy density, as a reliable metric for classifying bonds. Within this framework:

- Closed-shell interactions: $|V|/G \leq 1$
- Intermediate interactions: $1 < |V|/G < 2$
- Open-shell interactions: $|V|/G > 2$

Further refinement was provided by Cremer and Kraka [35], who analyzed the local total electronic energy density ($H = G + V$). When H is positive, the kinetic energy dominates, indicating closed-shell interactions and weaker bonding. Conversely, negative values of H reflect the dominance of potential energy, characteristic of stronger, covalent-like open-shell interactions.

Rozas and co-workers [36] extended this approach to hydrogen bonding by incorporating both H and $\nabla^2\rho$ into their classification. They distinguished three categories:

- Strong hydrogen bonds: $H < 0$ and $\nabla^2\rho < 0$, indicative of significant electron density accumulation and strong bonding.
- Intermediate hydrogen bonds: $H < 0$ and $\nabla^2\rho > 0$, showing mixed features with moderate bond strength.

- Weak hydrogen bonds: $H > 0$ and $\nabla^2\rho > 0$, associated with electron density depletion and weak interactions.

These combined topological descriptors (ρ, $\nabla^2\rho$) and energetic criteria (H, $|V|/G$) provide a comprehensive framework for characterizing bonding interactions. The methodology has proven broadly applicable, from small inorganic molecules to complex biological systems, and effectively captures the continuum of bonding phenomena between the extremes of purely electrostatic and fully covalent interactions.

II.9. Conclusion

Nonlinear optics stands at the heart of numerous modern technological advancements, offering powerful tools for manipulating light in ways that linear optical processes cannot achieve. By exploiting nonlinear polarization phenomena governed by higher-order susceptibilities, researchers have unlocked transformative effects like harmonic generation, wave mixing, and optical soliton formation. These effects not only deepen our fundamental understanding of light–matter interaction but also lay the groundwork for practical applications in fields as diverse as telecommunications, biophotonics, and quantum information processing.

A key enabler of these phenomena is the class of materials that exhibit strong nonlinear responses. From traditional inorganic crystals like $LiNbO_3$ and BBO to emerging organic molecules, hybrid composites, and 2D materials each offering unique combinations of nonlinear efficiency, optical transparency, and integration potential, making material selection a critical step in NLO device design.

Despite significant progress, challenges remain in balancing nonlinearity, stability, processability, and compatibility with integrated platforms. However, ongoing research into new materials, nanostructures, and hybrid systems is rapidly overcoming these limitations. Looking forward, nonlinear optics is expected to play an increasingly pivotal role in future technologies from all optical computing and on-chip photonics to quantum light sources and ultrafast signal processing.

By understanding the physical principles and engineering considerations behind NLO processes and materials, researchers and engineers are better equipped to design innovative systems that leverage the full potential of nonlinear light–matter interactions.

References

[1] R. W. Boyd, *Nonlinear Optics,* Academic P. New York, 1992.

[2] E. W. M. Born, *Principales of Optics., electromagnetic theory of propagation, interférence and diffraction of light*, ”6th Editi. 1980.

[3] P. A. Franken, A. E. Hill, C. W. Peters, and G. Weinreich, “Generation of optical harmonics,” *Phys. Rev. Lett.*, vol. 7, no. 4, pp. 118–119, 1961, doi: 10.1103/PhysRevLett.7.118.

[4] M. S. Kodikara, R. Stranger, and M. G. Humphrey, “Computational studies of the nonlinear optical properties of organometallic complexes,” *Coord. Chem. Rev.*, vol. 375, pp. 389–409, 2018, doi: 10.1016/j.ccr.2018.02.007.

[5] Y. Y. Liang, B. Li, X. Xu, F. Long Gu, and C. Zhu, “A Density Functional Theory Study on Nonlinear Optical Properties of Double Cage Excess Electron Compounds: Theoretically Design M[Cu(Ag)@(NH 3) n](M = Be, Mg and Ca; n = 1–3),” *J. Comput. Chem.*, vol. 40, no. 9, pp. 971–979, 2019, doi: 10.1002/jcc.25371.

[6] N. Baggi *et al.*, “Design of cyclometallated 5-π-delocalized donor-1,3-di(2-pyridyl)benzene platinum(II) complexes with second-order nonlinear optical properties,” *Polyhedron*, vol. 140, no. Ii, pp. 74–77, 2018, doi: 10.1016/j.poly.2017.11.051.

[7] J. Zyss, “NEW ORGANIC MOLECULAR MATERIALS FOR NONLINEAR OPTIC,” vol. 47, pp. 211–226, 1982, doi: doi:10.1016/0022-3093(82)90064-3.

[8] Bloembergen, “Nonlinearn Optics A lecture Note.” 1965.

[9] R. Y. Shen, *The Principles of Nonlinear Optics*. Wiley, New York, 1984.

[10] H. H, *Optical Nonlinearities and Instabilities in Semiconductors*. Academic Press, 1998. doi: 10.1016/b978-0-12-332915-8.x5001-6.

[11] D. A. B. Miller, D. S. Chemla, D. J. Eilenberger, P. W. Smith, A. C. Gossard, and W. T. Tsang, “Large room-temperature optical nonlinearity in GaAs/Ga1-x AlxAs multiple quantum well structures,” *Appl. Phys. Lett.*, vol. 41, no. 8, pp. 679–681, 1982, doi: 10.1063/1.93648.

[12] J. ZYSS and D. S. CHEMLA, “Quadratic Nonlinear Optics and Optimization of the

Second-Order Nonlinear Optical Response of Molecular Crystals," *Nonlinear Opt. Prop. Org. Mol. Cryst.*, vol. 2, pp. 23–191, 1987, doi: 10.1016/b978-0-12-170611-1.50006-1.

[13] and L. Z. Chunfei Li, Jinhai Si, Miao Yang, Ruibo Wang, "Excited-state nonlinear absorption in multi-energy-level molecular systems," *Phys. Rev. A*, vol. 51, no. 1, pp. 569–575, 1995.

[14] L. W. Tutt and S. W. Mccahon, "Reverse saturable absorption in metal cluster compounds," vol. 15, no. 12, pp. 700–702, 1990.

[15] R. Adair, L. L. Chase, and S. A. Payne, "Nonlinear refractive-index measurements of glasses using three-wave frequency mixing - Vnl," vol. 4, no. 6, 1987.

[16] N. V. KUKHTAREV, V. B. MARKOV, S. G. ODULOV, M. S. SOSKIN, and V. L. VINETSKII, "Holographic Storage in Electrooptic Crystals.: Ii. Beam Coupling—Light Amplification," *Landmark Pap. Photorefractive Nonlinear Opt.*, no. February 2014, pp. 49–52, 1995, doi: 10.1142/9789812832047_0007.

[17] R. E. Slusher, L. W. Hollberg, B. Yurke, J. C. Mertz, and J. F. Valley, "Observation of squeezed states generated by four-wave mixing in an optical cavity," *Phys. Rev. Lett.*, vol. 55, no. 22, pp. 2409–2412, 1985, doi: 10.1103/PhysRevLett.55.2409.

[18] R. E. S. B. J. Eggleton, *Nonlinear Photonic Crystals*. Springer, 2003.

[19] G. A. Wurtz, R. Pollard, and A. V. Zayats, "Optical bistability in nonlinear surface-plasmon polaritonic crystals," *Phys. Rev. Lett.*, vol. 97, no. 5, pp. 1–4, 2006, doi: 10.1103/PhysRevLett.97.057402.

[20] D. A. Kleinman, "Nonlinear dielectric polarization in optical media," *Phys. Rev.*, vol. 126, no. 6, pp. 1977–1979, 1962, doi: 10.1103/PhysRev.126.1977.

[21] J. Hecht, "How the Laser Launched Nonlinear Optics," *Opt. Photonics News*, vol. 21, no. 11, p. 34, 2010, doi: 10.1364/opn.21.11.000034.

[22] A. Plaquet *et al.*, "In silico optimization of merocyanine-spiropyran compounds as second-order nonlinear optical molecular switches," *Phys. Chem. Chem. Phys.*, vol. 10, no. 41, pp. 6223–6232, 2008, doi: 10.1039/b806561f.

[23] N. Hou, R. Feng, and X. H. Fang, "A theoretical comparison of the electrical and

nonlinear optical properties of GDY–π–TPA: The important role of π-conjugated bridge," *Int. J. Quantum Chem.*, vol. 122, no. 19, pp. 1–14, 2022, doi: 10.1002/qua.26965.

[24] D. Kamli, D. Hannachi, and H. Chermette, "Bis-TTF-Ge derivatives: promising linear and nonlinear optical properties, a theoretical investigation," *New J. Chem.*, vol. 47, pp. 1234–1246, 2023, doi: 10.1039/d2nj03671a.

[25] H. Li, H. Xu, X. Shen, K. Han, Z. Bi, and R. Xu, "Size-, electric-field-, and frequency-dependent third-order nonlinear optical properties of hydrogenated silicon nanoclusters," *Sci Rep*, vol. 6, p. 28067, 2016, doi: 10.1038/srep28067.

[26] H. A. Kurtz, J. J. P. Stewart, and K. M. Dieter, "Calculation of the nonlinear optical properties of molecules," *J. Comput. Chem.*, vol. 11, no. 1, pp. 82–87, 1990, doi: 10.1002/jcc.540110110.

[27] D. P. Shelton and J. E. Rice, "Measurements and Calculations of the Hyperpolarizabilities of Atoms and Small Molecules in the Gas Phase," *Chem. Rev.*, vol. 94, no. 1, pp. 3–29, 1994, doi: 10.1021/cr00025a001.

[28] C. Brée, A. Demircan, and G. Steinmeyer, "Method for computing the nonlinear refractive index via Keldysh theory," *IEEE J. Quantum Electron.*, vol. 46, no. 4, pp. 433–437, 2010, doi: 10.1109/JQE.2009.2031599.

[29] M. Tarazkar, D. A. Romanov, and R. J. Levis, "Higher-order nonlinearity of refractive index: The case of argon," *J. Chem. Phys.*, vol. 140, p. 214316, 2014, doi: 10.1063/1.4880716.

[30] T. Lu and F. Chen, "Multiwfn: A multifunctional wavefunction analyzer," *J. Comput. Chem.*, vol. 33, no. 5, pp. 580–592, 2012, doi: 10.1002/jcc.22885.

[31] T. Le Bahers, C. Adamo, and I. Ciofini, "A qualitative index of spatial extent in charge-transfer excitations," *J. Chem. Theory Comput.*, vol. 7, no. 8, pp. 2498–2506, 2011, doi: 10.1021/ct200308m.

[32] Z. Liu, T. Lu, Q. Chen, T. Lu, and Q. Chen, "Journal Pre-proof," *Carbon N. Y.*, vol. 165, pp. 461–467, 2020.

[33] R. F. W. Bader, T. T. Nguyen-Dang, and Y. Tal, "Quantum topology of molecular charge distributions. II. Molecular structure and its change," *J. Chem. Phys.*, vol. 70,

no. 9, pp. 4316–4329, 1979, doi: 10.1063/1.438006.

[34] E. Espinosa, E. Molins, and C. Lecomte, "Hydrogen bond strengths revealed by topological analyses of experimentally observed electron densities," *Chem. Phys. Lett.*, vol. 285, no. 3–4, pp. 170–173, 1998, doi: 10.1016/S0009-2614(98)00036-0.

[35] D. Cremer and E. Kraka, "A Description of the Chemical Bond in Terms of Local Properties of Electron Density and Energy," *Croat. Chem. Acta*, vol. 57, no. 6, pp. 1259–1281, 1984.

[36] I. Rozas, I. Alkorta, and J. Elguero, "Behavior of ylides containing N, O, and C atoms as hydrogen bond acceptors," *J. Am. Chem. Soc.*, vol. 122, no. 45, pp. 11154–11161, 2000, doi: 10.1021/ja0017864.

Chapter III

Second and Third-Order NLO Behavior of $M@b_{64/66}Al_{12}N_{12}$

III.1. Introduction

In the search for high-performance nonlinear optical (NLO) materials, excess electron compounds have emerged as a particularly promising class due to their extraordinary electronic response properties [1]–[4]. These systems, characterized by loosely bound or diffuse excess electrons, exhibit exceptionally high electronic polarizability and pronounced charge delocalization. When subjected to an external electric field, such materials demonstrate rapid and extensive charge redistribution, resulting in dramatically enhanced hyperpolarizabilities and superior NLO performance. This unique behavior makes them ideal candidates for advanced photonic [5] and optoelectronic applications [6], [7], driving growing research interest in their design and characterization.

The search for advanced materials with superior nonlinear optical (NLO) properties has driven researchers to investigate nanostructured systems capable of strong interactions with intense electromagnetic fields [8]–[10]. In this context, transition metal-doped nanocages have gained attention as a highly promising class of NLO-active materials [10], [11]. Their appeal lies in their tunable electronic structures, high charge delocalization, and inherent symmetry-breaking features. Whether the transition metals are incorporated within the cage or on the surface, their presence can induce substantial changes in the material's electronic and optical properties. Notably, the doping introduces strong charge-transfer interactions and localized d-electron effects, which significantly boost polarizability and hyperpolarizability critical factors in determining NLO performance [12], [13].

III.2. Nanomaterials

Nanomaterials are substances with at least one dimension in the nanometer range, generally from 1 up to 100 nanometers. Generally, materials at the nanoscale possess a much greater surface area-to-volume ratio with attendant quantum effects that can greatly alter behavior and interactions

These materials are commonly classified based on their dimensions: zero-dimensional (0D) nanoparticles, one-dimensional (1D) structures like nanowires and nanotubes, two-dimensional (2D) materials such as nanofilms and nanocoatings, and three-dimensional (3D) forms like nanocomposites. Each type brings specific advantages and is suited to different technological applications, ranging from electronics to medicine.

III.2.1. Classification of Nanomaterials

A widely used classification of nanomaterials is based on their dimensionality:

- Zero-Dimensional (0D) Nanomaterials: These are materials having all the three dimensions in the nanometric scale. Examples of such materials are nanoparticles, nanospheres and nanoclusters.
- One-Dimensional (1D) Nanomaterials: These are materials that have one dimension out of the nanometric scale Examples of such materials are nanowires, nanotubes, and nanorods. One-dimensional nanomaterials are used by electronic and photonic industries applications because these facilitate electricity and light conduction by them along their length.
- Two-Dimensional (2D) Nanomaterials: These materials are characterized by having two dimensions outside the nanoscale. For example, graphene, nanofilms, and nanocoatings. Two-dimensional nanomaterials known for their outstanding mechanical strength and electrical and thermal conductivity; their applications extend from flexible electronics to barrier coatings.
- Three-Dimensional (3D) Nanomaterials: These structures have all three dimensions larger than the nanoscale, but they contain internal nanoscale features. Examples include nanocomposites and bulk nanostructured materials. By combining nanoscale functionality with bulk properties, 3D nanomaterials are valuable in structural applications and the development of advanced multifunctional materials.

III. 2.2. Nanocages: Structure and Significance

Nanocages are a class of nanoscale materials characterized by their hollow, cage-like geometries. These zero-dimensional (0D) structures often exhibit high symmetry, large surface area, and strong quantum confinement effects.

These nanostructures are commonly composed of light main-group elements such as carbon, boron, nitrogen, or metals like aluminum, and they can be either homonuclear (e.g., C_{60} fullerenes) or heteronuclear configurations (e.g., $B_{12}N_{12}$, $Al_{12}N_{12}$). Their well-defined energy levels and adjustable electronic structure contribute to strong NLO responses, especially when modified through chemical doping or functionalization.

Moreover, these nanostructures often break centrosymmetry upon doping or substitution, enabling second-order NLO effects like second harmonic generation (SHG).

III.3. $Al_{12}N_{12}$ Nanocages

Among the various heteronuclear nanocages, the $Al_{12}N_{12}$ nanocage has gained considerable attention due to its excellent thermal stability, large HOMO–LUMO gap, and adaptable structure make it a topic in materials research. Structurally analogous to $B_{12}N_{12}$, this cage consists of alternating aluminum and nitrogen atoms arranged in a fullerene-like topology with high symmetry.

The $Al_{12}N_{12}$ nanocage possesses several unique features that make it an excellent candidate for nonlinear optical applications. Its chemical robustness, derived from strong Al–N bonds, imparts high thermal and chemical stability, ensuring durability in practical device environments. The nanocage also exhibits a wide HOMO–LUMO band gap exceeding 5 eV in its pristine form, which contributes to optical transparency in the visible range and resistance to photodegradation. One of its most advantageous characteristics is its doping versatility; it can accommodate transition metals, as well as alkali and alkaline earth metals, which significantly alter its electronic distribution, reduce molecular symmetry, and promote strong intramolecular charge-transfer states factors that substantially enhance its NLO response. Additionally, the low reorganization energy associated with $Al_{12}N_{12}$ supports rapid electronic transitions, making it particularly suitable for ultrafast optical switching and other high-speed photonic applications.

III.4. Transition Metals

Transition metals, the elements occupying the d-block of the periodic table. They have unique chemical and physical properties that set them apart from other elements. Because of things like their electron structure (those partially filled ‘d-orbitals’), their ability to have different charges, and ability to form coordination complexes with diverse geometries, they're fantastic for boosting the way nanomaterials handle light and electricity. This makes them key players in advanced areas like nonlinear optics.

III.4.1. 3*d* Elements

The first-row transition metals, comprising the elements from Scandium (Sc) to Zinc (Zn), represent the 3d series of the periodic table. These elements are defined by the progressive filling of the 3d orbitals, leading to diverse oxidation states, electronic configurations, and coordination behaviors. Such properties render them exceptionally versatile in materials

chemistry, especially for applications in catalysis, magnetism, optoelectronics, and more recently, nonlinear optics (NLO).

Table II.1: Electronic Configurations and Oxidation States of 3d Transition Metals.

Elements	Symbol	Electronic configuration	Oxidation states
Scandium	Sc	[Ar] $3d^1 4s^2$	+3
Titanium	Ti	[Ar] $3d^2 4s^2$	+2, +3, +4
Vanadium	V	[Ar] $3d^3 4s^2$	+2, +3, +4, +5
Chromium	Cr	[Ar] $3d^5 4s^1$	+2, +3, +6
Magnesium	Mn	[Ar] $3d^5 4s^2$	+2,+3, +4, +7
Iron	Fe	[Ar] $3d^6 4s^2$	+2, +3
Cobalt	Co	[Ar] $3d^7 4s^2$	+2, +3
Nickel	Ni	[Ar] $3d^8 4s^2$	+2, +3
Copper	Cu	[Ar] $3d^{10} 4s^1$	+1, +2
Zinc	Zn	[Ar] $3d^{10} 4s^2$	+2

III.5. Overview of Doping Strategies in Nanocage Systems

Doping nanocages with metal atoms has become a powerful method for tailoring their electronic and optical properties. These nanostructures such as fullerenes, boron nitride cages, and silicon-based clusters are known for their exceptional structural stability and delocalized π-electron systems, which make them excellent platforms for atomic-level modifications. Introducing metal atoms into these frameworks can lead to noticeable changes in their nonlinear optical (NLO) behavior, particularly enhancing third-order effects.

There are different ways metals can be doped into nanocages: endohedral and exohedral doping. In endohedral doping, metal atoms or small clusters are trapped inside the cage (e.g., M@C_{60}) [14], which often results in strong charge transfer interactions and enhanced polarization due to the confined environment. Substitutional doping involves swapping one or more atoms in the cage structure typically boron, nitrogen, or carbon with metal atoms. This strategy is useful for

adjusting the electronic band structure and creating new active sites [15]. In exohedral doping, metal atoms are attached to the outer surface of the nanocage, which can also significantly affect the material's polarizability and electron distribution [16].

Each type of doping offers unique advantages depending on the desired application. In the context of nonlinear optics, both the type of metal and how it is incorporated into the nanocage play a critical role in determining the material's third-order hyperpolarizability, optical limiting performance, and two-photon absorption behavior. Because of these tunable properties, metal-doped nanocages are gaining attention as promising materials for advanced photonic technologies, including optical switching, sensing, and light-harvesting systems.

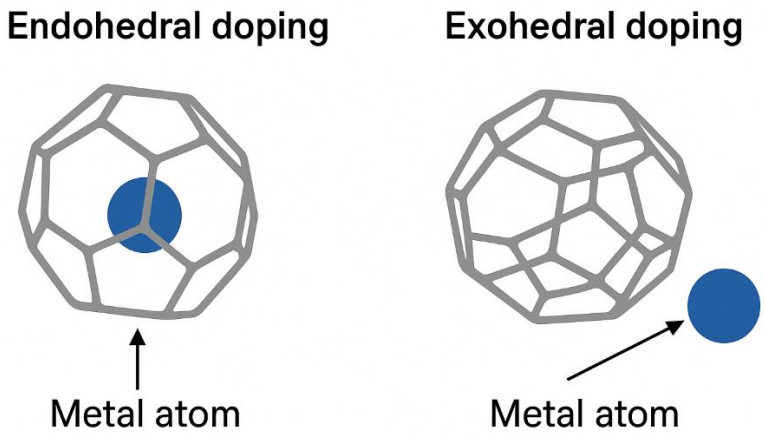

Scheme III.1: Representation of Endohedral and Exohedral Doping in Nanocages

III.5.1. $Al_{12}N_{12}$ Nanoparticles Doped with First-Row Transition Metals (Sc–Zn)

Recent advances in nanomaterial have opened exciting possibilities for enhancing nonlinear optical (NLO) properties, particularly through metal-doped nanocages and nanoparticles. Among these, the $Al_{12}N_{12}$ nanocage stands out due to its exceptional stability, wide electronic bandgap and ability to be finely tuned by doping. By introducing first-row transition metals (from Scandium to Zinc) into this cage, researchers can systematically adjust its electronic and optical properties. In this chapter, we focus on the second- and third-order NLO characteristics of transition metal-doped $Al_{12}N_{12}$ systems (denoted as $M@Al_{12}N_{12}$, where M = Sc–Zn), aiming to provide a deeper understanding of their structure-property relationships and potential application [11].

III.6. Computational method

The study conducted by Chołuj et al. demonstrates that global hybrid functionals are highly effective in precisely reproducing the absolute values of Two-Photon-Absorption strengths for donor-acceptor molecules.[17] On the other hand, long-range exchange correction have been considered the most suitable functionals to calculate spectroscopic parameters related to linear and nonlinear optical spectroscopy, such as first-and second-hyperpolarizabilities [18] probably because of the short amount of HF exchange in the short range part[19] . Prior studies have indicated that CAM-B3LYP with the 6-311+G(d) basis set, which was utilized in this study, can produce an absorption spectrum that closely resembles experimental results and has demonstrated effectiveness in calculating both static and dynamic nonlinear optical (NLO) responses [20]–[26].

III.7. Results and discussion

III.7.1 Quantum Theory Atoms in Molecules analysis

To gain deeper insight into the nature of the bonding interactions between the transition metal (M) atoms and the $Al_{12}N_{12}$ nanocage, we have carried out topological analysis of electron density on all doped geometries $M@Al_{12}N_{12}$ using the framework of the Quantum Theory of Atoms in Molecules (QTAIM) as formulated by Bader [27]–[31] using Amsterdam Density Functional (AMS) program developed by Baerends et al. [32], [33] Within the QTAIM approach, the topology of electron density is examined through the identification of critical points, specifically bond critical points (BCPs) and ring critical points (RCPs) defined as points where the gradient of the electron density is null. These critical points are classified based on several key parameters: the electron density (ρ), the Laplacian of the electron density ($\nabla^2(\rho)$), the total electron energy density (H), the kinetic electron energy density (G) and the potential electron energy density (V). [30], [34]. In the graphs, red circles indicate ring critical points (RCPs), while green circles represent bond critical points (BCPs), providing a visual map of electron density distribution and bonding pathways within the systems.

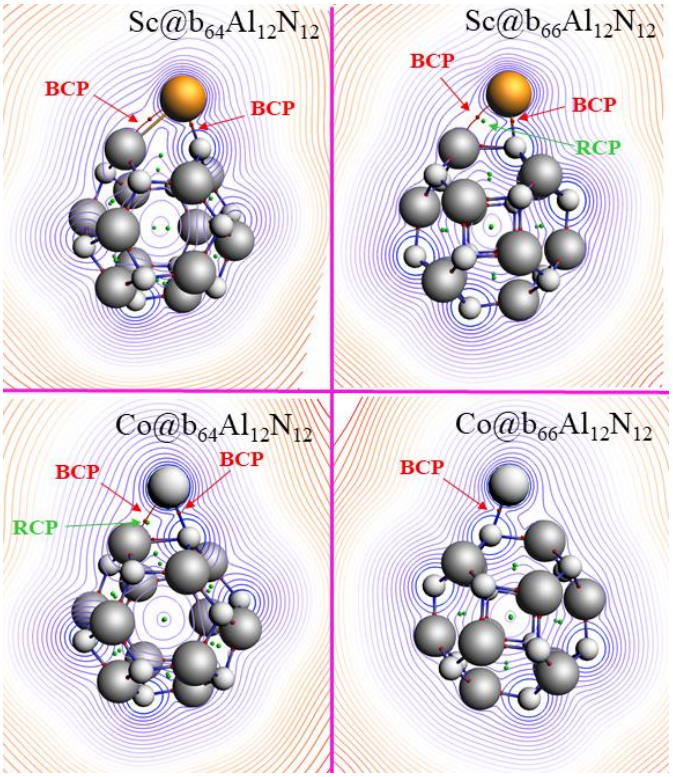

Figure III.1 Molecular topology of $Sc@Al_{12}N_{12}$ of $Co@Al_{12}N_{12}$ (b_{66} and b_{64})

Our topological analysis reveals that in several $M@Al_{12}N_{12}$ complexes specifically $Cr@b_{66}$, $Mn@b_{66}$, $Mn@b_{64}$, $Fe@b_{66}$, $Co@b_{66}$, $Ni@b_{66}$, $Zn@b_{66}$, and $Zn@b_{64}$ there is a single bond critical point (BCP) connecting the transition metal to a nitrogen atom, indicating the presence of M–N bonding. These bonds are characterized by negative values of the electron energy density (H_{BCP}) and high positive Laplacian values ($\nabla^2\rho$), suggesting a mixed covalent and electrostatic nature. However, for Mn and Zn doped systems, the M–N bond exhibits weaker, closed-shell (ionic) characteristics due to their low electron density at the BCP.

In contrast, other systems such as $M@b_{64}\,Al_{12}N_{12}$ (M = Cr, Fe, Co, Ni, Cu) and $M@b_{66}\,Al_{12}N_{12}$ (M = Sc, Ti, V) show two BCPs one between M–N and another between M–Al alongside a ring critical point (RCP), indicating a more complex bonding environment. The M–N bonds in these cases also display partial covalent character, while the M–Al bonds, with negative H_{BCP} and low $\nabla^2\rho_{BCP}$ values, are identified as mixed covalent–ionic. The covalent nature of these M–Al bonds increase in the order: Cu < Ni < Co < Fe, based on the $\frac{-V_{BCP}}{G_{BCP}}$ and H_{BCP} values.

For early transition metals (Sc, Ti, V) in the $b_{64}Al_{12}N_{12}$ cage, both M–N and M–Al interactions exhibit significant covalent character, particularly in comparison to their $b_{66}Al_{12}N_{12}$

counterparts. This is reflected in more negative H_{BCP} values, indicating stronger bonding. Notably, the Cu–N bond in Cu@b_{66} shows the highest covalent character among the late transition metals studied, with H_{BCP} (Cu–N) = –0.046 a.u., compared to weaker values observed in Zn–N and Mn–N bonds.

Table III.2 QTAIM calculated values of: the electron density (ρ, a.u.) and its Laplacian ($\nabla^2(\rho)$, a.u.), total electron energy density (H, a.u.), kinetic electron energy density (G, a.u.) and potential electron energy density (V, a.u.)

M		ρ	∇	G	V	H
$M@b_{64}Al_{12}N_{12}$						
Sc	BCP Sc-Al	0.039	-0.020	0.009	-0.024	-0.014
	BCP Sc-N	0.123	0.375	0.150	-0.208	-0.057
Ti	BCP Ti-Al	-5.361	-3.505	1.855	4.433	5.296
	BCP Ti-N	0.043	-0.025	0.011	-0.029	-0.017
V	BCP V-Al	0.139	0.413	0.177	-0.251	-0.073
	BCP V-N	-5.388	-2.708	2.680	4.048	3.057
Cr	RCP	0.048	-0.037	0.011	-0.033	-0.021
	BCP Cr-N	0.135	0.436	0.175	-0.242	-0.066
	BCP Cr-Al	-5.710	-2.914	2.795	4.312	3.326
Mn	BCP Mn-N	0.041	0.009	0.015	-0.029	-0.013
Fe	RCP	0.115	0.409	0.147	-0.192	-0.045
	BCP Fe-Al	0.041	-0.016	0.011	-0.027	-0.015
	BCP Fe-N	0.091	0.326	0.107	-0.134	-0.026
Co	RCP	0.043	0.012	0.017	-0.031	-0.014
	BCP Co-Al	0.043	0.004	0.016	-0.031	-0.015
	BCP Co-N	0.110	0.387	0.137	-0.179	-0.041
Ni	RCP	0.045	0.024	0.020	-0.035	-0.014
	BCP Ni-Al	0.045	0.018	0.019	-0.035	-0.015
	BCP Ni-N	0.111	0.406	0.141	-0.182	-0.040
Cu	RCP	0.048	0.058	0.028	-0.042	-0.013
	BCP Cu-Al	0.049	0.047	0.026	-0.041	-0.015
	BCP Cu-N	0.113	0.429	0.147	-0.188	-0.040
Zn	BCP Zn-N	0.050	0.069	0.031	-0.044	-0.013

M		ρ	∇	G	V	H
$M@b_{66}Al_{12}N_{12}$						
Sc	RCP	0.036	0.029	0.016	-0.025	-0.009
	BCP Sc-N	0.113	0.336	0.132	-0.181	-0.048
	BCP Sc-Al	0.037	-0.009	0.010	-0.022	-0.012
Ti	RCP	0.035	0.046	0.018	-0.025	-0.007
	BCP Ti-Al	0.035	-0.0005	0.011	-0.022	-0.011
	BCP Ti-N	0.110	0.329	0.127	-0.173	-0.045
V	RCP	0.042	0.016	0.017	-0.031	-0.013
	BCP V-Al	0.042	-0.012	0.012	-0.029	-0.016
	BCP V-N	0.115	0.370	0.140	-0.188	-0.047
Cr	BCP Cr-N	0.118	0.410	0.150	-0.197	-0.047
Mn	BCP Mn-N	0.093	0.332	0.111	-0.138	-0.027
Fe	BCP Fe-N	0.111	0.391	0.139	-0.181	-0.041
Co	BCP Co-N	0.112	0.410	0.143	-0.183	-0.040
Ni	BCP Ni-N	0.114	0.439	0.151	-0.192	-0.041
Cu	BCP Cu-N	0.126	0.490	0.173	-0.224	-0.050
Zn	BCP Zn-N	0.066	0.244	0.071	-0.082	-0.010

III.7.2. Electronic Spectra: UV–Vis Absorption and Excited-State Properties

To better understand the origin of the NLO behavior of the investigated complexes, TD-DFT calculations were performed. The results provide spectroscopic parameters associated with significant electronic transitions. These include the absorption wavelengths ($\lambda_{0\rightarrow n}$), oscillator strengths ($f_{0\rightarrow n}$), transition dipole moment changes

($\Delta\mu_{0\to n}$), orbital overlap integrals ($S_r(r)$), and the D and t descriptors related to charge transfer characteristics.

Table III.3 Presents the excitation wavelengths ($\lambda_{0\to n}$, in nm), oscillator strengths ($f_{0\to n}$, dimensionless), orbital overlap integrals ($S_r(r)$), and the D and t indices (in Å) corresponding to the $S_0 \rightarrow S_n$ transitions, as calculated using the CAM-B3LYP/6-311+G(d) level of theory for the studied M@b_{64}/$_{66}Al_{12}N_{12}$ complexes.

M	$S_{0\to n}$	$\lambda_{0\to n}$	$f_{0\to n}$	Sr	D	t	**M**	$S_{0\to n}$	$\lambda_{0\to n}$	$f_{0\to n}$	Sr	D	t
M@$b_{64}Al_{12}N_{12}$							**M@$b_{66}Al_{12}N_{12}$**						
Sc	$S_{0\to5}$	766	0.009	0.795	1.085	-0.434	Sc	$S_{0\to6}$	885	0.001	0.706	0.522	-0.710
	$S_{0\to13}$	463	0.144	0.578	1.187	-0.443		$S_{0\to13}$	527	0.251	0.658	1.022	-0.739
Ti	$S_{0\to5}$	996	0.005	0.597	0.628	-0.455	Ti	$S_{0\to8}$	837	<0.001	0.802	0.131	-1.166
	$S_{0\to16}$	428	0.055	0.662	1.044	-0.749		$S_{0\to13}$	590	0.177	0.670	0.853	-0.837
V	$S_{0\to5}$	822	0.001	0.596	0.442	-0.588	V	$S_{0\to7}$	859	<0.001	0.544	0.514	-0.455
	$S_{0\to15}$	407	0.116	0.757	0.896	-0.773		$S_{0\to12}$	495	0.075	0.594	1.841	-0.195
Cr	$S_{0\to1}$	917	0.001	0.602	0.558	-0.736	Cr	$S_{0\to1}$	861	<0.001	0.601	0.536	-0.723
	$S_{0\to7}$	484	0.088	0.590	1.213	-0.664		$S_{0\to7}$	495	0.097	0.579	1.409	-0.411
Mn	$S_{0\to1}$	850	0.01	0.86	0.245	-1.195	Mn	$S_{0\to1}$	845	0.011	0.858	0.332	-1.199
	$S_{0\to9}$	416	0.140	0.733	1.205	-0.443		$S_{0\to8}$	424	0.118	0.771	1.011	-0.542
Fe	$S_{0\to4}$	952	0.023	0.872	0.164	-1.171	Fe	$S_{0\to4}$	866	0.022	0.848	0.213	-1.111
	$S_{0\to9}$	512	0.057	0.486	3.156	1.111		$S_{0\to9}$	513	0.05	0.439	3.305	1.354
Co	$S_{0\to8}$	717	<0.001	0.581	0.329	-0.633	Co	$S_{0\to7}$	804	0.031	0.856	0.134	-1.170
	$S_{0\to9}$	671	0.072	0.805	0.358	-1.001		$S_{0\to9}$	510	0.049	0.438	3.214	1.260
Ni	$S_{0\to5}$	676	0.037	0.845	0.163	-1.305	Ni	$S_{0\to5}$	649	0.068	0.803	0.400	-0.940
	$S_{0\to7}$	480	0.055	0.469	3.107	1.098		$S_{0\to7}$	500	0.056	0.444	3.184	1.221
Cu	$S_{0\to1}$	591	0.076	0.726	0.667	-0.782	Cu	$S_{0\to1}$	622	0.077	0.711	0.689	-0.701
	$S_{0\to2}$	468	0.057	0.489	2.952	0.927		$S_{0\to2}$	491	0.053	0.424	3.085	1.128
Zn	$S_{0\to3}$	414	0.215	0.699	0.219	-1.546	Zn	$S_{0\to3}$	427	0.197	0.694	0.233	-1.505
	$S_{0\to5}$	372	0.09	0.413	3.057	1.006		$S_{0\to5}$	387	0.076	0.386	2.936	0.940

Materials with high first hyperpolarizability values are key components in nonlinear optics, particularly in second harmonic generation (SHG), where they enable frequency doubling (2ω). An ideal nonlinear optical (NLO) material must exhibit both a strong NLO response and high transparency at the operational laser wavelength [35]. To evaluate this, the UV–Vis–NIR absorption spectra of pristine $Al_{12}N_{12}$ and its transition metal-doped counterparts, M@$Al_{12}N_{12}$ (M = Sc to Zn, in b_{64} and b_{66} configurations).

Time-dependent density functional theory (TD-DFT) calculations were carried out using 120 excited states an adequate number for the scope of this study [36], [37]. The results indicate that the absorption spectrum of undoped $Al_{12}N_{12}$ lies within the ultraviolet region, specifically

between 170 and 300 nm. Upon incorporation of transition metals, the spectra of $M@Al_{12}N_{12}$ complexes exhibit red shifts, with absorption bands extending into the visible region.

Notably, the $Cr@b_{64/66}$, $Mn@b_{64/66}$, and $Cu@b_{64/66}$ complexes show transparent regions in the infrared (IR) region beyond 950 nm, indicating effective IR transparency. Additionally, all studied systems maintain full transparency in the deep ultraviolet range (≤ 200 nm). These optical characteristics suggest that these materials hold strong potential as high-performance NLO candidates, particularly for applications operating in the deep-UV region.

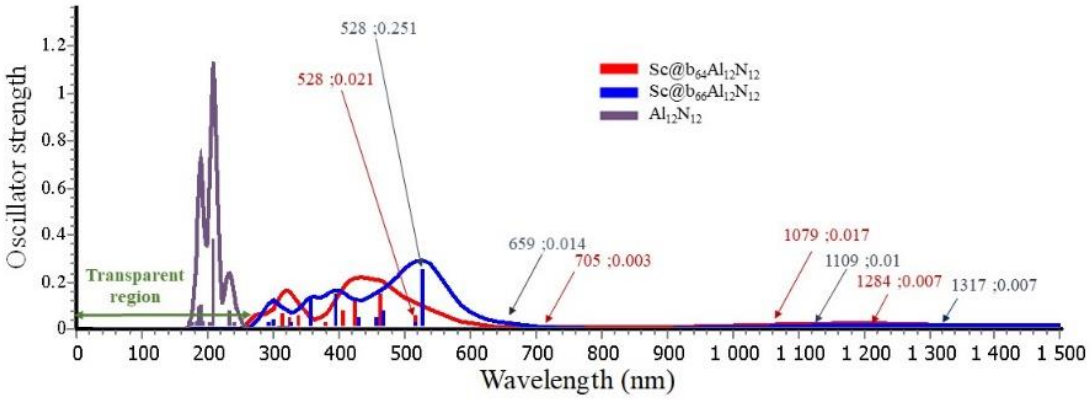

Figure III.2 Theoretical UV-Vis Absorption Spectra of $Al_{12}N_{12}$ and $Sc@b_{64/66}Al_{12}N_{12}$ Nanocages.

Distinct spectral features were observed for Sc, Ti, V, Cr, and Cu derivatives, with transitions attributed to specific HOMO–LUMO excitations. For instance, $Cu@b_{66}$ exhibits both ICT and NMCT transitions within the 328–622 nm range, while $Cr@b_{64/66}$ shows broad absorption spanning 600–900 nm, indicating strong NLO-relevant activity. In Mn, Fe, Co, and Ni-doped systems, strong absorption bands in the near-infrared (~850–950 nm) arise from local ICT within the metal centers, supported by high hole-electron overlap (Sr> 0.8), low charge separation (D < 0.4 Å), and negative centroid separation (t ≤ –1), all characteristic of local excitations. Additionally, transitions around 500 nm indicate significant MNCT contributions, while bands near 320–400 nm for Fe, Co, and Ni suggest mixed ICT/MNCT or NMCT behavior.

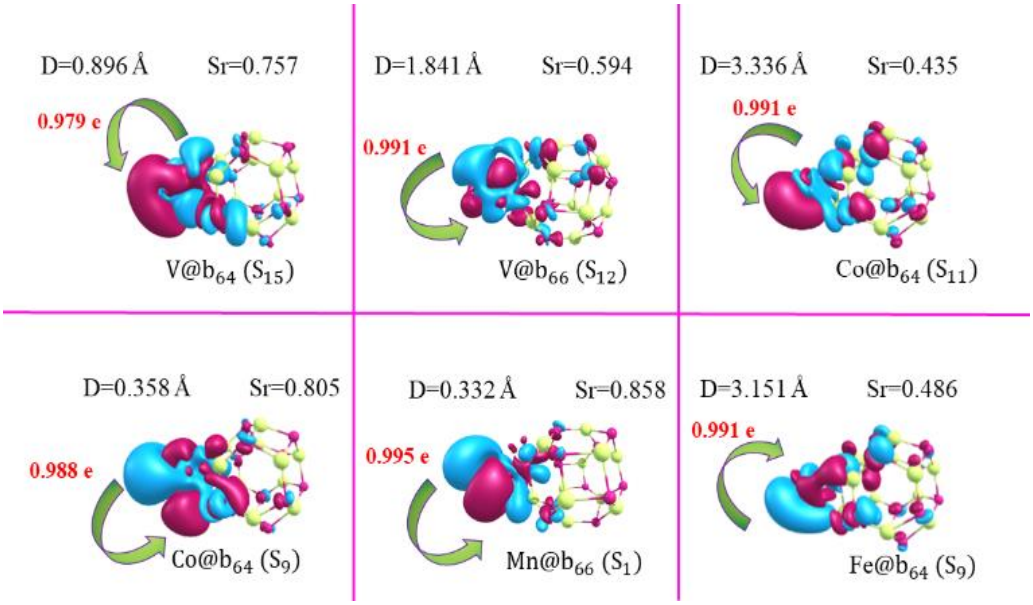

Figure III.3 Electron density difference maps of $V@b_{64}$, $V@b_{66}$, $Co@b_{64}$, $Co@b_{66}$, $Mn@b_{66}$ and $Fe@b_{64}$compounds from the ground state to the crucial excited state $S_0 \rightarrow S_n$ (S_n: S_{15}, S_{12}, S_{11}, S_9, S_1 and S_9, respectively), plotted using 0.0003 au isovalues (where pink and blue denotes the electrons and holes, respectively).

III.7.3. Nonlinear Optical Parameters

The nonlinear optical (NLO) properties of materials, particularly at the second and third order, are strongly influenced by key molecular descriptors such as the electric dipole moment, chemical hardness, and overall electronic structure.

Quantum chemical methods, especially those grounded in density functional theory (DFT), play a pivotal role in predicting and understanding these properties, offering valuable insight for guiding experimental efforts [20], [38]. Despite this, accurately modeling NLO behavior in large nanoparticle systems remains a significant computational challenge.

Table III.4 Magnetic moment, static and dynamic first hyperpolarizability (β_{HRS}, a.u), second harmonic generation [β_{SHG} (-2ω ; ω, ω), a.u], depolarization ratios (DR) and second-order hyperpolarizability ($\gamma(0\ ;\ 0,0,0)$, $\gamma(-2\omega\ ;\ \omega,\omega,0)$, $\gamma(-\omega\ ;\ \omega,0,0)$, γ^{DFWM}a.u and n_2 (cm²/W) of $M@b_{64}Al_{12}N_{12}$ nanoparticles

	$M@b_{64}Al_{12}N_{12}$	**Sc**	**Ti**	**V**	**Cr**	**Mn**	**Fe**	**Co**	**Ni**	**Cu**	**Zn**
	Most stable spin state	Doublet	Triplet	Quartet	Quintet	Sextet	Quintet	Quartet	Triplet	Doublet	Singlet
	Magnetic moment	10.439	10.479	10.519	10.559	10.599	10.639	10.679	10.72	10.759	10.800
$\lambda=\infty$	β_{HRS}^{∞}	6824	2844	1718	2022	769	813	873	923	1010	448
	DR^{∞}	7.614	7.769	7.812	7.325	3.725	3.779	5.085	5.550	5.584	5.462
	$\gamma(0\ ;\ 0,0,0)$	345236	253934	192576	267954	306434	212848	200176	200397	187169	152310
λ=1064	β_{SHG} (-2ω ; ω, ω)	391027	10472	14078	9120	20180	47175	10298	12645	17744	2609
	β_{HRS}^{λ}	236559	7129	7078	3640	8985	21727	6197	5417	7316	1136
	DR^{λ}	1.339	1.454	1.883	6.937	2.565	2.038	0.661	2.474	3.224	3.941
	$\gamma(-2\omega\ ;\ \omega,\omega,0)$	82236510	2035118	234015	1338979	4509417	16591340	4147931	1749344	1107949	360334
	$\gamma(-\omega\ ;\ \omega,0,0)$	98314110	18063860	272615	463597	685365	323649	245229	313902	290504	186927
	γ^{DFWM}	125611201	18657588	286428	820605	2086359	5783146	1561147	830217	597430	256268.333
	n_2 (cm²/W)	1.04×10^{-14}	1.54×10^{-15}	2.37×10^{-17}	6.79×10^{-17}	1.72×10^{-16}	4.78×10^{-16}	1.29×10^{-16}	6.87×10^{-17}	4.94×10^{-17}	2.1219E-17
λ=1341	β_{SHG} (-2ω ; ω, ω)	230157	47264	13401	42321	5938	4056	130387	48639	12423	1786
	β_{HRS}^{λ}	185510	19823	5857	17974	2724	2225	54858	20495	5108	747
	DR^{λ}	0.531	4.602	3.301	2.814	4.028	1.011	3.278	2.874	4.414	4.721
	$\gamma(-2\omega\ ;\ \omega,\omega,0)$	52964740	2793484	2078111	7755519	880009	986328	29036070	6279438	777884	237633
	$\gamma(-\omega\ ;\ \omega,0,0)$	65946960	502537	836282	360031	441008	206335	255234	258541	241221	171978
	γ^{DFWM}	83486794	1349053	1464793	2855886	632199	464161	9867198	2284888	438126	200419
	n_2 (cm²/W)	6.91×10^{-15}	1.11×10^{-16}	1.21×10^{-16}	2.36×10^{-16}	5.23×10^{-17}	3.84×10^{-17}	8.17×10^{-16}	1.89×10^{-16}	3.62×10^{-17}	1.6595E-17
λ=1906	β_{SHG} (-2ω ; ω, ω)	29663	716168	6097	8840	6701	10212	3446	3877	4214	1454
	β_{HRS}^{λ}	13779	317616	2370	3334	2899	8476	1473	1592	1709	592
	DR^{λ}	2.541	2.588	5.721	7.856	4.271	0.885	4.800	4.595	5.161	5.299
	$\gamma(-2\omega\ ;\ \omega,\omega,0)$	830340	732872500	271797	468308	735755	2325355	285028	294109	282428	184297
	$\gamma(-\omega\ ;\ \omega,0,0)$	3126709	1330356	211553	305011	355683	221614	221461	181224	211312	160842
	γ^{DFWM}	3288410	245536545	237960	371795	498790	925783	249745	212461	243065	171504.333
	n_2 (cm²/W)	2.72×10^{-16}	2.03×10^{-14}	1.97×10^{-17}	3.07×10^{-17}	4.13×10^{-17}	7.66×10^{-17}	2.06×10^{-17}	1.75×10^{-17}	2.01×10^{-17}	1.42×10^{-17}

Table III.5 Magnetic moment, static and dynamic first hyperpolarizability (β_{HRS}, a.u), second harmonic generation [β_{SHG} (-2ω ; ω, ω), a.u], depolarization ratios (DR) and second-order hyperpolarizability ($\gamma(0\ ;\ 0,0,0)$, $\gamma(-2\omega\ ;\ \omega,\omega,0)$, $\gamma(-\omega\ ;\ \omega,0,0)$, γ^{DFWM}a.u and n_2 (cm²/W) of $M@b_{66}Al_{12}N_{12}$ nanoparticles

	$M@b_{66}Al_{12}N_{12}$	**Sc**	**Ti**	**V**	**Cr**	**Mn**	**Fe**	**Co**	**Ni**	**Cu**	**Zn**
	Most stable spin state	Doublet	Triplet	Quartet	Quintet	Sextet	Quintet	Quartet	Triplet	Doublet	Singlet
	Magnetic moment	10.44	10.47	10.51	10.55	10.60	10.64	10.68	10.72	10.76	10.79
$\lambda=\infty$	β_{HRS}^{∞}	5857	4553	2701	2042	752	675	618	767	1012	428
	DR^{∞}	7.748	7.124	7.313	7.457	4.138	4.174	4.402	5.710	5.902	6.059
	$\gamma(0\ ;\ 0,0,0)$	334662	531334	310923	278703	321552	222456	199732	199353	195136	152891
λ=1064	β_{SHG} (-2ω ; ω, ω)	3187634	109971	51710	10250	149819	47834	36273	23244	20372	2725
	β_{HRS}^{λ}	1550925	55883	20770	4511	63933	20887	15803	9860	8468	1163
	DR^{λ}	1.746	2.885	4.882	4.064	2.806	2.340	2.393	2.653	2.886	3.982
	$\gamma(-2\omega\ ;\ \omega,\omega,0)$	155310900	26682340	822039	1915764	139672000	17137500	11033410	4442446	2299681	388926
	$\gamma(-\omega\ ;\ \omega,0,0)$	1233040	5526496	1608486	502203	752363	343558	267690	316381	319047	189152
	γ^{DFWM}	52891786	14243498	1778858	1047890	47202512	5981906	3878916	1730745	1020562	267830
	n_2 (cm²/W)	4.37×10^{-15}	1.17×10^{-15}	1.47×10^{-16}	8.67×10^{-17}	3.91×10^{-15}	4.95×10^{-16}	3.21×10^{-16}	1.43×10^{-16}	8.45×10^{-17}	2.21×10^{-17}
λ=1341	β_{SHG} (-2ω ; ω, ω)	6248106	84759	21823	39096	5895	4809	3275	36376	21939	1764
	β_{HRS}^{λ}	2587374.28	49485.370	11263.96	16938.99	2647.389	2435.229	1997.405	15324.284	9025.444	718.428
	DR^{λ}	5.005	1.946	2.569	2.394	2.813	1.604	0.617	3.215	4.169	5.087
	$\gamma(-2\omega\ ;\ \omega,\omega,0)$	32077140000	16552660	5269732	6872853	942345	755401	719943	3069455	1482664	244096
	$\gamma(-\omega\ ;\ \omega,0,0)$	18196700000	2123532	19981540	382725	475032	283100	243691	260403	258023	173415
	γ^{DFWM}	2.88×10^{10}	7463974	21634476	2580775	681963	460748	417094	1217103	687199	203816
	n_2 (cm²/W)	2.39×10^{-12}	6.18×10^{-16}	1.79×10^{-15}	2.13×10^{-16}	5.64×10^{-17}	3.81×10^{-17}	3.45×10^{-17}	1.01×10^{-16}	5.69×10^{-17}	1.68×10^{-17}
λ=1906	β_{SHG} (-2ω ; ω, ω)	8205	10900	4135	8983	6774	108286	3270	3244	4650	1423
	β_{HRS}^{λ}	4741	4247	1680	3419	2898	44318	1496	1328	1870	564
	DR^{λ}	1.010	6.705	3.706	6.743	4.448	5.150	3.664	4.821	5.244	5.834
	$\gamma(-2\omega\ ;\ \omega,\omega,0)$	892444	297653	868389	488483	797644	63013320	268039	308134	309511	186375
	$\gamma(-\omega\ ;\ \omega,0,0)$	2154396	204326	399667	320182	377603	69204200	222236	226894	222761	161804
	γ^{DFWM}	2042844	126432	585489	390108	536300	90134488	245005	263154	260886	172965
	n_2 (cm²/W)	1.69×10^{-16}	1.04×10^{-17}	4.84×10^{-17}	3.23×10^{-17}	4.44×10^{-17}	7.46×10^{-15}	2.02×10^{-17}	2.17×10^{-17}	2.16×10^{-17}	1.43×10^{-17}

In this study, we report the first hyperpolarizability $\beta^{\lambda}_{\mathrm{HRS}}$ (**Eq.II.17**) and $\beta^{\lambda}_{SHG}(-2\omega;\omega,\omega)$) (**Eq.II.13**), as well as the corresponding depolarization ratios (DR^{λ}) under both static ($\lambda = \infty$) and frequency-dependent (dynamic) conditions for all M@b_{64} and M@b_{66} $Al_{12}N_{12}$ nanostructures.

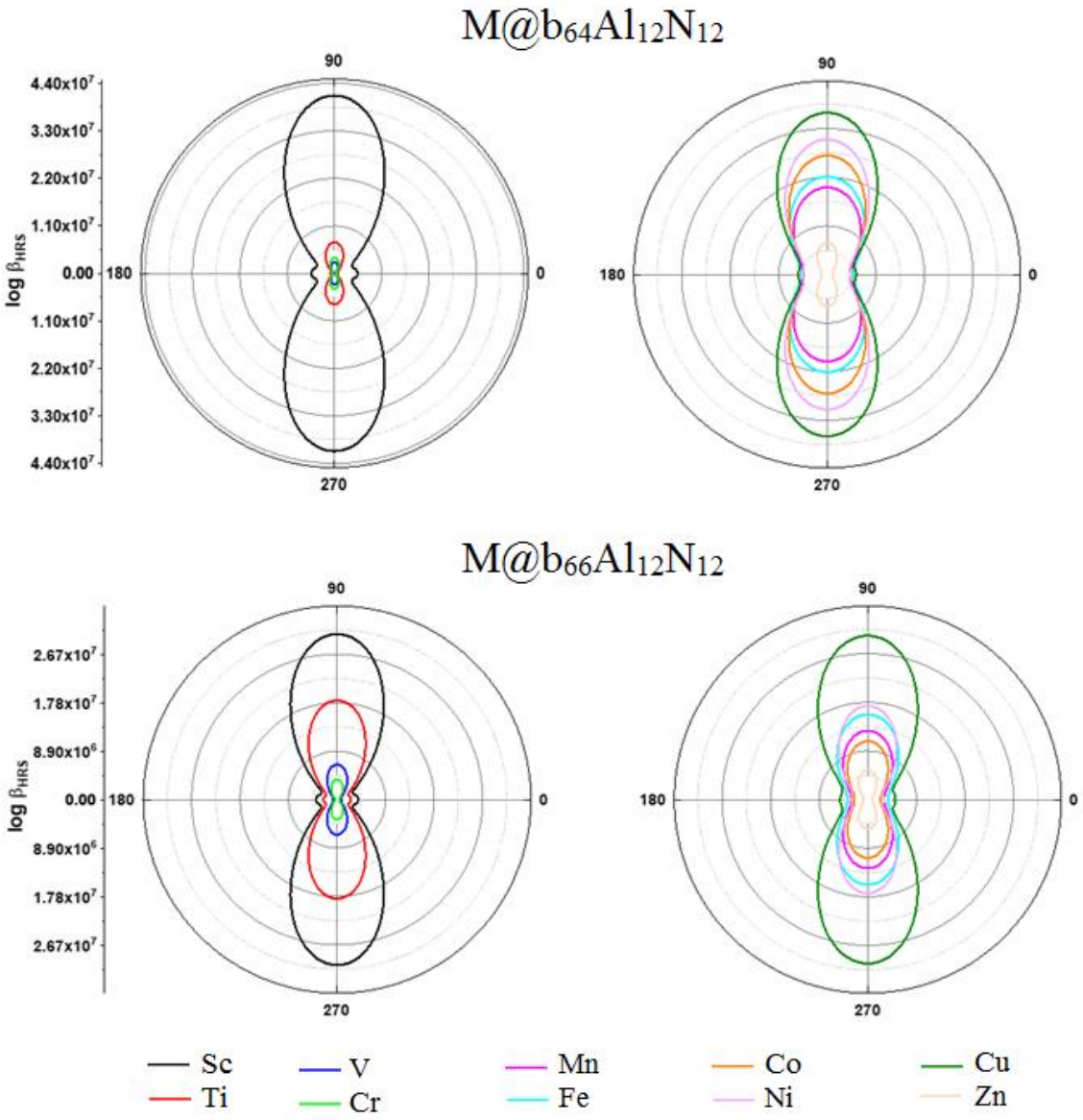

Figure III.4 Variation of hyper-Rayleigh scattering intensity $I^{2w}_{\Psi V}$ and polarization angle Ψ of $M@b_{64/66}Al_{12}N_{12}$

To explore dynamic NLO responses, three photon frequencies were employed: two laser-relevant frequencies at 0.0340 a.u. (1341 nm) and 0.0428 a.u. (1064 nm), selected to minimize resonance effects, along with a third, non-resonant frequency of 0.0239 a.u. (1906 nm) to assess low-energy field interactions.

First hyperpolarizability values (β_{HRS}^{∞}) show distinct dependencies on both dopant type and topological configuration. Notably, Ti@b_{66} $Al_{12}N_{12}$ and V@b_{66} $Al_{12}N_{12}$ exhibit approximately double the β_{HRS}^{∞} values of their $b_{64}Al_{12}N_{12}$ counterparts, suggesting that structural topology particularly the presence of a closed quasi-ring (CQR) with a ring critical point (RCP) enhances intramolecular charge transfer (ICT) and NLO response more significantly than dopant identity alone. For metals such as Fe, Co, Ni, and Cu, β_{HRS}^{∞} is greater in b_{64} $Al_{12}N_{12}$ isomers due to the CQR configuration present in these systems.

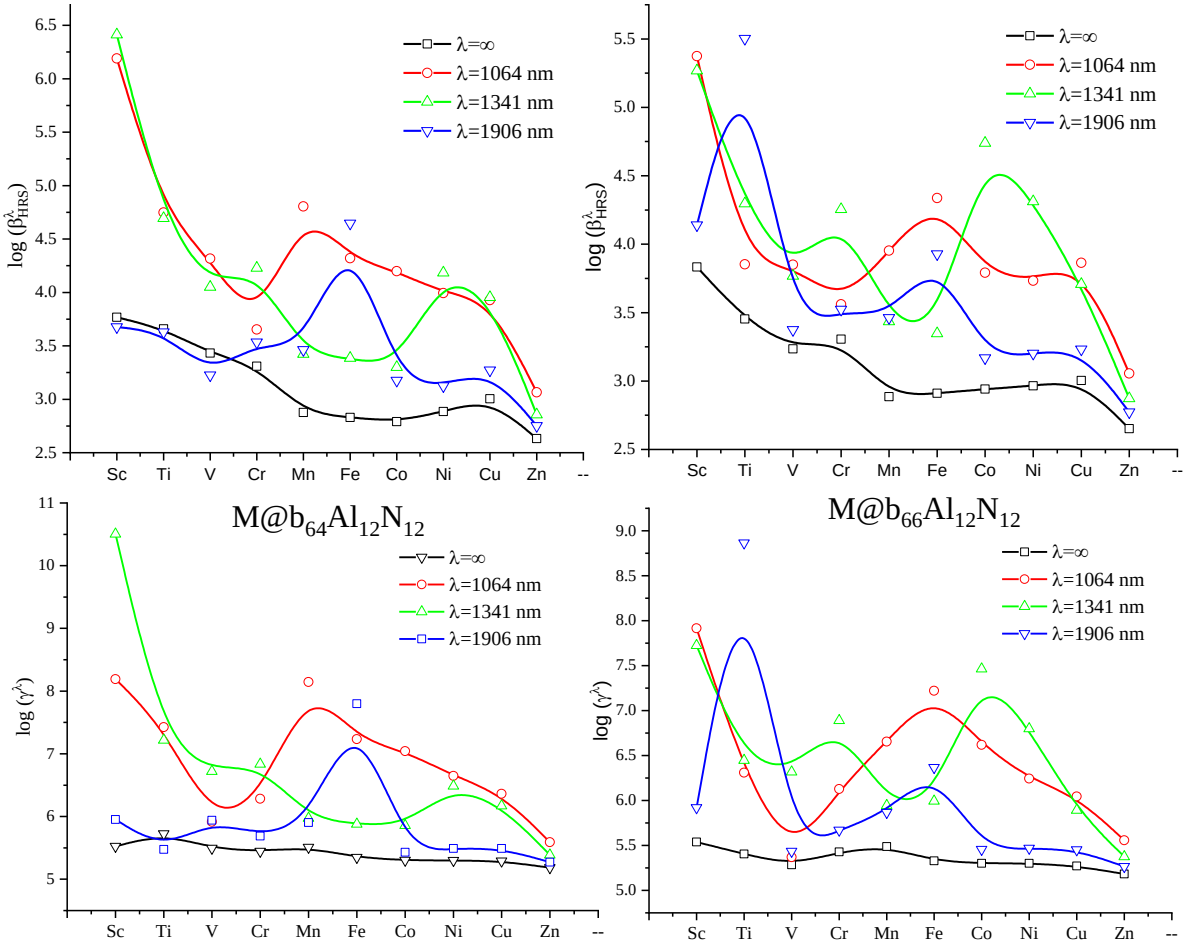

Figure III.5 Variation of static and dynamic first hyperpolarizability (β_{HRS}^{λ}) and second hyperpolarizability (γ^{λ}) of M@$b_{64}Al_{12}N_{12}$ and M@$b_{66}Al_{12}N_{12}$ (M from Sc to Zn)

Sc@b_{64} $Al_{12}N_{12}$ demonstrates the highest β_{HRS}^{∞} (6824 a.u.), nearly 15 times larger than Zn@b_{64} $Al_{12}N_{12}$, the lowest in the series. The static first hyperpolarizability trends follow:

Zn < Co < Fe < Mn < Ni < Cu < Cr < V < Ti < Sc, Among the studied M@$b_{66}Al_{12}N_{12}$ systems, follows the trend: Zn < Mn < Fe < Co < Ni < Cu < V < Cr < Ti < Sc. Polarization scans further indicate that depolarization ratios (DR) are dopant-dependent and range from 4.1 to 7.7,

consistent with a dominant dipolar NLO character. However, specific systems, particularly those involving Sc, Ti, and Co, exhibit octupolar character at certain excitation wavelengths.

A number of years ago, Hohm and Thakkar established an empirical relationship connecting atomic polarizability (α) to the second ionization potential (I_2) and the Waber–Cromer atomic radius (r_{WC}) for 101 elements ranging from helium to nobelium. This relationship is expressed as [39]:

$$\alpha = P_1 I_2^{-4} + P_2 r_{WC}^3 I_2^y \quad \text{(III.1)}$$

where the fitted parameters were $P_1 = 2.26$, $P_2 = 3.912$, and $y = 0.439$. The model suggests that atomic polarizability is largely governed by a combination of the atomic volume (r_{WC}^3) and the inverse square root dependence on the ionization potential.

Building upon this framework, we identified a similar trend in our work: the static first hyperpolarizability (β_{HRS}) of $M@b_{64}Al_{12}N_{12}$ and $M@b_{66}Al_{12}N_{12}$ nanoclusters (with M ranging from Sc to Zn) shows a strong positive correlation with the Waber–Cromer radius of the metal center. Excluding the Mn-doped systems, this correlation yields a coefficient of determination (R^2) of 0.910, indicating that atomic size is a key structural parameter influencing nonlinear optical response in these doped nanostructures.

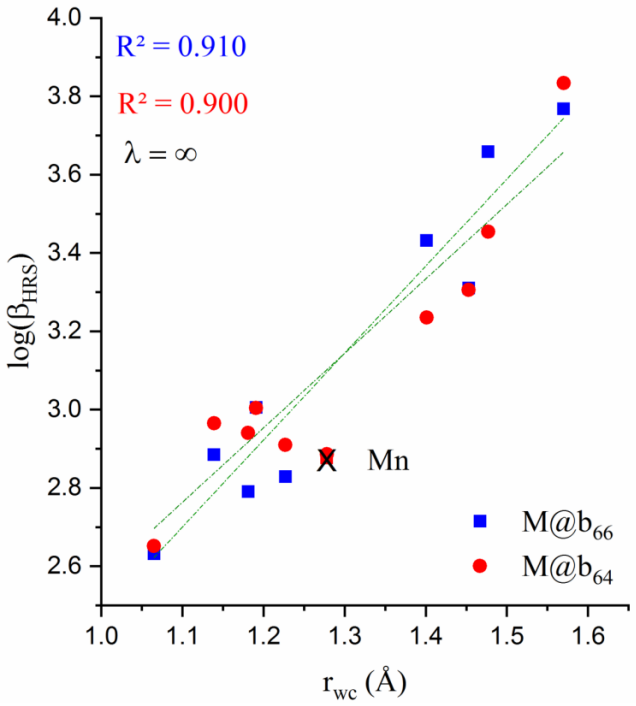

Figure III.6 Relation between the static first hyperpolarizability ($\boldsymbol{\beta_{HRS}^{\infty}}$) and Waber-Cromer radius ($\boldsymbol{r_{WC}}$)

Dynamic NLO responses were evaluated at three frequencies (λ = 1906, 1341, and 1064 nm). The results reveal that dynamic β^{λ}_{HRS} values are generally higher than their static counterparts, except for Sc@b_{66}, Ti@b_{66}, and V@b_{66} at 1906 nm. A strong linear correlation ($R^2 \approx 0.98$) was observed between β^{λ}_{HRS} and β^{λ}_{SHG} (−2ω; ω, ω), reinforcing the reliability of the data. Interestingly, β^{λ}_{SHG} values vary considerably between M@$b_{64}Al_{12}N_{12}$ and M@$b_{66}Al_{12}N_{12}$ forms, with some metals (e.g., Sc, Ti, Mn, Co) showing 2–10 times enhancements in the M@$b_{66}Al_{12}N_{12}$ structures at 1064 nm.

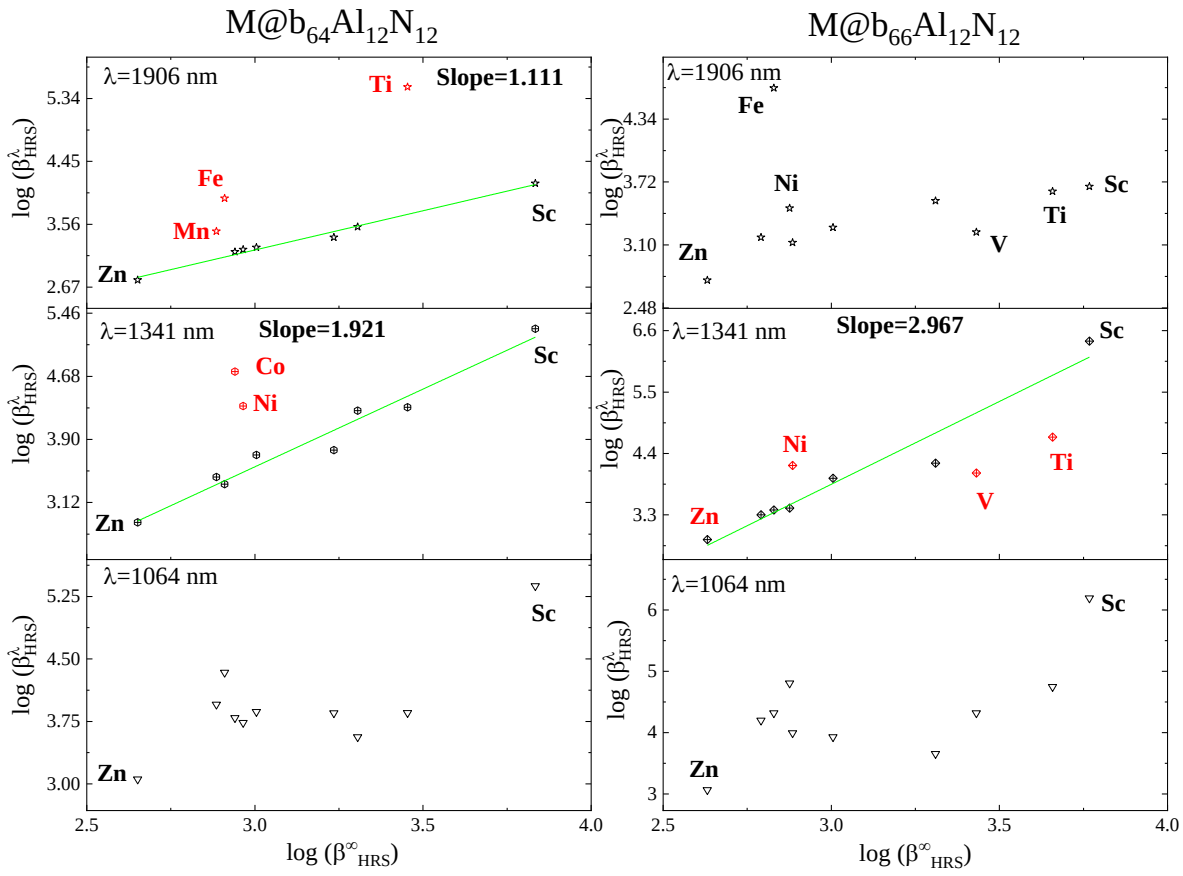

Figure III.7 The dynamic first hyperpolarizabilities of the $M@b_{64/66}Al_{12}N_{12}$ (M= Sr-Zn) versus their static value at 1906, 1341

Resonance effects at 1064 nm caused deviations from linearity in dispersion analysis, while trends at 1341 and 1906 nm remained largely consistent. These results highlight the crucial role of molecular topology, charge delocalization via CQR structures, and dopant selection in enhancing both static and frequency-dependent NLO properties, positioning M@$Al_{12}N_{12}$ nanoclusters as promising candidates for advanced photonic applications.

III.7.4. Frequency dispersion effects

The frequency dispersion factor (FDF^{λ}), describing the ratio between static and dynamic hyper-Rayleigh scattering (HRS) hyperpolarizabilities [26] ($\beta^{\lambda}_{\mathrm{HRS}}/\beta^{\infty}_{\mathrm{HRS}}$), exhibits significant wavelength-dependent variations in nanoclusters. Strong dispersion effects arise under near-resonant conditions, where one- or two-photon excitation energies align with incident light frequencies (λ = 1064, 1341, 1906 nm). Notably, Sc@b_{66}, Ti@b_{66}, and Mn@b_{66} show pronounced FDF^{λ} enhancements due to two-photon resonance ($2\omega \approx 2.33$ eV), while Sc@$b_{64/66}$ and V@b_{66} exhibit one-photon resonance ($\omega \approx 1.165$ eV). Comparative analysis reveals that structural isomerism (b_{64} vs. b_{66}) critically influences FDF^{λ} magnitudes, with Sc@b_{66} displaying a 9 times larger than that of Sc@b_{64} at 1064 nm, attributed to higher oscillator strength (f = 0.251). Conversely, off-resonant systems (e.g., V–Cr, Ni–Zn dopants at 1906 nm) exhibit modest FDF^{λ} values (0.62 to 1.8). Time-dependent DFT simulations confirm that two-photon resonance dominates β^{λ} enhancement, with oscillator strength acting as a key modulator.

III.7.5. Second Hyperpolarizability

This study investigates the second hyperpolarizability (γ) of $Al_{12}N_{12}$ and transition metal-doped M@$b_{64/66}Al_{12}N_{12}$ nanoclusters (M = Sc to Zn), both in the static regime and under frequency-dependent fields, using advanced quantum chemical methods. The static γ (0;0,0,0) values show significant enhancement upon doping with transition metals, with Ti@b_{66} exhibiting the largest increase approximately eightfold compared to the undoped system. The overall ordering of γ values reveals a strong dependence on both the dopant identity and structural isomer, highlighting the role of metal-induced electronic effects.

Dynamic third-order nonlinear optical responses were also evaluated at various wavelengths (1064, 1341, and 1906 nm), revealing that γ (−2ω; ω, ω, 0) (**Eq.II.21**) increases as the wavelength decreases, peaking at 1064 nm for most systems. Notably, Sc@b_{66} and Ti@b_{64} displayed contrasting trends, with maximum responses at 1341 and 1906 nm, respectively, indicating system-specific dispersion behaviors.

A strong linear correlation ($R^2 \approx 0.92$) between dynamic first (β^{λ}_{SHG}) and second hyperpolarizabilities ($\gamma^{\lambda}(-2\omega;\ \omega,\omega,0)$) further confirms their coupled optical behavior. The dc-Kerr effect values γ (−ω; ω, 0, 0) were also analyzed, showing enhanced responses at 1064 nm, with exceptions for Sc@b_{66}, V@$b_{64/66}$, and Fe@b_{66}, which peaked at higher wavelengths.

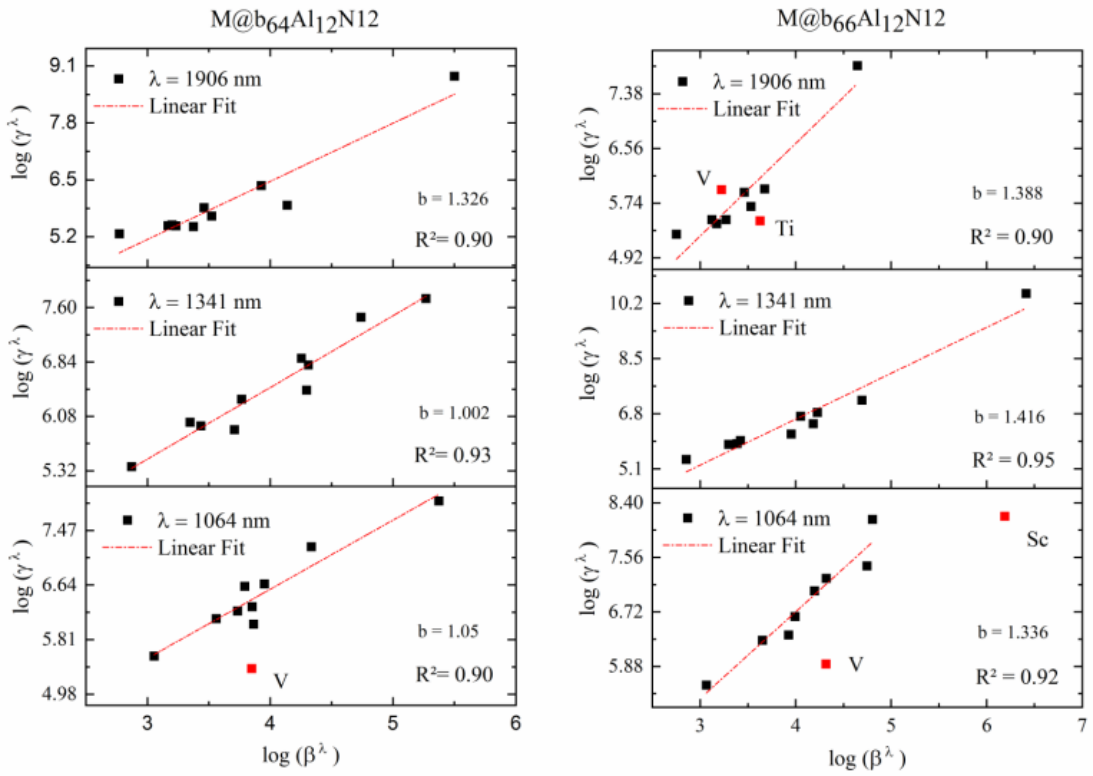

Figure III. 8 Correlation between dynamic second and third order of NLO responses of $M@b_{64/66}Al_{12}N_{12}$ (M= Sc to Zn, b = slope)

Additionally, notable values of the quadratic nonlinear refractive index (n_2) (**Eq.II.24**) were observed, particularly for Sc@b$_{66}$ at 1341 nm (2.39×10^{-12} a.u.). Most systems exhibited decreasing n_2 values with increasing wavelength, although Ti@b$_{64/66}$ and Fe@b$_{66}$ based nanoclusters showed enhanced responses at 1906 nm.

III.7.6. Two level model

To better understand the factors governing the first hyperpolarizability (β_0) of the studied systems, we employed the two-level model, which offers a simplified yet insightful framework for analyzing nonlinear optical responses. According to this model, the first hyperpolarizability is expressed as [40], [41]:

$$\beta_0 \propto \frac{f \times \Delta\mu}{\Delta E^3} \qquad \text{(III.2)}$$

where Δμ represents the change in dipole moment between the ground and the relevant excited state, f is the oscillator strength of the transition, and ΔE denotes the excitation energy. This relationship implies that systems exhibiting lower excitation energies, larger dipole moment differences, and stronger oscillator strengths will tend to have higher β_0 values.

To elucidate the origin of the variations in β_0 among the investigated compounds, the two-level model was applied (N = 120), and its predictions were compared with full theoretical calculations. Furthermore, a convergence study of the SOS approach demonstrated that β_{SOS} attains numerical stability when 120 excited states are considered, indicating that this cutoff ensures accurate and reliable evaluation of the first hyperpolarizability for the present systems.

For systems such as Fe@$b_{66}Al_{12}N_{12}$, Co@$b_{66}Al_{12}N_{12}$, Fe@$b_{64}Al_{12}N_{12}$, and Ni@$b_{64}Al_{12}N_{12}$, the dominant contributions originate from nonlocal transitions characterized by low electron-hole overlap (Sr ≈ 0.4), large charge separation (D_{index} ≈ 3.1-3.3 Å), and positive t_{index} (1< t_{index} < 1.35), indicating long-range charge transfer.

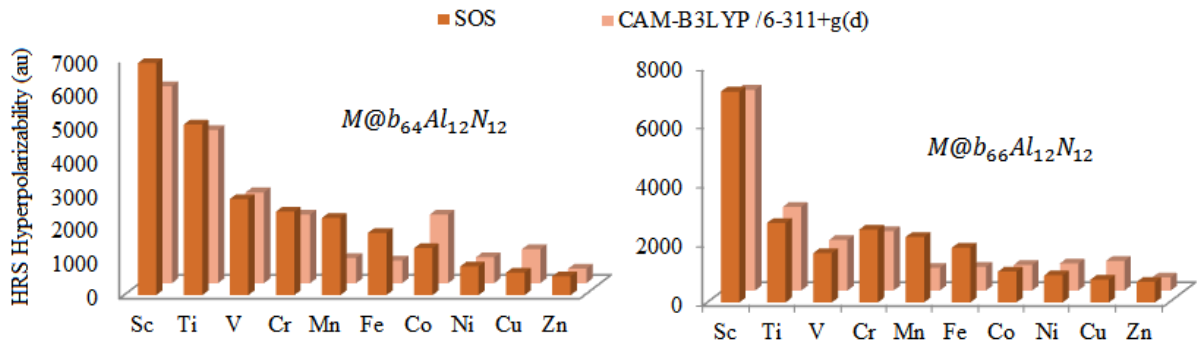

Figure III.9 Calculated static HRS-Hyperpolarizability of M@$b_{64/66}Al_{12}N_{12}$ by the different methods

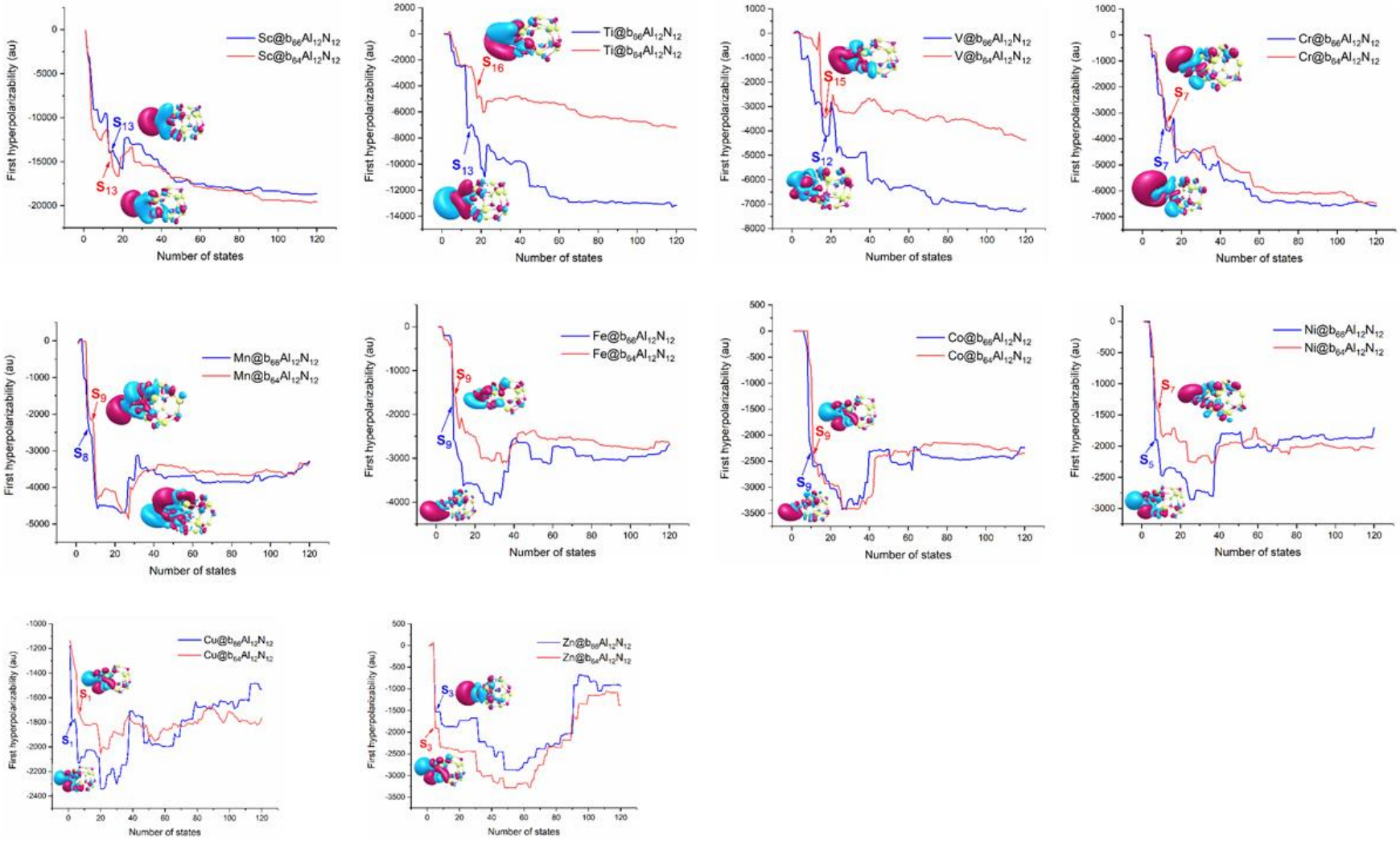

Figure III.10 Plots of static first hyperpolarizability values as computed in the SOS formalism as a function of the number of excited states for $M@b_{64/66}Al_{12}N_{12}$ (M= Sc to Zn) along with electron density difference maps, in which purple and blue colors indicate accumulation and depletion of electron density, respectively, obtained at CAM-B3LYP/6-311+G(d)

In contrast, most other doped nanoclusters, including Ti@$b_{64}Al_{12}N_{12}$, V@$b_{64}Al_{12}N_{12}$, and Cu@$b_{66}Al_{12}N_{12}$, exhibit local excitations with high overlap (Sr > 0.6), small D_{index} (0.2–1.2 Å), and negative t_{index}, suggesting that electron-hole pairs remain spatially confined. These localized transitions contribute significantly to large β values when supported by favorable oscillator strengths and low excitation energies.

The analysis further demonstrates that the first hyperpolarizability correlates strongly with the term $f/\Delta E^3$, with additional modulation by the dipole moment change (Δμ). For example, Ti@$b_{66}Al_{12}N_{12}$ and Sc@$b_{66}Al_{12}N_{12}$ show enhanced β values due to high $f/\Delta E^3$ and significant Δμ, while Zn@$b_{64/66}Al_{12}N_{12}$ shows the lowest β owing to its high excitation energy and minimal dipole difference. Comparative analyses also reveal that for systems with similar $f/\Delta E^3$ values, differences in Δμ become the deciding factor in β magnitude, as seen in V@$b_{64}Al_{12}N_{12}$ vs. V@$b_{66}Al_{12}N_{12}$ and Cu@$b_{64}Al_{12}N_{12}$ vs. Zn@$b_{64}Al_{12}N_{12}$. In cases where $I \times \Delta\mu$ values are similar, the excitation energy and oscillator strength regain importance, as demonstrated by Cr@$b_{64}Al_{12}N_{12}$ having higher β than Mn@$b_{64}Al_{12}N_{12}$ due to a lower ΔE.

Table III.6 Calculated transition energy ΔE (eV), oscillator strengths (f), transition dipole moment ($\Delta\mu_{0\to n}$, Debye) and $I = f/\Delta E^3$ of crucial excited state (S0→Sn)

M@$b_{64}Al_{12}N_{12}$							**M@$b_{66}Al_{12}N_{12}$**						
M	S_n	$\Delta E_{0\to n}$	$f_{0\to n}$	$\Delta\mu_{0\to n}$	I	$I \times \Delta\mu_{0\to n}$	**M**	S_n	$\Delta E_{0\to n}$	$f_{0\to n}$	$\Delta\mu_{0\to n}$	I	$I \times \Delta\mu_{0\to n}$
Sc	S_{13}	2.676	0.144	2.201	0.007	0.016	**Sc**	S_{13}	2.35	0.251	1.888	0.020	0.036
Ti	S_{16}	2.895	0.055	1.441	0.002	0.003	**Ti**	S_{13}	2.100	0.177	1.59	0.020	0.030
V	S_{15}	3.041	0.116	1.675	0.004	0.007	**V**	S_{12}	2.503	0.075	3.033	0.005	0.014
Cr	S_7	2.558	0.088	2.267	0.005	0.012	**Cr**	S_7	2.504	0.097	2.636	0.006	0.016
Mn	S_9	2.98	0.14	2.254	0.005	0.012	**Mn**	S_8	2.924	0.118	1.901	0.005	0.009
Fe	S_9	2.42	0.057	5.929	0.004	0.024	**Fe**	S_9	2.416	0.05	6.208	0.003	0.022
Co	S_9	1.848	0.072	0.672	0.011	0.008	**Co**	S_9	2.428	0.049	6.04	0.003	0.020
Ni	S_7	2.582	0.055	5.838	0.003	0.019	**Ni**	S_5	1.909	0.068	0.75	0.010	0.008
Cu	S_1	2.095	0.076	1.25	0.008	0.010	**Cu**	S_1	1.993	0.077	1.293	0.010	0.012
Zn	S_3	2.994	0.215	0.412	0.008	0.003	**Zn**	S_3	2.901	0.197	0.439	0.008	0.003

III.8. Conclusion

The present investigation systematically explores the molecular topology, electron delocalization characteristics, and nonlinear optical (NLO) properties specifically the first order hyperpolarizability of two series of transition metal-doped nanoclusters: $M@b_{64}Al_{12}N_{12}$ and $M@b_{66}Al_{12}N_{12}$, where M spans the 3d transition metals from Sc to Zn. Both static and dynamic NLO responses were analyzed to evaluate their potential for advanced photonic applications.

Our findings reveal that the incorporation of transition metals into the $Al_{12}N_{12}$ nanocage markedly enhances the first hyperpolarizability. This enhancement, particularly in the static regime, is closely linked to the presence of a closed quasi-ring (CQR) structure connecting the metal dopant with the nanocage. This structural motif facilitates efficient charge delocalization and contributes significantly to the nonlinear optical response. For example, $Ti@b_{66}$ displays a significantly higher static first hyperpolarizability (β_{HRS}^{∞} = 4554 a.u.) than its $Ti@b_{64}Al_{12}N_{12}$ counterpart (2844 a.u.), attributed to the presence of a CQR structure in the former.

Sum-over-states (SOS) analysis indicates that the dominant excited states contributing to the β values exhibit characteristics of local excitations, evidenced by high hole-electron overlap (S_r), small spatial separation (D_{index}), and negative t_{index} values. Additionally, UV–Vis spectral analysis shows that these nanoclusters are transparent below 200 nm, making them promising candidates for deep ultraviolet (DUV) optical devices.

In the dynamic regime, the frequency-dependent hyperpolarizabilities β_{HRS}^{λ}, β_{SHG}^{λ} (−2ω; ω, ω), are consistently higher than their static counterparts. This enhancement is attributed to strong one and two photon resonance effects, with the latter playing a more significant role in boosting dynamic NLO responses. The findings highlight the critical contribution of strong oscillator strengths and resonance conditions in maximizing NLO performance under laser excitation.

Beyond theoretical predictions, the practical relevance of these findings is underscored by the growing importance of picosecond and femtosecond laser technologies. These ultrafast lasers are widely applied in microfabrication, surface modification, corrosion resistance enhancement, and 3D nanostructure fabrication, demonstrating the relevance of materials with strong ultrafast NLO properties.

Finally, our analysis reveals a novel correlation between the static first hyperpolarizability of $M@b_{64/66}Al_{12}N_{12}$ and the Waber–Cromer atomic radius of the transition metal, suggesting that

atomic size plays a predictive role in tuning NLO behavior. Additionally, in the dynamic regime, offering new insights into structure property relationships in metal-doped nanoclusters.

References

[1] A. Ahsin and K. Ayub, "Remarkable electronic and NLO properties of bimetallic superalkali clusters: a DFT study," *J. Nanostructure Chem.*, no. 0123456789, 2021, doi: 10.1007/s40097-021-00429-2.

[2] A. Ahsan and K. Ayub, "Adamanzane based alkaline earthides with excellent nonlinear optical response and ultraviolet transparency," *Opt. Laser Technol.*, vol. 129, no. March, p. 106298, 2020, doi: 10.1016/j.optlastec.2020.106298.

[3] A. Ahsan, S. Sarfaraz, F. Fayyaz, M. Asghar, and K. Ayub, "Enhanced non-linear optical response of calix[4]pyrrole complexant based earthides in the presence of oriented external electric field," *J. Mol. Liq.*, vol. 350, p. 118504, 2022, doi: 10.1016/j.molliq.2022.118504.

[4] A. Ahsan and K. Ayub, "Extremely large nonlinear optical response and excellent electronic stability of true alkaline earthides based on hexaammine complexant," *J. Mol. Liq.*, vol. 297, pp. 36–40, 2020, doi: 10.1016/j.molliq.2019.111899.

[5] N. Baggi *et al.*, "Design of cyclometallated 5-π-delocalized donor-1,3-di(2-pyridyl)benzene platinum(II) complexes with second-order nonlinear optical properties," *Polyhedron*, vol. 140, no. Ii, pp. 74–77, 2018, doi: 10.1016/j.poly.2017.11.051.

[6] M. S. Kodikara, R. Stranger, and M. G. Humphrey, "Computational studies of the nonlinear optical properties of organometallic complexes," *Coord. Chem. Rev.*, vol. 375, pp. 389–409, 2018, doi: 10.1016/j.ccr.2018.02.007.

[7] Y. Y. Liang, B. Li, X. Xu, F. Long Gu, and C. Zhu, "A Density Functional Theory Study on Nonlinear Optical Properties of Double Cage Excess Electron Compounds: Theoretically Design M[Cu(Ag)@(NH 3) n](M = Be, Mg and Ca; n = 1–3)," *J. Comput. Chem.*, vol. 40, no. 9, pp. 971–979, 2019, doi: 10.1002/jcc.25371.

[8] D. Paul, J. Deb, and U. Sarkar, "A Detailed DFT Study on Electronic Structures and Nonlinear Optical Properties of Doped C 30," *ChemistrySelect*, vol. 5, pp. 6987–6999, 2020, doi: 10.1002/slct.202001988.

[9] F. Khaliq, T. Mahmood, K. Ayub, S. Tabassum, and M. Amjad, "Exploring Li 4 N and Li 4 O superalkalis as efficient dopants for the Al 12 N 12 nanocage to design high

performance nonlinear optical materials with high thermodynamic stability," *Polyhedron*, vol. 200, p. 115145, 2021.

[10] Y. Arshad, M. Asghar, M. Yar, T. Bibi, and K. Ayub, "Transition Metal Doped Boron Nitride Nanocages as High Performance Nonlinear Optical Materials: A DFT Study," *J. Inorg. Organomet. Polym. Mater.*, 2023, doi: 10.1007/s10904-023-02546-7.

[11] Y. Arshad, S. Khan, M. A. Hashmi, and K. Ayub, "Transition metal doping: A new and effective approach for remarkably high nonlinear optical response in aluminum nitride nanocages," *New J. Chem.*, vol. 42, no. 9, pp. 6976–6989, 2018, doi: 10.1039/c7nj04971d.

[12] P. N. Prasad, *Introduction to biophotonics*. 2003.

[13] S. Thakur, S. M. Borah, A. Singh, and N. C. Adhikary, "Investigating the electronic and nonlinear optical properties of fullerene by substituting N, P, As, and Sb in the lattice structure: a DFT study," *Appl. Phys. A Mater. Sci. Process.*, vol. 126, no. 2, 2020, doi: 10.1007/s00339-020-3300-7.

[14] N. M. Umran, N. Kaur, K. Seema, and R. Kumar, "Study of endohedral doped C60 fullerene using model potentials," *Mater. Res. Express*, vol. 2, no. 5, p. 55603, 2015, doi: 10.1088/2053-1591/2/5/055603.

[15] Y. Chen, C. R. Cho, and S. Manzhos, "Lithium attachment to C60 and nitrogen- and boron-doped C60: A mechanistic study," *Materials (Basel).*, vol. 12, no. 13, pp. 1–12, 2019, doi: 10.3390/ma12132136.

[16] S. Khan, M. A. Gilani, S. Munsif, S. Muhammad, R. Ludwig, and K. Ayub, "Inorganic electrides of alkali metal doped Zn12O12 nanocage with excellent nonlinear optical response," *J. Mol. Graph. Model.*, vol. 106, no. May, p. 107935, 2021, doi: 10.1016/j.jmgm.2021.107935.

[17] M. Chołuj *et al.*, "Choosing Bad versus Worse: Predictions of Two-Photon-Absorption Strengths Based on Popular Density Functional Approximations," *J. Chem. Theory Comput.*, vol. 18, no. 2, pp. 1046–1060, Feb. 2022, doi: 10.1021/acs.jctc.1c01056.

[18] P. Besalú-Sala, S. P. Sitkiewicz, P. Salvador, E. Matito, and J. M. Luis, "A new tuned range-separated density functional for the accurate calculation of second hyperpolarizabilities," *Phys. Chem. Chem. Phys.*, vol. 22, no. 21, pp. 11871–11880, Jun.

2020, doi: 10.1039/d0cp01291b.

[19] D. Grabarek and T. Andruniow, "Assessment of functionals for TDDFT calculations of one- and two-photon absorption properties of neutral and anionic fluorescent proteins chromophores," *J. Chem. Theory Comput.*, vol. 15, pp. 490–508, 2019, doi: 10.1021/acs.jctc.8b00769.

[20] D. Kamli, D. Hannachi, and H. Chermette, "Bis-TTF-Ge derivatives: promising linear and nonlinear optical properties, a theoretical investigation," *New J. Chem.*, vol. 47, pp. 1234–1246, 2023, doi: 10.1039/d2nj03671a.

[21] S. Irshad, F. Ullah, S. Khan, R. Ludwig, and T. Mahmood, "First row transition metals decorated boron phosphide nanoclusters as nonlinear optical materials with high thermodynamic stability and enhanced electronic properties ; A detailed quantum chemical study," *Opt. Laser Technol. J.*, vol. 134, pp. 106570–9, 2021.

[22] Maria, J. Iqbal, and K. Ayub, "Theoretical study of the non linear optical properties of alkali metal (Li, Na, K) doped aluminum nitride nanocages," *RSC Adv.*, vol. 6, no. 96, pp. 94228–94235, 2016, doi: 10.1039/c6ra21797d.

[23] S. Sarwar *et al.*, "Deciphering the Role of Alkali Metals (Li, Na, K) Doping for Triggering Nonlinear Optical (NLO) Properties of T-Graphene Quantum Dots: Toward the Development of Giant NLO Response Materials," *ACS Omega*, vol. 7, no. 28, pp. 24396–24414, 2022, doi: 10.1021/acsomega.2c01746.

[24] L. M. G. Abegaõ *et al.*, "First molecular electronic hyperpolarizability of series of π-conjugated oxazole dyes in solution: An experimental and theoretical study," *RSC Adv.*, vol. 9, no. 45, pp. 26476–26482, 2019, doi: 10.1039/c9ra05246a.

[25] H. M. He, H. Yang, Y. Li, and Z. R. Li, "Theoretical Study of Alkaline-Earth Metal (Be, Mg, and Ca)-Substituted Aluminum Nitride Nanocages With High Stability and Large Nonlinear Optical Responses," *Front. Chem.*, vol. 10, no. June, pp. 1–10, 2022, doi: 10.3389/fchem.2022.918704.

[26] L. Lescos *et al.*, "Performance of DFT functionals for calculating the second-order nonlinear optical properties of dipolar merocyanines," *Phys. Chem. Chem. Phys.*, vol. 22, no. 29, pp. 16579–16594, 2020, doi: 10.1039/d0cp02992k.

[27] R. F. W. Bader, T. T. Nguyen-Dang, and Y. Tal, "Quantum topology of molecular charge

distributions. II. Molecular structure and its change," *J. Chem. Phys.*, vol. 70, no. 9, pp. 4316–4329, 1979, doi: 10.1063/1.438006.

[28] R. F. W. Bader, "A Quantum Theory of Molecular Structure and Its Applications," *Chem. Rev.*, vol. 91, no. 5, pp. 893–928, 1991, doi: 10.1021/cr00005a013.

[29] R. F. W. Bader, "Atoms-in-molecules," *Acc. Chem*, vol. 18, no. 1, pp. 9–15, 1985, doi: 10.1021/ar00109a003.

[30] P. S. V. Kumar, V. Raghavendra, and V. Subramanian, "Bader's Theory of Atoms in Molecules (AIM) and its Applications to Chemical Bonding," *J. Chem. Sci.*, vol. 128, no. 10, pp. 1527–1536, 2016, doi: 10.1007/s12039-016-1172-3.

[31] D. Hannachi, N. Ouddai, M. Arotçaréna, and H. Chermette, "Addition-fragmentation reaction of thionoesters compounds in free-radical polymerisation (methyl, cyanomethyl and styryl): A theoretical interpretation," *Mol. Phys.*, vol. 113, no. 13–14, pp. 1541–1550, 2015, doi: 10.1080/00268976.2014.985275.

[32] G. te Velde *et al.*, "Chemistry with ADF," *J. Comput. Chem.*, vol. 22, no. 9, pp. 931–967, 2001, doi: 10.1002/jcc.1056.

[33] H. scm. co. ADF2016, SCN, Theoretical Chemistry, Vrije Universiteit, Amsterdam, The Netherlands *et al.*, "Adf2016," *Theor. Chem. Acc.*, vol. 99, no. 9, pp. 931–967, 1998, [Online]. Available: http://doi.wiley.com/10.1002/jcc.1056%0Ahttp://dx.doi.org/10.1007/s002140050353%0Ahttp://www.scm.com

[34] E. Espinosa, I. Alkorta, J. Elguero, and E. Molins, "From weak to strong interactions: A comprehensive analysis of the topological and energetic properties of the electron density distribution involving X-H···F-Y systems," *J. Chem. Phys.*, vol. 117, no. 12, pp. 5529–5542, 2002, doi: 10.1063/1.1501133.

[35] R. Arun Kumar, M. Arivanandhan, and Y. Hayakawa, "Recent advances in rare earth-based borate single crystals: Potential materials for nonlinear optical and laser applications," *Prog. Cryst. Growth Charact. Mater.*, vol. 59, no. 3, pp. 113–132, 2013, doi: 10.1016/j.pcrysgrow.2013.07.001.

[36] F. Ullah, N. Kosar, K. Ayub, M. A. Gilani, and T. Mahmood, "Theoretical study on a boron phosphide nanocage doped with superalkalis: novel electrides having significant

nonlinear optical response," *New J. Chem.*, vol. 43, no. 15, pp. 5727–5736, 2019, doi: 10.1039/C9NJ00225A.

[37] C. C. Yang, L. Li, W. Q. Tian, W. Q. Li, and L. Yang, "Strong second order nonlinear optical properties of azulene-based porphyrin derivatives," *Phys. Chem. Chem. Phys.*, vol. 24, no. 21, pp. 13275–13285, 2022, doi: 10.1039/d2cp00735e.

[38] M. Zaidi, D. Hannachi, and H. Chermette, "Correlation between Second Ionization Potential and Nonlinear Optical Properties of Bivalent Transition-Metal Complexes : A Quantum Chemical Study," *Inorg. Chem.*, vol. 60, pp. 6616–6632, 2021.

[39] U. Hohm and A. J. Thakkar, "New relationships connecting the dipole polarizability, radius, and second ionization potential for atoms," *J. Phys. Chem. A*, vol. 116, no. 1, pp. 697–703, 2012, doi: 10.1021/jp2094438.

[40] J. L. Oudar and D. S. Chemla, "Hyperpolarizabilities of the nitroanilines and their relations to the excited state dipole moment," *J. Chem. Phys.*, vol. 66, no. 6, pp. 2664–2668, 1976, doi: 10.1063/1.434213.

[41] J. L. Oudar, "Optical nonlinearities of conjugated molecules. Stilbene derivatives and highly polar aromatic compounds," *J. Chem. Phys.*, vol. 67, no. 2, pp. 446–457, 1977, doi: 10.1063/1.434888.

Chapter IV

Tuning Second-Order NLO Responses in Multi-Decker Sandwich Clusters

IV.1. Introduction

Numerous strategies have been developed to enhance and modulate the nonlinear optical (NLO) response of molecular and supramolecular systems. These approaches encompass the reinforcement of intramolecular push–pull effects [1]–[4], the rational design of octupolar architectures[5], [6], and the construction of asymmetric coordination complexes [7]–[9]. Additional methodologies include the incorporation of diffuse excess electrons, [10]–[13], the engineering of multi-decker sandwich clusters [14], [15], as well as the development of metal–organic frameworks (MOFs) with tailored electronic environments [16]. Collectively, these strategies highlight the diversity of structural and electronic modifications that can be employed to achieve improved and tunable NLO performances.

Among these, multi-decker sandwich clusters [14], [15] have recently emerged as particularly promising candidates owing to their unique π-conjugated frameworks, extensive electron delocalization, and remarkable structural tunability. In the present work, we introduce a new class of NLO-active materials based on multi-decker sandwich clusters and undertake a comprehensive investigation of their structural, electronic, linear optical, and nonlinear optical properties, with the objective of achieving enhanced and robust NLO responses.

IV.2. Discovery of Sandwich Complexes

The discovery of sandwich complexes began with the synthesis of ferrocene, the first and archetypal example, in 1951. T. J. Kealy and P. L. Pauson synthesized a novel organometallic compound with the empirical formula $C_{10}H_{10}Fe$ by reacting cyclopentadienyl magnesium bromide with ferric chloride. The unusual properties of this compound prompted further investigation into its structure, eventually leading to its identification as ferrocene[17]. The structure of ferrocene remained uncertain until 1952–1953, when Wilkinson et al. determined that the iron atom was symmetrically sandwiched between two η^5-cyclopentadienyl (Cp) rings, giving rise to the classic sandwich structure [18]. This structural elucidation of ferrocene marked the birth of the sandwich complex model, which would later apply to numerous other metallocene complexes. Fischer (1960) contributed critical theoretical insights into the bonding in ferrocene and other similar complexes. His work explained the η^5-coordination of cyclopentadienyl ligands to the metal center and provided a deeper understanding of the metallocene bonding model, further cementing the significance of the sandwich structure in organometallic chemistry.[19] In 1973, Fischer and Wilkinson were awarded the Nobel Prize in Chemistry for their groundbreaking work on sandwich complexes, particularly for their

contributions to understanding the structure and bonding of ferrocene and related compounds. Since then, the concept of metallocene bonding has provided the foundation for the development of a broad range of organometallic systems with wide-ranging applications.

Scheme IV.1: a: Pentagonal antiprismatic structure of ferrocene "The Structure of Iron Bis-Cyclopentadienyl"; **b:** Sandwich courtesy of Prof. Peter W. Roesky.[18], [20]

IV.3. Types of Sandwich Complexes

Sandwich complexes are a diverse class of organometallic compounds characterized by a metal atom coordinated between two (or more) planar aromatic ligands. They can be classified based on several factors:

IV.3.1. Based on the Nature of the Ligands:

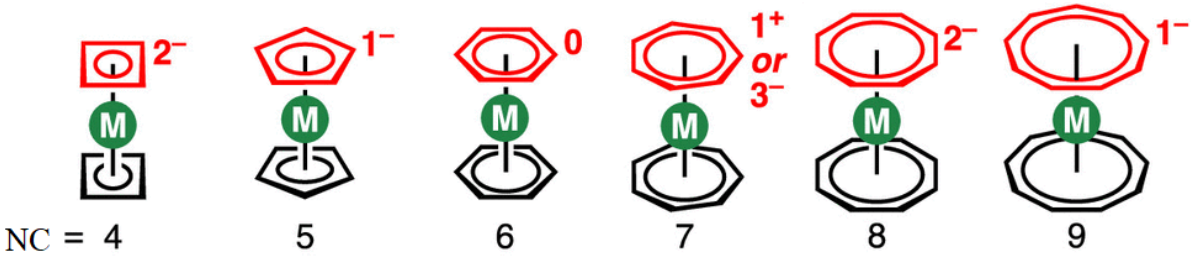

Scheme IV.2: Structures of sandwich complexes with $\{C_nH_n\}$ π-aromatic carbocycles [20]

- **Cyclopentadienyl Complexes:** These are the most common type and feature cyclopentadienyl (Cp, $C_5H_5^-$) ligands. Examples include ferrocene ($Fe(C_5H_5)_2$) and chromocene ($Cr(C_5H_5)_2$).
- **Arene Complexes:** These complexes have arene ligands (e.g., benzene, toluene). A classic example is dibenzenechromium ($Cr(C_6H_6)_2$).

- **Cyclooctatetraene Complexes:** These feature cyclooctatetraene (COT, $C_8H_8^{2-}$) ligands, such as uranocene ($U(C_8H_8)_2$).
- **Mixed-Ligand Complexes:** These contain different types of aromatic ligands. For example, a complex might have one Cp ligand and one arene ligand.

IV.3.2. Based on the Number of Rings:

- **True Sandwich Complexes:** These have two aromatic rings directly coordinated to the metal center in a parallel arrangement. This is the classic definition.
- **Half-Sandwich Complexes (Piano-Stool Complexes):** These have only one aromatic ring coordinated to the metal. The coordination sphere is completed by other ligands (e.g., carbonyls, halides, phosphines). An example is $(\eta^5\text{-}C_5H_5)Fe(CO)_2Cl$.
- **Triple-Decker Complexes:** These are less common and feature three metal atoms sandwiched between two aromatic rings.

IV.3.3. Based on the Metal:

- **Transition Metal Complexes:** These are the most prevalent, involving transition metals such as iron, chromium, nickel, ruthenium, etc.
- **Lanthanide and Actinide Complexes:** These feature f-block elements, such as uranium in uranocene.

IV.3.4. Based on the Hapticity (η) of the Ligands:

- **η^5-Complexes:** This is the most common type, where all five carbon atoms of a cyclopentadienyl ring are bonded to the metal center.
- **η^6-Complexes:** All six carbon atoms of an arene ring are bonded to the metal center.

  Note: Hapticity describes the number of atoms in a ligand that are directly bonded to the metal.

IV.3.5. Heterobimetallic Sandwich Complexes

Description: These complexes feature two different metals sandwiched between ligands, such as cobalt and manganese. For example, $[CoMn(CO)_4(\eta^5\text{-}C_5H_5)_2]$ is a heterobimetallic sandwich complex.

IV.4. Heterotrimetallic triple-decker sandwich complex

In 2020, Joseph et al.[21] reported the synthesis and characterization of a new class of heterotrimetallic triple-decker sandwich complexes with the general formula $[(Cp^*M)_2\{\mu\text{-}B_2H_2E_2Pd(Cl_2)\}]$ (M = Co, Rh, Ir; E = S, Se). These compounds feature a planar five-membered $\{B_2E_2Pd\}$ palladacycle as the central deck, in which the Pd(II) center adopts an uncommon pseudo-octahedral coordination geometry (**Scheme IV.3)**. Structural and spectroscopic analyses demonstrated high molecular symmetry, with strong Pd–E and Pd–Cl bonds accompanied by elongated, weak Pd–M interactions. Density functional theory (DFT) calculations supported these observations, revealing that the B_2E_2 fragment acts as the primary electron donor to the axial metals, while Pd–M interactions remain weak and essentially non-covalent. Electronic absorption spectra, corroborated by time-dependent DFT (TD-DFT), displayed multiple bands between 290–700 nm attributable to metal-centered d–d transitions and metal-to-ligand charge transfer (MLCT) processes. Collectively, these results establish a novel synthetic route to stable, high-yield heterotrimetallic triple-decker complexes and highlight their unique bonding features, thereby opening promising perspectives for future catalytic applications.

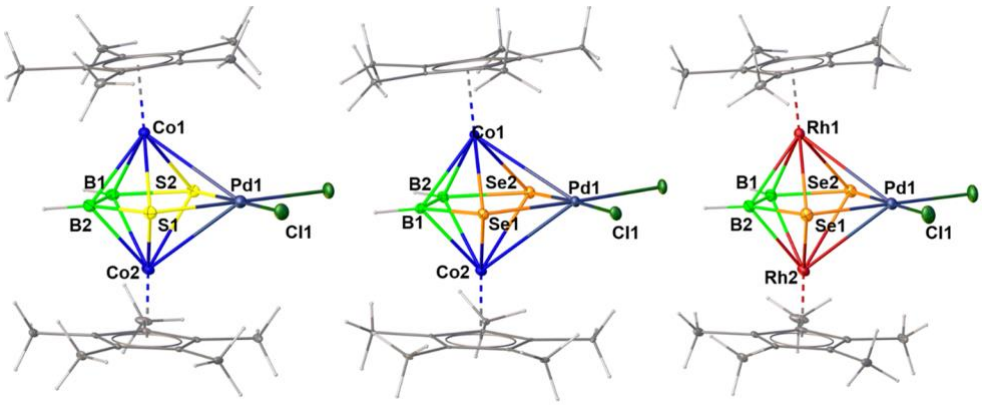

Scheme IV.3. Molecular structures of complexes synthesized by Joseph et al. [21]

IV.5. Multidecker Sandwich Cluster and NLO

To investigate strategies for enhancing nonlinear optical (NLO) properties and for the rational design of novel NLO-active organometallic systems, we selected the triple-decker sandwich complexes synthesized by Joseph *et al.* [21] as a prototypical framework. Building upon this structural motif, we developed two distinct series of molecular complexes, hereafter denoted as $[\{B_2H_2S_2Pd(Cl)_2\}\text{-}(CoCp)_n]$ where n = 2 to 5 (please see **Scheme IV.4**)

- ✓ The first series (MDSn/MDSna,) was engineered by systematically varying the number of (CoCp) units (n = 2–5) and the positional arrangement of the square-planar $\{B_2H_2S_2Pd(Cl)_2\}$ fragment.
- ✓ The second series (MDS′n) retained a fixed position of the $\{B_2H_2S_2Pd(Cl)_2\}$ core while incrementally increasing the layer count (n = 2–5).
- ✓ To evaluate these systems, we employed Density Functional Theory (DFT) and Time-Dependent DFT (TD-DFT) calculations to probe their electronic structures, excited-state properties, and frequency-dependent NLO responses (ω = 0, 0.0239, 0.0340, and 0.0428 a.u.). This computational approach provides insights into how structural modifications influence first hyperpolarizabilities, offering a pathway to optimize NLO performance in multidecker organometallic frameworks.

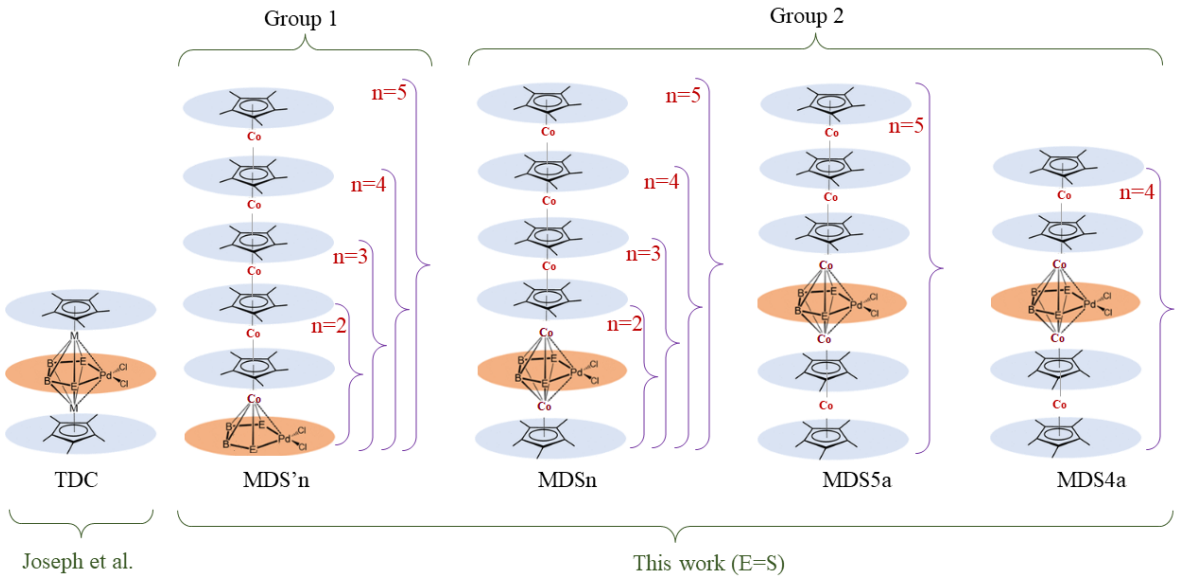

Scheme IV.4. Molecular Design of Multi-Decker Sandwich Complexes $[(CoCp)_n\{B_2H_2E_2Pd(Cl)_2\}]$, E=S, Se and n = 2 to 5 (from ref. [21] for triple-decker sandwich

IV.6. Results and discussion

IV.6.1. Choice of Computational Method

The selection of an appropriate computational method is a critical step in ensuring the reliability and predictive accuracy of quantum chemical investigations. To determine the most suitable methodology for describing the structural, electronic, and optical properties of the multi-decker sandwich cluster (**Scheme IV.4**), a systematic assessment of density functional theory based approaches was carried out. Calculations were performed on a simplified model, $[(CoCp)_2\{B_2H_2S_2Pd(Cl)_2\}]$, in which Cp* was replaced by Cp to reduce computational cost

without altering the essential electronic characteristics of the system. A range of exchange–correlation functionals, including B3LYP,[22], [23] ωB97X-D, [24], [25] CAM-B3LYP,[26] TPSSH,[27]–[29] M06,[30] M06-2X[30], [31], were employed to evaluate their performance. For H, B, S, C and Cl atoms, the 6–311G(d) basis sets were employed, while the Stuttgart-Dresden effective core potentials (ECPs) with SDD basis sets were used for the cobalt and palladium atom [32], [33]. Scalar relativistic effects were addressed through the use of ECPs. No symmetry constraints were imposed, and all ground state frequencies were verified as real at this theoretical level. The optimized geometrical parameters obtained with each functional are provided in **Table S1** (Supplementary Information **Annex II**), while the simulated absorption spectra are presented in **Figure IV. 1**. Theoretical predictions were systematically benchmarked against the available experimental data for the parent complex $[(CoCp^*)_2\{B_2H_2S_2Pd(Cl)_2\}]$, enabling a rigorous validation of the computational protocol.

The analysis of the geometrical parameters shows that the experimental Co-B distance is 2.118 Å [21]. This value is smaller than those calculated by the ωB97X-D, B3LYP, CAM-B3LYP M06 and TPSSH functionals by 0.012, 0.01, 0.03, 0.017 and 0.022 Å, respectively, and larger than those obtained using M06-2X by 0.003 Å. Additionally, DFT calculations underestimate the experimental Co-Co, S-B and Pd-Cl distances by 0.051, 0.022 and 0.017 Å, respectively; in contrast, the Pd-Co and Co-S bond lengths are overestimated by 0.047 and 0.015 Å, respectively. Furthermore, it is observed that the bond lengths B1-B2 and S1-B1 exhibit minor discrepancies between the experimental measurements and the computed values. The calculated bond angles exhibit very slight deviations from the experimental results, ranging from 1° to 3°. Overall, there is excellent agreement between the calculated parameters and the crystallographic data of $[(CoCp)_2\{B_2H_2S_2Pd(Cl)_2\}]$ complex.

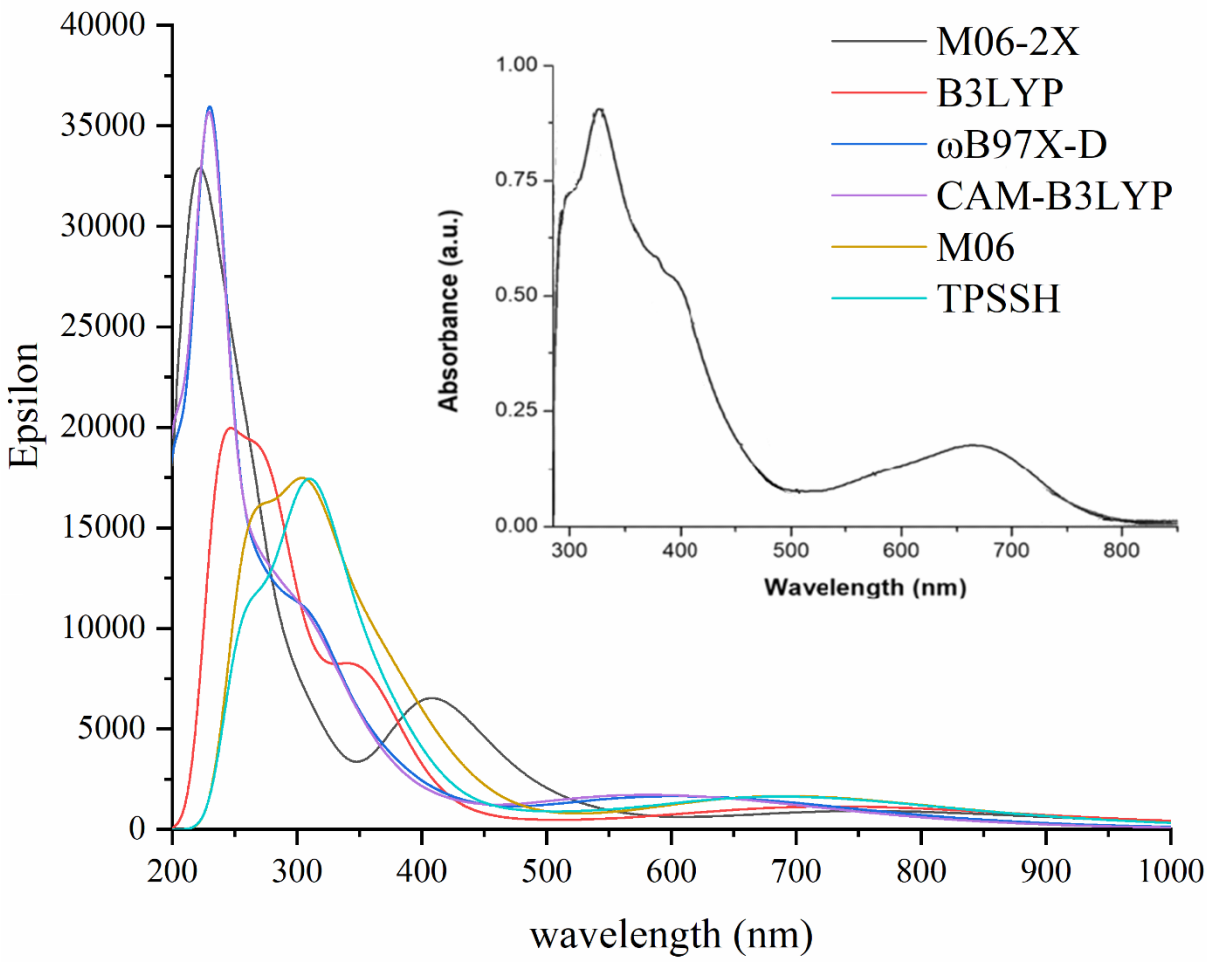

Figure IV.1 Calculated and experimental UV − vis of [$(CoCp)_2\{B_2H_2S_2PdCl_2\}$] (experimental spectra from refs [21])

Figure IV.1 illustrates the absorption spectra of the compound under investigation, incorporating both theoretical results derived from six distinct exchange–correlation functionals and the corresponding experimental data. The experimental spectrum prominently features a sharp absorption peak within the 200–400 nm range, broad absorption bands extending from 400 to 800 nm, and a clearly defined shoulder near 400 nm. The results obtained using the M06 and TPSSH functionals are nearly identical, indicating that both functionals provide a comparable depiction of the electronic excited states and transition energies of the $[(CoCp)_2\{B_2H_2S_2Pd(Cl)_2\}]$ complex. On the other hand, the CAM-B3LYP and ωB97X-D functionals yield nearly identical spectra, with a minor shift relative to B3LYP, which can be attributed to long-range correction effects. Among all the functionals tested, the UV-Vis absorption spectrum calculated using M06-2X exhibits the closest agreement with the experimental data, both in terms of spectral shape and absorption maxima. Notably, an electronic transition near 400 nm, observed experimentally, is also present in the simulated

spectrum obtained with M06-2X, further validating its accuracy in modeling the optical properties of this system.

To assess the efficacy of the M06-2X functional in accurately predicting the first hyperpolarizability of the studied complexes, a comparative analysis was conducted. The second-order nonlinear optical (NLO) response of the organometallic complex MDS_2 was computed using various exchange–correlation functionals, including ωB97X-D, B3LYP, CAM-B3LYP, M06, and TPSSH, while maintaining consistent basis sets for uniformity. As shown in **Figure IV.2**, the first hyperpolarizability values derived from M06-2X exhibit excellent agreement with those obtained from CAM-B3LYP and ωB97X-D, both of which are renowned for their accuracy in predicting the NLO responses of compounds.[2], [9], [34]–[39] In contrast, TPSSH and M06 functionals significantly underestimate the first hyperpolarizability (β_0) values. Based on these findings, the M06-2X functional was considered well-suited for the subsequent evaluation of the NLO properties of the multidecker sandwich complex derivatives investigated in this study.

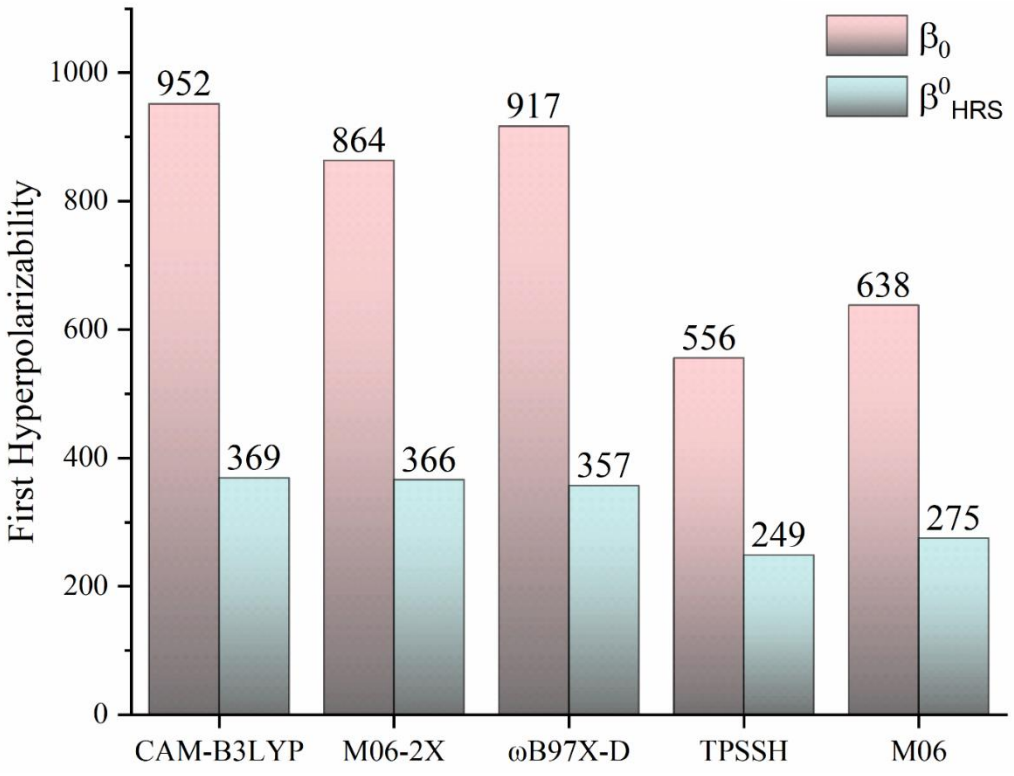

Figure IV. 2 First hyperpolarizability of MDS2 complex calculated at different theoretical levels

Based on the obtained results, the M06-2X functional was chosen for the computation of both linear and nonlinear optical properties of all target complexes in this investigation. This

selection is further substantiated by prior studies that affirm the robustness and predictive reliability of the M06-2X functional, particularly in the context of transition metal complexes.[40]–[45]

IV.6.2. Comparative study of NLO responses in metallocene complexes

In order to gain a more comprehensive understanding of the nonlinear optical responses of the investigated complexes, the static first hyperpolarizability ((β^0 and β^0_{HRS}) was calculated at the M06-2X/6-311G(d)/SDD level of theory for the complexes MDS_2, MDS'_2, and a set of reference metallocenes, including $3NH_2{-}VBz_2{-}3CN$, VBz_2-$(C_2H_2)_3$-NO_2 and Fe_1Cp_2-$(C_2H_2)_3$-NO_2, with urea serving as a standard benchmark. The computational results are presented in **Table IV.1**. Notably, the MDS'_2 complex demonstrates a significantly enhanced NLO response, with β^0 and β^0_{HRS}values approximately 194 times and 198 times greater, respectively, than those of urea. In contrast, the MDS2 complex exhibits moderate hyperpolarizability values, approximately 10 times greater than those of urea.

On the other hand, within the metallocene-based series, VBz_2-$(C_2H_2)_3$-NO_2 demonstrates the highest first hyperpolarizability (β^0 = 7.01×10^4 a.u.), exceeding that of MDS′2 by a factor of approximately 4.3. Notably, the β^0 value for MDS′2 is nearly twice that of Fe_1Cp_2-$(C_2H_2)_3$-NO_2 and more than 30 times greater than that of $3NH_2{-}VBz_2{-}3CN$, highlighting its significantly superior nonlinear optical performance. In comparison, the MDS2 complex exhibits moderate NLO activity, with a β^0 value approximately 1.6 times greater than that of $3NH_2{-}VBz_2{-}3CN$. Based on this comparative analysis, both MDS_2 and MDS'_2 emerge as promising molecular platforms for further structural optimization aimed at the development of efficient NLO materials.

Table IV.1. Calculated first hyperpolarizability value (β^0 and β^0_{HRS}) for MDS2, MDS′2, $3NH_2-VBz_2-3CN$, VBz_2-$(C_2H_2)_3$-NO_2 and Fe_1Cp_2-$(C_2H_2)_3$-NO_2 and urea at the M06-2X/6-311G(d)/SDD level of theory

	β^0	β^0_{HRS}
MDS2	8.64×10^2	3.66×10^2
MDS'2	1.63×10^4	6.72×10^3
VBz_2-$(C_2H_2)_3$-NO_2	7.01×10^4	2.93×10^4
Fe_1Cp_2-$(C_2H_2)_3$-NO_2	8.96×10^3	3.75×10^3
$3NH_2-VBz_2-3CN$	5.21×10^2	4.93×10^2
urea molecule	84	34

IV.6.3. Structural and electronic study multi-decker sandwich cluster

The geometry optimization of the 10 multi-decker sandwich cluster $[(CoCp)_n\{B_2H_2S_2Pd(Cl)_2\}]$ with n = 2 to 5 was performed using the M06-2X/6–311G(d)/SDD method. The optimized geometries are illustrated in **Figure IV.3**, and the calculated bond distances and angles are detailed in **Table S2.AII**.

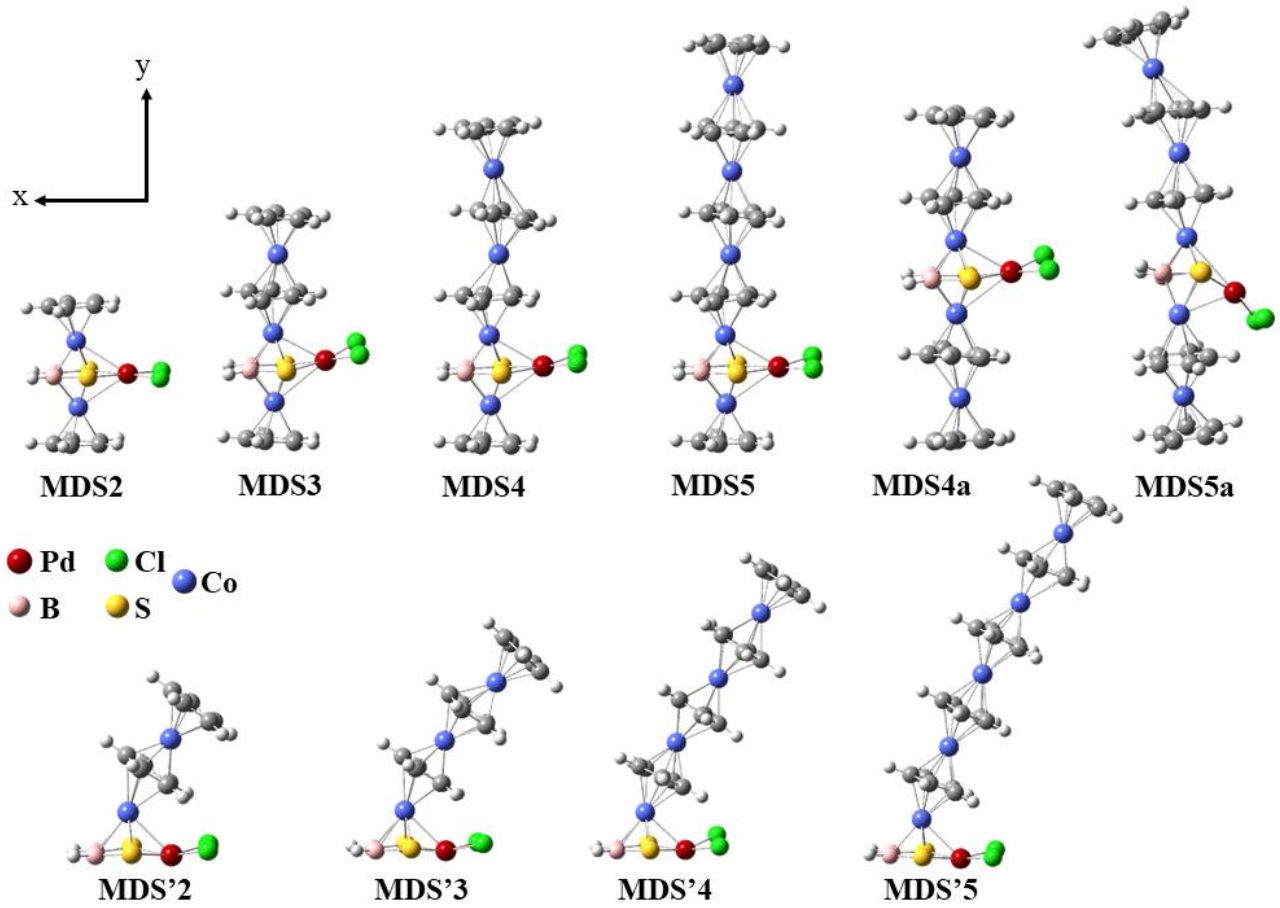

Figure IV. 3 The optimized geometry of multi-decker sandwich cluster $[(CoCp)_n\{H_2B_2S_2Pd(Cl)_2\}]$, n=2 to 5

The optimized geometries of the MDS'n complexes exhibit inclined configurations, characterized by the angle (φ') calculated at the centroid of the square planar arrangement $\{B_2S_2Cl_2\}$ between the cobalt (Co) atom and the centroid of the B-B bond (**Scheme IV.2**). These angles range from 54° to 65°, as illustrated in Fig. 3 and detailed in **Table S2.AII**. Notably, MDS'2 and MDS'3 exhibit inclinations of 54°, while MDS'5 shows an inclination of 65°. For the MDSn cluster, the angular parameter φ is defined as the angle formed between the centroids of the cyclopentadienyl (Cp) and centroids of the ring $\{B_2S_2Pd\}$ and the palladium atom (see **Scheme IV. 5**), the calculated values for this angle are provided in **Table S2.AII**. As presented in **Table S2.AII**, the φ angle of MDSn ranges from 82° to 95°, indicating a slight inclination that is nearly perpendicular to the molecular axis (y-axis) of the multidecker sandwich complexes $[(CoCp)_n\{H_2B_2S_2Pd(Cl)_2\}]$ n=2 to 5. Additionally, the Cl...H induces a deformation in the $\{H_2B_2S_2Pd(Cl)_2\}$ and Cp rings within the title complexes.

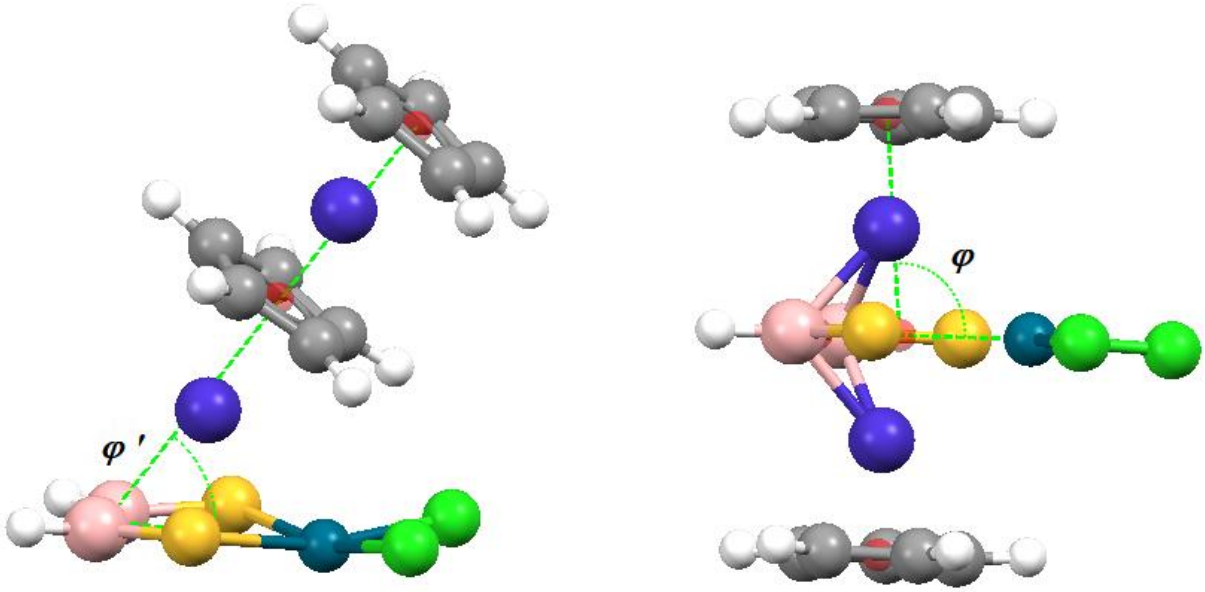

Scheme IV.5. The bond angles φ and φ' of MDS'n and MDSn complexes

One should notice that the geometry optimization of MDS5a does not retain the linearity of the Co alignment, as shown in **Figure IV. 3**. Indeed, some constrained geometry optimizations deliver quasi degenerated structures (no imaginary frequencies) which, however, reoptimize towards the tilted structure. In the meantime, the two chlorines move below the $\{B_2S_2Pd)_2\}$ plane (**Figure. S1.AII**).

The computed values of the highest occupied molecular orbital (HOMO), lowest unoccupied molecular orbital (LUMO) energies, chemical potential (μ), and hardness (η) for MDSn, MDSna, and MDS'n complexes (where n = 2 to 5) are presented in **Table S3.AII** and **Figure IV.4**. Chemical hardness (η) serves as an indicator of a molecule's stability by reflecting its resistance to electron transfer, while the chemical potential (μ) quantifies the molecule's tendency for electron escape from the equilibrium system [46].

Where:

$$\eta = \varepsilon_L - \varepsilon_H \quad \text{(IV.1)}$$

$$\mu = 1/2(\varepsilon_H + \varepsilon_L) \quad \text{(IV.2)}$$

The ionization potentials (I) of these complexes provide insight into their thermal stability. Most of the complexes exhibit ionization potential values greater than 5 eV, with exceptions for the MDS_5, MDS_5a, and MDS'_5 complexes, which have values of 4.534, 4.591, and 4.865 eV, respectively. These results suggest that the complexes generally exhibit good thermal stability.

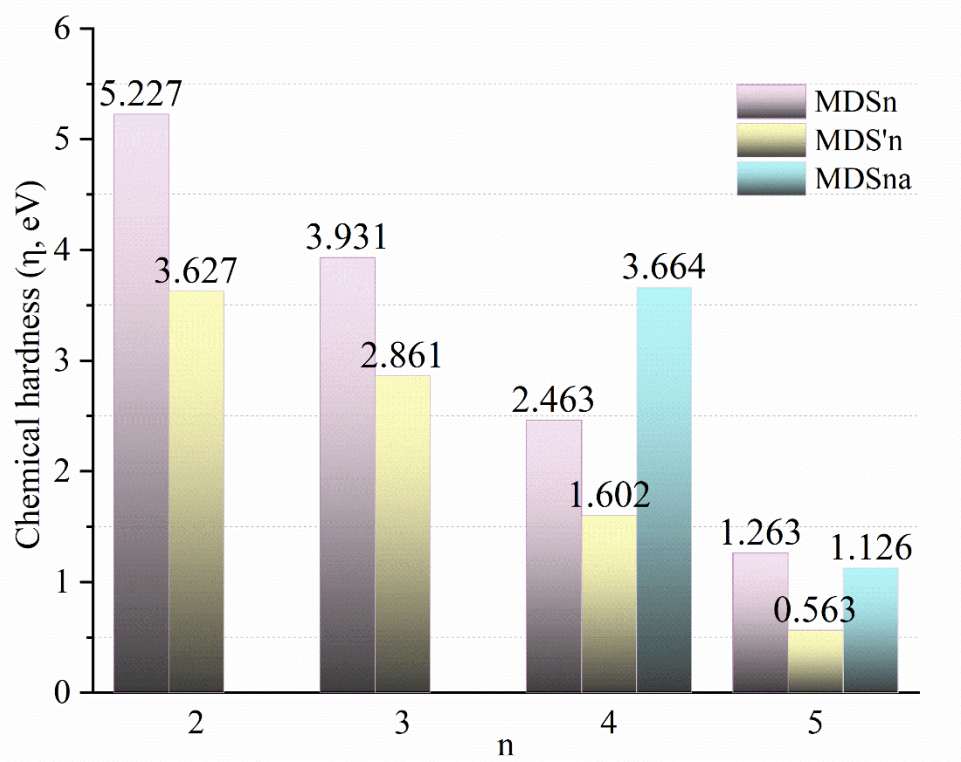

Figure IV. 4 The calculated chemical hardness indices of MDSn, MDSna and MDS'n, (n=2 to 5) at M06-2X/6–311G(d)/SDD level of theory.

Chemical hardness (η) quantifies a compound's resistance to variations in electron distribution, with higher values corresponding to lower reactivity and enhanced stability. Our analysis reveals that the MDSn complexes exhibit higher hardness values than their corresponding MDS'n counterparts. For example, MDS2 has a hardness of 5.227 eV, which is 1.6 eV greater than that of MDS'2 (3.627 eV). Likewise, MDS3 demonstrates a higher hardness by 1.07 eV compared to MDS'3. Furthermore, it is observed that the hardness of the complexes increases as the number of (CoCp) units decreases within the clusters. The complexes can be ranked in ascending order of hardness as follows:

MDS'5< MDS5< MDS'4< MDS4< MDS'3< MDS3 ≈ MDS'2< MDS2, as shown in **Figure IV.4.**

From this study, it is observed that the position of $\{H_2B_2S_2Pd(Cl)_2\}$ and the number of (*CoCp*) units significantly influence the stability of the studied clusters. Notably, the $[(CoCp)_5\{H_2B_2S_2Pd(Cl)_2\}]$ complexes exhibit the lowest chemical hardness, indicating a higher reactivity and lower stability compared to other configurations.

IV.6.4. Absorption Spectra

It is significant to note that the molecule's ability to exhibit a prominent absorption maximum positions it as a promising candidate for optoelectronic applications.[47] In this context, time-dependent density functional theory (TD-DFT) calculations on the optimized geometries are crucial for predicting the excited-state properties of the complexes. Accordingly, TD-DFT calculations were performed at the TD-M06-2X/6-311G(d)/SDD level of theory to determine the vertical singlet excitation energies. A total of 120 excited states were considered in all optical property calculations to ensure a thorough spectral analysis. The detailed absorption spectra for the complexes MDSn, MDSna, and MDS'n are provided in Tables 2, 4S-5S, and **Figures S2 and 5.AII**. The optical properties analyzed include the excitation wavelength (($\lambda_{0\rightarrow n}$), nm), oscillator strengths ($f_{0\rightarrow n}$), transition dipole moment ($\Delta\mu_{CT}$, a.u.), overlap integrals (Sr(r)), D_{CT} and t index (Å) associated with the $S_0 \rightarrow S_n$ transition.

Table IV.2. Excitation wavelength ($\lambda_{0\rightarrow n}$, nm), oscillator strengths ($f_{0\rightarrow n}$, dimensionless), transition dipole moment ($\Delta\mu_{CT}$, a.u.) , overlap (S_r (r)), D_{CT} and t indice (Å) associated with the $S_0 \rightarrow S_n$ transitions, as calculated at M06-2X/SDD/6-311G(d) of the MDSn and MDS'n complexes

	$S_{0\rightarrow n}$	$\Delta\lambda_{0\rightarrow n}$	$f_{0\rightarrow n}$	$\Delta\mu_{CT}$	Sr	D_{CT}	t index
MDS2	$S_{0\rightarrow 8}$	761.74	0.021	2.034	0.643	2.145	0.770
	$S_{0\rightarrow 20}$	403.01	0.137	3.177	0.537	1.687	0.003
MDS'2	$S_{0\rightarrow 9}$	664.13	0.088	3.537	0.712	2.960	0.842
	$S_{0\rightarrow 18}$	474.84	0.051	6.547	0.171	4.471	3.227
MDS3	$S_{0\rightarrow 14}$	722.66	0.261	0.863	0.929	1.278	-1.011
	$S_{0\rightarrow 29}$	384.99	0.002	2.876	0.773	3.476	0.870
MDS'3	$S_{0\rightarrow 5}$	1876.95	0.003	2.657	0.722	2.706	0.274
	$S_{0\rightarrow 13}$	854.55	0.426	6.605	0.252	5.858	4.032
MDS4a	$S_{0\rightarrow 14}$	1130.64	0.007	3.643	0.786	4.207	0.840

	$S_{0\rightarrow20}$	705.13	0.408	1.021	0.878	1.341	-0.866
MDS4	$S_{0\rightarrow19}$	813.46	0.002	14.926	0.051	9.359	7.408
	$S_{0\rightarrow25}$	605.04	0.405	2.007	0.786	2.153	-0.796
MDSS'4	$S_{0\rightarrow6}$	1380.64	0.098	2.275	0.884	2.307	-2.027
	$S_{0\rightarrow15}$	1080.53	0.692	2.299	0.822	2.871	-1.440
MDS5	$S_{0\rightarrow3}$	1942.02	0.001	24.085	0.059	12.869	10.902
	$S_{0\rightarrow29}$	671.82	0.017	15.233	0.209	8.025	5.911
MDS'5	$S_{0\rightarrow6}$	1566.12	<0.001	1.852	0.499	1.583	-3.054
	$S_{0\rightarrow21}$	1009.40	0.06	6.321	0.746	6.804	1.209
MDS5a	$S_{0\rightarrow10}$	1243.56	<0.001	27.38	0.0001	14.794	13.052
	$S_{0\rightarrow28}$	615.89	0.0025	17.194	0.062	10.058	7.858

The TD-DFT calculations indicate that the simulated absorption spectra of the investigated clusters display two distinct absorption regions (**Figure IV.5** and **Figure S2.AII**). The first region, observed between 200 and 350 nm, corresponds to intra-ligand π–π* transitions within the Cp ligands [48]. The second absorption region extends from 400 nm and spans beyond 1000 nm; for example, the clusters with n = 3 exhibit absorption up to 2400 nm, as seen in the MDS'4 cluster.

Furthermore, a significant bathochromic shift is observed in the first electronic transitions with notable oscillator strength within the second absorption region of the MDS'n series, relative to the corresponding MDSn clusters (where n = 2 to 5). For example, in the case of n = 4, the first electronic transition of MDS'4 occurs at 1080 nm (f = 0.692), whereas for MDS4, it is positioned at 605 nm (f = 0.405) (**Figure IV.5**). This redshift is attributed to the specific positioning of the $\{H_2B_2S_2Pd(Cl)_2\}$ fragment within the MDS'n clusters, implying the potential for enhanced second-order nonlinear optical (NLO) responses under suitable conditions.

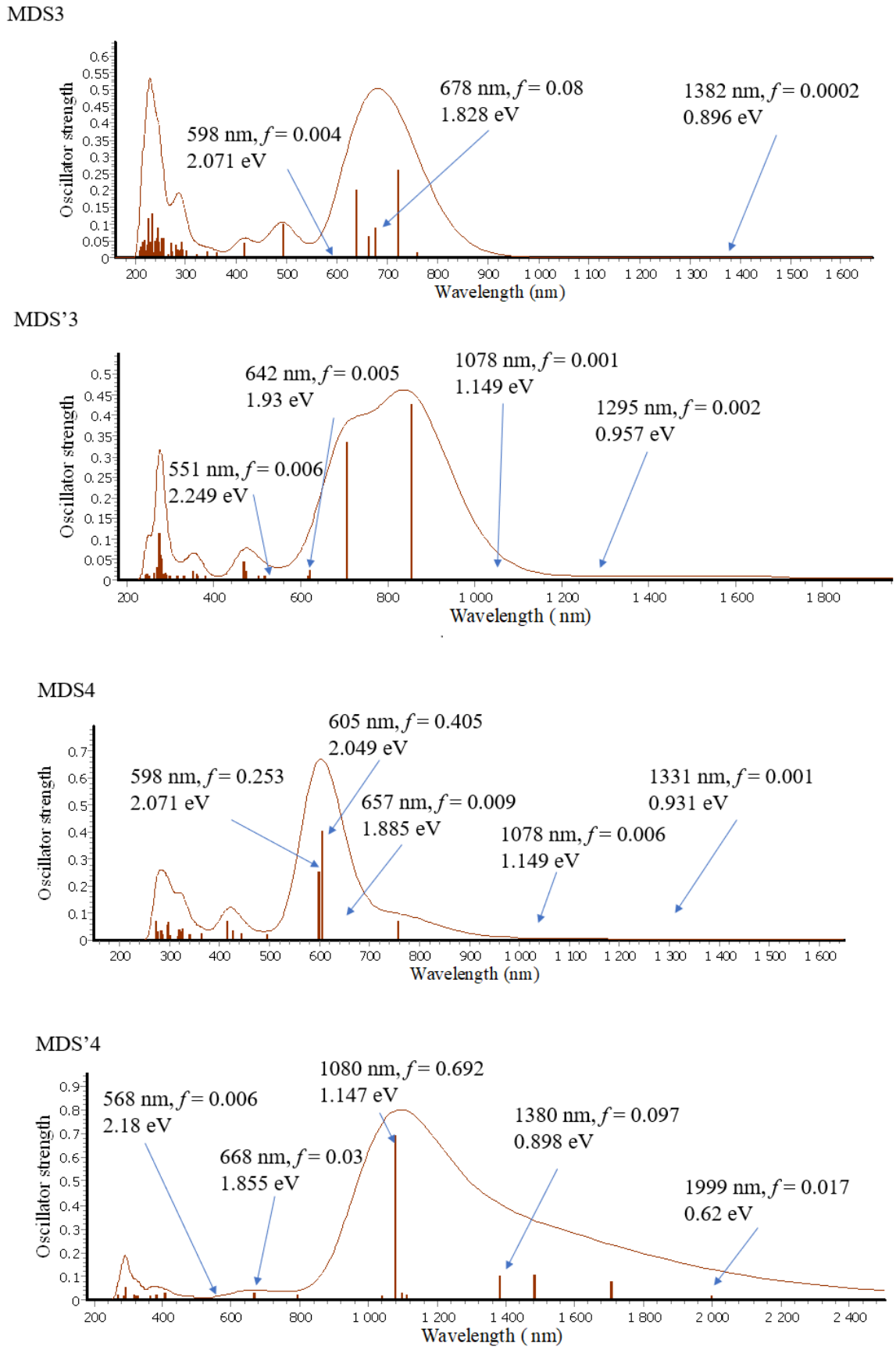

Figure IV.5. Calculated UV-Vis absorption spectra of MDSn and MDS'n (n= 3 and 4).

To attain a deeper insight into the nature of the electronic excitations within the investigated clusters, the essential excited-state wavefunctions were analyzed through the framework of natural transition orbitals (NTOs). This formalism enables the decomposition of the transition density matrix into its fundamental components, namely the "excited electron" and the corresponding "vacant hole" distributions. Furthermore, the electron density difference maps (EDDMs) associated with these representative excited states are illustrated in **Figure IV.6** and systematically summarized in **Table S4.AII**.

The simulated UV–Vis absorption spectrum of MDS2 reveals two principal bands located at 761 nm (f = 0.021) and 403 nm (f = 0.137), which are attributed to intra-metallic *d–d* transitions in conjunction with metal-to-ligand charge transfer (MLCT) excitations, specifically from the $Pd(Cl)_2$ moiety toward the B–B bonding framework (**Table S4.AII**). In the case of the MDS'2 derivative, distinct electronic excitations are identified: transition S9, characterized predominantly by a HOMO→LUMO contribution (23%) at 664 nm; transition S15, assigned to HOMO–2→LUMO (30%) at 567 nm; and transition S18, involving HOMO–6, –7→LUMO (12%) at 475 nm. Collectively, these transitions are diagnostic of charge-transfer (CT) processes, wherein electron density is redistributed from the $Pd(Cl)_2$ and Co metallic centers—embedded within the square-planar $[B_2S_2]$ coordination environment—toward the $CoCp_2$ fragment, as corroborated by the spectral data in **Table S4.AII** and **Figure IV.6**.

For the MDS'3 complex, intense absorption features are observed at 854 nm and 705 nm, with appreciable oscillator strengths (f = 0.426 and 0.334, respectively). These transitions are predominantly ascribed to charge-transfer (CT) processes originating from the $\{B_2S_2Pd(Cl)_2\}$ fragment and the Co metallic centers, coordinated within the $[B_2S_2]$ environment, and directed toward the Co_2Cp_3 moiety. Moreover, the transition S0→S23, detected at 542 nm, corresponds to a $PdCl_2$-to-$(CoCp)_3$ charge transfer, arising specifically from the HOMO-3→LUMO excitation with a substantial 40% orbital contribution. In contrast, the MDS3 analogue exhibits a major absorption band at 722 nm (f = 0.261), which is primarily attributed to a HOMO→LUMO excitation. This process is classified as an intramolecular charge-transfer (ICT) transition, displaying a pronounced local excitation component (Sr = 0.929). This ICT character is further observed in electronic transitions at 759 nm and 385 nm.

For the MDS4a cluster, the absorption features within the 700–800 nm region, characterized by appreciable oscillator strengths, are predominantly associated with charge-transfer (CT) excitations emanating from the $\{S_2Pd(Cl)_2\}$ moiety toward the Co centers

coordinated within the square-planar [B_2S_2] scaffold, as well as toward the B–B bond and the cyclopentadienyl (Cp) ligands **(Table S4.AII**). In contrast, the excitation S0→S26, located at 566 nm (f = 0.05), is primarily governed by the HOMO→LUMO+1 transition (18%), which reflects CT processes originating from the peripheral $CoCp_2$ fragments and directed toward the {$B_2S_2PdCl_2$} and (CoCp) subunits (**Figure IV. 6** and **Table S4.AII**).

In the case of the MDS4 analogue, the electronic excitations observed at 813 nm and 539 nm (f = 0.002 and 0.003, respectively) are predominantly assigned to CT from the outer $CoCp_2$ unit toward the {$B_2S_2Pd(Cl)_2$} and (CoCp) fragments anchored to the [B_2S_2] framework. Additionally, the absorption at 781 nm arises chiefly from CT localized within the $PdCl_2$ unit, directed toward the {$B_2S_2Pd(Cl)_2$} and (CoCp) moieties coordinated with the [B_2S_2] core. Notably, the pronounced band at 605 nm (f = 0.405) is assigned to an intramolecular charge-transfer (ICT) process localized within the {$B_2S_2Pd(Cl)_2$} fragment.

For the MDS'4 complex, pronounced low-energy absorptions are detected at 1380 nm and 1080 nm, with considerable oscillator strengths (f = 0.098 and 0.692, respectively). These transitions are predominantly assigned to charge-transfer processes originating from the peripheral CoCp fragment and the {$B_2S_2Pd(Cl)_2$} unit, directed toward the central $(CoCp)_2$ domain of the cluster. Additionally, the excitations corresponding to HOMO–1→LUMO (46%) and HOMO–2→LUMO (43%) are located at 902 nm and 728 nm, respectively. Both transitions are primarily characterized by CT events from the $(CoCp)_4$ to {$B_2S_2Pd(Cl)_2$} fragment.

In the MDS5 cluster, the S0→S3 excitation at 1942 nm is attributed to CT from the $CoCp_2$ unit toward the {$H_2B_2S_2Pd$} moiety, dominated by a HOMO→LUMO contribution (49%). Furthermore, the S0→S10 transition at 1375 nm involves charge flow from $CoCp_2$ toward the {$B_2S_2Pd(Cl)_2$} fragment. Higher-energy transitions, located at 818 nm (HOMO→LUMO+2, 47%) and 672 nm (HOMO–1→LUMO+1, 39%), also reveal CT processes from $CoCp_2$ into the {$B_2S_2Pd(Cl)_2$} and CoCp units associated with the [B_2S_2] framework.

For the MDS'5 analogue, the absorption band at 1566 nm is assigned to a CT excitation from the central core region toward the terminal Cp rings, specifically involving the HOMO–1→LUMO transition. The transition at 1009 nm, largely defined by HOMO–3→LUMO (22%), represents an intramolecular charge-transfer process delocalized across the entire molecular scaffold. Additionally, the absorption feature at 912 nm corresponds to CT from the CoCp fragment into both the {$H_2B_2S_2Pd$} and CoCp moieties, as summarized in **Table S4.AII**.

For the MDS5a cluster, the electronic excitations S0→ S10, S23, and S26, appearing at 1244 nm, 761 nm, and 650 nm, respectively, are predominantly associated with charge-transfer processes occurring between opposing $CoCp_2$ units within the cluster. These excitations are characterized by negligible frontier orbital overlap (approaching zero), highlighting the weak electronic coupling between the donor and acceptor fragments. Importantly, the $\{B_2S_2Pd(Cl)_2\}$ fragment does not participate in these transitions. The corresponding orbital contributions are assigned to the HOMO→LUMO+1, HOMO–1→LUMO, and HOMO–2→LUMO excitations, respectively (see **Figure IV. 6** and **Table S4.AII**).

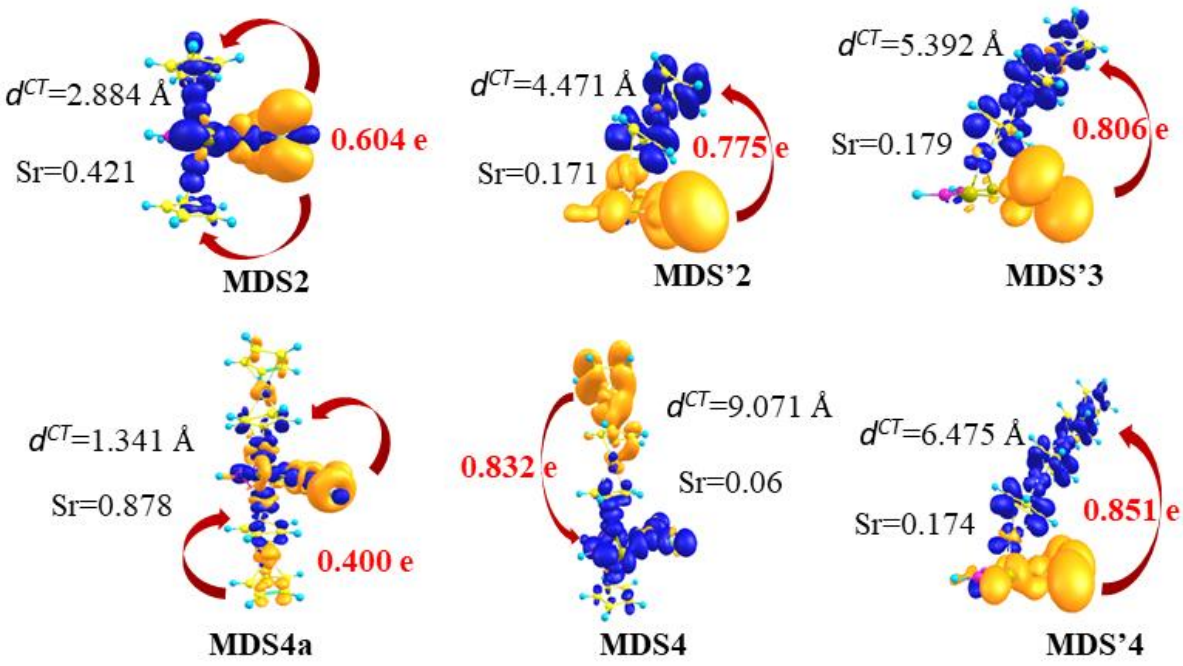

Figure IV.6 Electron density difference maps of MDS2 (S_{12}), MDS'2 (S_{18}), MDS'3 (S_{23}), MDS4a (S_{20}), MDS4 (S_{28}) and MDS'4 (S_{20}) complexes from the ground state to the crucial excited state $S_0 \rightarrow S_n$, plotted using 0.0006 a.u. isovalues (where orange and blue denote the electrons and holes, respectively).

IV.6.5. Linear and Nonlinear optical parameters

a- Dipole moments and polarizability

According to the computed data summarized in **Table S2.AII**, the dipole moments (μ) follow the increasing trend: MDS2 < MDS3 < MDS4a (11.76 D) < MDS4 (13.46 D) < MDS5 (21.51 D) < MDS5a (28.71 D). For the MDS' series, the ordering is MDS'2 (21.69 D) < MDS'5 (25.31 D) < MDS'4 (26.22 D) < MDS'3 (26.31 D). These results clearly demonstrate that the

dipole moment increases markedly with the number of (CoCp) substituents (n), reflecting the progressive asymmetry induced by the expansion of peripheral Cp-based fragments. An exception is noted within the MDS'n series, where the dipole moments converge to comparable values, suggesting that structural and electronic compensation effects mitigate further enhancement of polarity despite the increase in cluster size.

The calculated static polarizabilities and their anisotropies are summarized in **Table S6.AII** and depicted in **Figure IV.7**. For the MDSn series, the static polarizability $\alpha(0,0)$ increases systematically as follows: 282 au (MDS2) < 500 au (MDS3) < 580 au (MDS4) < 1532 au (MDS5a). A similar progression is observed in the MDS'n series: 323 au (MDS'2) < 599 au (MDS'3) < 1245 au (MDS'4) < 2154 au (MDS'5). The anisotropy of polarizability, $\Delta\alpha(0,0)$, mirrors these trends across the multidecker sandwich clusters, further corroborating the strong size-dependence of the electronic response.

Our analysis reveals that increasing the number of layers markedly enhances both $\alpha(0,0)$ and $\Delta\alpha(0,0)$ for n = 2–5 in both families. An exception arises in the "a"-designated structures, where MDS5a (648 au) displays a lower $\alpha(0,0)$ than MDS4a (754 au), highlighting the sensitivity of polarizability to subtle structural variations. Furthermore, direct comparison between MDSn and MDS'n complexes demonstrates that the latter consistently exhibit higher $\alpha(0,0)$ and $\Delta\alpha(0,0)$ values. These findings further underscore that the positioning of the (CoCp) units plays a crucial role in determining the polarizability and anisotropy polarizability of these complexes.

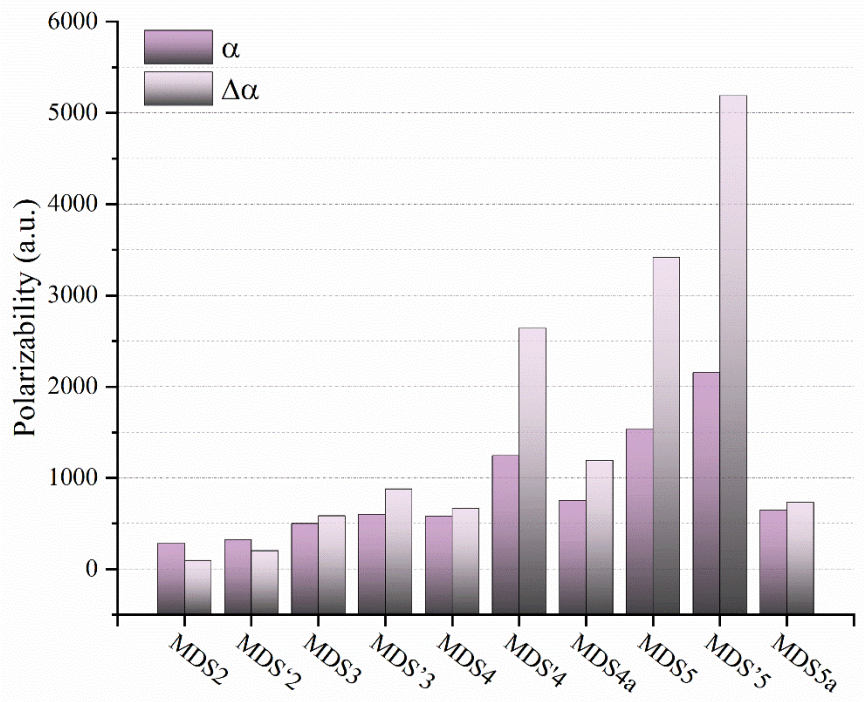

Figure IV.7 Relationship between polarizability and anisotropy of polarizability with the number of (CoCp) units (n) and the positional of $\{H_2B_2S_2Pd(Cl)_2\}$ fragment within the clusters

b- 2nd-order NLO responses

Quantum chemical methodologies have proven highly effective in elucidating, forecasting, and optimizing the nonlinear optical responses of materials. [9], [49] These computational techniques are instrumental in the advancement and rational design of novel NLO materials, offering a molecular-level understanding of electronic structures that is essential for predicting the materials' behavior under electromagnetic fields. Sophisticated approaches, such as DFT and TD-DFT are employed to simulate and predict the NLO behavior of materials, enabling the identification of optimal molecular configurations for enhanced performance. To examine and predict the influence of the number of $(CoCp)_n$ units and the positioning of the $\{H_2B_2S_2Pd(Cl)_2\}$ fragment on the NLO responses, we conducted quantum chemical calculations on the studied complexes within both static and dynamic regimes. The detailed results of these computations are summarized in **Tables IV.3** and **S6.AII** of the Supplementary Information. Notably, for the dynamic regime, three frequencies (ω) were selected: two laser frequencies, 0.0340 a.u. (1341 nm) and 0.0428 a.u. (1064 nm), chosen to to avoid resonance enhancement effects, and a non-resonant frequency of 0.0239 a.u. (1906 nm) included in the analysis. It is noteworthy that the static first hyperpolarizability (β^0) exhibits an

excellent correlation with the hyper-Rayleigh scattering (β^0_{HRS}) hyperpolarizability, with a correlation coefficient (R^2) of 0.999 (see **Figure. S3.AII**).

The computed first hyperpolarizability (β^0 and β^0_{HRS}) values for the MDSn complexes in the static regime, as illustrated in **Figure IV.8-9** and summarized in **Table IV.3**, reveal a pronounced enhancement from n = 2 to n = 5. Specifically, the β value demonstrates a steady increase with the progressive incorporation of (CoCp) units from n = 2 to n = 5, reflecting a behavior akin to that observed in classical push-pull π-systems. For example, the β value of MDS3 is nearly ten times greater than that of MDS2. Likewise, MDS4 exhibits a β value approximately eight times higher than MDS3, and the β value of MDS5 is roughly five times greater than that of MDS4. This trend underscores a significant amplification in NLO responses with the successive addition of (CoCp) units.Moreover, a comparative analysis reveals that MDS4 displays a β value nearly two times that of MDS4a, and MDS5 exhibits a β value approximately four times greater than MDS5a. Notably, MDS5 achieves the highest first hyperpolarizability value (β^0 and β^0_{HRS}), which is approximately 407 times larger than that of MDS2.

On the other hand, the analysis of the first hyperpolarizability (β^0 and β^0_{HRS}) for the MDS'n series reveals that the β^0_{HRS} values in the static regime exhibit an increasing trend from n = 2 to n = 4, followed by a decrease from n = 4 to n = 5. This observed trend is in good agreement with the DFT calculations of Wang et al.. [14], [15] Notably, MDS'3 demonstrates a β^0_{HRS} value approximately three times greater than that of MDS'2, while MDS'4 shows a β^0_{HRS} value roughly twice that of MDS'3. In contrast, the β^0_{HRS} value for MDS'5 is about three times smaller than that of MDS'4. These trends for the calculated β^0_{HRS} values mirror those observed for β^0. For this series, MDS'4 stands out with the highest first hyperpolarizability, being approximately four times greater than that of MDS'2. Our results also indicate a clear correlation between the static first hyperpolarizability (β) values and the chemical hardness (η) of the MDSn complexes, as evidenced by the trend of increasing β with decreasing chemical hardness.

Our results demonstrate that the static first hyperpolarizability values of the MDSn complexes increase as their chemical hardness decreases. A similar trend is observed in the MDS'n clusters, further strengthening the correlation between these two properties. This observation aligns with the established literature, which suggests that a reduction in chemical hardness can facilitate enhanced NLO responses in materials [50].

Additionally, a comparative analysis between the two series reveals that the MDS'n complexes exhibit higher first hyperpolarizability values than their corresponding MDSn counterparts, with the exception of n = 5. The observed difference in first hyperpolarizability, β(MDS'n) > β(MDSn), which increases from n = 2 to n = 4, can be attributed to the tilted geometries of the MDS'n complexes, as defined by the angle φ (Fig. S1). For instance, the β values for MDS'2 and MDS'3 (φ = 51°) are 19 and 5 times greater, respectively, than those for MDS2 and MDS3 (φ = 90°). In contrast, for MDS5 (φ = 95°), the β value is observed to be 5 times greater than that of MDS'5. The highest first hyperpolarizability (β^0) value of 3.553 × 10^5 a.u. (and β^0_{HRS} of 1.472 × 10^5 a.u.) is recorded for the MDS5 cluster.

As depicted in **Figure IV.8**, both the static polarizability and first hyperpolarizability generally increase with the number of (CoCp) units (n), indicating enhanced delocalization and polarizability as the structure elongates. Notably, the MDSn systems exhibit a more pronounced increase in first hyperpolarizability at n = 5, suggesting a significant NLO response at higher chain lengths. In contrast, MDS'$_n$ shows a peak at n = 4, followed by a decline at n = 5, indicating potential structural or electronic saturation beyond this point [51]–[53].

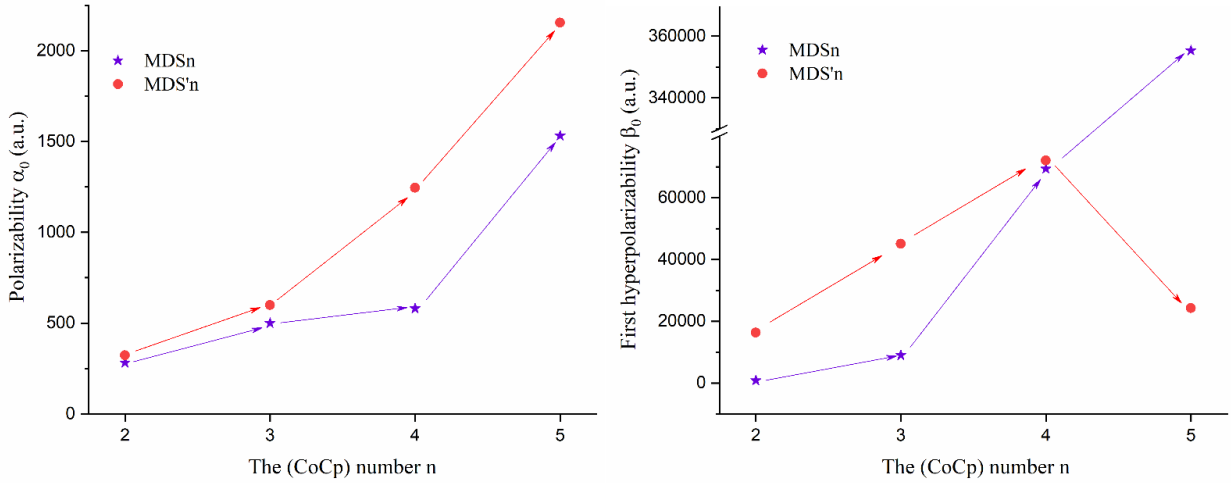

Figure IV.8 Variation of static polarizability and first hyperpolarizability as a function of the number of (CoCp) Units (n)

Based on this study, we conclude that four key factors play a significant role in enhancing the static first hyperpolarizability of the examined clusters: chemical hardness, the structural geometry of the multi-decker sandwich complexes, the number of (CoCp) units, and their specific spatial arrangements within the cluster.

Regarding the dynamic regime, it is observed that MDS'2, MDS3, MDS'4, MDS4, MDS4a, and MDS5a exhibit the highest values of dynamic second-order hyperpolarizability (β_{SHG}^{ω}) at 0.034 a.u., in comparison to those measured at 0.0428 and 0.0239 a.u. In contrast, the MDS2, MDS'3, and MDS'5 clusters demonstrate enhanced SHG responses at 0.0239 a.u., surpassing the values observed at 0.0428 and 0.034 a.u. Notably, the MDS5 cluster exhibits the largest dynamic first hyperpolarizability at 0.0428 a.u., with an exceptional β_{SHG}^{ω} value of 6.639 × 10^8 a.u. (see **Figure IV. 9** and **Table IV.3**). For instance, at the frequency of 0.0239 a.u. (1906 nm), the β_{SHG}^{ω} values of the studied clusters decrease in the following order: MDS'4 > MDS5 > MDS'3 > MDS'5 > MDS5a > MDS4 > MDS4a > MDS'2 > MDS2 > MDS3. At the frequency of 0.0428 a.u. (1064 nm), it is evident that the β_{SHG}^{ω} values for MDS'2, MDS'3, and MDS'5 are approximately 17, 3, and 18 times greater than those of MDS2, MDS3, and MDS5, respectively. Furthermore, the variations in dynamic regime β_{HRS}^{ω} values exhibit a close correspondence with the trends observed in β_{SHG}^{ω} values (see **Figure. S3.AII**).

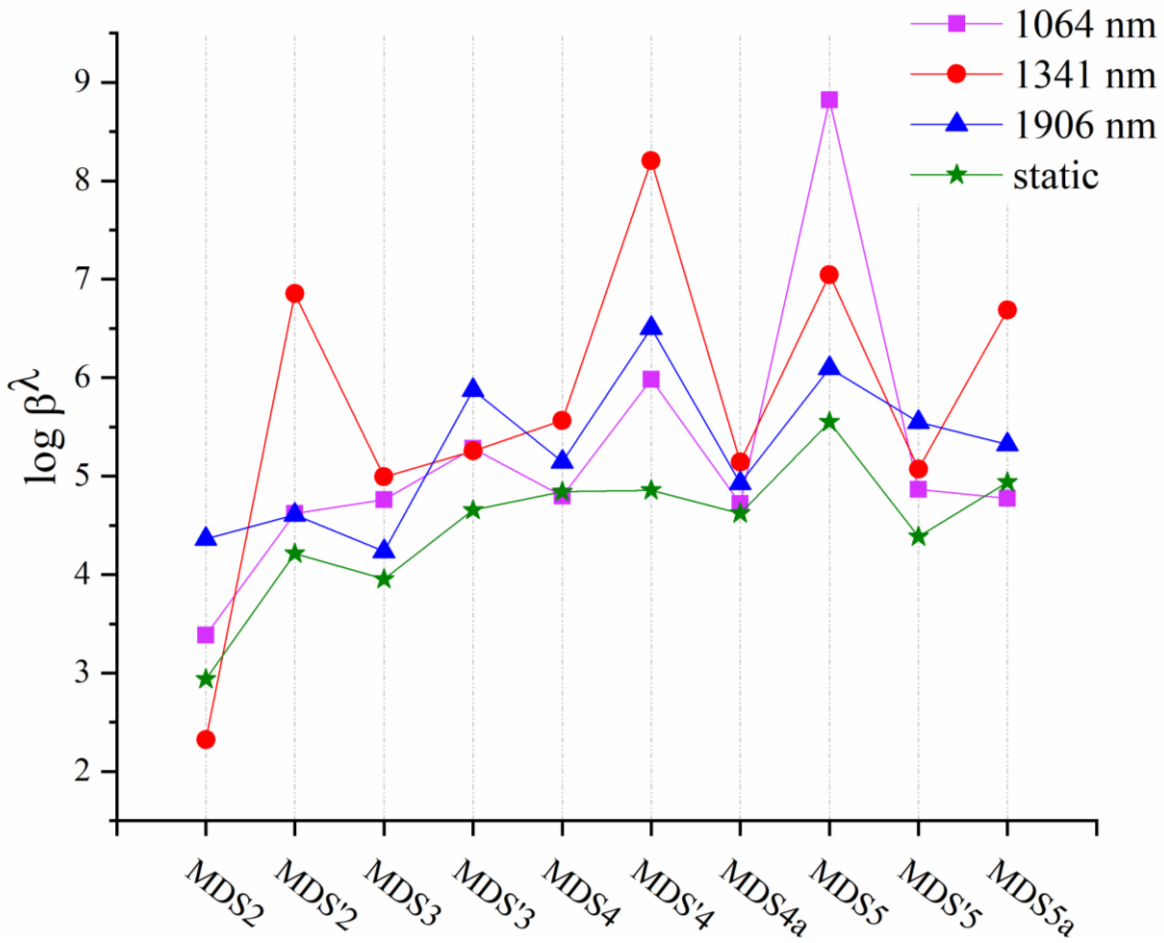

Figure IV.9 Variation of the static and dynamic first hyperpolarizability $\beta(0; 0, 0)$, and β_{SHG} $(-2\omega; \omega, \omega)$ of MDSn and MDS'n.

The electro-optical Pockels effect (EOPE) values, $\beta(-\omega;\omega,0)$, for the complexes $\{H_2B_2S_2Pd(Cl)_2\}$-$(CoCp)_n$ (where n = 2 to 5) are provided in **Table S6.AII**. The β^{ω}_{EOPE} values at 0.0428 a.u. are markedly higher compared to those at 0.034 and 0.0239 a.u., indicating that the electro-optical Pockels effect $\beta(-\omega;\omega,0)$ is more pronounced at higher frequencies. However, exceptions are noted for MDS2 and MDS'4, where the highest β^{ω}_{EOPE} values are observed at 0.0239 a.u. and 0.034 a.u., respectively.

For the MDSn series, the β^{ω}_{EOPE} values generally increase with the number of (CoCp) units (n = 2, 3, 4), demonstrating a positive correlation between the number of layers and electro-optical sensitivity. Notably, a decline in β^{ω}_{EOPE} values is observed when the number of layers is increased to 5. For most frequencies, the β^{ω}_{EOPE} values increase with the addition of layers in the MDSn series (n = 1, 2, 3, 4, 5), except at ω = 0.0239 a.u., where the values follow the trend: MDS3 (1.13×10^4) < MDS1 (2.15×10^4) < MDS4 (8.91×10^4) < MDS5 (1.13×10^6).

It is important to highlight that the values of β^{ω}_{EOPE} at 0.0428 and 0.034 a.u. for the MDS'n series (n = 2 to 4) are significantly greater than those observed for the corresponding MDSn clusters. This observed trend is in strong agreement with the results derived from the first hyperpolarizability measurements, suggesting that the specific arrangement of the $\{H_2B_2S_2Pd(Cl)_2\}$ fragment and the number of (CoCp)n units within the multidecker sandwich complexes offer an efficient approach for the modulation and enhancement of nonlinear optical properties.

Table IV.3. Static and dynamic first hyperpolarizability (β^0 , β^{ω}_{HRS} a.u.), second harmonic generation [β^{ω}_{HRS}(-2ω; ω, ω), a.u.], depolarization ratios (DR) of MDSn, MDSna and MDS'n complexes

	β^0	β^{ω}_{SHG}			β^{ω}_{HRS}				DR^{ω}			
ω	**0**	0.0428	0.0340	0.0239	**0**	0.0428	0.0340	0.0239	**0**	0.0428	0.0340	0.0239
MDS2	8.64×10^{2}	2.42×10^{3}	2.09×10^{2}	2.31×10^{4}	3.66×10^{2}	1.11×10^{3}	8.31×10^{2}	2.19×10^{4}	4.63	3.55	0.80	0.35
MDS'2	1.63×10^{4}	4.18×10^{4}	7.15×10^{6}	4.05×10^{4}	6.72×10^{3}	1.92×10^{4}	2.96×10^{6}	1.66×10^{4}	5.10	4.41	5.01	5.18
MDS3	8.98×10^{3}	5.76×10^{4}	9.85×10^{4}	1.71×10^{4}	3.68×10^{3}	2.42×10^{4}	4.12×10^{4}	7.03×10^{3}	5.18	4.58	4.87	5.34
MDS'3	4.51×10^{4}	1.91×10^{5}	1.80×10^{5}	7.46×10^{5}	1.88×10^{4}	1.11×10^{5}	7.61×10^{4}	3.11×10^{5}	4.84	0.95	4.18	4.85
MDS4	6.93×10^{4}	6.28×10^{4}	3.68×10^{5}	1.39×10^{5}	2.86×10^{4}	2.72×10^{4}	1.53×10^{5}	8.60×10^{4}	5.04	3.90	5.19	0.77
MDS'4	7.20×10^{4}	9.64×10^{5}	1.60×10^{8}	3.19×10^{6}	2.99×10^{4}	4.04×10^{5}	6.77×10^{7}	1.34×10^{6}	4.92	4.72	4.19	4.21
MDS4a	4.18×10^{4}	5.25×10^{4}	1.39×10^{5}	8.47×10^{4}	1.74×10^{4}	4.63×10^{4}	6.01×10^{4}	3.54×10^{4}	4.89	0.46	3.28	4.66
MDS5	3.55×10^{5}	6.63×10^{8}	1.11×10^{7}	1.25×10^{6}	1.47×10^{5}	2.75×10^{8}	4.59×10^{6}	5.18×10^{5}	4.99	4.87	4.97	4.96
MDS'5	2.43×10^{4}	7.29×10^{4}	1.17×10^{5}	3.53×10^{5}	1.07×10^{4}	9.64×10^{4}	4.76×10^{4}	1.47×10^{5}	4.16	0.24	5.93	5.04
MDS5a	8.67×10^{4}	5.96×10^{4}	4.86×10^{6}	2.11×10^{5}	3.56×10^{4}	2.99×10^{4}	2.06×10^{6}	8.68×10^{4}	5.14	1.78	3.9	5.08

c- Frequency dispersion effects

To examine the influence of frequency dispersion on the nonlinear optical (NLO) behavior of these clusters, dynamic perturbations were introduced. This methodology facilitated the assessment of the effect of dispersion corrections on the NLO properties. To quantify this influence, the frequency dispersion factor (FDF^{ω}) was utilized, which represents the ratio of the static to dynamic HRS hyperpolarizability[39] at distinct wavelengths (λ = 1064, 1341, and 1906 nm, corresponding to 1.165, 0.942, and 0.65 eV, respectively). The precise values of FDF^{ω} are presented in **Table IV.4**.

Table IV.4. Frequency dispersion factor (FDF^{ω}) for the static and dynamic HRS hyperpolarizability at specific frequencies (ω = 0.0428, 0.034, 0.0239 a.u.)

ω	0.0428 a.u. (1.165 eV)	0.034 a.u. (0.924 eV)	0.0239 a.u. (0.65 eV)
		FDF^{ω}	
MDS2	3.03	2.27	60
MDS'2	2.86	441	2.48
MDS3	6.59	11.22	1.91
MDS'3	5.93	4.04	16.48
MDS4	0.95	5.35	3.00
MDS'4	13.49	2259	45
MDS4a	2.66	3.45	2.04
MDS5	1872	31.22	3.52
MDS'5	9.01	4.45	13.74
MDS5a	0.84	58	2.44

The TD-DFT calculations (**Figure. S2.AII** and **Figure IV.5**) reveal that the excitation energies for MDS'2 (1.867 eV, f = 0.088), MDS'4 (1.855 eV, f = 0.031), MDS5 (1.845 eV, f = 0.017), and MDS5a (1.893 eV, f = 0.214) are closely aligned with the energy of the incident light at 2ω (1.848 eV). Conversely, MDS3 (1.829 eV, f = 0.088) and MDS4 (1.885 eV, f = 0.009) exhibit small deviations from 1.848 eV, suggesting they are in near two-photon resonance, as indicated in **Table IV.4**. In contrast, the excitation energies for MDS3, MDS4, MDS'4, and MDS'5 at 0.896, 0.931, 0.898, and 0.942 eV, respectively, are closer to the one-photon resonance energy of ω = 0.924 eV. Furthermore, the optical nonlinearity dispersion for MDS5 at 1.165 eV demonstrates a significant frequency dispersion factor (FDF = 1872), attributed to electronic transitions occurring at 2.136 eV (f = 0.451) and 1.167 eV (f = 0.002), suggesting that MDS5 is in proximity to both one- and two-photon resonance. The moderate FDF^{ω} values recorded for MDS3, MDS'3, MDS'4, and MDS'5 at 1.165 eV (6.59, 5.93, 13.49, and 9.01, respectively), and

for MDS'3 and MDS'5 at 0.65 eV (16.42 and 13.74, respectively), indicate that these clusters are approaching resonance conditions. In contrast, FDF^{ω} values below 5 suggest that the systems are significantly distant from resonance.

To gain a deeper insight into the factors affecting the first hyperpolarizability of the complexes under investigation, polarization scans of the hyper-Rayleigh scattering (HRS) intensity, denoted as $I_{\Psi V}^{2\omega}$, were conducted. The relationship between $I_{\Psi V}^{2\omega}$ and the polarization angle (ψ) was computed and the results are presented graphically (**Figure IV.10** and **S4.AII**), with the corresponding $\beta_{J=1}$ and $\beta_{J=3}$ values provided in **Table S7.AII**. At λ = ∞, the depolarization ratio (DR) values were found to exhibit minimal dependence on the number of (CoCp) units, with DR^{∞} values ranging from 4 to 5.2 (see **Table IV.3**). Specifically, the DR^{∞} values follow the sequence: MDS'2 (5.1) > MDS'4 (4.92) ≈ MDS'3 (4.84) > MDS'5 (4.16). It is noteworthy that the MDSn and MDS'n clusters predominantly exhibit near-ideal dipolar symmetry in their nonlinear optical (NLO) responses, as indicated by DR values close to 5. However, exceptions were observed for MDS2 and MDS'5, which display a more pronounced dipolar character in their NLO responses ($\beta_{J=1} > \beta_{J=3}$), as evidenced by DR values that deviate from 5.

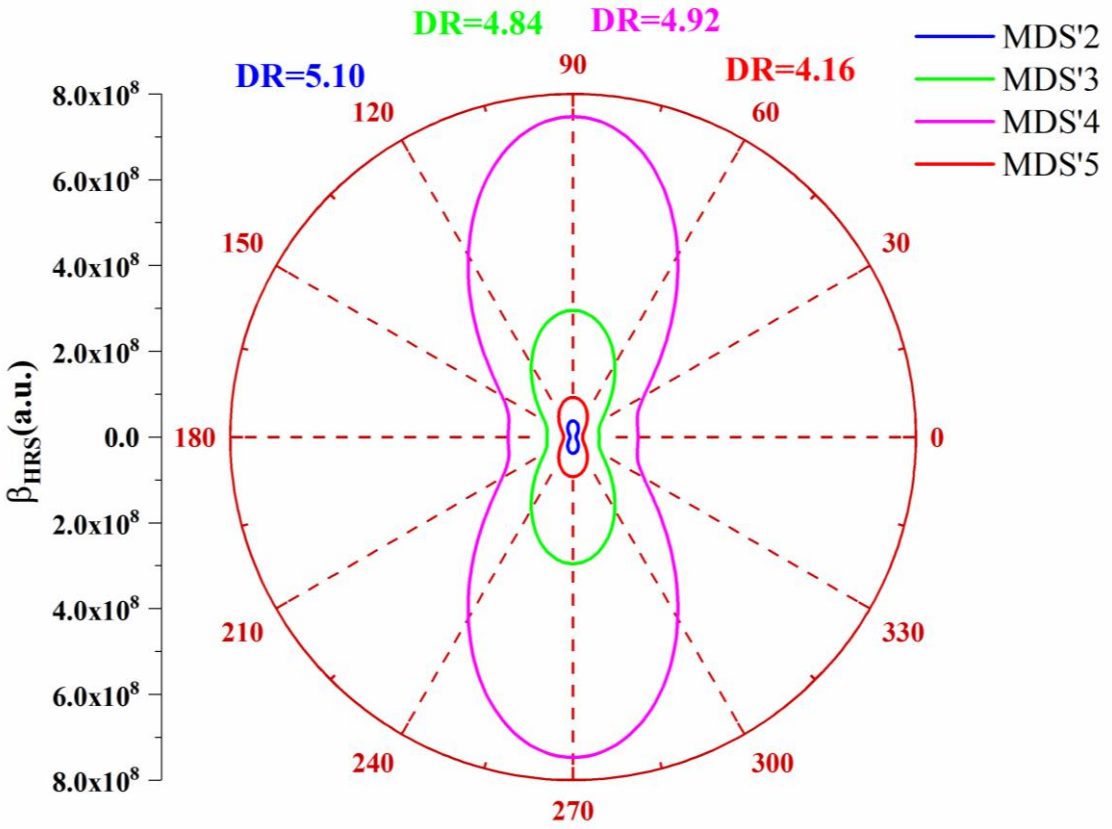

Figure IV. 10 Relationship between $I_{\Psi V}^{2w}$ and polarization angle Ψ of MDS'n serie.

Regarding the dynamic depolarization ratio, the clusters MDS2, MDS'2, MDS3, MDS4, MDS'4, and MDS5 at ω = 0.0428 a.u. are classified as dipolar compounds, with the dipolar contributions $\beta_{J=1}$ being larger than $\beta_{J=3}$ (see **Table IV.3** and **Table S7.AII**). In contrast, MDS5a is identified as an octupolar complex, exhibiting significant octupolar contributions ($\beta_{J=3} > \beta_{J=1}$), while the DR values for MDS'3, MDS4a, and MDS'5 are 0.95, 0.46, and 0.24, respectively. At ω = 0.0340 and 0.0239 a.u., the remaining complexes are considered dipolar compounds (**Table S7.AII**), except for MDS4a, which is characterized as an octupolar compound. Additionally, the clusters MDS2, MDS4 (at 0.0239 a.u.), and MDS4a (at 0.0340 a.u.) exhibit DR values below 1.5.

IV.6.6. Two level model

Building on the definition introduced in **Chapter III**, we proceed here with the calculation of the first hyperpolarizability (**Eq.III.2**) as presented in **Figure IV. 11** and **Figure.S5.AII** illustrate the relationship between the β_{SOS} value and 120 excited states, showing that 120 excited states are sufficient to achieve convergence of the β_{SOS} value. Furthermore, the trend observed in hyper-Rayleigh scattering (HRS) hyperpolarizability, calculated via the SOS method, aligns well with the results obtained using the M06-2X/SDD/6-311G(d) level of theory, with only minor deviations attributed to the inherent limitations of the SOS method (**Table S8.AII**). The critical excited state data is presented in **Figure IV. 11** and **Figure. S5** in **Annex II**.

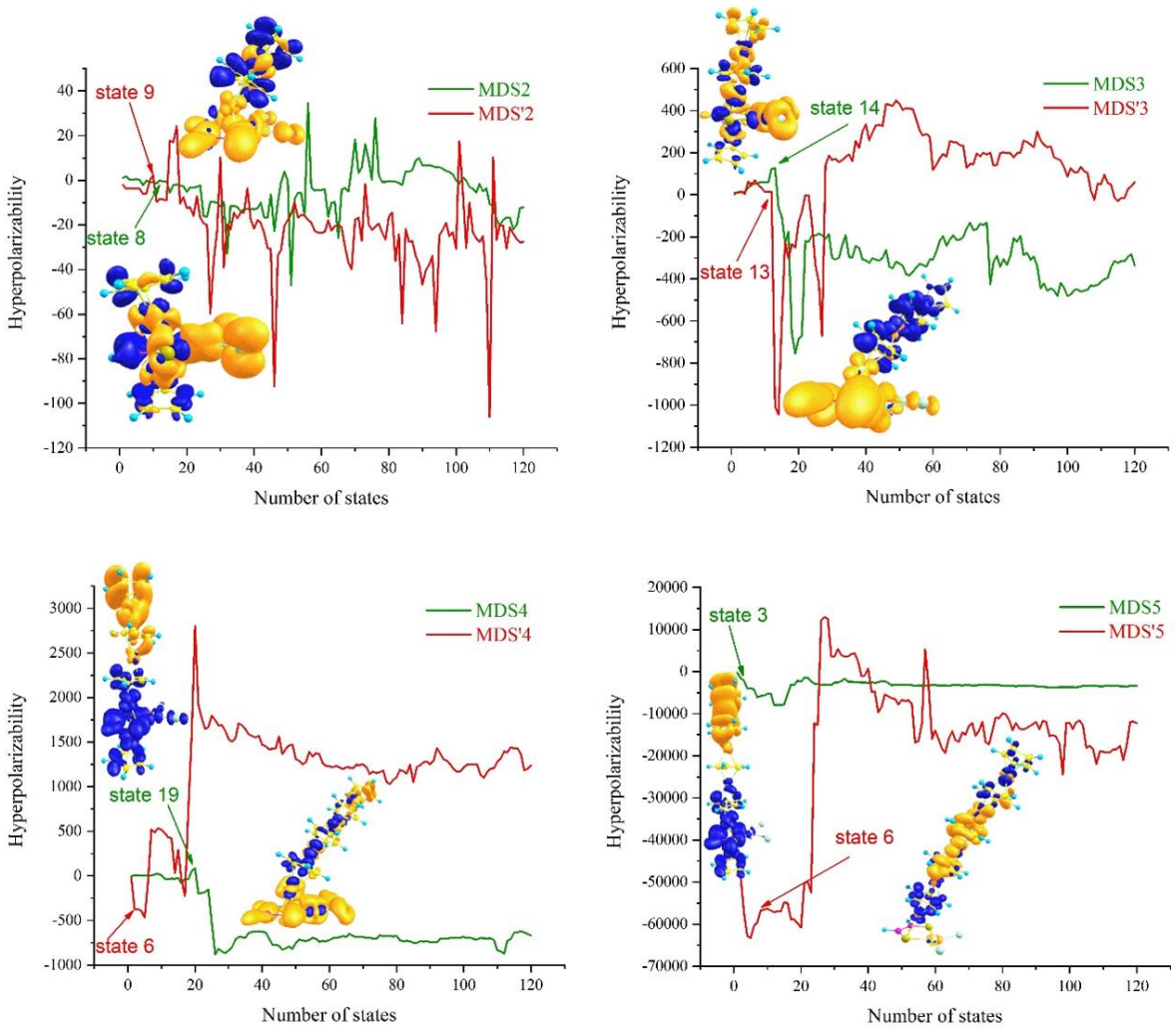

Figure IV. 11 Plots of static first hyperpolarizability values as computed in the SOS formalism as a function of the number of excited states for MDSn and MDS'n complexes, obtained at M06-2X/ SDD/6-311G(d) level

To further investigate this trend, the values of $((f \times \Delta\mu)/\Delta E^3)$ corresponding to the critical excited states were computed. The correlation between the static β_{HRS} values and their respective $((f \times \Delta\mu)/\Delta E^3)$ values for the examined complexes is presented in **Figure IV. 12**. A satisfactory level of agreement is observed for the β_{HRS} values of complexes 2−5. This observation suggests that the $((f \times \Delta\mu)/\Delta E^3)$ value offers a reliable qualitative depiction of the trend, capturing a substantial fraction of the first hyperpolarizability and validating its effectiveness in forecasting nonlinear optical properties in these systems.

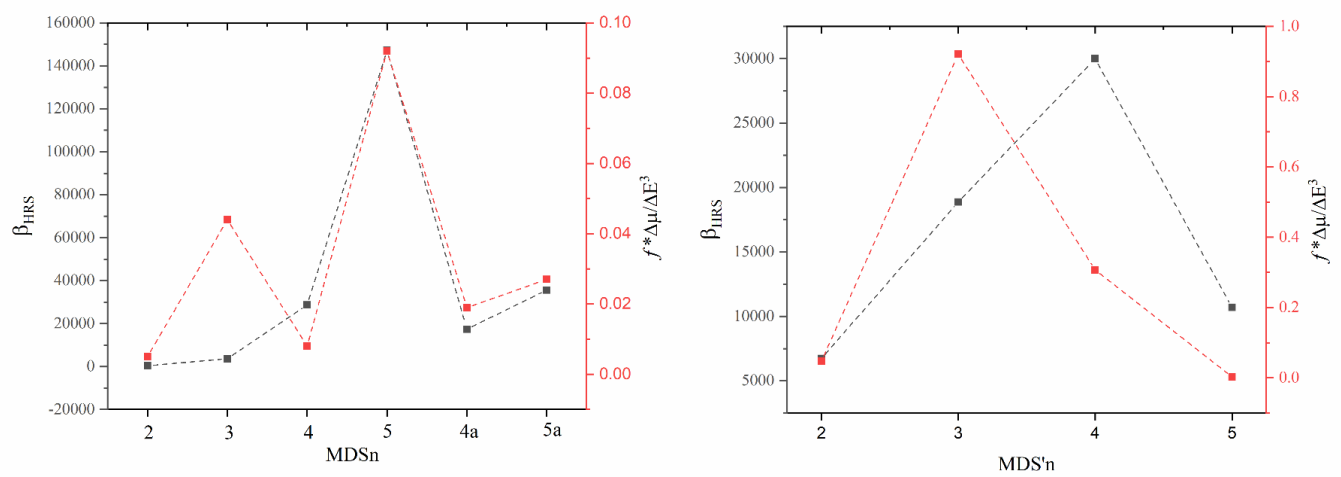

Figure IV.12 Relationship between the β_{HRS} values (black) and the corresponding $((f \times \Delta\mu)/\Delta E^3)$ (red) for the studied complexes.

To investigate the origin of the second-order nonlinear optical responses, the EDDM of the critical excited states was extensively analyzed (**Figure IV.11**, **Figure. S5.AII**, and **Tables S4-S5.AII**). The two-level model analysis reveals that the excited states S8, S9, and S14 play a dominant role in the first hyperpolarizability of the MDS2, MDS'2, and MDS3 complexes. These states are characterized as local excitations, with relatively small charge transfer distances (d^{ct}) of 2.145, 2.960, and 0.278 Å, respectively, and correspondingly high Sr indices of 0.643, 0.712, and 0.929 (see **Table IV.2**). On the other hand, the critical excited states S19 and S3 exhibit the highest first hyperpolarizability in the MDS4 and MDS5 complexes, associated with non-local charge transfer between the CoCp2 units located on opposite sides (**Figure IV.11**). These non-local excitations show significant variations in dipole moments, 14.926 and 15.233 a.u., accompanied by negligible Sr indices (Sr ≈ 0). Furthermore, the non-local excited state S13, with an Sr index of 0.252 (Δμ=6.605 a.u and d^{ct} = 5.858 Å), exhibits the highest hyperpolarizability in MDS'3, resulting from the charge transfer between the $\{B_2S_2Pd(Cl)_2\}$ fragment and the Co_2Cp_3 moiety (**Figure IV.12**).

The excited state S6 predominantly contributes to the first hyperpolarizability of the MDS'4 and MDS'5 complexes. In the case of MDS'5, the excited state S6 (Δμ=1.852 a.u and d^{ct} = 1.583 Å) primarily arises from an electronic transition between the central $CoCp_2$ moiety and the two $CoCp_2$ fragments positioned at the periphery of the complex. Notably, the $\{B_2S_2Pd(Cl)_2\}$ group does not participate in this electronic transition, indicating a non-localized charge transfer (Sr = 0.499), which is confined to the $CoCp_2$ fragments within the structure (see **Figure IV.12**). For the MDS4a and MDS5a complexes, the excited states S14 and S10, respectively, make

significant contributions to the hyperpolarizability. These correspond to local ($\Delta\mu$= 3.643 a.u and d^{ct} = 4.207 Å) and nonlocal electronic transitions ($\Delta\mu$= 27.38 a.u and d^{ct} = 14.794 Å).

The transition energies (ΔE) of the critical excited states for the MDS'n complexes (n = 2 to 5) are quantified as 1.866 eV, 1.451 eV, 0.898 eV, and 0.792 eV, respectively. In contrast, the transition energies for the corresponding MDSn complexes are 2.034 eV, 1.715 eV, 1.524 eV, and 0.638 eV, respectively. It is apparent that, for both the MDS'n and MDSn complexes, the transition energies follow the trend: $\Delta E(2) > \Delta E\ (3) > \Delta E\ (4) > \Delta E\ (5)$. Notably, the transition energies of MDSn complexes are generally higher than those of their MDS'n counterparts, with the exception of the n = 5 case, where MDS'5 (S1 → S6) demonstrates a higher transition energy compared to MDS5 (S1 → S3). The sequence of transition energies for the critical excited states closely mirrors the trend observed in the first hyperpolarizability values, suggesting a correlation between excitation energy and the nonlinear optical response of the complexes.

The EDDM analysis provides insight into the variations in first hyperpolarizability among the MDS complexes. The significant increase in β for MDS4 and MDS5, compared to MDS1 and MDS2, can be primarily attributed to non-local charge transfer mechanisms. Notably, MDS'n complexes exhibit higher β values than their MDSn counterparts, with the exception of n = 5, where the charge transfer from the $\{B_2S_2Pd(Cl)_2\}$ fragment to the $(CoCp)_n$ units in the critical excited state leads to a higher β in MDS'5 (**Figure IV. 11**). The EDDM analysis reveals that the enhancement in β is driven by the increased transition dipole moments and the extended charge transfer distances in the key excited states, which are crucial factors in amplifying the nonlinear optical response of these systems.

IV.7. Conclusion

A comprehensive investigation has been conducted on the structural characteristics, reactivity indices, and both linear and nonlinear optical properties of a series of ten multi-decker sandwich clusters, [{$B_2H_2S_2Pd(Cl)_2$}-$(CoCp)_n$] (n = 2 to 5). These clusters vary in the spatial arrangement of the {$H_2B_2S_2Pd(Cl)_2$} fragment and the number of (CoCp) units, categorized as MDSn, MDSna, and MDS'n. Advanced Density Functional Theory (DFT) and Time-Dependent DFT (TD-DFT) calculations were performed at the M06-2X/6-311G(d)/SDD level. The sum-over-states (SOS) method was employed to investigate both static and frequency-dependent nonlinear optical (NLO) responses, offering a detailed understanding of their electronic and optical behavior.

Our findings reveal that the MDS'n clusters exhibit inclined geometries, with angular deviations (φ) ranging from 50° to 64°, whereas the MDSn complexes display near-perpendicular orientations relative to the molecular axis. Additionally, MDS'n structures show Cl...H-induced deformations in the {{$H_2B_2S_2Pd(Cl)_2$} fragment and Cp rings, an effect absent in MDSn complexes. Notably, the MDSn complexes exhibit higher chemical hardness values compared to their corresponding MDS'n counterparts. TD-DFT calculations reveal that the absorption spectra of the clusters are divided into two distinct regions: one between 200–350 nm, attributed to intra-ligand π–π* transitions in the Cp ligands, and another between 400–1400 nm, characterized by mixed charge transfer (CT and ICT) interactions between the fragments.

The NLO analysis indicates that increasing the number of (CoCp) units significantly enhances both the polarizability α (0,0) and its anisotropy Δα (0,0) across both MDSn and MDS'n series (n = 2 to 5). The first hyperpolarizability (β) of the MDS'n series demonstrates an increasing trend with the addition of (CoCp) units from n = 2 to 4, while a decrease in β is observed when n reaches 5. In contrast, the β values for the MDSn complexes consistently increase as the number of (CoCp) units increases from n = 2 to 5, exhibiting behavior typical of conventional push-pull π-systems. A detailed comparative analysis reveals that, in general, the MDS'n complexes exhibit higher first hyperpolarizability values than their MDSn counterparts, except in the case of n = 5. This deviation is attributed to charge transfer (CT) between the {$H_2B_2S_2Pd(Cl)_2$} fragment and the $(CoCp)_n$ units in the critical excited state of MDS'n.

The EDDM analysis further highlights that enhanced transition dipole moments and extended charge transfer pathways in the essential excited states are key contributors to the observed

increase in β. In conclusion, this study provides a conceptual framework for designing highly efficient NLO materials based on multi-decker sandwich clusters. The significant enhancement in their NLO responses underscores their promising potential for advanced applications in nonlinear optoelectronic devices.

References

[1] M. Blanchard-Desce, I. Ledoux, J. M. Lehn, J. Malthête, and J. Zyss, "Push-pull polyenes and carotenoids: Synthesis and non-linear optical properties," *J. Chem. Soc., Chem. Commun.*, no. 11, pp. 737–739, 1988, doi: 10.1039/C39880000737.

[2] D. Hannachi *et al.*, "The effect of resonance-assisted hydrogen bond on the second-order nonlinear optical properties of pyridine hydrazone photoswitches: a quantum chemistry investigation," *New J. Chem.*, vol. 47, pp. 18359–18373, 2023, doi: 10.1039/d3nj02848h.

[3] E. Cariati, C. Dragonetti, E. Lucenti, F. Nisic, S. Righetto, and E. Tordin, "An acido-triggered reversible luminescent and nonlinear optical switch based on a substituted styrylpyridine : EFISH measurements as an unusual method to reveal a protonation – deprotonation NLO contrast," *Chem. Commun.*, vol. 50, no. 13, pp. 1608–1610, 2014, doi: 10.1039/c3cc48149b.

[4] F. Ricci, F. Elisei, P. Foggi, A. Marrocchi, A. Spalletti, and B. Carlotti, "Photobehavior and Non − Linear Optical Properties of Push − Pull , Symmetrical and Highly Fluorescent Benzothiadiazole Derivatives," *J. Phys. Chem.*, vol. 120, no. 41, pp. 23726–23739, 2016, doi: 10.1021/acs.jpcc.6b07290.

[5] F. Chérioux, H. Maillotte, P. Audebert, and J. Zyss, "Synthesis and characterisation of an octupolar polymer and new molecular octupoles with off-resonant third order optical nonlinearities," *Chem. Commun.*, no. 20, pp. 2083–2084, 1999, doi: 10.1039/a905899k.

[6] M. Fontani, A. Colombo, C. Dragonetti, S. Righetto, D. Roberto, and D. Marinotto, "Cyclometalated Ir(III) complexes with curcuminoid ligands as active second-order nlo chromophores and building blocks for shg polymeric films," *Inorganics*, vol. 8, no. 5, 2020, doi: 10.3390/INORGANICS8050036.

[7] D. Hannachi, M. F. Haroun, A. Khireddine, and H. Chermette, "Optical and nonlinear optical properties of Ln(Tp)2, where Ln = La,...,Lu and Tp = tris(pyrazolyl)borate: a DFT+TD-DFT study," *New J. Chem.,* vol. 43, p. 14377, 2019, doi: 10.1039/c9nj03232k.

[8] M. Zaidi, D. Hannachi, and H. Chermette, "Correlation between Second Ionization Potential and Nonlinear Optical Properties of Bivalent Transition-Metal Complexes : A Quantum Chemical Study," *Inorg. Chem.*, vol. 60, pp. 6616–6632, 2021.

[9] D. Kamli, D. Hannachi, and H. Chermette, "Bis-TTF-Ge derivatives: promising linear and nonlinear optical properties, a theoretical investigation," *New J. Chem.,* vol. 47, pp. 1234–1246, 2023, doi: 10.1039/d2nj03671a.

[10] A. Ahsin and K. Ayub, "Remarkable electronic and NLO properties of bimetallic superalkali clusters: a DFT study," *J. Nanostructure Chem.*, no. 0123456789, 2021, doi: 10.1007/s40097-021-00429-2.

[11] A. Ahsan and K. Ayub, "Adamanzane based alkaline earthides with excellent nonlinear optical response and ultraviolet transparency," *Opt. Laser Technol.*, vol. 129, no. March, p. 106298, 2020, doi: 10.1016/j.optlastec.2020.106298.

[12] A. Ahsan, S. Sarfaraz, F. Fayyaz, M. Asghar, and K. Ayub, "Enhanced non-linear optical response of calix[4]pyrrole complexant based earthides in the presence of oriented external electric field," *J. Mol. Liq.*, vol. 350, p. 118504, 2022, doi: 10.1016/j.molliq.2022.118504.

[13] A. Ahsan and K. Ayub, "Extremely large nonlinear optical response and excellent electronic stability of true alkaline earthides based on hexaammine complexant," *J. Mol. Liq.*, vol. 297, pp. 36–40, 2020, doi: 10.1016/j.molliq.2019.111899.

[14] S. J. Wang, Y. F. Wang, and C. Cai, "Multidecker Sandwich Cluster VnBenn +1 (n = 1, 2, 3, 4) as a Polarizable Bridge for Designing 1D Second-Order NLO Chromophore: Metal-π Sandwich Multilayer Structure as a Particular Charge-Transfer Axis for Constructing Multidimensional NLO Molecules," *J. Phys. Chem. C*, vol. 119, no. 28, pp. 16256–16262, 2015, doi: 10.1021/acs.jpcc.5b04656.

[15] S. J. Wang, Y. F. Wang, and C. Cai, "Multidecker sandwich complexes VnBenn+1 (n = 1, 2, 3) as stronger electron donor relative to ferrocene for designing high-performance organometallic second-order nlo chromophores: Evident layer effect on the first hyperpolarizability and two-dimensional N," *J. Phys. Chem. C*, vol. 119, no. 10, pp. 5589–5595, 2015, doi: 10.1021/jp5123272.

[16] B. Ni, W. Sun, J. Kang, and Y. Zhang, "Understanding the Linear and Second-Order Nonlinear Optical Properties of UiO-66-Derived Metal-Organic Frameworks: A Comprehensive DFT Study," *J. Phys. Chem. C*, vol. 124, no. 21, pp. 11595–11608, 2020, doi: 10.1021/acs.jpcc.0c01580.

[17] T. J. KEALY and P. L. PAUSON, "A new type of organo-iron compound," *Nature*, vol.

168, pp. 1039–1040, 1951, doi: 10.1038/168162a0.

[18] G. Wilkinson, M. Rosenblum, M. C. Whiting, and R. B. Woodward, "The structure of iron bis-cyclopentadienyl," *J. Am. Chem. Soc.*, vol. 74, no. 8, pp. 2125–2126, 1952, doi: 10.1021/ja01128a527.

[19] Ernst Otto Fischer and Walter Pfab, "Über Di-Cyclopentadienyl-Eisen, Di-Cyclopentadienyl-Nickel und Di- Cyclopentadienyl-Kobalt," *Z. Naturforsch., B*, vol. 7b, pp. 377–379, 1952.

[20] C. A. P. Goodwin, "What is a Sandwich Complex?," *Organometallics*, vol. 43, pp. 595–597, 2024, doi: 10.1021/acs.organomet.4c00017.

[21] B. Joseph, R. Prakash, R. Bag, and S. Ghosh, "' Triple-Decker Sandwich ' Containing Planar {B 2 E 2 Pd} Ring (E = S or Se)," vol. 2, pp. 2–10, 2020.

[22] A. D. Becke, "Density-functional thermochemistry. III. The role of exact exchange," *J. Chem. Phys.*, vol. 98, no. 7, pp. 5648–5652, 1993, doi: 10.1063/1.464913.

[23] C. Lee, W. Yang, and R. G. Parr, "Development of the Colle-Salvetti correlation-energy formula into a functional of the electron density," *Phys. Rev. B*, vol. 37, no. 2, pp. 785–789, 1988, doi: org/10.1103/PhysRevB.37.785.

[24] J. Da Chai and M. Head-Gordon, "Systematic optimization of long-range corrected hybrid density functionals," *J. Chem. Phys.*, vol. 128, no. 8, 2008, doi: 10.1063/1.2834918.

[25] J. Da Chai and M. Head-Gordon, "Long-range corrected hybrid density functionals with damped atom-atom dispersion corrections," *Phys. Chem. Chem. Phys.*, vol. 10, no. 44, pp. 6615–6620, 2008, doi: 10.1039/b810189b.

[26] T. Yanai, D. P. Tew, and N. C. Handy, "A new hybrid exchange-correlation functional using the Coulomb-attenuating method (CAM-B3LYP)," *Chem. Phys. Lett.*, vol. 393, no. 1–3, pp. 51–57, 2004, doi: 10.1016/j.cplett.2004.06.011.

[27] V. N. Staroverov, G. E. Scuseria, J. Tao, and J. P. Perdew, "Erratum: Comparative assessment of a new nonempirical density functional: Molecules and hydrogen-bonded complexes(Journal of Chemical Physics (2003) 119 (12129))," *J. Chem. Phys.*, vol. 121, p. 11507, 2004, doi: 10.1063/1.1795692.

[28] V. N. Staroverov, G. E. Scuseria, J. Tao, and J. P. Perdew, "Comparative assessment of a new nonempirical density functional: Molecules and hydrogen-bonded complexes," *J. Chem. Phys.*, vol. 119, no. 23, pp. 12129–12137, 2003, doi: 10.1063/1.1626543.

[29] J. Tao, J. P. Perdew, V. N. Staroverov, and G. E. Scuseria, "Climbing the density functional ladder: Nonempirical meta–generalized gradient approximation designed for molecules and solids," *Phys. Rev. Lett.*, vol. 91, no. 14, pp. 3–6, 2003, doi: 10.1103/PhysRevLett.91.146401.

[30] Y. Zhao and D. G. Truhlar, "The M06 suite of density functionals for main group thermochemistry, thermochemical kinetics, noncovalent interactions, excited states, and transition elements: Two new functionals and systematic testing of four M06-class functionals and 12 other function," *Theor. Chem. Acc.*, vol. 120, no. 1–3, pp. 215–241, 2008, doi: 10.1007/s00214-007-0310-x.

[31] Y. Zhao and D. G. Truhlar, "Applications and validations of the Minnesota density functionals," *Chem. Phys. Lett.*, vol. 502, no. 1–3, pp. 1–13, 2011, doi: 10.1016/j.cplett.2010.11.060.

[32] G. A. Petersson and A.-L. Mohammad A, "A Complete Basis Set Model Chemistry. II. The Total Energies of open-Shell Atoms and Hydrides of the First-Row Atoms," *J. Chem. Phys.*, vol. 9, no. September 1990, pp. 6081–6090, 1991.

[33] G. A. Petersson, A. Bennett, T. G. Tensfeldt, M. A. Al-Laham, W. A. Shirley, and J. Mantzaris, "A complete basis set model chemistry. I. The total energies of closed-shell atoms and hydrides of the first-row elements," *J. Chem. Phys.*, vol. 89, no. 4, pp. 2193–2218, 1988, doi: 10.1063/1.455064.

[34] S. Irshad, F. Ullah, S. Khan, R. Ludwig, and T. Mahmood, "First row transition metals decorated boron phosphide nanoclusters as nonlinear optical materials with high thermodynamic stability and enhanced electronic properties ; A detailed quantum chemical study," *Opt. Laser Technol. J.*, vol. 134, pp. 106570–9, 2021.

[35] Maria, J. Iqbal, and K. Ayub, "Theoretical study of the non linear optical properties of alkali metal (Li, Na, K) doped aluminum nitride nanocages," *RSC Adv.*, vol. 6, no. 96, pp. 94228–94235, 2016, doi: 10.1039/c6ra21797d.

[36] S. Sarwar *et al.*, "Deciphering the Role of Alkali Metals (Li, Na, K) Doping for Triggering Nonlinear Optical (NLO) Properties of T-Graphene Quantum Dots: Toward

the Development of Giant NLO Response Materials," *ACS Omega*, vol. 7, no. 28, pp. 24396–24414, 2022, doi: 10.1021/acsomega.2c01746.

[37] L. M. G. Abegaõ *et al.*, "First molecular electronic hyperpolarizability of series of π-conjugated oxazole dyes in solution: An experimental and theoretical study," *RSC Adv.*, vol. 9, no. 45, pp. 26476–26482, 2019, doi: 10.1039/c9ra05246a.

[38] H. M. He, H. Yang, Y. Li, and Z. R. Li, "Theoretical Study of Alkaline-Earth Metal (Be, Mg, and Ca)-Substituted Aluminum Nitride Nanocages With High Stability and Large Nonlinear Optical Responses," *Front. Chem.*, vol. 10, no. June, pp. 1–10, 2022, doi: 10.3389/fchem.2022.918704.

[39] L. Lescos *et al.*, "Performance of DFT functionals for calculating the second-order nonlinear optical properties of dipolar merocyanines," *Phys. Chem. Chem. Phys.*, vol. 22, no. 29, pp. 16579–16594, 2020, doi: 10.1039/d0cp02992k.

[40] A. M. Arif, A. Yousaf, H. liang Xu, and Z. M. Su, "N-(O-methoxyphenyl)aza-15-crown-5-ether derivatives: Highly efficient and wide range nonlinear optical response based cation recognition," *J. Mol. Liq.*, vol. 301, pp. 22–24, 2020, doi: 10.1016/j.molliq.2020.112492.

[41] A. Sajjad *et al.*, "Theoretical Study of Dodecafluorophenylene-Based Superalkalides with Significantly High NLO Response," *ACS Omega*, vol. 8, pp. 45589–45598, 2023, doi: 10.1021/acsomega.3c05791.

[42] A. Shokuhi Rad and K. Ayub, "Substitutional doping of zirconium-, molybdenum-, ruthenium-, and palladium: An effective method to improve nonlinear optical and electronic property of C20 fullerene," *Comput. Theor. Chem.*, vol. 1121, pp. 68–75, 2017, doi: 10.1016/j.comptc.2017.10.015.

[43] B. Zhang *et al.*, "Design a novel type of excess electron compounds with large nonlinear optical responses using group 12 elements (Zn, Cd and Hg)," *J. Mol. Graph. Model.*, vol. 109, p. 108003, 2021, doi: 10.1016/j.jmgm.2021.108003.

[44] A. Ahsin, A. Ali, and K. Ayub, "Alkaline earth metals serving as source of excess electron for alkaline earth metals to impart large second and third order nonlinear optical response; a DFT study," *J. Mol. Graph. Model.*, vol. 101, p. 107759, 2020, doi: 10.1016/j.jmgm.2020.107759.

[45] Ragheb Khalil Bouriche, Douniazed Hannachi, Amel Messai, Christophe Morell, Amor Azizi, and Henry Chermette, "Electronic and Optical Properties of Copper Nanostructures for Advanced Applications," *New J. Chem.,* vol. 49, pp. 10730–10750, 2025, doi: 10.1039/D5NJ01220A.

[46] H. Chermette, "Chemical reactivity indexes in density functional theory," *J. Comput. Chem.*, vol. 20, no. 1, pp. 129–154, 1999, doi: 10.1002/(SICI)1096-987X(19990115)20:1<129::AID-JCC13>3.0.CO;2-A.

[47] R. T. Cherumannil Femina, Pookkottu K. Sajith, Karunakaran Remya and and R. V. Solomon, "Theoretical insights into the structural and optical properties of D-π-A based cyanostilbene systems of α and β Variants," *ACS Omega*, vol. 9, p. 22764−22776, 2024, doi: doi.org/10.1021/acsomega.4c00850.

[48] B. Joseph, R. Prakash, R. Bag, and S. Ghosh, "' Triple-Decker Sandwich ' Containing Planar {B2E2Pd} Ring (E = S or Se)," *Inorg. Chem.*, vol. 59, pp. 16272–16280, 2020.

[49] M. Zaidi, D. Hannachi, N. Chaouia, and H. Chermette, "Understanding the second and third order nonlinear optical responses of M@b66/64Al12N12:a comprehensive DFT and TD-DFT study," *New J. Chem.,* vol. 48, pp. 11812–11828, 2024, doi: 10.1039/d4nj01849d.

[50] K. S. Thanthiriwatte and K. M. Nalin de Silva, "Non-linear optical properties of novel fluorenyl derivatives - Ab initio quantum chemical calculations," *J. Mol. Struct. THEOCHEM*, vol. 617, pp. 169–175, 2002, doi: 10.1016/S0166-1280(02)00419-0.

[51] C. Karthika, P. K. Das, and A. G. Samuelson, "Electro-switching of first hyperpolarizability of metallorganic complexes via ligand reduction/oxidation," *Chem. Phys. Lett.*, vol. 768, p. 138351, 2021, doi: 10.1016/j.cplett.2021.138351.

[52] S. Sarkar, S. Niyogi, E. Bekyarova, and R. C. Haddon, "Organometallic chemistry of extended periodic π-electron systems: Hexahapto-chromium complexes of graphene and single-walled carbon nanotubes," *Chem. Sci.*, vol. 2, pp. 1326–1333, 2011, doi: 10.1039/c0sc00634c.

[53] N. A. Murugan, J. Kongsted, Z. Rinkevicius, and H. Ågren, "Breakdown of the first hyperpolarizability/bond-length alternation parameter relationship," *Proc. Natl. Acad. Sci. U. S. A.*, vol. 107, pp. 16453–16458, 2010, doi: 10.1073/pnas.1006572107.

Chapter V

Tuning Third-Order NLO Responses in Multi-Decker Sandwich Clusters

V.1 . Introduction

The field of nonlinear optics (NLO) has experienced remarkable progress over the past five decades, particularly in the development of third-order NLO materials. Third-order effects such as third-harmonic generation (THG), two-photon absorption (TPA), the optical Kerr effect, and nonlinear refractive index modulation are of central importance for applications in ultrafast photonics, optical switching, data storage, and nonlinear imaging [1]–[4].

Early studies in the 1970s and 1980s focused on π-conjugated organic molecules and inorganic crystals, which provided the first evidence of significant $\chi^{(3)}$ responses [5]–[7]. In the 1990s, organometallic complexes notably metallocenes and sandwich clusters were introduced as promising alternatives, exploiting strong metal-to-ligand charge transfer and redox tunability to enhance nonlinear responses [8]–[12]. The 2000s marked the rise of nanostructured systems, including quantum dots, fullerenes, and semiconductors, which offered size-dependent $\chi^{(3)}$ values and broadband responses[13].

The subsequent emergence of two-dimensional materials such as graphene and transition metal dichalcogenides (TMDs) further revolutionized the field, enabling ultrafast third-order NLO responses with atomic-layer thickness [14], [15]. More recently, hybrid materials such as perovskites, metal–organic frameworks (MOFs), and plasmonic nanocomposites have attracted significant attention for their ability to combine organic and inorganic properties synergistically, yielding enhanced stability, tunable band gaps, and large nonlinear coefficients [16]–[18]. In parallel, advances in computational chemistry and machine learning approaches have accelerated the design of new NLO chromophores by providing predictive insights into charge-transfer pathways, electronic excitations, and structure–property relationships [19], [20].

In this chapter, the results obtained in Chapter IV are employed to investigate the third-order nonlinear optical (NLO) responses of multi-decker cluster compounds. The analysis focuses on extracting key parameters that govern the second hyperpolarizability, while systematically comparing these findings with those of metallocenes

V.2. Applications of Third-Order Nonlinear Optical (NLO) Materials

Materials with strong third-order responses are crucial for next-generation technologies, particularly those that rely on rapid, tunable, and high-efficiency light manipulation.

V.2.1. Optical Limiting and Protection Devices

A key application of third-order nonlinear optical (NLO) materials is optical limiting, where the material protects sensitive optical components or human eyes from high-intensity laser damage. Carbon-based nanomaterials, such as carbon nanotubes, fullerenes (e.g., C_{60}), and graphene exhibit strong nonlinear absorption and are commonly used in protective eyewear and optical sensors [21]–[23] .

V.2.2. All-Optical Switching and Signal Processing

In telecommunications and information technology, all-optical switches based on third-order NLO materials allow light signal to be modulated without the need for electronic conversion. Materials like organic polymers and chalcogenide glasses [24] are used in devices that direct light signals in optical circuits, forming the backbone of optical computing and ultrafast data networks.

V.2.3. Third-Harmonic Generation (THG)

Third-order nonlinear optical (NLO) materials facilitate third-harmonic generation, a process where three identical photons combine inside a material to create a single photon with three times the original frequency. This effect allows devices to transform infrared light into visible or ultraviolet wavelengths, opening up applications in biological imaging and spectroscopy. Materials like gallium phosphide (GaP) crystals and engineered silicon nanostructures are commonly used for this purpose [25], [26].

V.2.4. Optical Kerr Effect and Ultrafast Lasers

The optical Kerr effect, where the refractive index of a material changes in response to the intensity of light, is crucial for producing ultrafast laser pulses. Materials such as carbon disulfide (CS_2), fused silica, and nonlinear polymers are used in Kerr lens mode-locking systems. This technology enables femtosecond laser applications in precision machining and ultrafast spectroscopy [27].

V.2.5. Two-Photon Absorption (TPA)

Third-order materials can absorb two photons at once, a phenomenon known as two-photon absorption. This is used in deep-tissue imaging and targeted drug activation. For example, organic dyes like Rhodamine B and semiconductor quantum dots are

commonly used in advanced applications [28], such as high-resolution fluorescence microscopy and light-activated cancer treatments.

V.2.6. Nonlinear Waveguides and Photonic Devices

Third-order NLO materials are integral to the development of nonlinear optical waveguides, enabling the miniaturization of photonic circuits [29]. Materials like silicon-based photonic waveguides and indium phosphide (InP) platforms allow for compact, high-performance components for optical signal processing and sensing.

V.3. Bis(benzene)metal complexes and metallocene.

$FeCp_2(C_2H_2)_3NO_2$ based on ferrocene core utilizes the symmetry in the sandwich structure of $FeCp_2$ along with conjugated spacers to extend the π-system, though an intrinsic stability and localization of electronic ferrocene structure make its γ value slightly more moderate compared to systems based on vanadium. Nevertheless, the NO_2 group do enhance NLO response by pulling electron density across the conjugated backbone thus showing that even in ferrocene derivatives there should be considered donor-acceptor tuning.

In contrast, $3NH_2$-VBz_2-3CN demonstrates a strong push-pull system [30] where amino (NH_2) groups act as electron donors and cyano (CN) groups as robust electron acceptors. This pattern of substitution maximizes internal electric field across molecule resulting in large changes in dipole moment with excitation corresponding to high second hyperpolarizability. The vanadium center further lowers excitation energies and increases delocalization, which makes this complex very promising for strong third-order NLO applications.

In recent years, the discovery of new third-order nonlinear optical (NLO) materials has shown significant progress, largely due to their potential applications across diverse technological fields. In this final chapter, we focus on the third-order NLO responses of a novel class of multidecker complexes. The optimized geometries of MDSn and MDS′n, obtained in Chapter IV, were employed in this study. The resulting properties were analyzed and compared with those of metallocene complexes to evaluate their relative performance and potential advantages

V.4. Results and discussions

V.4. 1. Methode of calculation

To assess the influence of the computational methodology on the third-order nonlinear optical (NLO) response of MDS2, we performed density functional theory (DFT) calculations employing a set of representative functionals: the long-range corrected hybrids ωB97X-D[31], [32] and CAM-B3LYP[33], the hybrid meta-GGA TPSSH[34]–[36], and the Minnesota meta-hybrids M06[37] and M06-2X[37], [38]. The 6-311G(d) basis set was applied for light atoms (H, B, C, S, Cl), while the Stuttgart–Dresden (SDD) effective core potentials (ECPs) with their corresponding basis sets were employed for the Co. Scalar relativistic effects were incorporated through the ECP formalism. [39], [40] The corresponding static hyperpolarizabilities γ(0;0,0,0) are presented in **Figure V.1**

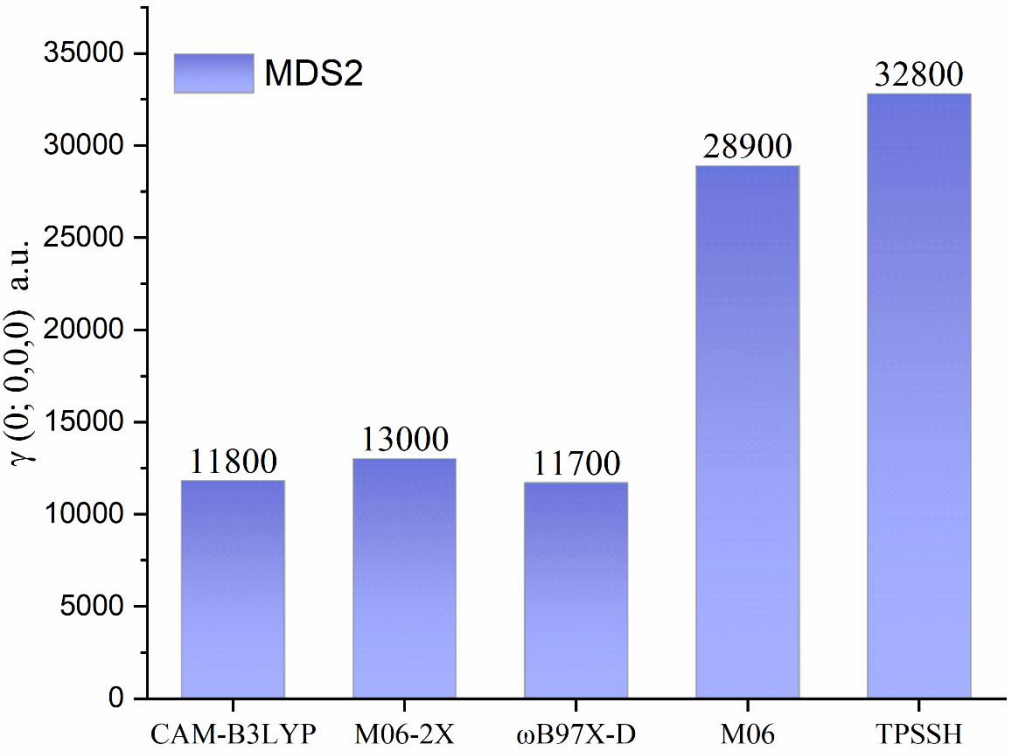

Figure V.1 Static second hyperpolarizability γ(0;0,0,0) of MDS2 calculated with different density functional approximations. Values are given in atomic units (a.u.).

The static third-order NLO responces γ(0;0,0,0) of MDS2 exhibits a pronounced dependence on the density functional applied. The long-range corrected hybrids CAM-B3LYP and ωB97X-D yield the lowest values (11,800 and 11,700 a.u., respectively), The meta-hybrid M06-2X gives a slightly larger response (13,000 a.u.), while the meta-

GGA M06 and the hybrid meta-GGA TPSSH predict much larger values (28,900 and 32,800 a.u., respectively).

From the present benchmark analysis, the M06-2X functional emerged as the most reliable approach for evaluating the third-order nonlinear optical properties of the multidecker sandwich complexes. All subsequent calculations in this work were therefore performed at the M06-2X level. This selection is supported by extensive literature evidence demonstrating the functional's robustness and predictive accuracy in modeling charge-transfer phenomena and optical responses in transition-metal and π-conjugated systems [41], [42].

V.4.2. Static second hyperpolarizability of sandwich complexes

Computational investigations were carried out on MDS2, MDS′2, $FeCp_2$–$(C_2H_2)_3$–NO_2 (**Figure. S6.AII)**, and $3NH_2$–VBz_2–3CN (**Figure. S7.AII**) to enable a comparative evaluation of their static second hyperpolarizabilities. The objective of this analysis is to clarify the role of substitution patterns and electronic configurations within the multidecker framework, while emphasizing the differences between cobaltocenyl-, vanadocenyl-, and ferrocenyl-based donor–π–acceptor systems. The results of these calculations are presented in **Figure V.2**. All calculations were carried out with the M06-2X functional using the 6-311G(d) basis set for light atoms (H, B, C, N, O, S, Cl) and the SDD ECPs for transition metals (Co, Pd, Fe, V). Scalar relativistic effects were included via the ECP formalism

The static second hyperpolarizability γ(0;0,0,0) values obtained at the M06-2X level highlight strong structure–property correlations across the studied complexes. Among them, MDS′2 complex exhibits the highest response (~4.6×10^5 a.u.), significantly surpassing all other systems. This pronounced enhancement can be ascribed to its inclined molecular configuration (**Figure IV-3**). The nitro-substituted ferrocenyl derivative $FeCp_2$–$(C_2H_2)_3$–NO_2 also shows an elevated response (~3.1×10^5 a.u.), confirming the role of strong electron-accepting groups in amplifying γ through donor–π–acceptor interactions.

On the other hand, the amino/cyano-substituted vanadobenzene system $3NH_2$–VBz_2–3CN displays a markedly lower γ (~2.0×10^4 a.u.), comparable to the MDS2 (~1.8×10^4 a.u.). This reduction indicates that despite the presence of donor and acceptor

substituents, the geometric and electronic configuration in this complex does not efficiently facilitate long-range charge transfer, leading to weaker nonlinear responses.

Overall, the observed trend (MDS′2 > $FeCp_2$–$(C_2H_2)_3$–NO_2 ≫ $3NH_2$–VBz_2–3CN ≈ MDS2) emphasizes the critical influence of substitution pattern, metal center identity, and donor–acceptor asymmetry on the third-order NLO activity of multidecker sandwich complexes. These results further demonstrate that selection of the metal, ligand and shape of the sandwich complex are essential design principles for achieving enhanced third-order nonlinear optical properties.

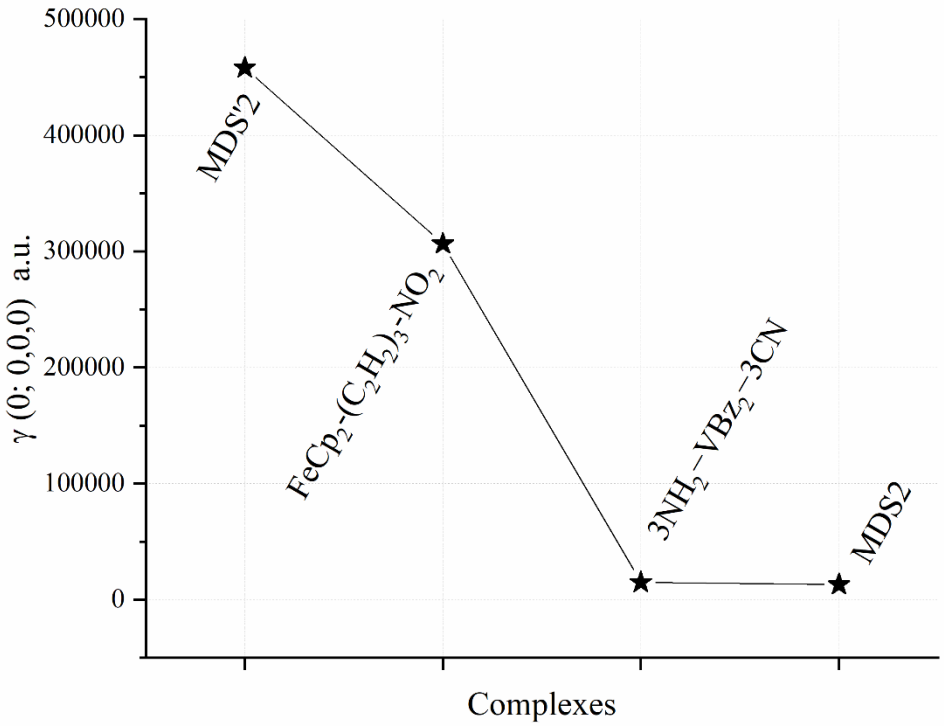

Figure V-2. Static second hyperpolarizability γ(0;0,0,0) of multidecker sandwich complexes calculated at the M06-2X/6-311G(d)/SDD level.

The comparative analysis of the static first (β) and second (γ) hyperpolarizabilities reveals a consistent trend across the investigated complexes, with both quantities following the same order of magnitude: MDS′2 > $FeCp_2$–$(C_2H_2)_3$–NO_2 ≫ $3NH_2$–VBz_2–3CN ≈ MDS2 (**Figure V-3**). Among the series, MDS′2 displays the largest responses, with γ reaching about 4.6×10^5 a.u. and β around 1.6×10^4 a.u., which are nearly five times larger than those of the ferrocenyl derivative $FeCp_2$–$(C_2H_2)_3$–NO_2 ($\gamma \approx 3.0 \times 10^5$ a.u., $\beta \approx 9 \times 10^3$ a.u.). In contrast, both γ and β for MDS′2 exceed those of the MDS2 by more than an order of magnitude, highlighting the decisive role of the inclined

configuration in enhancing NLO responses. The ferrocenyl nitro complex also shows substantially greater values than MDS2 (about sixteen times larger in γ and almost ten times larger in *β*), confirming the strong influence of donor–π–acceptor substitution and rigid conjugated bridges on the nonlinear response. By comparison, $3NH_2$–VBz_2–3CN and MDS2 exhibit much weaker hyperpolarizabilities, with γ values around 2.0×10^4 and 1.8×10^4 a.u., respectively, while β is nearly quenched. The parallel evolution of *β* and γ across the series demonstrates that structural modifications which promote long-range charge transfer simultaneously reinforce both second- and third-order nonlinear optical responses, providing clear molecular design strategies for enhancing the performance of multidecker sandwich complexes.

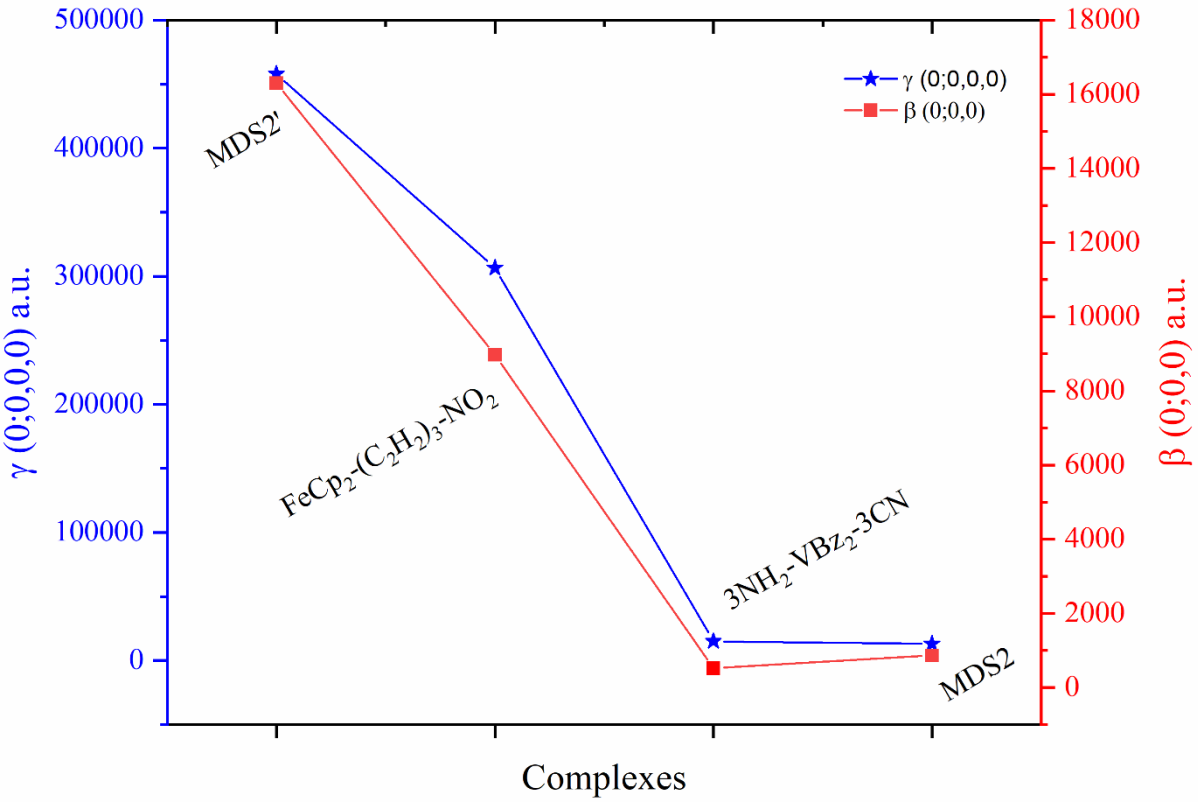

Figure V.3 Comparison of static first hyperpolarizability β(0;0,0) and second hyperpolarizability γ(0;0,0,0) values for selected sandwich complexes

V.4.3. Multi-decker sandwich clusters (MDSn and MDS'n)

In this study, the previously optimized structures of multi-decker sandwich complexes [{$B_2H_2S_2Pd(Cl)_2$} -$(CoCp)_n$] (n = 2 to 5) proposed in Chapter IV (**Scheme IV.4**) were employed to evaluate their third-order nonlinear optical responses. Particular emphasis was placed on elucidating the influence of the number of (CoCp) units as well as the

relative position of the square-planar $\{B_2H_2S_2Pd(Cl)_2\}$ fragment on the magnitude of the third-order susceptibilities. The static hyperpolarizabilities were determined in the zero-frequency limit, and dynamic responses were further computed under frequency-dependent external fields (ω = 0, 0.0428, 0.034, and 0.0239 a.u.), maintaining a consistent level of theory across all calculations. Result of calculation listed in **Table V.1**.

Table V.1 Static and dynamic second hyperpolarizability values of MDSn and MDS'n complexes

	γ^0	$\gamma(-2\omega;\omega,\omega,0)$		
ω	**0**	0.0428	0.0340	0.0239
MDS2	1.30×10^4	1.45×10^5	2.57×10^4	8.57×10^7
MDS'2	4.58×10^5	6.46×10^6	2.31×10^9	2.01×10^6
MDS3	9.11×10^5	1.84×10^6	5.14×10^6	2.08×10^6
MDS'3	1.24×10^5	2.78×10^7	2.93×10^7	1.45×10^8
MDS4	2.93×10^6	8.24×10^6	1.88×10^8	3.06×10^7
MDS'4	7.27×10^6	1.15×10^8	1.37×10^{11}	1.83×10^9
MDS5	1.28×10^9	2.02×10^{14}	2.39×10^9	4.35×10^8
MDS'5	1.05×10^7	8.65×10^8	1.02×10^7	1.02×10^7

V.4.3.1. Frequency-independent

The static third-order nonlinear optical responses [γ(0;0,0,0)] of the multi-decker sandwich complexes (MDS_n and MDS_n') were evaluated at the M06-2X level of theory, and the results are summarized in **Figure V.4** and **Table V.1**. Taking the n=2 derivatives as references, a remarkable length-dependent enhancement is observed upon increasing the number of (CoCp) units. For the MDS_n series, γ increases from 1.3×10^4 a.u. (MDS_2) to 91×10^4 a.u. (MDS_3, ~70-fold), and to 293×10^4 a.u. (MDS_4, ~225-fold). A dramatic jump is then recorded at MDS_5, reaching 1.28×10^9 a.u., which corresponds to an enhancement of nearly five orders (10^5) of magnitude relative to MDS_2. By contrast, the MDS_n' series show a different growth pattern: MDS'_2 (45×10^4 a.u.) is already ~35 times larger than MDS_2 due to symmetry-breaking effects induced by the $\{B_2H_2S_2Pd(Cl)_2\}$ fragment, but γ decreases at n=3 (12×10^4 a.u., ~73% reduction relative to MDS'_2), before rising significantly at n=4 (727×10^4 a.u., ~16-fold increase) and n=5 (1052×10^4 a.u., ~23-fold increase). Direct comparisons between corresponding members highlight the critical role of fragment positioning: while MDS'_2 and MDS'_4 are superior to their

counterparts, MDS_3 and especially MDS_5 outperform the analogues MDS_3' and MDS_5' by factors of ~7.6 and ~122, respectively.

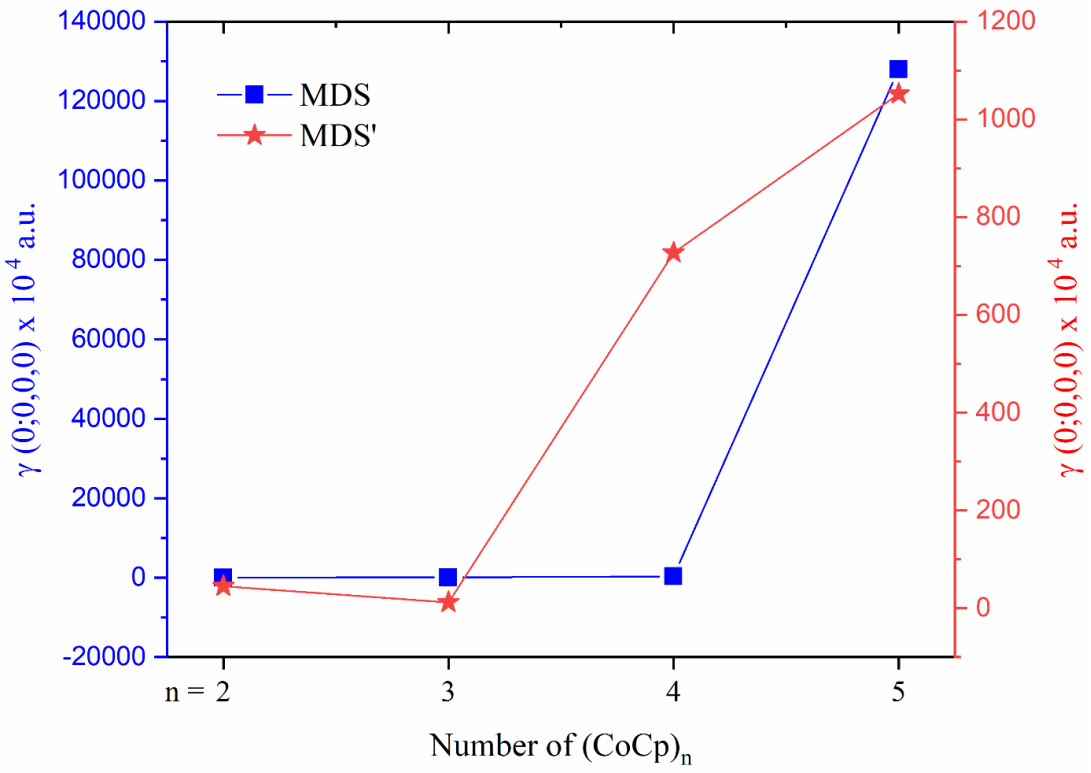

Figure V.4 Static third-order NLO responses (γ(0;0,0,0)) of multi-decker sandwich complexes as a function of the number of (CoCp) units

From this analysis, it can be concluded that the third-order nonlinear optical (NLO) response of multi-decker sandwich complexes is essentially dictated by the number of (CoCp) units, nnn. The static second hyperpolarizability, γ (0;0,0,0), increases consistently with increasing nnn, with the only deviation from this trend observed for the MDS′$_3$ complex. In addition, the inclined configurations of the MDS′ series display larger γ(0;0,0,0) values than those of the corresponding MDS complexes only when n= 2 and 4, whereas for n=3 and 5 the inverse relationship is observed. This alternating evolution generates a characteristic zigzag pattern, demonstrating that the overall molecular shape of multi-decker sandwich complexes does not provide a systematic enhancement of the third-order NLO response. This behavior stands in clear contrast to the second-order NLO regime, where inclined configurations are widely recognized as a dominant structural factor for enhancing the optical response.

V.4.3.2. Frequency-dependent

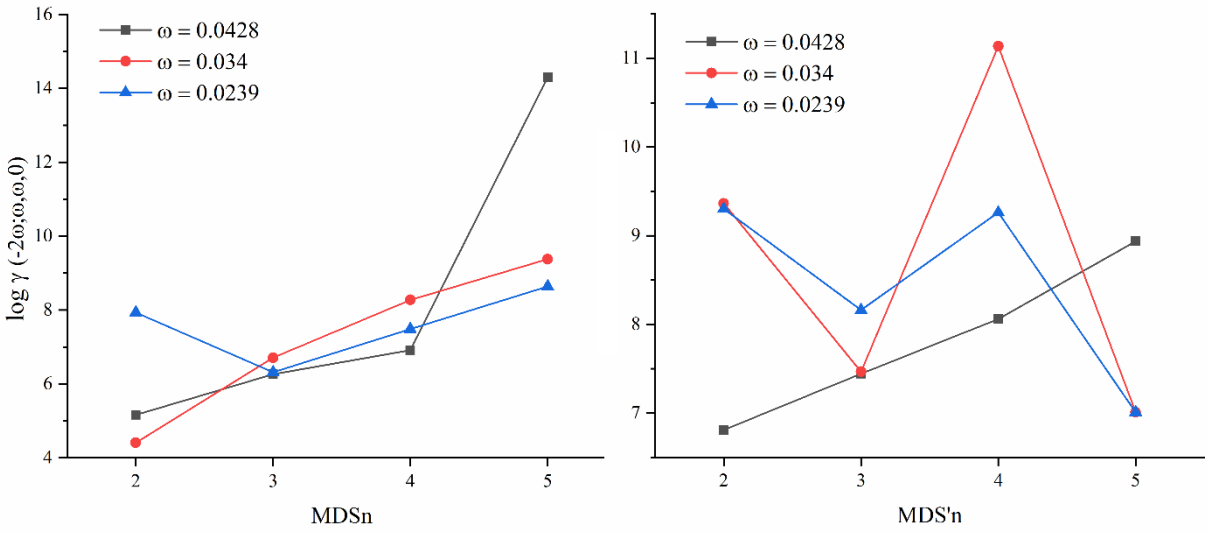

Figure V.5 Variation of the dynamic second hyperpolarizability (γ(-2ω; ω,ω,0)) of MDSn and MDS'n.

The frequency-dependent third-order NLO responses ($\gamma(-2\omega;\omega,\omega,0)$) (**Eq.II.21**) of the MDS_n and MDS'_n complexes, summarized in **Table V.1** and presented in **Figure V.5**, reveal pronounced variations in $\gamma(-2\omega;\omega,\omega,0)$ as a function of both excitation frequency (ω = 0, 0.0428, 0.034, and 0.0239 a.u.), and molecular topology. In general, the dynamic regime introduces strong resonance enhancements, particularly at lower frequencies, leading to values of $\gamma(-2\omega;\omega,\omega,0)$) several orders of magnitude larger than those obtained in the static limit.

- For the smaller complexes (n = 2), the MDS'_2 derivative displays significantly larger $\gamma(-2\omega;\omega,\omega,0))$ values than MDS_2 at all three frequencies. For instance, at ω = 0.034 a.u., $\gamma(-2\omega;\omega,\omega,0))$ (MDS'_2) reaches 2.31×10^9, compared to only 2.57×10^4 for MDS_2, demonstrating an enhancement of more than four orders of magnitude. This clearly highlights the sensitivity of the dynamic response to the terminal placement of the $\{B_2H_2S_2Pd(Cl_2)\}$ fragment in shorter stacks.
- For n = 3, both complexes exhibit larger $\gamma(-2\omega;\omega,\omega,0))$ values than at the static regime, but the MDS'_3 analogue again dominates, particularly at ω = 0.0239 a.u., where $\gamma(MDS'_3) = 1.45 \times 10^8$, nearly 70 times larger than MDS_3.
- In the case of n = 4, a dramatic frequency dependence is observed. The MDS'_4 complex exhibits an exceptionally large $\gamma(-2\omega;\omega,\omega,0))$ value of 1.37×10^{11} a.u; at ω = 0.034 a.u., which surpasses MDS_4 by nearly three orders of magnitude.

This pronounced resonance effect illustrates that increasing the deck number while maintaining the inclined MDS′ topology can lead to giant dynamic NLO responses.

- The most striking behavior is observed for n = 5. At ω = 0.0428 a.u., MDS_5 reaches an extraordinary $\gamma(-2\omega;\omega,\omega,0))$ value of 2.02×10^{14}a.u., which is more than five orders of magnitude higher than the corresponding MDS'_5 complex (8.65×10^8 a.u.). This indicates that in longer stacks, the unprimed arrangement supports a more coherent and extended charge-transfer pathway that resonates strongly with the applied field. At lower frequencies, however, the response of MDS_5 decreases, highlighting the role of frequency in modulating charge delocalization and polarization dynamics.

Overall, the dynamic regime results indicate that the $\gamma(-2\omega;\omega,\omega,0))$ values of the MDS′ series are, in most cases, significantly larger than those of the corresponding MDS complexes, reflecting the favorable influence of inclined geometries on the dynamic third-order NLO response. The deviation from this general trend occurs for n = 5 and at ω = 0.0239 a.u for n=2, where MDS_5 exhibits an exceptionally large $\gamma(-2\omega;\omega,\omega,0))$, surpassing its inclined analogue by several orders of magnitude. This observation allows us to conclude that inclined configurations generally enhance the dynamic second hyperpolarizability relative to non-inclined geometries. Furthermore, at ω = 0.0428 a.u., $\gamma(-2\omega;\omega,\omega,0)$ values increase systematically with the number of (CoCp) units, confirming the strong dependence of the dynamic third-order NLO response on molecular length.

On the other hand, the correlations between $\log\beta^{\omega}_{SHG}$ and $\log\gamma(-2\omega;\omega,\omega,0)$ presented in **Figure V.6** demonstrate a clear frequency-dependent relationship between the second- and third-order nonlinear optical responses of the studied complexes (β^{ω}_{SHG} Calculted in Chapter IV). At ω=0.034 a.u., the linear regression exhibits excellent agreement with an $R^2 = 0.953$, indicating that the third-order hyperpolarizability is strongly coupled to the second-order response in this spectral region. A similarly high degree of correlation is observed at ω=0.0428 a.u. (R^2=0.841), further supporting the presence of a proportional scaling rule linking β^{ω}_{SHG} and $\gamma(-2\omega;\omega,\omega,0)$. In contrast, at the lowest frequency, ω=0.0239 a.u., the correlation is considerably weaker (R^2=0.601), reflecting increased

dispersion effects and possible topology-dependent deviations that disrupt the simple proportionality. These results confirm that, except weak frequency (long-wavelength) resonance conditions, the dynamic second hyperpolarizability can be reasonably anticipated from the second-order NLO response, thereby highlighting a practical structure–property guideline for predicting high-order NLO performance in multi-decker sandwich complexes.

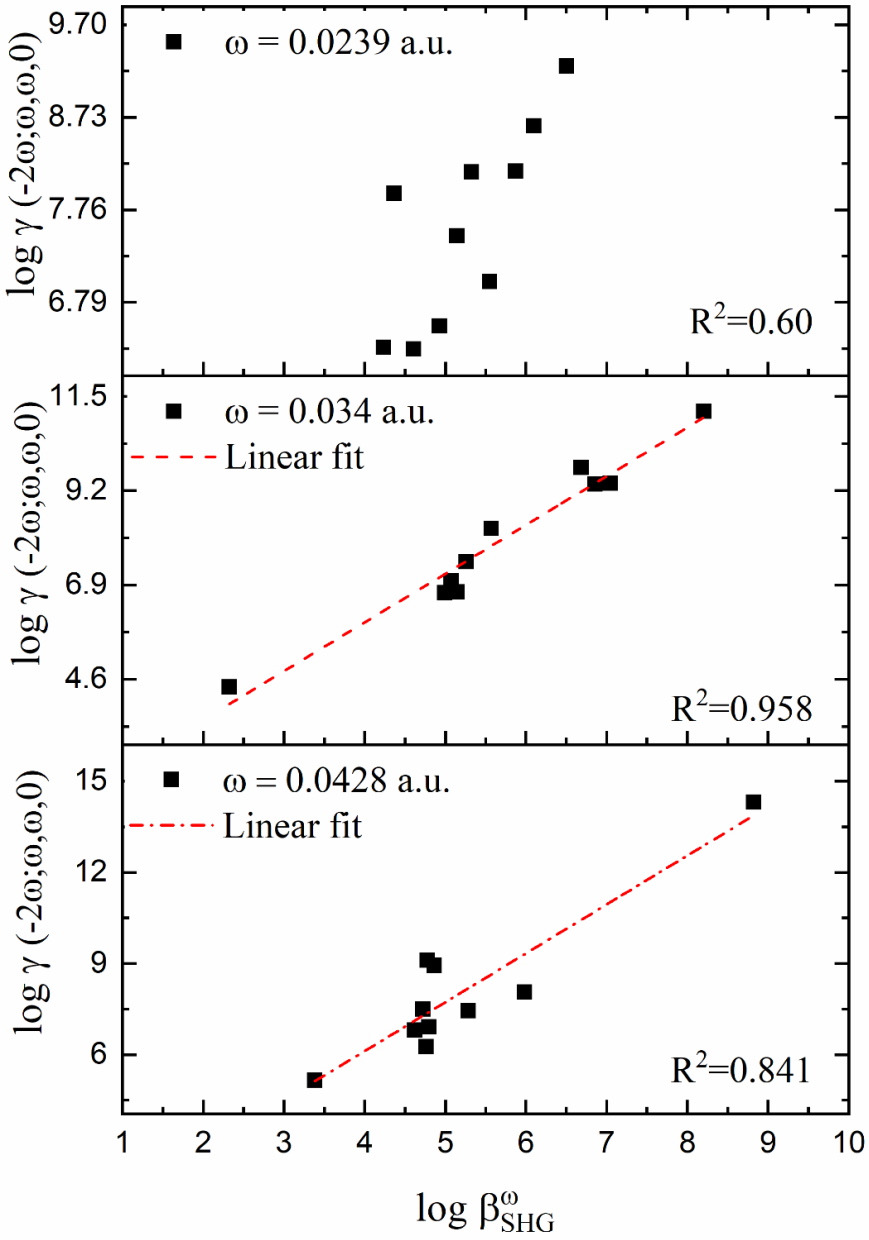

Figure V.6 Correlation plots of $\log \beta_{SHG}^{\omega}$ versus $\log\gamma(-2\omega;\omega,\omega,0)$ for multi-decker sandwich complexes at dynamic regime

V.4.3.3. DC Kerr effect

Table V.2 The dc-Kerr second hyperpolarizability, γ (−ω; ω,0,0) of MDSn and MDS'n complexes

ω	MDS2	MDS'2	MDS3	MDS'3	MDS4	MDS'4	MDS5	MDS'5
0.0428	7.93×10^{4}	2.27×10^{6}	2.31×10^{6}	4.74×10^{7}	1.14×10^{7}	1.77×10^{8}	2.22×10^{13}	2.28×10^{9}
0.034	1.46×10^{4}	1.12×10^{6}	1.48×10^{6}	3.87×10^{6}	3.08×10^{7}	2.16×10^{10}	1.10×10^{10}	4.70×10^{5}
0.0239	7.33×10^{7}	6.78×10^{5}	1.15×10^{6}	7.18×10^{5}	1.91×10^{7}	3.52×10^{7}	4.41×10^{8}	2.24×10^{5}

The results collected in **Table V.2** reveal that the dc-Kerr second hyperpolarizability, γ(−ω;ω,0,0), is strongly dependent on both the intensity of the incident frequency and the structural features of the multi-decker sandwich complexes. At ω = 0.0428 a.u., the inclined configurations (MDS′n) exhibit significantly larger responses than the corresponding MDS complexes for n=2,3 and 4, with values reaching 4.74×10^{7} a.u. for MDS′3 and 1.77×10^{8} for MDS′4, compared to only 2.31×10^{6} and 1.14×10^{7} for MDS3 and MDS4, respectively. This trend, however, is reversed at higher length, where MDS5 shows an extraordinary enhancement of γ(−ω;ω,0,0)=2.22×10^{13} a.u., surpassing its inclined analogue by nearly four orders of magnitude, which points to a cooperative length-driven effect dominating at large stack numbers. A similar pattern is observed at ω=0.034 a.u., where MDS′n again dominates for n≤4, yielding extremely large values, such as 2.16×10^{10} a.u. for MDS′4 compared to 3.08×10^{7} a.u. for MDS4, while at n=5 the situation is inverted and MDS5 reaches 1.10×10^{10} a.u., nearly five orders of magnitude higher than MDS′5. At lower frequency, ω=0.0239 a.u., the dispersion pattern shifts: MDS complexes exhibit larger responses for n=2,3 and 5, with γ(−ω;ω,0,0) is 7.33×10^{7}, 1.15×10^{6} and 4.41×10^{8} a.u., respectively, while the inclined topology gives the highest enhancement only at n=4 (3.52×10^{7} vs. 1.91×10^{7} a.u.).

Overall, our analysis demonstrates that the dc-Kerr second hyperpolarizability of the investigated multi-decker sandwich complexes increases markedly with the extension of the (CoCp)n framework, with the exception of specific frequency–topology combinations where inversion of the trend is observed. These findings establish that the γ (−ω; ω,0,0) is dictated by the coupled effects of frequency dispersion, molecular length, and structural topology, thereby providing robust design principles for engineering dc-Kerr second hyperpolarizabilities in organometallic multi-decker architectures.

V.4.3.4. The quadratic nonlinear refractive index n_2

The quadratic nonlinear refractive index, n_2 (**Eq.II.24**) is a macroscopic parameter that quantifies the change in refractive index of a medium as a function of optical intensity, according to $n = n_0 + n_2 E$, (where n_0, n_2 are the linear and nonlinear refractive index respectively and E is applied external electric field) [43]. It arises directly from the third-order nonlinear optical susceptibility, $\chi^{(3)}$, and is closely related to the dynamic second hyperpolarizability, γ^{DFWM}, through degenerate four-wave mixing processes. A positive n_2 indicates self-focusing behavior, whereas a negative n_2 corresponds to self-defocusing. As such, n_2 provides an essential link between molecular-scale hyperpolarizability and macroscopic optical phenomena, making it a key figure of merit for nonlinear photonic applications.

Table V.3: The γ^{DFWM} and $n_2(cm^2/W)$ at dynamic regime of MDSn and MDS'n.

	ω = 0.0428		ω = 0.034		ω = 0.0239	
	γ^{DFWM}	$n_2(cm^2/W)$	γ^{DFWM}	$n_2(cm^2/W)$	γ^{DFWM}	$n_2(cm^2/W)$
MDS2	1.12×10^{5}	9.35×10^{-18}	1.02×10^{4}	8.49×10^{-19}	1.01×10^{8}	8.44×10^{-15}
MDS'2	3.98×10^{6}	3.29×10^{-16}	7.70×10^{8}	6.38×10^{-14}	8.94×10^{5}	7.41×10^{-17}
MDS3	2.02×10^{6}	1.67×10^{-17}	2.28×10^{6}	1.89×10^{-16}	9.42×10^{5}	7.80×10^{-17}
MDS'3	5.66×10^{7}	4.68×10^{-15}	1.35×10^{7}	1.13×10^{-15}	4.91×10^{7}	4.08×10^{-15}
MDS4	1.13×10^{7}	9.36×10^{-16}	9.08×10^{7}	7.51×10^{-15}	2.64×10^{6}	2.19×10^{-15}
MDS'4	5.25×10^{7}	4.35×10^{-15}	3.37×10^{7}	2.79×10^{-15}	2.94×10^{5}	2.43×10^{-17}
MDS5	8.89×10^{13}	7.36×10^{-9}	1.0587×10^{10}	8.7×10^{-13}	-7.003×10^{8}	-5.79×10^{-14}
MDS'5	4.55×10^{8}	3.77×10^{-14}	1.93×10^{9}	1.61×10^{-13}	9.62×10^{7}	7.96×10^{-15}

The data in **Table V.3** evidence a pronounced dependence of both γ^{DFWM} and n_2 on incedent frequency and molecular length/topology across the MDSn and MDS′n series. At ω=0.0428 a.u., MDS′n members generally surpass their MDSn counterparts for n=2 to 4, for example n_2 in MDS′2 is 3.29×10^{-16} cm^2/W vs MDS2 $=9.35\times10^{-18}$ and for MDS′4 n_2 is 4.35×10^{-15} vs MDS4 is 9.36×10^{-16}, while an exceptional length-driven surge is observed for MDS5, where $\gamma^{DFWM}=8.89\times10^{13}$ translates into a colossal $n_2=7.36\times10^{-9}$ cm^2/W. At ω=0.034 a.u., the same qualitative picture persists for n ≤ 4

(e.g., γ^{DFWM} (MDS′2) =6.38×10^{-14} vs γ^{DFWM} (MDS2) =8.49×10^{-19}; γ^{DFWM} (MDS′4) =2.79×10^{-15} vs γ^{DFWM} (MDS4) =7.51×10^{-15}), yet the five-deck member of the MDS series again dominates strongly ($n_2=8.70\times10^{-13}$ cm^2/W). At the lowest frequency, ω=0.0239 a.u., dispersion reshuffles the ordering: several MDS′n complexes retain high positive n_2 (for example, n_2 value of MDS′3 and MDS′5 is 4.08×10^{-15} and 7.96×10^{-15} cm^2/W, respectively), whereas MDS5 exhibits a sign inversion with $\gamma^{DFWM}=-7.003\times10^{8}$ a.u. and $n_2=-5.79\times10^{-14}$ cm^2/W, indicating a transition to self-defocusing in the long-stack limit at this red-shifted condition. Collectively, the results establish three design-relevant points:

- n_2 generally grows with the number of (CoCp) units, with spectacular cooperative amplification at n=5 in the MDS series near ω=0.0428–0.034 a.u..
- For n=2 to 4 and at shorter wavelengths, the inclined MDS′n topology tends to yield larger n_2 than the corresponding MDS members
- Spectral dispersion can invert both magnitude and sign of n_2, as seen for MDS5 at ω=0.0239 a.u.

These features underscore that accurate prediction and tailoring of the quadratic nonlinear refractive index in multi-decker organometallic scaffolds require joint control of molecular length, topology, and operating frequency.

V.5 Conclusion

In this study, the third-order nonlinear optical responses of multi-decker sandwich complexes were systematically investigated using the M06-2X functional. Benchmarking against MDS2, MDS′2, $FeCp_2$–$(C_2H_2)_3$–NO_2, and $3NH_2$–VBz_2–3CN confirmed that MDS'2 exhibits the largest γ(0;0,0,0), surpassing reference complexes and the MDS_2, while the static first and second hyperpolarizability values were found to follow a consistent trend. Extension to multi-decker sandwich clusters (MDSn and MDS′n, n = 2 to 5) revealed that the γ(0;0,0,0) grows strongly with deck number, culminating in the colossal response of MDS5. At dynamic regime, both γ(−2ω;ω,ω,0) and γ(−ω;ω,0,0) displayed pronounced frequency dispersion and topology-dependent alternation: MDS′n complexes dominate at n = 2 to 4, while cooperative length effects render MDS5 overwhelmingly superior, with values exceeding 10^{13} at ω = 0.0428 a.u. Notably, the dc-Kerr regime highlighted an inversion in MDS5 at ω = 0.0239 a.u., where n_2 assumes a negative value (-5.79×10^{-14} cm^2/W), evidencing a transition from self-focusing to self-defocusing. The analysis of n_2 across the series confirmed its general growth with increasing (CoCp) deck number. Collectively, these results establish that both molecular length and fragment topology act as decisive parameters in tuning static and dynamic third-order NLO responses. The discovery of colossal second hyperpolarizability values, parity-dependent alternation, and sign inversion of n_2 underscores the potential of multi-decker complexes as versatile candidates for high-performance nonlinear optical and photonic applications.

References

[1] J. Zyss and I. Ledoux, "Nonlinear Optics in Multipolar Media: Theory and Experiments," *Chem. Rev.*, vol. 94, no. 1, pp. 77–105, 1994, doi: 10.1021/cr00025a003.

[2] S. Barlow *et al.*, "Polymethine materials with solid-state third-order optical susceptibilities suitable for all-optical signal-processing applications," *Mater. Horizons*, vol. 1, no. 6, pp. 577–581, 2014, doi: 10.1039/c4mh00068d.

[3] J. M. Hales *et al.*, "Design of polymethine dyes with large third-order optical nonlinearities and loss figures of merit," *Science (80-.).*, vol. 327, no. 5972, pp. 1485–1488, 2010, doi: 10.1126/science.1185117.

[4] and J.-L. B. S. Mukhopadhyay, Chad Risko, Seth R. Marder, "Polymethine dyes for all-optical switching applications: A quantum-chemical characterization of counter-ion and aggregation effects on the third-order nonlinear optical response," *Chem. Sci.*, vol. 3, no. 10, pp. 3103–3112, 2012, doi: 10.1021/cen-v068n020.p042.

[5] P. N. Prasad and D. J. Williams, *Introduction to Nonlinear Optical Effects in Molecules and Polymers*. Wiley-Interscience: New York, 1991.

[6] T. Verbiest, S. Houbrechts, M. Kauranen, K. Clays, and A. Persoons, "Second-order nonlinear optical materials: Recent advances in chromophore design," *J. Mater. Chem.*, vol. 7, no. 11, pp. 2175–2189, 1997, doi: 10.1039/a703434b.

[7] J. L. Oudar, "Optical nonlinearities of conjugated molecules. Stilbene derivatives and highly polar aromatic compounds," *J. Chem. Phys.*, vol. 67, no. 2, pp. 446–457, 1977, doi: 10.1063/1.434888.

[8] G. M. Gray and C. M. Lawson, "Structure-Property Relationships in Transition Metal-Organic Third-Order Nonlinear Optical Materials," in *Optoelectronic Properties of Inorganic Compounds*, Springer., J. P. Fackler and A. Texas, Eds. Boston, MA, 1999, pp. 1–27. doi: https://doi.org/10.1007/978-1-4757-6101-6_1.

[9] J. C. Calabrese, L. T. Cheng, J. C. Green, S. R. Marder, and W. Tam, "Molecular Second-Order Optical Nonlinearities of Metallocenes," *J. Am. Chem. Soc.*, vol. 113, no. 19, pp. 7227–7232, 1991, doi: 10.1021/ja00019a020.

[10] L. Wang, J. Ye, H. Wang, H. Xie, and Y. Qiu, "The novel link between planar möbius aromatic and third order nonlinear optical properties of metal-bridged polycyclic

complexes," *Sci. Rep.*, vol. 7, no. 1, pp. 1–11, 2017, doi: 10.1038/s41598-017-10739-7.

[11] J. Tan *et al.*, "Thiophene-based terpyridine and its zinc halide complexes: Third-order nonlinear optical properties in the near-infrared region," *Dalt. Trans.*, vol. 44, pp. 1473–1482, 2014, doi: 10.1039/c4dt02933j.

[12] A. Popczyk *et al.*, "Selected organometallic compounds for third order nonlinear optical application," *Nanomaterials*, vol. 9, pp. 1–15, 2019, doi: 10.3390/nano9020254.

[13] L. Wu *et al.*, "Few-Layer Tin Sulfide: A Promising Black-Phosphorus-Analogue 2D Material with Exceptionally Large Nonlinear Optical Response, High Stability, and Applications in All-Optical Switching and Wavelength Conversion," *Adv. Opt. Mater.*, vol. 6, pp. 1–10, 2017, doi: 10.1002/adom.201700985.

[14] E. Hendry, P. J. Hale, J. Moger, A. K. Savchenko, and S. A. Mikhailov, "Coherent nonlinear optical response of graphene," *Phys. Rev. Lett.*, vol. 105, pp. 1–4, 2010, doi: 10.1103/PhysRevLett.105.097401.

[15] G. Soavi *et al.*, "Hot Electrons Modulation of Third-Harmonic Generation in Graphene," *ACS Photonics*, vol. 6, pp. 2841–2849, 2019, doi: 10.1021/acsphotonics.9b00928.

[16] J. Yu, Y. Sun, K. Geng, J. Huang, Y. Cui, and H. Hou, "Third-Order Nonlinear Optical Modulation Behavior of Photoresponsive Bimetallic MOFs," *Inorg. Chem.*, vol. 63, pp. 6526–6536, 2024, doi: 10.1021/acs.inorgchem.4c00503.

[17] Z. Zhu, Z. Wang, Q. H. Li, Z. Ma, F. Wang, and J. Zhang, "Porphyrin metal-organic frameworks with bilayer and pillar-layered frameworks and third-order nonlinear optical properties," *Dalt. Trans.*, vol. 52, no. 14, pp. 4309–4314, 2023, doi: 10.1039/d3dt00440f.

[18] R. Abazari *et al.*, "Third-Order Nonlinear Optical Behavior of an Amide-Tricarboxylate Zinc(II) Metal-Organic Framework with Two-Fold 3D+3D Interpenetration," *Inorg. Chem.*, vol. 60, pp. 9700–9708, 2021, doi: 10.1021/acs.inorgchem.1c00997.

[19] L. Jia, J. Wu, Y. Zhang, Y. Qu, B. Jia, and D. J. Moss, "Third-Order Optical Nonlinearities of 2D Materials at Telecommunications Wavelengths," *Micromachines*, vol. 14, pp. 1–20, 2023, doi: 10.3390/mi14020307.

[20] F. Hussain *et al.*, "Calculated Bond Length (Å) at CAM- Experimental Length (Å) Bond Length (Å)," *J. Phys. Chem. A*, vol. 129, pp. 7853–7862, 2025, doi: https://doi.org/10.1021/acs.jpca.5c04139.

[21] R. E. Kroto, H. W., Heath, J. R., O'Brien, S. C., Curl, R. F., Smalley, "Minimal realization of linear system based on new smith-mcmillan normal form of transfer function matrix," *Nature*, vol. 318, no. 3, pp. 162–163, 1985, doi: 10.1038/318162a0.

[22] R. E. Haufler *et al.*, "Efficient production of C60 (buckminsterfullerene), C60H36, and the solvated buckide ion," *J. Phys. Chem.*, vol. 94, no. 24, pp. 8634–8636, 1990, doi: 10.1021/j100387a005.

[23] G. B. Talapatra, N. Manickam, M. Samoc, M. E. Orczyk, S. P. Karna, and P. N. Prasad, "Nonlinear optical properties of the C60 molecule: Theoretical and experimental studies," *J. Phys. Chem.*, vol. 96, no. 13, pp. 5206–5208, 1992, doi: 10.1021/j100192a003.

[24] A. Z. S. R. Elliott, "Optical Nonlinearities in Chalcogenide Glasses and their Applications." 2007. doi: 10.1007_978-3-540-71068-4.

[25] B. McLaughlin, D. P. Lake, M. Mitchell, and P. E. Barclay, "Nonlinear optics in gallium phosphide cavities: simultaneous second and third harmonic generation," *J. Opt. Soc. Am. B*, vol. 39, no. 7, p. 1853, 2022, doi: 10.1364/josab.455234.

[26] B. Tilmann *et al.*, "Comparison of Harmonic Generation from Crystalline and Amorphous Gallium Phosphide Nanofilms," *Adv. Opt. Mater.*, vol. 11, no. 16, 2023, doi: 10.1002/adom.202300269.

[27] S. Semin, X. Li, Y. Duan, and T. Rasing, "Nonlinear Optical Properties and Applications of Fluorenone Molecular Materials," *Adv. Opt. Mater.*, vol. 9, no. 23, 2021, doi: 10.1002/adom.202100327.

[28] S. B. Nariyangadu *et al.*, "New nonlinear optical crystal of rhodamine 590 acid phthalate," *ACS Omega*, vol. 5, no. 33, pp. 20863–20873, 2020, doi: 10.1021/acsomega.0c02303.

[29] L. Sirleto and G. C. Righini, "An Introduction to Nonlinear Integrated Photonics Devices: Nonlinear Effects and Materials," *Micromachines*, vol. 14, no. 3, 2023, doi: 10.3390/mi14030604.

[30] S. J. Wang, Y. F. Wang, and C. Cai, "Multidecker Sandwich Cluster VnBenn +1 (n = 1, 2, 3, 4) as a Polarizable Bridge for Designing 1D Second-Order NLO Chromophore: Metal-π Sandwich Multilayer Structure as a Particular Charge-Transfer Axis for

Constructing Multidimensional NLO Molecules," *J. Phys. Chem. C*, vol. 119, no. 28, pp. 16256–16262, 2015, doi: 10.1021/acs.jpcc.5b04656.

[31] J. Da Chai and M. Head-Gordon, "Systematic optimization of long-range corrected hybrid density functionals," *J. Chem. Phys.*, vol. 128, no. 8, 2008, doi: 10.1063/1.2834918.

[32] J. Da Chai and M. Head-Gordon, "Long-range corrected hybrid density functionals with damped atom-atom dispersion corrections," *Phys. Chem. Chem. Phys.*, vol. 10, no. 44, pp. 6615–6620, 2008, doi: 10.1039/b810189b.

[33] T. Yanai, D. P. Tew, and N. C. Handy, "A new hybrid exchange-correlation functional using the Coulomb-attenuating method (CAM-B3LYP)," *Chem. Phys. Lett.*, vol. 393, no. 1–3, pp. 51–57, 2004, doi: 10.1016/j.cplett.2004.06.011.

[34] V. N. Staroverov, G. E. Scuseria, J. Tao, and J. P. Perdew, "Erratum: Comparative assessment of a new nonempirical density functional: Molecules and hydrogen-bonded complexes(Journal of Chemical Physics (2003) 119 (12129))," *J. Chem. Phys.*, vol. 121, p. 11507, 2004, doi: 10.1063/1.1795692.

[35] V. N. Staroverov, G. E. Scuseria, J. Tao, and J. P. Perdew, "Comparative assessment of a new nonempirical density functional: Molecules and hydrogen-bonded complexes," *J. Chem. Phys.*, vol. 119, no. 23, pp. 12129–12137, 2003, doi: 10.1063/1.1626543.

[36] J. Tao, J. P. Perdew, V. N. Staroverov, and G. E. Scuseria, "Climbing the density functional ladder: Nonempirical meta–generalized gradient approximation designed for molecules and solids," *Phys. Rev. Lett.*, vol. 91, no. 14, pp. 3–6, 2003, doi: 10.1103/PhysRevLett.91.146401.

[37] Y. Zhao and D. G. Truhlar, "The M06 suite of density functionals for main group thermochemistry, thermochemical kinetics, noncovalent interactions, excited states, and transition elements: Two new functionals and systematic testing of four M06-class functionals and 12 other function," *Theor. Chem. Acc.*, vol. 120, no. 1–3, pp. 215–241, 2008, doi: 10.1007/s00214-007-0310-x.

[38] Y. Zhao and D. G. Truhlar, "Applications and validations of the Minnesota density functionals," *Chem. Phys. Lett.*, vol. 502, no. 1–3, pp. 1–13, 2011, doi: 10.1016/j.cplett.2010.11.060.

[39] G. A. Petersson and A.-L. Mohammad A, "A Complete Basis Set Model Chemistry. II. The Total Energies of open-Shell Atoms and Hydrides of the First-Row Atoms," *J. Chem. Phys.*, vol. 9, no. September 1990, pp. 6081–6090, 1991.

[40] G. A. Petersson, A. Bennett, T. G. Tensfeldt, M. A. Al-Laham, W. A. Shirley, and J. Mantzaris, "A complete basis set model chemistry. I. The total energies of closed-shell atoms and hydrides of the first-row elements," *J. Chem. Phys.*, vol. 89, no. 4, pp. 2193–2218, 1988, doi: 10.1063/1.455064.

[41] Ragheb Khalil Bouriche, Douniazed Hannachi, Amel Messai, Christophe Morell, Amor Azizi, and Henry Chermette, "Electronic and Optical Properties of Copper Nanostructures for Advanced Applications," *New J. Chem.,* vol. 49, pp. 10730–10750, 2025, doi: 10.1039/D5NJ01220A.

[42] M. Zaidi, D. Hannachi, D. Samsar, G. Hoffmann, and H. Chermette, "Predicting and controlling the second-order NLO response in a new class of multi-decker sandwich clusters {μ-B2H2S2Pd(Cl)2}-(CoCp) n, (n = 2 to 5)," *J. Photochem. Photobiol. A Chem.*, vol. 469, p. 116523, 2025, doi: 10.1016/j.jphotochem.2025.116523.

[43] C. Brée, A. Demircan, and G. Steinmeyer, "Method for computing the nonlinear refractive index via Keldysh theory," *IEEE J. Quantum Electron.*, vol. 46, no. 4, pp. 433–437, 2010, doi: 10.1109/JQE.2009.2031599.

General Conclusion

General Conclusion

Nonlinear optical (NLO) responses have advanced significantly in recent decades, enabling a wide range of scientific and technological applications. Phenomena such as second-harmonic generation, optical switching, and frequency conversion are now central to telecommunications, ultrafast laser systems, quantum information processing, and biophotonics. These developments highlight the crucial role of NLO-active materials in modern research and applied technologies.

Alongside experimental progress, quantum chemical calculations have demonstrated remarkable efficiency in explaining and predicting NLO behavior. Methods such as Density Functional Theory (DFT) and Time-Dependent DFT (TD-DFT) allow accurate evaluation of electronic structures, charge-transfer mechanisms, and hyperpolarizabilities. This theoretical insight not only supports experimental findings but also accelerates the discovery and design of new high-performance NLO materials.

This thesis is dedicated to the exploration of the linear and nonlinear optical (NLO) properties of two distinct categories of molecular systems. The first category consists of two series of transition-metal-doped nanocages, $M@B_{64}Al_{12}N_{12}$ and $M@B_{66}Al_{12}N_{12}$, where M spans the transition metal series from Sc to Zn. The second category encompasses multidecker sandwich clusters of the type $\{\mu\text{-}B_2H_2S_2Pd(Cl)_2\}$–$(CoCp)_n$, with n ranging from 2 to 5. These clusters differ in the positioning of the $\{H_2B_2S_2Pd(Cl)_2\}$ fragment and the number of (CoCp) units namely MDSn, MDSna and MDS'n.

The results demonstrate that doping $Al_{12}N_{12}$ nanocages with transition metals leads to a substantial enhancement of both first- and second-order hyperpolarizabilities. Delocalization index (DI) analysis confirms a stronger degree of electron delocalization between the transition metal and nitrogen atoms compared to that between the metal and aluminum. Furthermore, QTAIM analysis highlights that the formation of a closed quasi-ring structure involving the transition metal, combined with charge delocalization, plays a decisive role in amplifying the first-order hyperpolarizability. TD-DFT calculations further suggest that these doped nanocages are promising candidates for deep ultraviolet laser applications due to their strong transparency below 200 nm. The SOS analysis reveals that the dominant excited states contributing to the NLO response correspond to local excitations, characterized by large Sr values, small D values, and negative t values. In the dynamic regime, the computed values of β_{HRS}, $\beta_{SHG}(-2\omega;\omega,\omega)$ and $\gamma_{ESHG}(-2\omega;\ \omega,\omega,0)$ were found to be significantly larger than

their static counterparts. This enhancement is primarily attributed to resonance effects, where two-photon resonances, coupled with large oscillator strengths, contribute more effectively than one-photon processes. Importantly, our findings establish a correlation between the static first hyperpolarizability of $M@B_{64/66}Al_{12}N_{12}$ and the Waber–Cromer atomic radius of the incorporated transition metal. Moreover, under dynamic conditions, a clear relationship emerges between the first- and second-order hyperpolarizabilities, providing deeper insight into the structure–property interplay governing these systems.

For the multidecker sandwich clusters (MDSn, MDSna and MDS'n, n = 2–5), our study shows that MDS'_n clusters adopt inclined geometries with φ angles between 50° and 64°, while MDS_n complexes maintain nearly perpendicular orientations. The TD-DFT absorption spectra show two distinct regions: 200–350 nm, dominated by intra-ligand π–π* transitions in the Cp ligands, and 400–1400+ nm, governed by mixed charge-transfer (CT/ICT) processes between fragments. Nonlinear optical calculations highlight that increasing the number of (CoCp) units significantly enhances both the mean polarizability α (0,0) and its anisotropy Δα(0,0) across both series (n = 2–5). In the MDS'_n series, the first hyperpolarizability increases steadily from n = 2 to 4, but decreases when n = 5, whereas in the MDS_n series first hyperpolarizability grows consistently with the number of (CoCp) units, displaying behavior analogous to conventional push–pull π-systems. A comparative analysis shows that, overall, MDS'_n clusters exhibit larger first hyperpolarizability values than MDS_n, except at n = 5. This exception is attributed to strong charge transfer from the $\{H_2B_2S_2Pd(Cl)_2\}$ fragment toward the $(CoCp)_n$ moieties in the key excited state of MDS'_n. Furthermore, EDDMs confirm that extended charge-transfer pathways and enhanced transition dipole moments are the principal contributors to the amplified NLO responses.

On the other hand, the third-order nonlinear optical responses of multidecker sandwich clusters (MDS_n and MDS'_n, n = 2–5) demonstrate a strong dependence on molecular length and topology. The static second hyperpolarizability increases significantly with the number of decks, reaching its maximum in the longest cluster. Under dynamic conditions, marked frequency dispersion and topology-dependent alternation are observed: MDS'_n complexes dominate at lower deck numbers, while cooperative length effects render the longest MDS clusters overwhelmingly superior. In the dc-Kerr regime, the analysis highlights an inversion of the nonlinear refractive index, reflecting a transition from self-focusing to self-defocusing behavior. Examination of the series further confirms that the nonlinear refractive index grows consistently with the addition of (CoCp) units. Overall, these results establish that both

molecular length and fragment topology are decisive parameters governing static and dynamic third-order NLO responses. The emergence of colossal hyperpolarizabilities, parity-dependent alternation, and sign inversion underscores the promise of multidecker sandwich clusters as versatile candidates for advanced nonlinear optical and photonic applications.

Supplementary Information

Table S1.AI Delocalization Indices (δ(M, A) where A= N or Al and M: from Sc to Zn) for $M@b_{64}Al_{12}N_{12}$ and $M@b_{66}Al_{12}N_{12}$

$M@b_{64}Al_{12}N_{12}$	Sc	Ti	V	Cr	Mn	Fe	Co	Ni	Cu	Zn	$M@b_{66}Al_{12}N_{12}$	Sc	Ti	V	Cr	Mn	Fe	Co	Ni	Cu	Zn
1(AL)	0.93	0.94	0.95	0.81	0.72	0.81	0.81	0.82	0.77	0.65	**1(AL)**	0.01	0.01	0.01	0.01	0.009	0.009	0.009	0.008	0.009	0.007
2(AL)	0.27	0.27	0.23	0.18	0.15	0.16	0.15	0.14	0.15	0.11	**2(AL)**	0.005	0.004	0.003	0.003	0.003	0.002	0.002	0.002	0.002	0.002
3(N)	1.74	1.74	1.65	1.29	1.14	1.17	1.12	1.08	1.20	0.80	**3(N)**	0.002	0.002	0.001	0.001	0.001	0.001	0.001	0.001	0.001	0.001
4(N)	0.11	0.11	0.09	0.06	0.06	0.06	0.05	0.05	0.06	0.05	**4(N)**	0.01	0.01	0.01	0.009	0.008	0.008	0.007	0.007	0.008	0.005
5(AL)	0.01	0.01	0.01	0.01	0.009	0.009	0.01	0.009	0.01	0.007	**5(AL)**	0.02	0.01	0.01	0.01	0.01	0.01	0.01	0.01	0.01	0.01
6(AL)	0.01	0.01	0.01	0.008	0.008	0.009	0.008	0.008	0.009	0.007	**6(AL)**	0.90	0.87	0.86	0.84	0.74	0.85	0.83	0.83	0.79	0.66
7(N)	0.06	0.06	0.06	0.04	0.04	0.04	0.04	0.04	0.04	0.04	**7(N)**	0.04	0.04	0.04	0.03	0.03	0.03	0.03	0.03	0.03	0.03
8(N)	0.003	0.003	0.003	0.002	0.002	0.003	0.002	0.002	0.002	0.002	**8(N)**	0.04	0.04	0.04	0.03	0.03	0.03	0.03	0.03	0.03	0.03
9(AL)	0.0008	0.0007	0.0006	0.0005	0.0006	0.0006	0.0005	0.0004	0.0004	0.0004	**9(AL)**	0.005	0.004	0.003	0.003	0.003	0.002	0.002	0.002	0.002	0.002
10(AL)	0.002	0.002	0.002	0.002	0.002	0.002	0.001	0.001	0.001	0.001	**10(AL)**	0.01	0.01	0.01	0.01	0.009	0.009	0.009	0.008	0.009	0.007
11(N)	0.001	0.001	0.001	0.0007	0.0007	0.0006	0.0005	0.0005	0.0005	0.0004	**11(N)**	0.002	0.002	0.001	0.001	0.001	0.001	0.001	0.001	0.001	0.001
12(N)	0.0002	0.0002	0.0002	0.0002	0.0002	0.0002	0.0001	0.0001	0.0001	0.0001	**12(N)**	0.01	0.01	0.01	0.009	0.008	0.008	0.007	0.007	0.008	0.005
13(AL)	0.005	0.004	0.004	0.003	0.004	0.004	0.003	0.003	0.004	0.003	**13(AL)**	0.001	0.0009	0.0007	0.0006	0.0006	0.0005	0.0005	0.0004	0.0004	0.0003
14(AL)	0.004	0.003	0.003	0.003	0.003	0.003	0.003	0.003	0.003	0.003	**14(AL)**	0.01	0.009	0.008	0.007	0.008	0.008	0.007	0.007	0.007	0.007
15(N)	0.0008	0.0008	0.0006	0.0006	0.0006	0.0005	0.0005	0.0004	0.0004	0.0003	**15(N)**	0.001	0.0009	0.0007	0.0006	0.0006	0.0006	0.0005	0.0005	0.0005	0.0004
16(N)	0.01	0.01	0.011	0.009	0.01	0.01	0.009	0.008	0.009	0.008	**16(N)**	0.001	0.0009	0.0007	0.0006	0.0006	0.0006	0.0005	0.0005	0.0005	0.0004
17(AL)	0.02	0.02	0.02	0.01	0.01	0.01	0.01	0.01	0.01	0.01	**17(AL)**	0.23	0.21	0.19	0.16	0.01	0.14	0.13	0.12	0.13	0.08
18(AL)	0.001	0.001	0.001	0.001	0.001	0.001	0.001	0.001	0.001	0.001	**18(AL)**	0.24	0.22	0.19	0.17	0.14	0.14	0.13	0.12	0.13	0.08
19(N)	0.001	0.001	0.001	0.001	0.001	0.001	0.001	0.001	0.001	0.001	**19(N)**	1.58	1.46	1.41	1.28	1.14	1.18	1.12	1.10	1.19	0.80
20(N)	0.002	0.002	0.002	0.002	0.002	0.002	0.001	0.001	0.001	0.001	**20(N)**	0.03	0.02	0.02	0.02	0.02	0.02	0.01	0.01	0.02	0.01
21(AL)	0.29	0.28	0.26	0.20	0.17	0.16	0.16	0.14	0.16	0.11	**21(AL)**	0.002	0.002	0.001	0.001	0.001	0.001	0.001	0.001	0.001	0.001
22(AL)	0.008	0.008	0.007	0.005	0.005	0.005	0.004	0.004	0.004	0.004	**22(AL)**	0.002	0.002	0.001	0.001	0.001	0.001	0.001	0.001	0.001	0.001
23(N)	0.031	0.02	0.02	0.01	0.01	0.009	0.009	0.008	0.01	0.005	**23(N)**	0.003	0.003	0.003	0.002	0.002	0.002	0.002	0.002	0.002	0.002
24(N)	0.01	0.01	0.01	0.009	0.009	0.009	0.008	0.008	0.008	0.008	**24(N)**	0.0003	0.0003	0.0002	0.0002	0.0002	0.0002	0.0002	0.0001	0.0001	0.0001
25(M)	3.55	3.55	3.40	2.69	2.39	2.52	2.45	2.38	2.50	1.85	**25(M)**	3.21	3.01	2.86	2.65	2.34	2.50	2.39	2.35	2.42	1.79

Table S2a.AI Excitation energy ($E_{0\to n}$, eV) and wavelength ($\lambda_{0\to n}$, nm), oscillator strengths ($f_{0\to n}$, dimensionless), Integral of hole and electron, transition dipole moment ($\Delta\mu_{0\to n}$, a.u), S_m index, $S_r(r)$ overlap, charge transfer distance (D index, Å), RMSD of hole and electron (Å), H and t indexes (Å), the hole delocalization index (HDI) and electron delocalization index (EDI)associated to the S0 → Sn transition, as calculated at the cam-b3lyp/6-311+g(d) of the studied compounds **M@b$_{64}$Al$_{12}$N$_{12}$**

	$S_{0\to n}$	$\Delta E_{0\to n}$	$\Delta\lambda_{0\to n}$	$f_{0\to n}$	Integral of hole	Integral of electron	$\Delta\mu_{0\to n}$	Sm	Sr	D index	RMSD hole	RMSD electron	H index	t index	HDI	EDI
Sc@b$_{64}$Al$_{12}$N$_1$	$S_{0\to5}$	1.617	766.853	0.009	0.999	0.988	2.037	0.499	0.795	1.085	2.210	2.607	2.408	-0.434		
	$S_{0\to11}$	2.478	500.262	0.01	0.997	0.986	3.399	0.398	0.690	1.813	2.196	3.711	2.953	-0.095	8.77	4.39
	$S_{0\to13}$	2.676	463.235	0.144	0.999	0.964	2.201	0.278	0.578	1.187	2.368	3.284	2.826	-0.443	6.94	7.12
	$S_{0\to15}$	2.925	423.836	0.121	0.999	0.986	1.952	0.377	0.667	1.04	2.379	2.456	2.418	-0.534	6.87	10.08
Ti@b$_{64}$Al$_{12}$N$_1$	$S_{0\to5}$	1.245	996.102	0.005	0.999	0.986	1.177	0.305	0.597	0.628	1.481	2.030	1.755	-0.455	20.22	13.05
	$S_{0\to15}$	2.886	429.638	0.022	0.998	0.987	4.024	0.282	0.589	2.144	2.115	3.814	2.964	0.237	11.54	3.73
	$S_{0\to18}$	3.151	393.528	0.126	0.999	0.988	1.178	0.425	0.732	0.628	2.163	2.597	2.38	-0.796	10.72	8.07
	$S_{0\to16}$	2.895	428.302	0.055	0.999	0.983	1.441	0.366	0.662	1.044	2.252	3.693	2.972	-0.749	7.91	4.34
V@b$_{64}$Al$_{12}$N$_{12}$	$S_{0\to5}$	1.508	822.454	0.001	0.999	0.993	0.831	0.292	0.596	0.442	1.327	1.984	1.655	-0.588	25.90	15.88
	$S_{0\to14}$	2.985	415.346	0.057	0.999	0.984	2.59	0.286	0.579	1.381	2.302	3.913	3.107	-0.602	7.84	3.76
	$S_{0\to15}$	3.041	407.751	0.116	0.999	0.979	1.675	0.453	0.757	0.896	2.250	2.742	2.496	-0.773	8.61	7.87
	$S_{0\to17}$	3.358	369.211	0.024	1.000	0.987	2.82	0.329	0.628	1.502	2.207	3.692	2.949	-0.329	12.52	4.12
Cr@b$_{64}$Al$_{12}$N$_1$	$S_{0\to1}$	1.352	917.319	0.001	0.999	0.990	1.048	0.321	0.602	0.558	1.460	2.115	1.788	-0.736	29.66	14.99
	$S_{0\to7}$	2.558	484.695	0.088	0.998	0.980	2.267	0.285	0.590	1.213	2.305	3.931	3.118	-0.664	7.31	3.7
	$S_{0\to11}$	3.08	402.588	0.110	0.999	0.986	0.629	0.353	0.669	0.335	1.814	2.977	2.396	-1.147	19.82	5.23
	$S_{0\to16}$	3.508	353.465	0.054	0.999	0.981	1.512	0.456	0.759	0.808	2.349	3.547	2.948	-0.935	9.9	7.96
Mn@b$_{64}$Al$_{12}$N	$S_{0\to1}$	1.458	850.610	0.01	0.997	0.993	0.46	0.603	0.86	0.245	2.223	2.487	2.355	-1.195	6.73	6.34
	$S_{0\to6}$	2.563	483.730	0.043	0.996	0.993	3.736	0.322	0.631	1.987	2.319	3.543	2.931	0.020	6.64	8.82
	$S_{0\to8}$	2.928	423.402	0.073	0.999	0.987	1.525	0.41	0.715	0.813	2.301	3.456	2.878	-1.067	8.85	14.91
	$S_{0\to9}$	2.98	416.112	0.140	0.999	0.98	2.254	0.414	0.733	1.205	2.289	2.795	2.542	-0.443	8.8	8.75

$Fe@b_{64}Al_{12}N_1$	$S_{0\to4}$	1.301	952.704	0.023	0.997	0.993	0.309	0.603	0.872	0.164	2.126	2.286	2.206	-1.171	9.6	11.55
	$S_{0\to9}$	2.42	512.334	0.057	0.996	0.991	5.929	0.187	0.486	3.156	2.348	3.891	3.12	1.111	7.88	3.11
	$S_{0\to13}$	3.17	391.119	0.085	0.999	0.980	1.568	0.421	0.727	0.839	2.104	2.913	2.508	-0.842	14.84	7.7
	$S_{0\to15}$	3.538	350.467	0.022	0.999	0.989	4.551	0.2	0.465	2.421	2.56	3.944	3.252	0.279	13.44	2.92
$Co@b_{64}Al_{12}N$	$S_{0\to8}$	1.728	717.713	<0.001	1.000	0.996	0.620	0.293	0.581	0.329	1.565	1.394	1.479	-0.633	27.88	36.89
	$S_{0\to9}$	1.848	671.059	0.072	0.997	0.988	0.672	0.512	0.805	0.358	2.179	2.573	2.376	-1.001	8.77	6.24
	$S_{0\to11}$	2.545	487.113	0.064	0.997	0.991	6.270	0.158	0.435	3.336	2.342	3.901	3.121	1.325	7.55	2.98
	$S_{0\to13}$	3.062	404.862	0.008	1.001	0.987	0.124	0.18	0.45	0.066	1.244	2.563	1.903	-1.186	38.63	6.19
$Ni@b_{64}Al_{12}N_{12}$	$S_{0\to5}$	1.833	676.220	0.037	0.998	0.989	0.306	0.594	0.845	0.163	1.963	2.461	2.212	-1.305	18.65	8.03
	$S_{0\to7}$	2.582	480.152	0.055	0.997	0.991	5.838	0.175	0.469	3.107	2.35	3.884	3.117	1.098	8.29	2.99
	$S_{0\to13}$	3.657	339.007	0.002	0.999	0.987	1.209	0.225	0.519	0.644	3.035	4.007	3.521	-1.244	9.55	4.70
	$S_{0\to14}$	3.755	330.221	<0.001	0.999	0.986	0.764	0.271	0.562	0.407	3.499	4.082	3.79	-1.782	7.33	2.62
$Cu@b_{64}Al_{12}N$	$S_{0\to1}$	2.095	591.955	0.076	0.998	0.984	1.25	0.445	0.726	0.667	2.175	2.54	2.357	-0.782	11.00	5.77
	$S_{0\to2}$	2.647	468.362	0.057	0.998	0.99	5.548	0.194	0.489	2.952	2.328	3.930	3.129	0.927	9.12	2.89
	$S_{0\to9}$	3.61	343.448	0.001	0.999	0.988	0.817	0.277	0.586	0.435	3.072	3.916	3.494	-1.369	10.80	4.56
	$S_{0\to11}$	3.745	331.041	<0.001	0.999	0.988	0.362	0.209	0.501	0.193	3.264	4.015	3.639	-1.765	8.63	2.71
$Zn@b_{64}Al_{12}N$	$S_{0\to3}$	2.994	414.111	0.215	0.999	0.990	0.412	0.409	0.699	0.219	2.286	2.649	2.468	-1.546	9.10	6.09
	$S_{0\to5}$	3.332	372.070	0.09	0.999	0.992	5.752	0.153	0.413	3.057	2.425	3.887	3.156	1.006	8.24	3.03
	$S_{0\to8}$	3.863	320.922	0.085	0.999	0.993	1.449	0.329	0.598	0.770	2.496	3.28	2.888	-0.699	8.04	3.66
	$S_{0\to11}$	3.977	311.723	0.002	0.999	0.987	0.671	0.233	0.514	0.357	3.289	4.085	3.687	-1.748	8.36	2.49

Table S2b.AI Excitation energy ($E_{0\to n}$, eV) and wavelength ($\lambda_{0\to n}$, nm), oscillator strengths ($f_{0\to n}$, dimensionless), Integral of hole and electron, transition dipole moment ($\Delta\mu_{0\to n}$, A.u.), S_m index, $S_r(r)$ overlap, charge transfer distance (D index, Å), RMSD of hole and electron (Å), H and t indexes (Å), the hole delocalization index (HDI) and electron delocalization index (EDI)associated to the S0 → Sn transition, as calculated at the cam-b3lyp/6-311+g(d) of the studied compounds **M@b$_{66}$Al$_{12}$N$_{12}$**

	$S_{0\to n}$	$E_{0\to n}$	$\lambda_{0\to n}$	$f_{0\to n}$	Integral of hole	Integral of electron	$\Delta\mu_{0\to n}$	Sm	Sr	D index	RMSD hole	RMSD electron	H index	t index	HDI	EDI
Sc@b$_{66}$Al$_{12}$N$_1$	$S_{0\to6}$	1.401	885.227	0.001	0.997	0.996	0.982	0.398	0.706	0.522	1.882	2.268	2.084	-0.710	11.90	9.94
	$S_{0\to10}$	2.095	591.898	0.013	0.998	0.990	3.866	0.387	0.702	2.058	2.012	3.617	2.814	0.238	10.98	4.55
	$S_{0\to13}$	2.350	527.618	0.251	0.998	0.957	1.888	0.348	0.658	1.022	2.413	3.045	2.729	-0.739	6.24	6.04
	$S_{0\to24}$	3.482	356.125	0.121	0.998	0.989	2.618	0.354	0.641	1.394	2.413	3.224	2.818	-0.141	6.14	4.78
Ti@b$_{66}$Al$_{12}$N$_1$	$S_{0\to8}$	1.480	837.905	<0.001	0.999	0.996	0.247	0.521	0.802	0.131	1.927	2.277	2.102	-1.166	11.43	9.98
	$S_{0\to13}$	2.100	590.264	0.177	0.998	0.975	1.590	0.356	0.670	0.853	2.310	2.942	2.626	-0.837	7.16	7.15
	$S_{0\to15}$	2.330	532.192	<0.001	0.998	0.991	3.371	0.368	0.667	1.793	2.380	3.689	3.034	-0.229	6.62	6.69
	$S_{0\to16}$	2.392	518.310	0.01	0.999	0.993	3.392	0.343	0.640	1.802	1.684	3.427	2.556	0.187	15.77	4.92
V@b$_{66}$Al$_{12}$N$_{12}$	$S_{0\to7}$	1.443	859.34	<0.001	0.999	0.990	0.966	0.256	0.544	0.514	1.078	1.749	1.414	-0.455	28.06	16.45
	$S_{0\to8}$	1.830	677.550	0.003	0.998	0.991	1.382	0.570	0.847	0.735	2.157	2.488	2.322	-0.691	8.06	7.41
	$S_{0\to12}$	2.503	495.325	0.075	0.999	0.991	3.033	0.309	0.594	1.841	2.297	3.770	3.033	-0.195	7.33	7.50
	$S_{0\to16}$	2.834	437.552	0.059	0.998	0.984	2.476	0.340	0.652	1.321	2.139	3.361	2.750	-0.308	8.60	9.12
Cr@b$_{66}$Al$_{12}$N$_{12}$	$S_{0\to1}$	1.439	861.664	<0.001	0.999	0.991	1.008	0.318	0.601	0.536	1.383	2.022	1.702	-0.723	30.24	15.24
	$S_{0\to7}$	2.504	495.127	0.097	0.999	0.981	2.636	0.278	0.579	1.409	2.272	3.890	3.081	-0.411	7.46	3.61
	$S_{0\to11}$	3.072	403.610	0.006	0.999	0.994	2.829	0.422	0.737	1.502	2.203	2.816	2.510	0.118	8.69	7.10
	$S_{0\to16}$	3.473	356.976	0.061	0.999	0.987	4.548	0.277	0.582	2.423	2.313	3.868	3.089	0.367	11.94	3.34
Mn@b$_{66}$Al$_{12}$N$_1$	$S_{0\to1}$	1.466	845.563	0.011	0.995	0.995	0.624	0.594	0.858	0.332	2.195	2.478	2.336	-1.199	6.72	6.23
	$S_{0\to4}$	2.354	526.699	0.024	0.994	0.992	4.788	0.269	0.566	2.550	2.297	3.631	2.964	0.560	6.85	5.59
	$S_{0\to8}$	2.924	424.054	0.118	0.998	0.990	1.901	0.469	0.771	1.011	2.230	2.874	2.552	-0.542	9.51	8.10
	$S_{0\to9}$	2.990	414.665	0.085	0.998	0.989	4.717	0.289	0.561	2.512	2.318	3.905	3.112	0.416	8.82	7.14

$Fe@b_{66}Al_{12}N_1$	$S_{0\to4}$	1.431	866.119	0.022	0.997	0.995	0.400	0.576	0.848	0.213	2.082	2.299	2.191	-1.111	8.64	9.01
	$S_{0\to9}$	2.416	513.182	0.05	0.996	0.991	6.208	0.157	0.439	3.305	2.304	3.761	3.032	1.354	7.60	3.24
	$S_{0\to13}$	3.244	382.162	0.129	0.999	0.985	1.181	0.435	0.723	0.630	2.092	3.139	2.615	-0.852	14.39	6.42
	$S_{0\to14}$	3.143	356.555	0.037	0.999	0.989	5.005	0.194	0.445	2.663	2.387	3.899	3.143	0.608	13.28	2.97
$Co@b_{66}Al_{12}N$	$S_{0\to7}$	1.542	804.000	0.031	0.998	0.993	0.252	0.587	0.856	0.134	1.926	2.367	2.147	-1.170	15.37	8.94
	$S_{0\to9}$	2.428	510.604	0.049	0.997	0.991	6.040	0.158	0.438	3.214	2.307	3.770	3.039	1.260	8.13	3.28
	$S_{0\to13}$	3.284	377.508	0.088	0.999	0.986	0.815	0.374	0.659	0.435	1.865	3.010	2.437	-0.962	22.13	5.36
	$S_{0\to18}$	3.769	328.968	0.022	1.000	0.988	2.971	0.226	0.506	1.582	3.510	4.075	3.792	-1.001	11.58	2.62
$Ni@b_{66}Al_{12}N_{12}$	$S_{0\to5}$	1.909	649.646	0.068	0.997	0.989	0.750	0.501	0.803	0.400	2.101	2.501	2.301	-0.940	10.00	6.09
	$S_{0\to7}$	2.479	500.221	0.056	0.997	0.991	5.983	0.161	0.444	3.184	2.301	3.818	3.060	1.221	8.35	3.12
	$S_{0\to14}$	3.685	336.467	<0.001	0.999	0.990	1.219	0.202	0.485	0.648	2.982	3.925	3.454	-1.345	10.55	3.63
	$S_{0\to16}$	3.843	322.642	0.001	0.999	0.987	1.024	0.240	0.523	0.546	2.848	3.857	3.353	-1.413	10.75	2.88
$Cu@b_{66}Al_{12}N_1$	$S_{0\to1}$	1.993	622.195	0.077	0.997	0.987	1.293	0.437	0.711	0.689	2.120	2.476	2.298	-0.701	11.12	5.97
	$S_{0\to2}$	2.521	491.847	0.053	0.997	0.991	5.799	0.158	0.424	3.085	2.295	3.836	3.065	1.128	9.29	3.14
	$S_{0\to9}$	3.609	343.525	<0.001	0.999	0.991	1.435	0.235	0.533	0.763	2.800	3.800	3.300	-1.040	11.07	4.60
	$S_{0\to12}$	3.776	328.385	<0.001	0.999	0.989	0.629	0.215	0.508	0.335	3.256	3.995	3.625	-1.638	8.29	2.63
$Zn@b_{66}Al_{12}N$	$S_{0\to3}$	2.901	427.416	0.197	0.999	0.992	0.439	0.404	0.694	0.233	2.286	2.581	2.434	-1.505	9.41	6.12
	$S_{0\to5}$	3.198	387.695	0.076	0.999	0.993	5.527	0.137	0.386	2.936	2.448	3.769	3.108	0.940	8.66	3.25
	$S_{0\to11}$	3.975	311.888	0.02	0.999	0.990	0.555	0.245	0.525	0.296	3.428	4.195	3.812	-1.776	8.26	2.35
	$S_{0\to15}$	4.076	304.190	0.002	0.999	0.990	1.240	0.229	0.506	0.660	2.704	3.807	3.255	-1.252	11.14	2.93

Appendix I

Table S3.AI Static and dynamic of $\beta_{J=1}$ and $\beta_{J=3}$ of $M@b_{64/66}Al_{12}N_{12}$ (M= Sc to Zn)

	M@b$_{64}$Al$_{12}$N$_{12}$	**Sc**	**Ti**	**V**	**Cr**	**Mn**	**Fe**	**Co**	**Ni**	**Cu**	**Zn**
λ=∞	$\beta_{J=1}$	14082.173	5891.150	3560.841	4142.269	1292.168	1374.754	1640.612	1777.973	1948.246	860.349
	$\beta_{J=3}$	5119.968	1993.380	1179.743	1696.278	1519.675	1589.217	1309.425	1253.303	1360.834	620.968
λ=1064	$\beta_{J=1}$	/	/	6318.396	7379.356	12029.27	22404.68	/	7024.467	11448.645	1956.270
	$\beta_{J=3}$	800942.12	23387.25	20807.15	3471.322	22583.75	61527.43	25976.228	13889.98	16006.481	2150.988
λ=1341	$\beta_{J=1}$	/	36131.39	9285.109	25843.95	4731.52	/	86633.456	29896.341	9180.305	1372.268
	$\beta_{J=3}$	816418.85	32861.10	12613.71	42822.67	5067.94	8296.31	118686.56	48219.500	8795.594	1208.057
λ=1906	$\beta_{J=1}$	18301.438	428459.85	4600.096	6918.910	5148.929	/	2721.066	2900.709	3226.935	1125.387
	$\beta_{J=3}$	34813.893	794286.71	3096.453	2242.221	5137.823	32898.960	2344.314	2642.910	2523.836	848.388
	M@b$_{66}$Al$_{12}$N$_{12}$	**Sc**	**Ti**	**V**	**Cr**	**Mn**	**Fe**	**Co**	**Ni**	**Cu**	**Zn**
λ=∞	$\beta_{J=1}$	12125.018	9280.389	5533.168	4197.558	1319.535	1188.119	4197.558	1488.229	1979.818	842.727
	$\beta_{J=3}$	4145.306	4093.373	2276.701	1631.493	1368.097	1219.031	1631.493	1004.836	1268.424	516.981
λ=1064	$\beta_{J=1}$	1137438.70	81721.71	38578.18	7862.451	91739.242	25656.773	7862.451	13567.942	12388.328	2010.291
	$\beta_{J=3}$	4715675.00	131175.95	32515.08	8331.589	152580.42	55179.804	8331.589	24315.702	19872.785	2182.833
λ=1341	$\beta_{J=1}$	4841922.84	47146.105	15101.44	21294.39	3805.077	1193.521	21294.394	23943.400	15885.973	1350.866
	$\beta_{J=3}$	3948308.13	143268.74	28285.74	44212.05	6309.325	7677.550	44212.058	33586.982	16323.787	1077.724
λ=1906	$\beta_{J=1}$	/	8551.052	2817.618	6892.510	5221.953	83629.240	2496.547	2457.599	3547.729	1100.944
	$\beta_{J=3}$	17685.454	4336.656	3333.323	3454.442	4956.441	65608.133	2993.989	2105.365	2713.623	718.640

Appendix I

Table S4.AI The frequency dispersion factor (FDF^{λ}) between static and dynamic HRS hyperpolarizability at a specific wavelength (λ=1064, 1341 and 1906 nm)

$M@b_{64}Al_{12}N_{12}$	Sc	Ti	V	Cr	Mn	Fe	Co	Ni	Cu	Zn
FDF^{1064}	34.6664845	2.50648812	4.12105122	1.80046299	11.6878049	26.7342996	7.10155856	5.86796377	7.24475428	2.53310594
FDF^{1341}	27.1856166	6.96903773	3.41029855	8.8909197	3.54362276	2.73763412	62.8675877	22.2032457	5.05852634	1.66451311
FDF^{1906}	2.01924192	111.662467	1.37965208	1.64926272	3.77133919	10.4290727	1.68769196	1.72485592	1.69229307	1.31889156
$M@b_{66}Al_{12}N_{12}$	Sc	Ti	V	Cr	Mn	Fe	Co	Ni	Cu	Zn
FDF^{1064}	264.789643	12.2723311	7.68900761	2.20928456	85.0416993	30.9573248	25.5779815	12.8545885	8.36765175	2.7158968
FDF^{1341}	441.742669	10.8674289	4.1697784	8.29611044	3.52146153	3.60934547	3.23285776	19.978546	8.91788538	1.6781584
FDF^{1906}	0.80945292	0.93275904	0.62191629	1.67478826	3.85503873	65.6862151	2.42172551	1.73170134	1.8480803	1.3183448

Table S5.AI Static and dynamic second hyperpolarizability (au) for $Al_{12}N_{12}$

γ (0;0,0,0)	λ = ∞	6.335988×10^4
γ (-2ω ; ω, ω,0)	λ=1064	8.257221×10^4
	λ=1341	7.497657×10^4
	λ=1906	6.927832×10^4

Table S6.AI Static and dynamic first hyperpolarizability (au) and depolarization ratio (DR) for $M@b_{64/66}Al_{12}N_{12}$ (M= Sc- Zn) calculated by the sum-over-states method

M@b$_{64}$Al$_{12}$N$_{12}$	$DR_{SOS}^{\lambda=\infty}$	$\beta_{SOS}^{\lambda=\infty}$	$DR_{SOS}^{\lambda=1064}$	$\beta_{SOS}^{\lambda=1064}$	$\beta_{HRS,SOS}^{\lambda=1064}$	$DR_{SOS}^{\lambda=1341}$	$\beta_{SOS}^{\lambda=1341}$	$\beta_{HRS,SOS}^{\lambda=1341}$	$DR_{SOS}^{\lambda=1906}$	$\beta_{SOS}^{\lambda=1906}$	$\beta_{HRS,SOS}^{\lambda=1906}$
Sc	7.95	7169	3.39	579762.42	254237.97	3.77	25158.28	11935.39	2.91	25910.15	11545.39
Ti	7.57	2705	1.26	5615.41	4934.89	9.04	8127.36	6420.25	2.23	50405.91	24799.03
V	7.08	1677	2.29	32777.03	17301.48	5.24	9602.01	3848.64	8.11	6064.56	2288.99
Cr	6.63	2482	2.51	9460.03	4564.17	2.58	136959.32	57986.40	5.26	10129.52	3998.01
Mn	6.00	2225	4.23	44516.06	17989.43	7.06	15525.84	6215.46	5.46	15765.60	6287.04
Fe	4.95	1861	2.53	100581.62	43999.02	2.70	13131.09	5623.80	8.46	357206.52	296872.55
Co	5.07	1049	4.21	38457.14	15169.58	1.70	521762.19	244368.38	4.77	4471.14	1932.44
Ni	4.52	921	3.00	25495.52	10581.42	1.85	65945.66	29236.42	4.51	3325.50	1440.67
Cu	4.36	772	3.00	25131.65	10283.45	3.60E	9422.90	4051.41	4.21	3003.85	1305.23
Zn	3.32	696	3.17	3858.29	1792.65	3.32	2480.44	1165.14	3.34	1826.75	873.24
M@b$_{66}$Al$_{12}$N$_{12}$	$DR_{SOS}^{\lambda=\infty}$	$\beta_{SOS}^{\lambda=\infty}$	$DR_{SOS}^{\lambda=1064}$	$\beta_{SOS}^{\lambda=1064}$	$\beta_{HRS,SOS}^{\lambda=1064}$	$DR_{SOS}^{\lambda=1341}$	$\beta_{SOS}^{\lambda=1341}$	$\beta_{HRS,SOS}^{\lambda=1341}$	$DR_{SOS}^{\lambda=1906}$	$\beta_{SOS}^{\lambda=1906}$	$\beta_{HRS,SOS}^{\lambda=1906}$
Sc	7.87	6899	1.99	895675.94	429355.59	1.95	100867.76	55537.23	2.56	13434.65	6274.06
Ti	7.70	5076	3.48	1249970.54	534462.42	4.39	143939.35	56509.46	6.91	21802.09	8663.13
V	7.46	2861	5.42	57731.03	24521.52	0.381	16862.81	20891.26	6.06	8546.79	3261.79
Cr	7.21	2484	1.59	12078.97	6555.81	2.25	72657.45	31325.23	5.80	10999.14	4227.26
Mn	6.14	2300	3.16	223110.52	93353.11	5.71	15095.19	6004.87	5.61	16605.87	6611.32
Fe	5.47	1853	2.70	83657.01	35652.31	2.90	12622.29	5415.79	5.80	10788.63	4505.63
Co	5.11	1398	2.92	68371.19	28797.71	1.42	8395.61	3905.82	5.42	6431.38	2763.05
Ni	4.24	852	2.96	42823.59	17857.47	1.91	21322.15	10293.98	4.54	3452.04	1520.84
Cu	4.20	672	2.86	33042.36	13688.67	3.21	16463.31	7098.13	4.15	3001.29	1318.85
Zn	2.61	558	2.64	3307.94	1618.21	2.75	1913.48	973.17	2.69	1314.08	703.96

Liste of figures

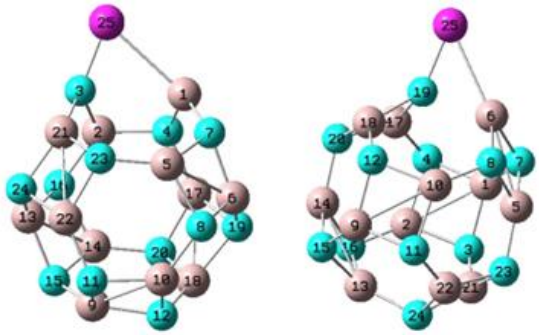

$M@b_{64}Al_{12}N_{12}$ $M@b_{66}Al_{12}N_{12}$

Scheme S1.AI Optimized geometry of the title compounds

TM	$M@b_{64}$	$M@b_{66}$	$M@b_{64}$	$M@b_{66}$
Ti	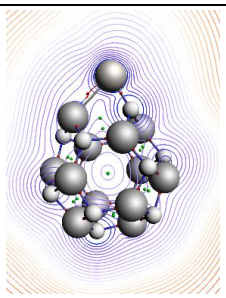	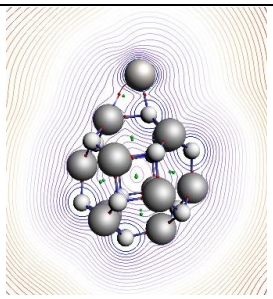	**Fe**	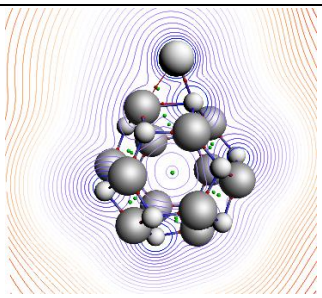 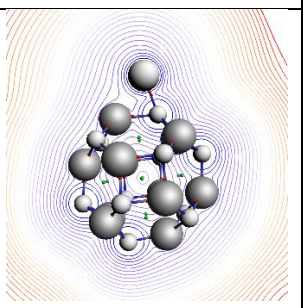
V	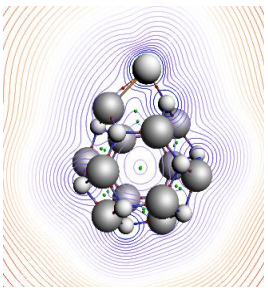	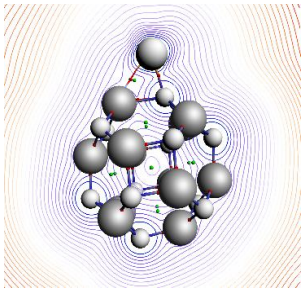	**Ni**	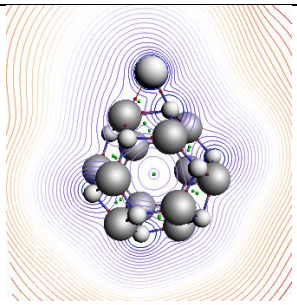 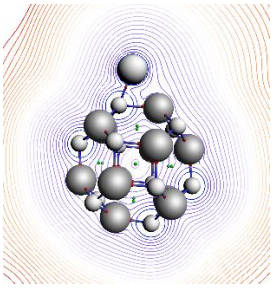
Cr	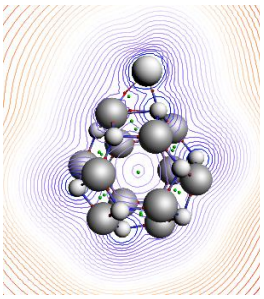	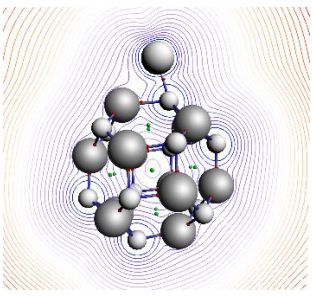	**Cu**	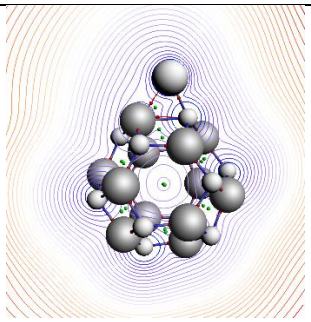 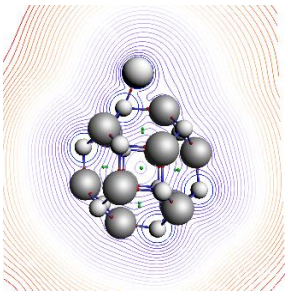

Mn	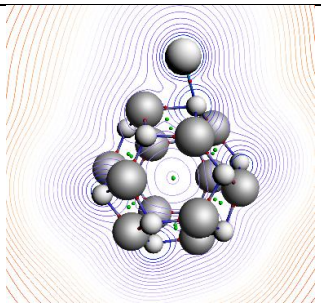 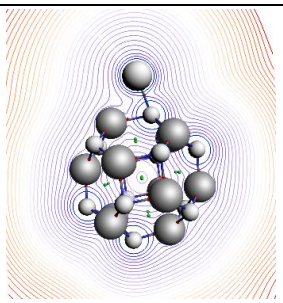	**Zn** 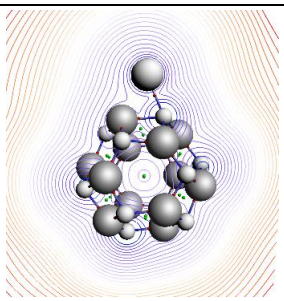 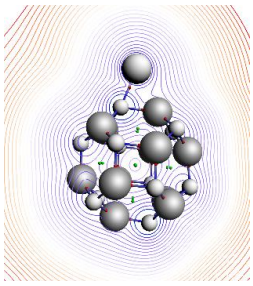

Figure S1.AI Molecular topology of $M@b_{64/66}Al_{12}N_{12}$ (M= Sc- Zn) where in the nanocage, nitrogen atoms: are small spheres, while aluminum atoms: are large spheres.

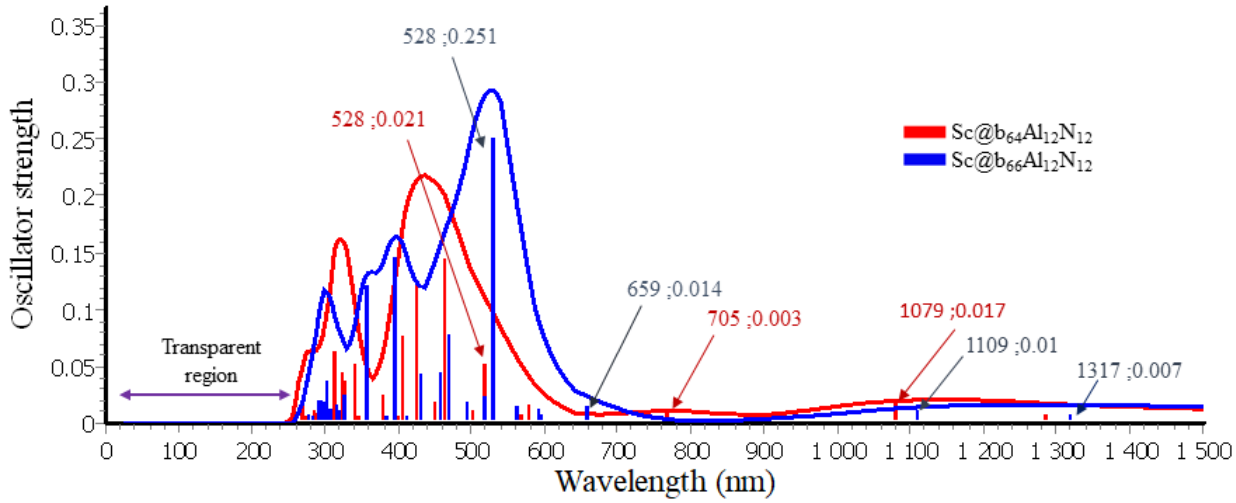
Oscillator strength
Wavelength (nm)
Transparent region
528 ;0.251
528 ;0.021
659 ;0.014
705 ;0.003
1079 ;0.017
1109 ;0.01
1317 ;0.007
Sc@b64Al12N12
Sc@b66Al12N12

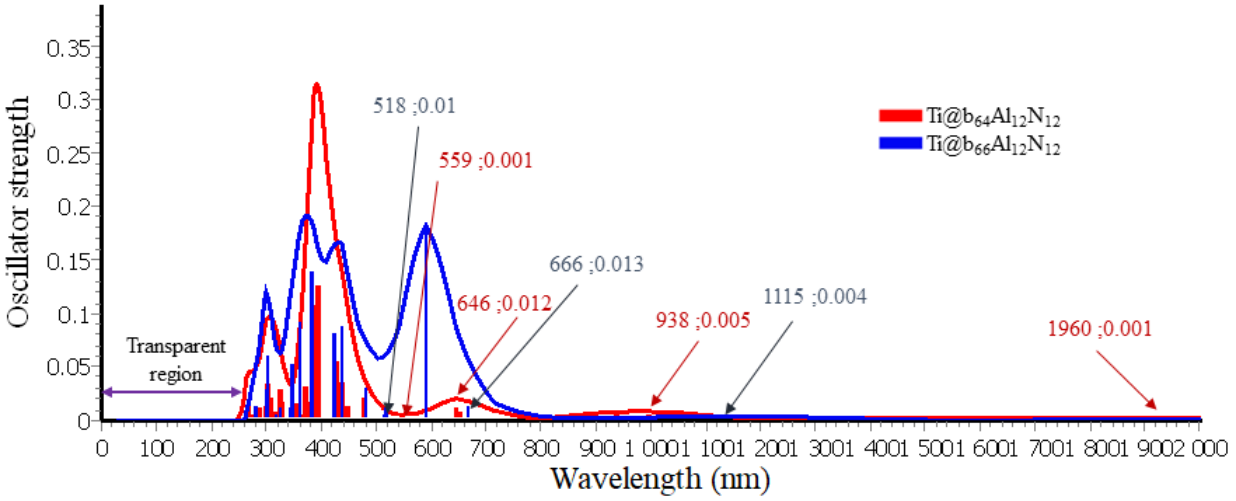
Oscillator strength
Wavelength (nm)
Transparent region
518 ;0.01
559 ;0.001
666 ;0.013
646 ;0.012
938 ;0.005
1115 ;0.004
1960 ;0.001
Ti@b64Al12N12
Ti@b66Al12N12

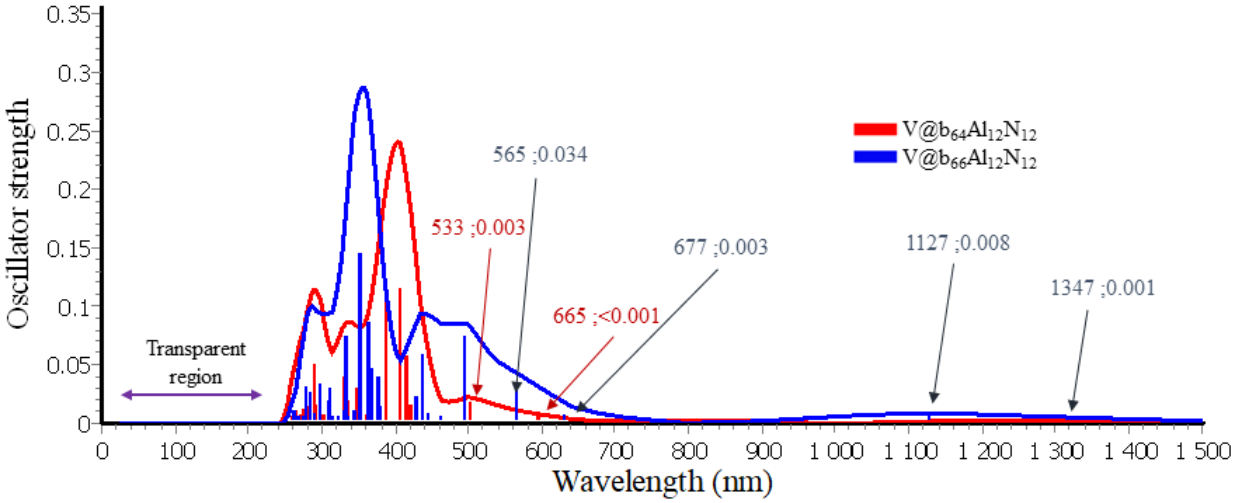
Oscillator strength
Wavelength (nm)
Transparent region
565 ;0.034
533 ;0.003
677 ;0.003
665 ;<0.001
1127 ;0.008
1347 ;0.001
V@b64Al12N12
V@b66Al12N12

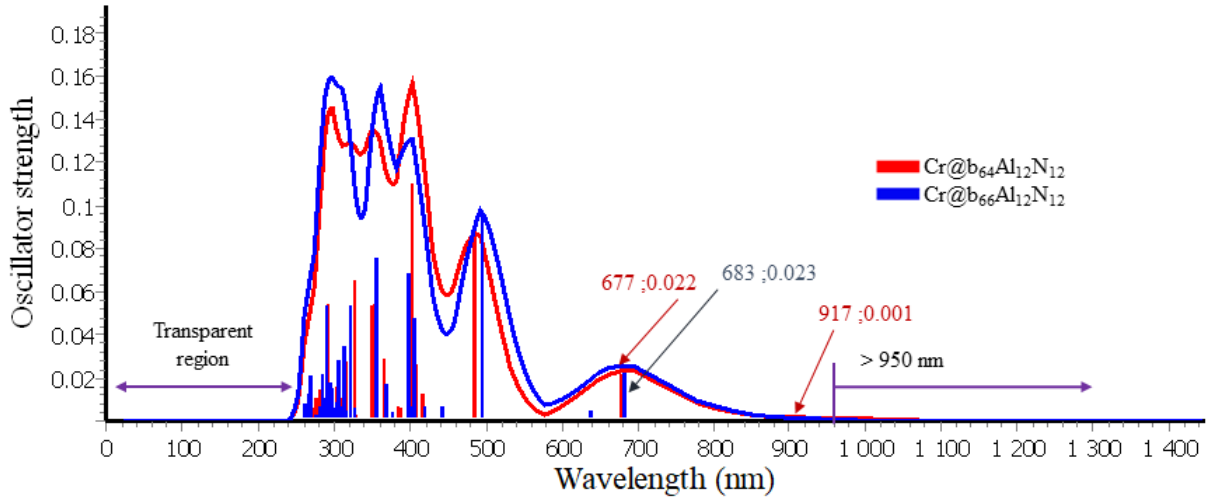
Oscillator strength
Wavelength (nm)
Cr@b64Al12N12
Cr@b66Al12N12
677 ;0.022
683 ;0.023
917 ;0.001
> 950 nm
Transparent region

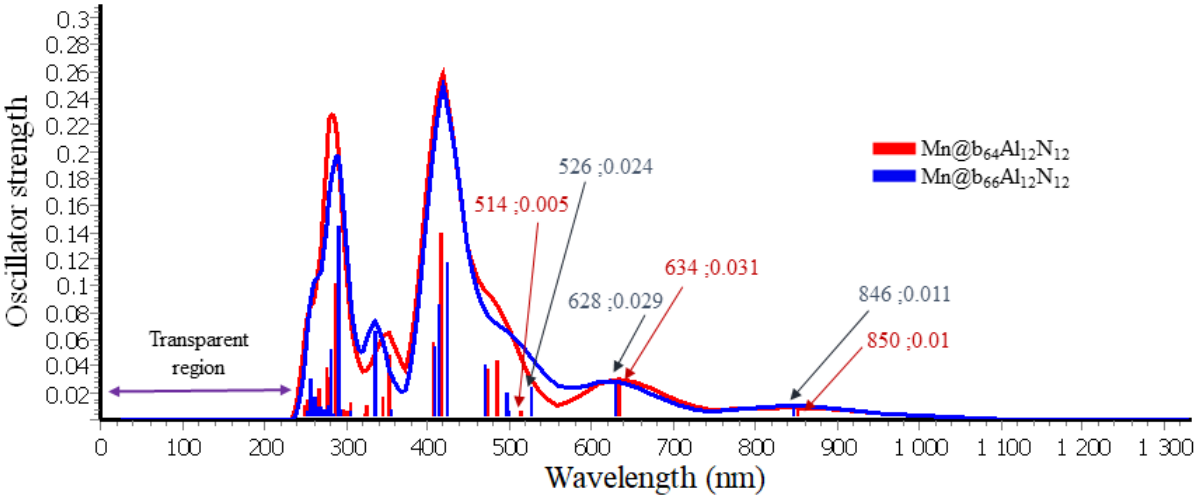
Oscillator strength
Wavelength (nm)
Mn@b64Al12N12
Mn@b66Al12N12
526 ;0.024
514 ;0.005
634 ;0.031
628 ;0.029
846 ;0.011
850 ;0.01
Transparent region

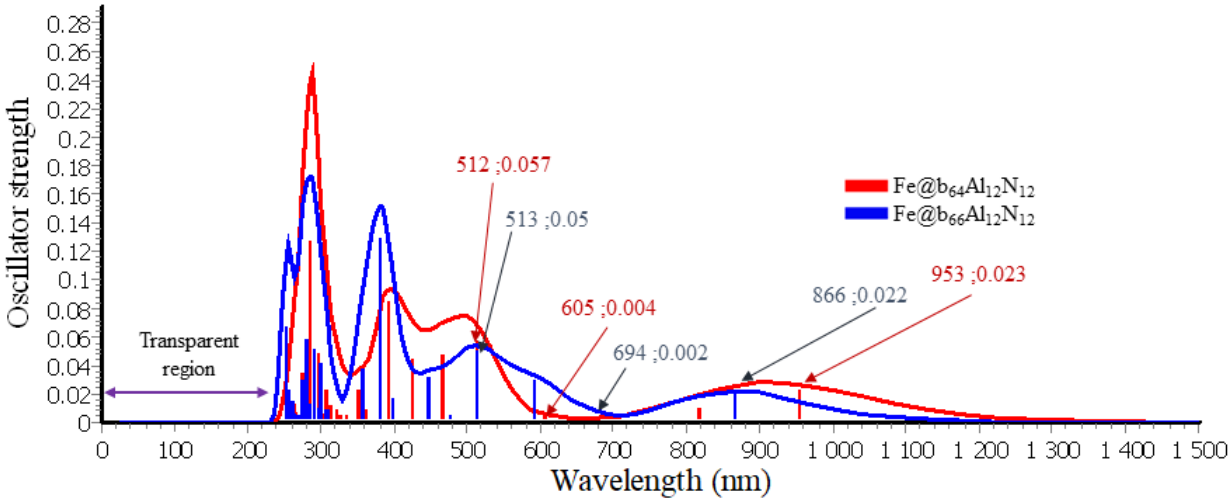
Oscillator strength
Wavelength (nm)
Fe@b64Al12N12
Fe@b66Al12N12
512 ;0.057
513 ;0.05
605 ;0.004
694 ;0.002
866 ;0.022
953 ;0.023
Transparent region

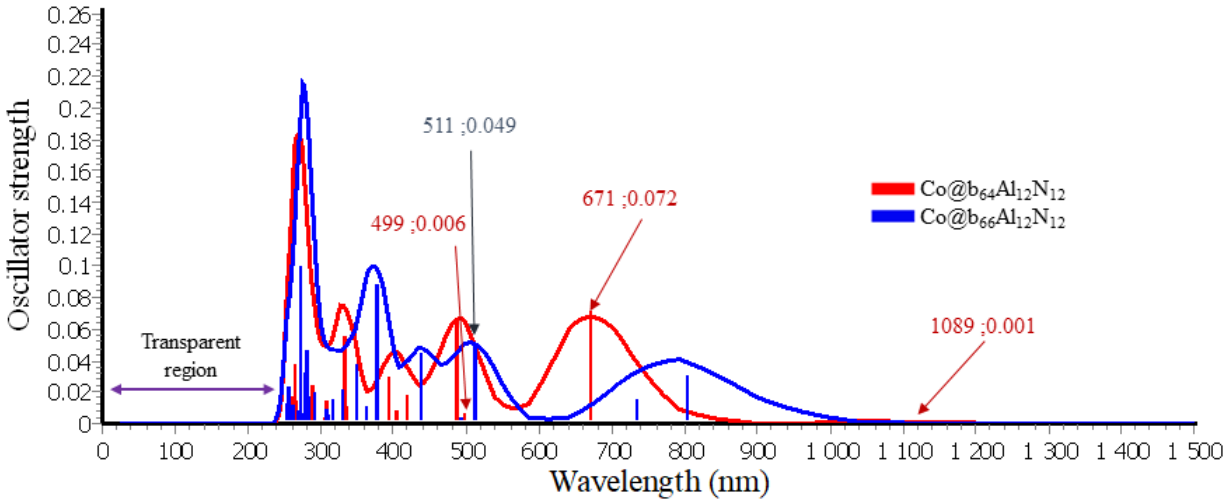
Oscillator strength
Wavelength (nm)
Transparent region
511 ;0.049
499 ;0.006
671 ;0.072
1089 ;0.001
Co@b64Al12N12
Co@b66Al12N12

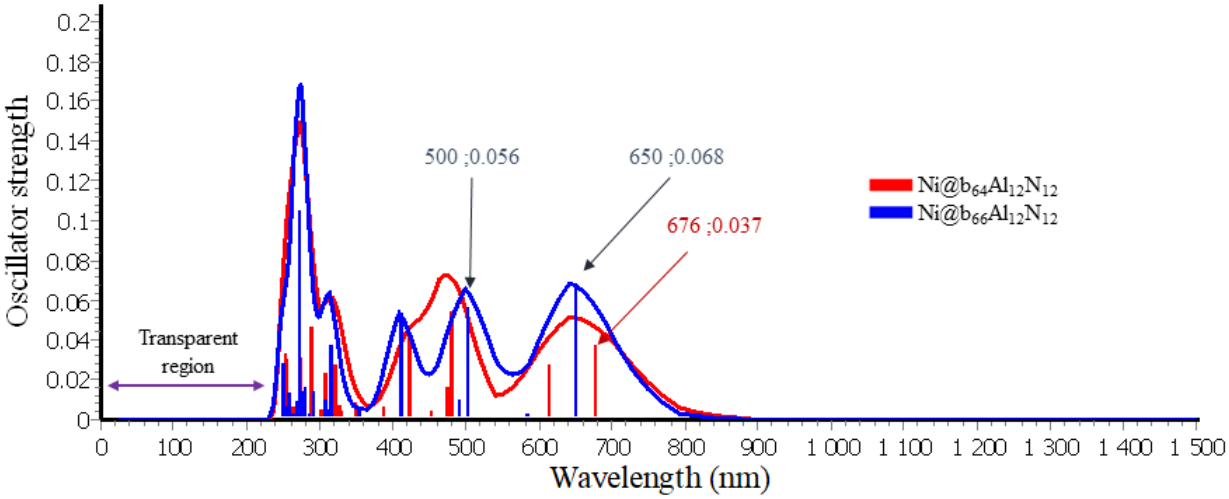
Oscillator strength
Wavelength (nm)
Transparent region
500 ;0.056
650 ;0.068
676 ;0.037
Ni@b64Al12N12
Ni@b66Al12N12

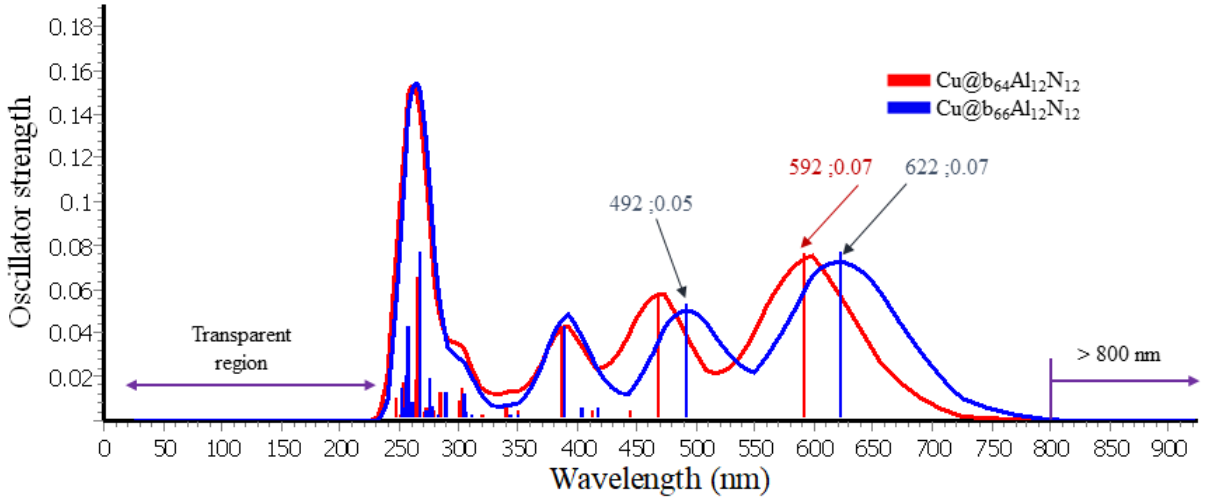
Oscillator strength
Wavelength (nm)
Transparent region
492 ;0.05
592 ;0.07
622 ;0.07
> 800 nm
Cu@b64Al12N12
Cu@b66Al12N12

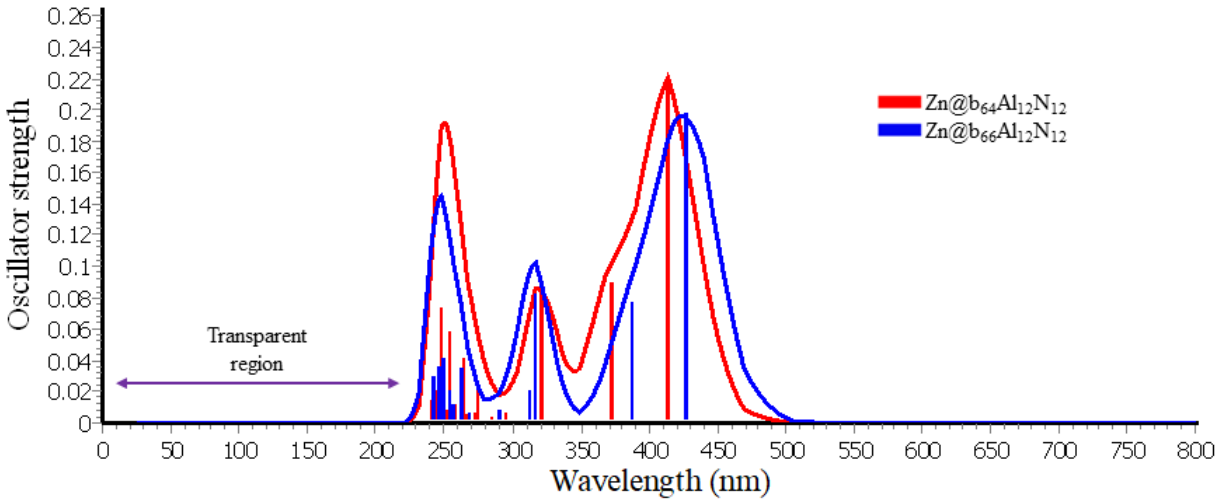

Figure S2.AI Calculated UV − vis absorption spectra of $M@b_{64/66}Al_{12}N_{12}$ (M from Sr to Zn)

$M@b_{64}Al_{12}N_{12}$	$S_{0\rightarrow n}$	MO		(EDDM)
		(β HOMO → β LUMO)) **49 %**		ICT in Metal Sc
	$S_{0\rightarrow 5}$	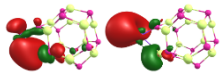		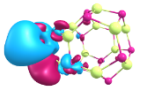
		(βHOMO→ βLUMO)+4) **10%**	(α HOMO → α LUMO)) **36%**	ICT in Metal Sc + MLCT from Sc to nanocage
	$S_{0\rightarrow 11}$	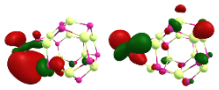	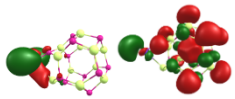	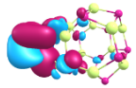
$Sc@b_{64}Al_{12}N_{12}$		(α HOMO-1 → α LUMO)+1) **15%**	(βHOMO→ β LUMO)+1)**31%**	ICT in Metal Sc + MLCT from Sc to nanocage
	$S_{0\rightarrow 13}$	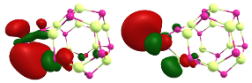	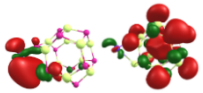	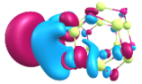
		(β HOMO → β LUMO)+2) **18%**	(α HOMO-1→ α LUMO)+3) **29%**	ICT in Metal Sc + MLCT from Sc to nanocage
	$S_{0\rightarrow 15}$	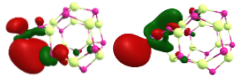	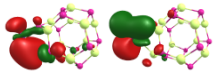	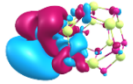
		(α HOMO → α LUMO)+1) **22%**		ICT in Metal Ti
	$S_{0\rightarrow 5}$	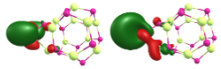		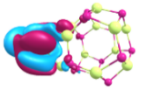
$Ti@b_{64}Al_{12}N_{12}$		(β HOMO → β LUMO)+1) **10%**	(α HOMO → α LUMO)) **43%**	ICT in Metal Ti + MLCT from Ti to nanocage
	$S_{0\rightarrow 15}$	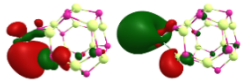	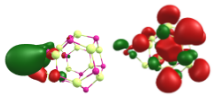	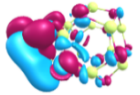
	$S_{0\rightarrow 18}$	(α HOMO-2→ α LUMO)+3) **13%**	(βHOMO → β LUMO)+3)**11%**	ICT in Metal Ti + MLCT from Ti to nanocage

	$S_{0\rightarrow16}$	(β HOMO → β LUMO)+2) **17%** 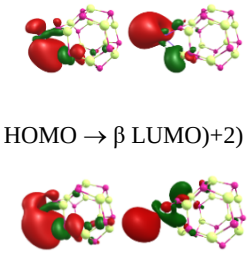	(β HOMO → β LUMO)) **25%** 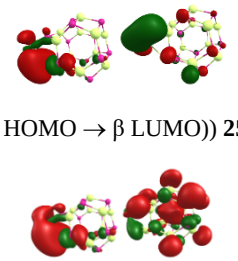	ICT in Metal Ti + MLCT from Ti to nanocage 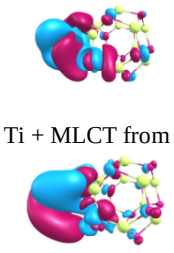
V@b$_{64}$Al$_{12}$N$_{12}$	$S_{0\rightarrow5}$	(α HOMO-3 → α LUMO)+2) **23%** 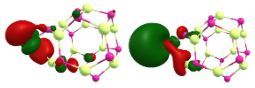		ICT in Metal V 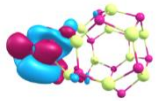
	$S_{0\rightarrow14}$	(β HOMO → β LUMO)+1) **10%** 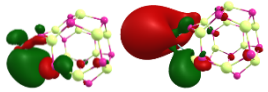	(β HOMO → β LUMO)) **54%** 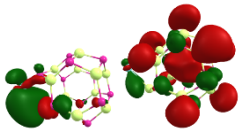	ICT in Metal V + MLCT from V to nanocage 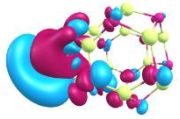
	$S_{0\rightarrow15}$	(α HOMO-1 → α LUMO)+1)**20%** 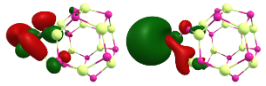	(βHOMO→ β LUMO)+2) **14%** 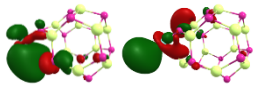	ICT in Metal V + MLCT from V to nanocage 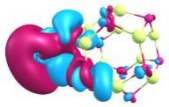
	$S_{0\rightarrow17}$	(α HOMO → α LUMO)+1) **26%** 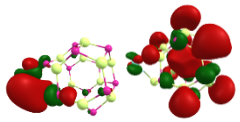	(α HOMO → α LUMO)+3) **12%** 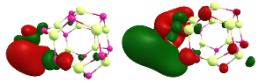	ICT in Metal V + MLCT from V to nanocage 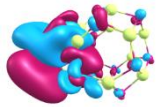

Cr@b$_{64}$Al$_{12}$N$_{12}$	$S_{0\rightarrow1}$	(α HOMO-1 → α LUMO)+2) **55%**	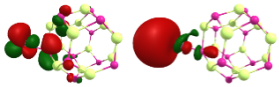	ICT in Metal Cr 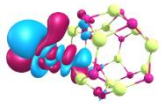
	$S_{0\rightarrow7}$	(β HOMO → β LUMO)) **52%**	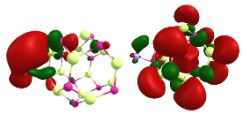	MLCT from Cr to nanocage 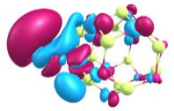
	$S_{0\rightarrow11}$	(α HOMO → α LUMO)+2) **30%**	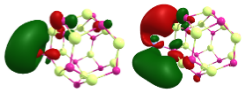	MLCT from Cr to nanocage 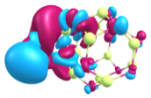
	$S_{0\rightarrow16}$	(β HOMO → β LUMO)+1) **10%** 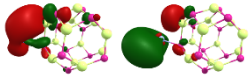	(α HOMO → α LUMO)) **25%** 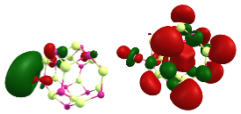	ICT in Metal Cr + MLCT from Cr to nanocage 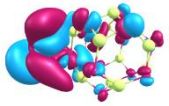
Mn@b$_{64}$Al$_{12}$N$_{12}$	$S_{0\rightarrow1}$	(α HOMO → α LUMO)+1) **44%**	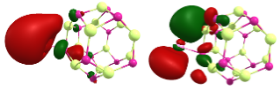	ICT in Metal Mn 
	$S_{0\rightarrow6}$	(α HOMO → α LUMO)) **36%**	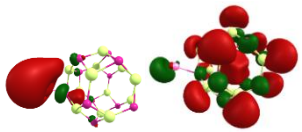	MLCT from Mn to nanocage 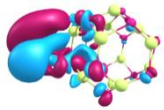
	$S_{0\rightarrow8}$	(β HOMO → β LUMO)) **28%**	(β HOMO → β LUMO)+6) **10%**	MLCT from Mn to nanocage

		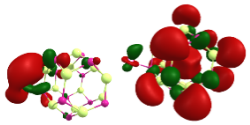 (β HOMO → β LUMO)+1) **33%**	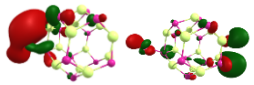 (α HOMO → α LUMO)+1) **10%**	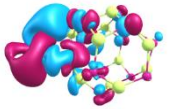 ICT in Metal Mn + MLCT from Mn to nanocage
	$S_{0\rightarrow9}$	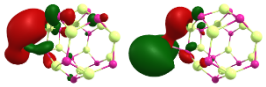	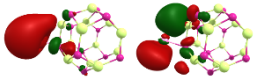	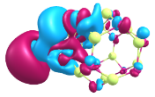
		(α HOMO → α LUMO)+1) **51%**		ICT in Metal Fe
	$S_{0\rightarrow4}$	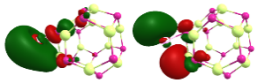		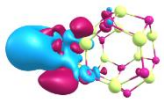
		(α HOMO → α LUMO)) **73%**		MLCT from Fe to nanocage
	$S_{0\rightarrow9}$	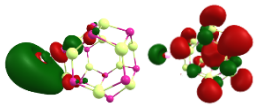		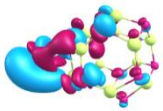
Fe@b$_{64}$Al$_{12}$N$_{12}$		(β HOMO → β LUMO)+1) **29%**	(β HOMO → β LUMO)+6) **13%**	MLCT from Fe to nanocage
	$S_{0\rightarrow13}$	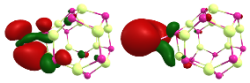	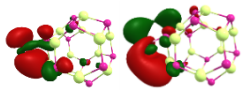	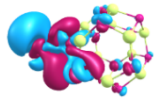
		(β HOMO → β LUMO)) **61%**		ICT in Metal Fe + MLCT from Fe to nanocage
	$S_{0\rightarrow15}$	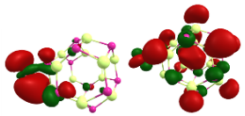		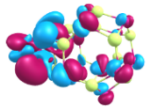
Co@b$_{64}$Al$_{12}$N$_{12}$	$S_{0\rightarrow8}$	(β HOMO-2 → β LUMO)+14) **35%**		ICT in Metal Co

		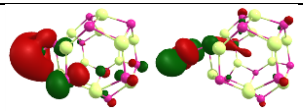	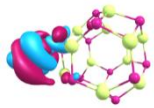	
		(α HOMO → α LUMO)+1) **72%**		ICT in Metal Co
	$S_{0\rightarrow9}$	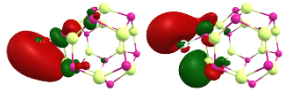	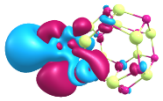	
		(α HOMO → α LUMO)) **83%**		MLCT from Co to nanocage
	$S_{0\rightarrow11}$	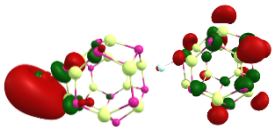	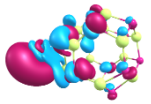	
		(β HOMO → β LUMO)+2) **37%**		ICT in Metal Co + MLCT from Co to nanocage
	$S_{0\rightarrow13}$	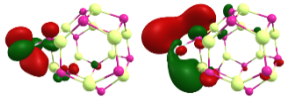	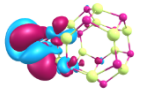	
		(α HOMO → α LUMO)+1) **49%**		ICT in Metal Ni
	$S_{0\rightarrow5}$	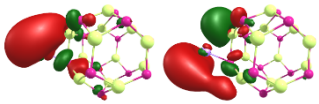	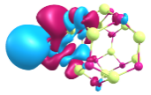	
Ni@b$_{64}$Al$_{12}$N$_{12}$		(α HOMO → α LUMO)) **81%**		MLCT from Ni to nanocage
	$S_{0\rightarrow7}$	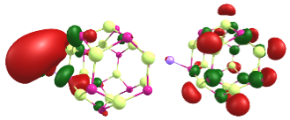	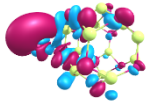	
	$S_{0\rightarrow13}$	(β HOMO → β LUMO)) **36%**	(α HOMO-1→αLUMO)) **10%**	LMCT from nanocage to Ni + ICT in nanocage

		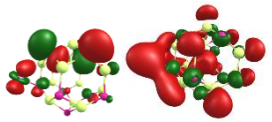 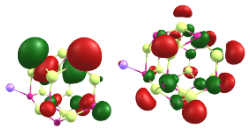 (β HOMO-2 → β LUMO)) **40%**	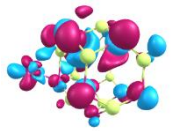 LMCT from nanocage to Ni
	$S_{0\rightarrow14}$	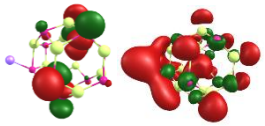 (α HOMO → α LUMO)+1) **81%**	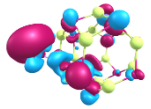 ICT in Metal Cu
	$S_{0\rightarrow1}$	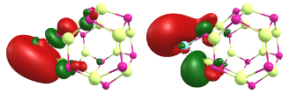 (α HOMO → α LUMO)) **83%**	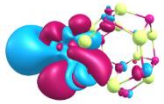 MLCT from Cu to nanocage
	$S_{0\rightarrow2}$	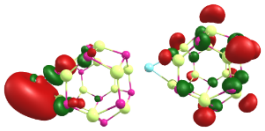 (β HOMO → β LUMO)) **55%**	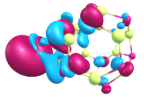 LMCT from nanocage to Cu
Cu@b$_{64}$Al$_{12}$N$_{12}$	$S_{0\rightarrow9}$	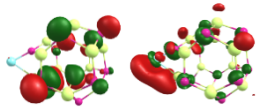 (β HOMO-1 → β LUMO)) **56%**	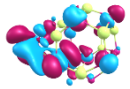 LMCT from nanocage to Cu
	$S_{0\rightarrow11}$	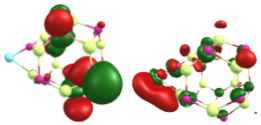	
Zn@b$_{64}$Al$_{12}$N$_{12}$	$S_{0\rightarrow3}$	(HOMO →LUMO)+1) **43%**	ICT in Metal Zn

		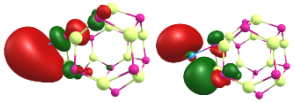	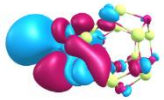
		(HOMO →LUMO)) **39%**	MLCT from Zn to nanocage
	$S_{0\to5}$	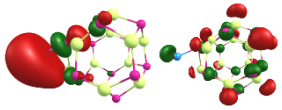	
		(HOMO →LUMO)+2) **37%**	MLCT from Zn to nanocage
	$S_{0\to8}$	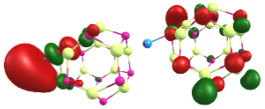	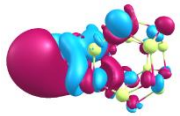
		(HOMO -1 →LUMO)) **22%**	ICT in nanocage + LMCT from nanocage to Zn
	$S_{0\to11}$	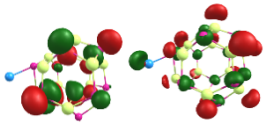	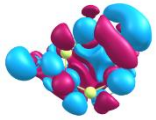

M@$b_{66}Al_{12}N_{12}$	$S_{0\to n}$	**MO**	EDDM
		(α HOMO → α LUMO+1) **30%**	ICT in Metal Sc
	$S_{0\to6}$	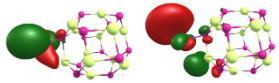	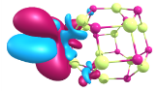
Sc@$b_{66}Al_{12}N_{12}$		(α HOMO → α LUMO) **45%**	MLCT from Sc to nanocage
	$S_{0\to10}$	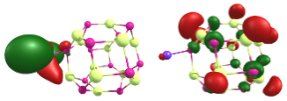	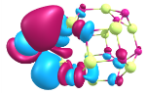
	$S_{0\to13}$	(α HOMO-1 → α LUMO+2) **22%** (β HOMO → β LUMO) **20%**	ICT in Metal Sc + MLCT from Sc to nanocage

		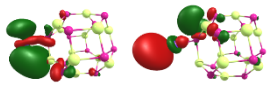	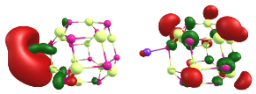	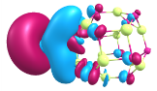
		(α HOMO-1 → α LUMO+3) **19%**	(βHOMO → β LUMO+2) **21%**	ICT in Metal Sc + LMCT from nanocage to Sc
	$S_{0\rightarrow24}$	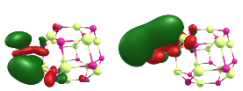	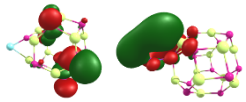	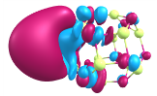
		(α HOMO → α LUMO+2) **24%**		ICT in Metal Ti
	$S_{0\rightarrow8}$	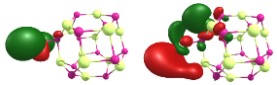		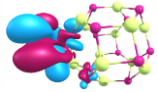
		(β HOMO → β LUMO+2) **27%**		ICT in Metal Ti
	$S_{0\rightarrow13}$	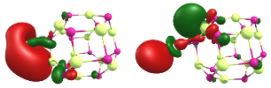		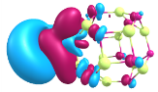
Ti@b$_{66}$Al$_{12}$N$_{12}$		(β HOMO → β LUMO) **45%**	(β HOMO → β LUMO+6)**10%**	MLCT from Ti to nanocage +ICT in Metal Ti
	$S_{0\rightarrow15}$	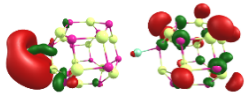	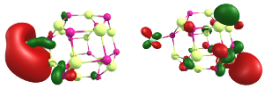	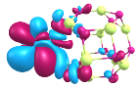
		(α HOMO → α LUMO+2) **10%**	(α HOMO → α LUMO) **41%**	ICT in Metal Ti + MLCT from Ti to nanocage
	$S_{0\rightarrow16}$	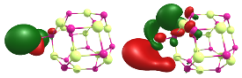	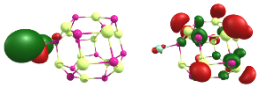	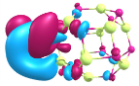
		(αHOMO-3 → α LUMO+2) **58%**		ICT in Metal V
	$S_{0\rightarrow7}$	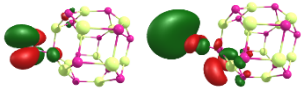		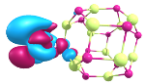
V@b$_{66}$Al$_{12}$N$_{12}$				
	$S_{0\rightarrow8}$	(βHOMO→ β LUMO+1) **44%**		ICT in Metal V

	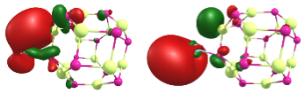 (βHOMO → β LUMO+2) **40%**		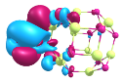 MLCT from V to nanocage
$S_{0\rightarrow12}$	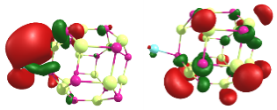 (β HOMO → β LUMO+2) **35%**	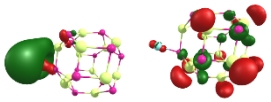 (α HOMO → α LUMO) **18%**	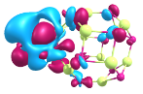 ICT in Metal V + MLCT from V to nanocage
$S_{0\rightarrow16}$	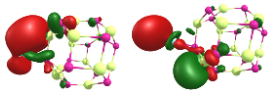		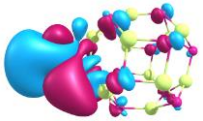
	(α HOMO-1→ α LUMO+1) **56%**		ICT in Metal Cr
$S_{0\rightarrow1}$	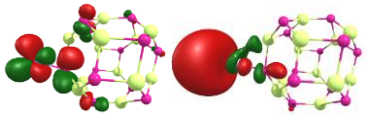 (β HOMO → β LUMO) **53%**		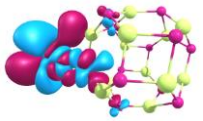 MLCT from Cr to nanocage
$S_{0\rightarrow7}$	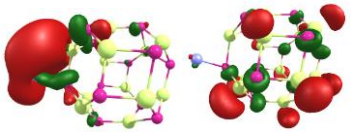 (α H → α LUMO+3) **41%**		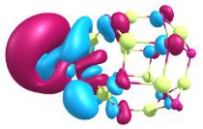 MLCT from Cr to nanocage
$S_{0\rightarrow11}$	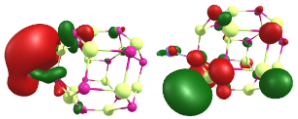 (α HOMO → α LUMO) **58%**		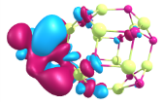 ICT in Metal Cr+ MLCT from Cr to nanocage
$S_{0\rightarrow16}$	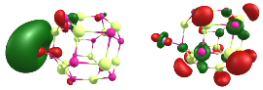	(α HOMO → α LUMO+2) **10%**	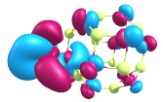

Cr@$b_{66}Al_{12}N_{12}$

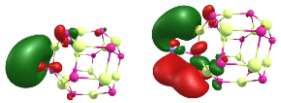

		(α HOMO → α LUMO+1) **49%**	ICT in Metal Mn
Mn@b$_{66}$Al$_{12}$N$_{12}$	$S_{0\rightarrow1}$	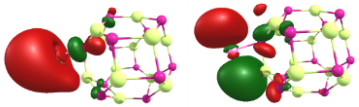	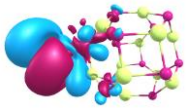
		(α HOMO → α LUMO) **56%**	MLCT from Mn to nanocage
	$S_{0\rightarrow4}$	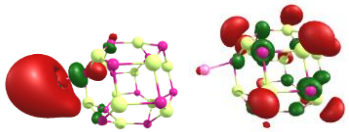	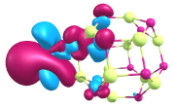
		(β HOMO → β LUMO+1) **30%** (α HOMO → α LUMO+1) **11%**	MLCT from Mn to nanocage + ICT in Metal Mn
	$S_{0\rightarrow8}$		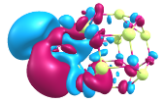
		(β HOMO → β LUMO) **69%** (β HOMO → β LUMO+1) **10%**	ICT in Metal Mn+ MLCT from Mn to nanocage
	$S_{0\rightarrow9}$		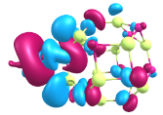
		(α HOMO → α LUMO+1) **52%**	ICT in Metal Fe
Fe@b$_{66}$Al$_{12}$N$_{12}$	$S_{0\rightarrow4}$	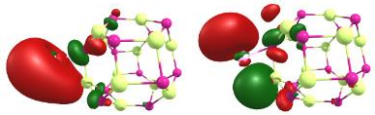	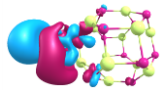
	$S_{0\rightarrow9}$	(α HOMO → α LUMO) **78%**	MLCT from Fe to nanocage

		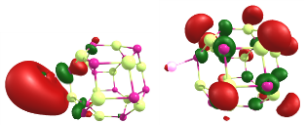	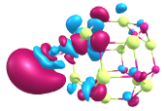
		(β HOMO → β LUMO+1) **41%** (α HOMO → α LUMO+1) **10%**	MLCT from Fe to nanocage +ICT in Metal Fe
	$S_{0\rightarrow13}$		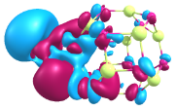
		(β HOMO → β LUMO) **71%**	ICT in Metal Fe + MLCT from Fe to nanocage
	$S_{0\rightarrow14}$	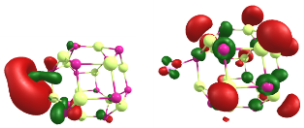	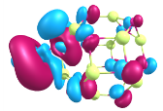
		(α HOMO → α LUMO+1) **52%**	ICT in Metal Co
	$S_{0\rightarrow7}$	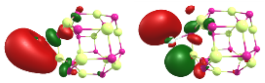	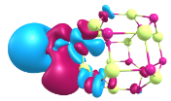
		(α HOMO → α LUMO) **80%**	MLCT from Co to nanocage
Co@b$_{66}$Al$_{12}$N$_{12}$	$S_{0\rightarrow9}$	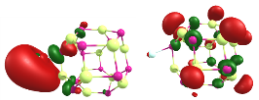	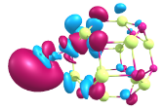
		(β HOMO → β LUMO+1) **44%**	ICT in Metal Co
	$S_{0\rightarrow13}$	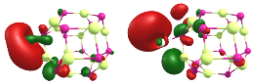	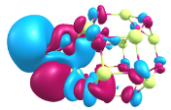

		(β HOMO → β LUMO) **51%**	ICT in Metal Co + MLCT from Co to nanocage
	$S_{0\rightarrow18}$	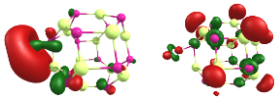	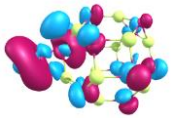
		(α HOMO → α LUMO+1) **67%**	ICT in Metal Ni
	$S_{0\rightarrow5}$	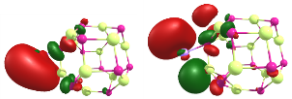	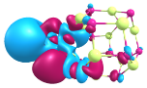
		(α HOMO → α LUMO) **83%**	MLCT from Ni to nanocage
	$S_{0\rightarrow7}$	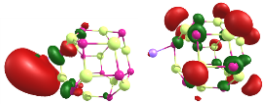	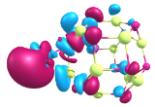
Ni@b$_{66}$Al$_{12}$N$_{12}$		(β HOMO → β LUMO) **69%**	LMCT from nanocage to Ni + ICT in nanocage
	$S_{0\rightarrow14}$	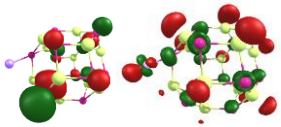	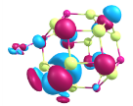
		(β HOMO-1 → β LUMO) **27%**	ICT in Metal Ni +MLCT from Metal Ni to nanocage
	$S_{0\rightarrow16}$	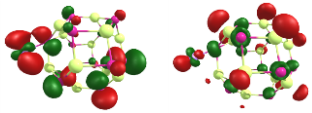	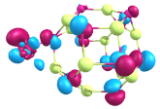
		(α HOMO → α LUMO+1) **78%**	ICT in Metal Cu
Cu@b$_{66}$Al$_{12}$N$_{12}$	$S_{0\rightarrow1}$	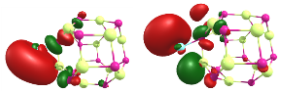	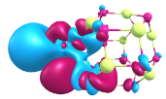
	$S_{0\rightarrow2}$	(α HOMO → α LUMO) **85%**	MLCT from Cu to nanocage

		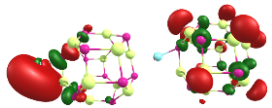 (β HOMO → β LUMO) **69%**	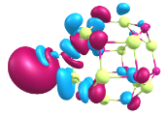 LMCT from nanocage to Cu
	$S_{0\rightarrow9}$	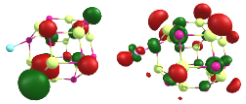 (β HOMO-1 → β LUMO) **48%**	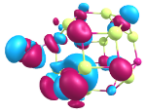 LMCT from nanocage to Cu
	$S_{0\rightarrow12}$	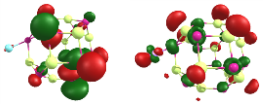	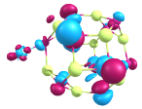
Zn@b$_{66}$Al$_{12}$N$_{12}$		(HOMO →LUMO+1) **44%**	ICT in Metal Zn
	$S_{0\rightarrow3}$	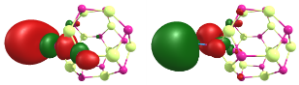 (HOMO →LUMO) **40%**	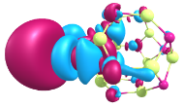 MLCT from Zn to nanocage
	$S_{0\rightarrow5}$	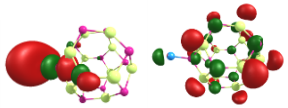 (HOMO-1 →LUMO) **39%**	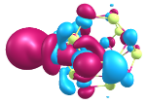 LMCT from nanocage to Zn + ICT in nanocage
	$S_{0\rightarrow11}$	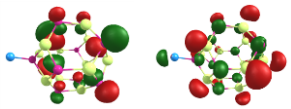	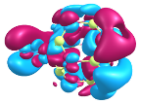
	$S_{0\rightarrow15}$	(HOMO -3 →LUMO) **35%**	ICT in nanocage + LMCT from nanocage to Zn

Figure S3.AI Molecular orbitals (MO) and electron density difference maps (EDDM) for the crucial excited states of **M@b$_{64}$Al$_{12}$N$_{12}$** and **M@b$_{66}$Al$_{12}$N$_{12}$**

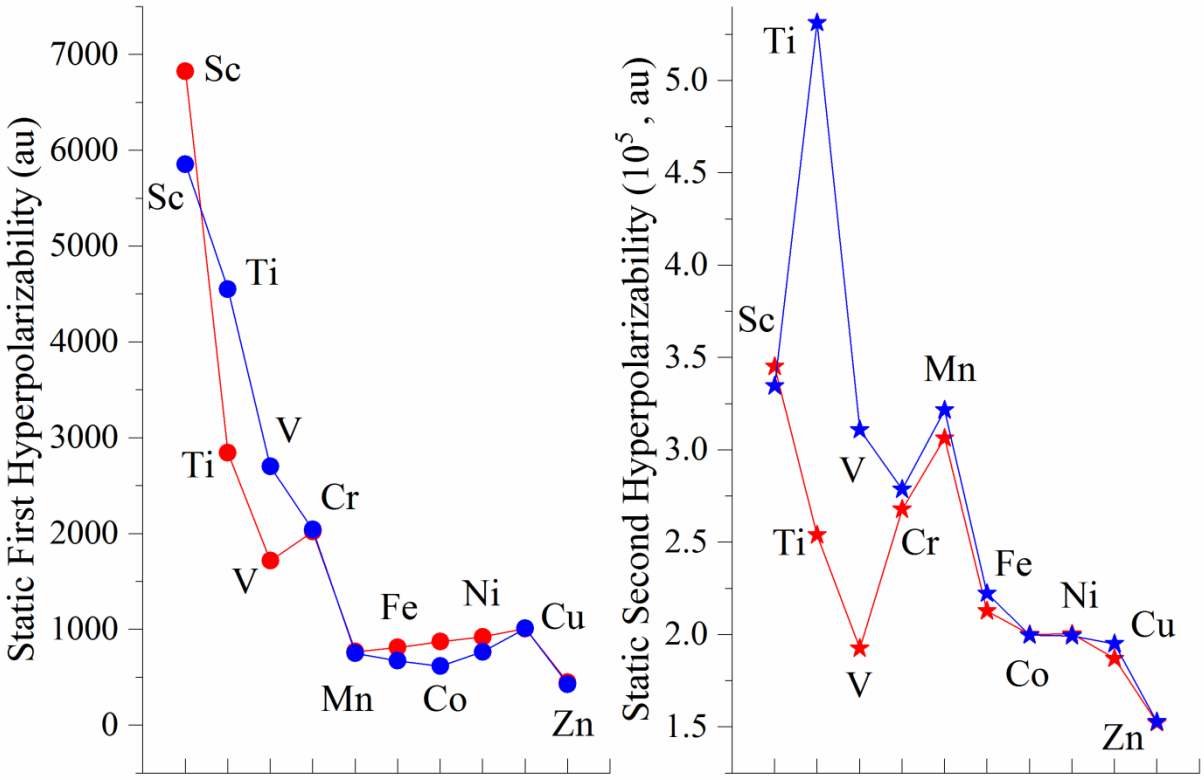

Figure S4.AI Variation of first hyperpolarizability (β_{HRS}^{∞}) and second hyperpolarizability ($\gamma(0;0,0,0)$) of $M@b_{64}Al_{12}N_{12}$ (red) and $M@b_{66}Al_{12}N_{12}$ (blue) where M= Sc-Zn

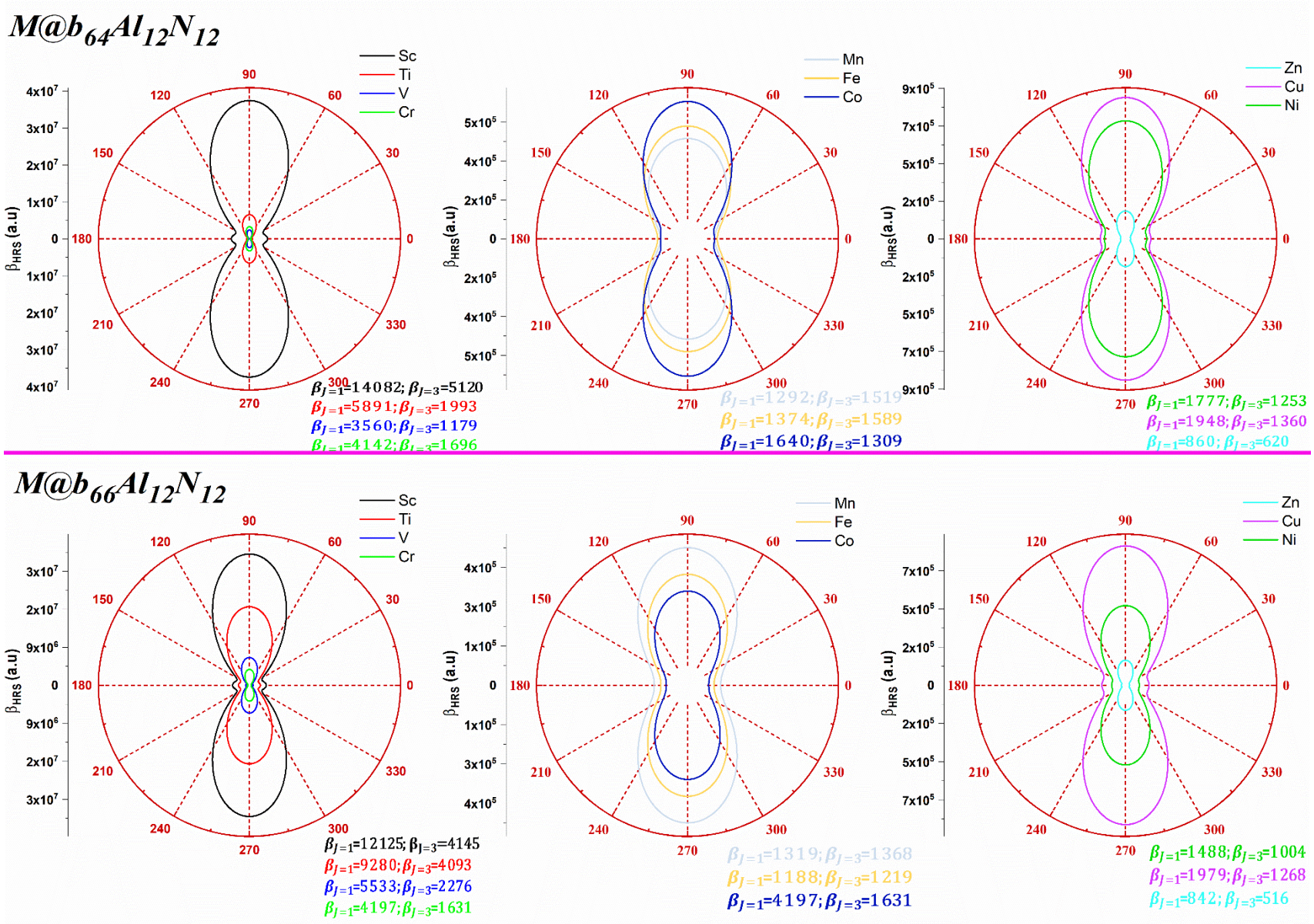

Figure S5.AI Relationship between I_{Ψ}^{2w} and polarization angle Ψ of $M@b_{64/66}Al_{12}N_{12}$

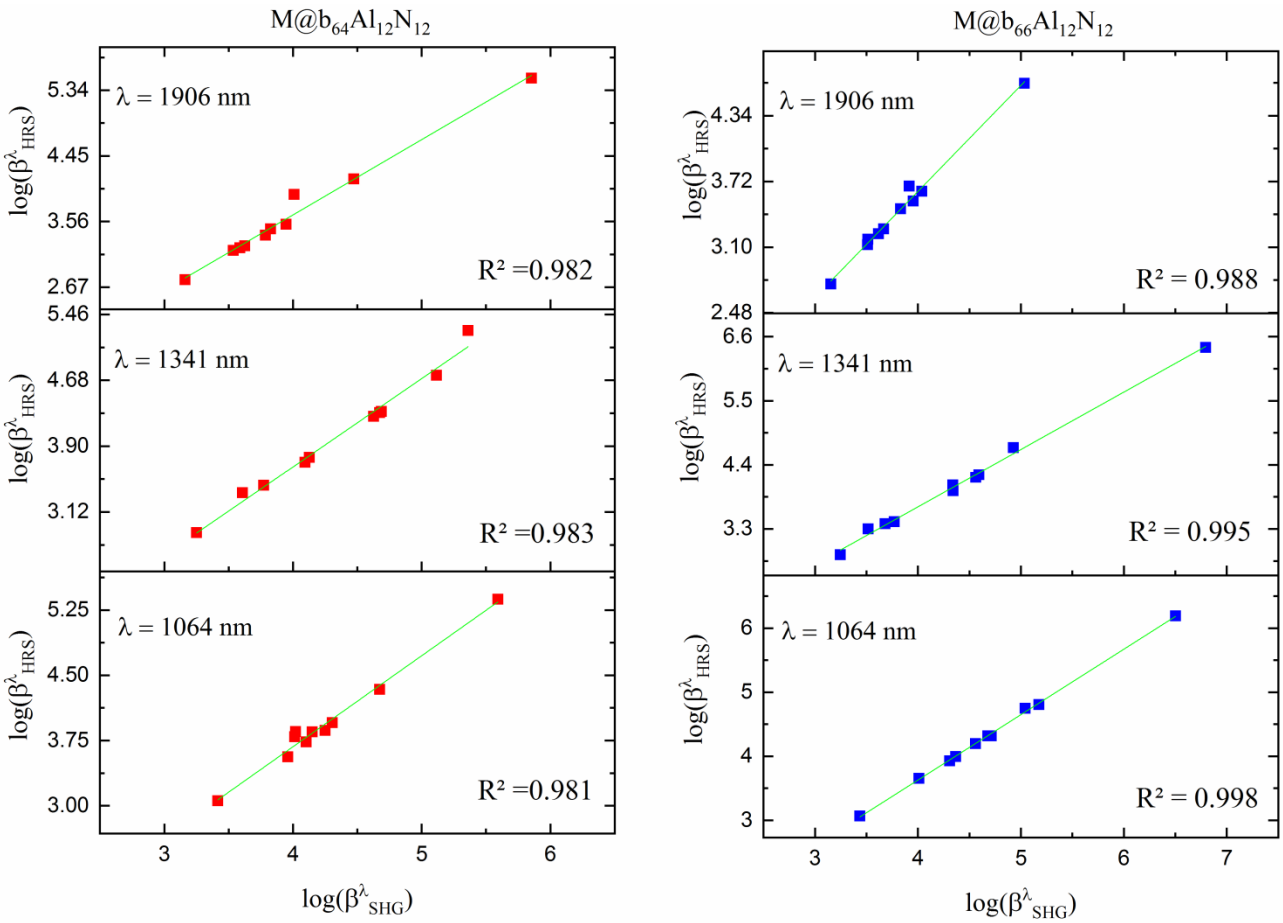

Figure S6.AI Plot of β^{λ}_{HRS} as a function of β^{λ}_{SHG} for $M@b_{64/66}Al_{12}N_{12}$, where M= Sc to Zn), 1906, 1341, and 1064 nm

Supporting information

Table S1.AII Selected geometrical parameters (the bond angles θ (º) and the bond length (Å)) of the [(*CoCp)₂ {B₂H₂S₂Pd(Cl)₂}*] obtained at the B3LYP, B3LYP-GD3(BJ) , ωB97XD, M06-2X and Cam-B3LYP methods and corresponding experimental data.

		MDS2					
		exp	B3LYP	B3LYP-GD3BJ	ωB97XD	M06-2X	Cam-B3LYP
Distance	Cp-Cp	6.529	6.581	6.495	6.443	6.643	6.481
	Co1-Co2	3.205	3.183	3.136	3.137	3.178	3.139
	B1-B2	1.684	1.687	1.680	1.686	1.711	1.684
	S-B	1.884	1.868	1.867	1.860	1.836	1.851
	Pd-Cl	2.330	2.324	2.312	2.300	2.300	2.298
	Pd-Co	2.802	2.887	2.824	2.818	2.895	2.852
	Pd-S	2.309	2.429	2.416	2.407	2.508	2.411
	Co-B	2.118	2.108	2.106	2.106	2.121	2.088
	Co-S	2.322	2.351	2.331	2.327	2.361	2.328
Angle	Co1-Pd-Co2	69.79	66.90	67.46	67.65	66.57	66.79
	S1-Pd-S2	86.70	83.82	84.86	84.88	82.73	84.16
	Co1-B2-Co2	98.0	98.0	96.27	96.27	97.10	97.45
	B1-S2-Pd	113.43	113.43	112.55	112.76	112.72	113.22
Torsion angle	Pd-B16-C13-C11	5.09	3.38	3.97	11.42	4.02	3.27

Table S2.AII Selected Bond Parameters (Distance in Å and Angles in deg) and Dipole moments (Debye) of MDSn and MDS'n

	MDS2	MDS'2	MDS3	MDS'3	MDS4	MDS4a	MDS'4	MDS5	MDS5a	MDS'5
μ	11.265	21.695	11.522	26.315	13.468	11.766	26.114	21.515	28.707	25.314
Pd − Co	2.922	2.684	2.895	2.700	2.973	2.772	2.668	2.848	3.234	2.645
B1-B2	1.711	1.688	1.700	1.684	1.714	1.701	1.688	1.718	1.699	1.701
Pd-Cl	2.300	2.383	2.318	2.397	2.301	2.320	3.375	2.294	2.396	2.355
Co-B	2.121	2.474	2.113	2.447	2.108	2.107	2.435	2.110	2.076	2.380
S1-S2	3.315	3.336	3.326	3.329	3.335	3.361	3.332	3.339	3.293	3.355
Co1-Pd-Co2	66.57	44.68	67.26	44.82	66.34	67.33	42.09	66.36	70.61	38.85
S1-Pd-S2	82.73	86.95	83.97	86.88	83.10	85.09	86.96	82.95	86.15	87.23
Co1-B2-Co2	97.10	13.21	98.47	14.06	66.34	98.93	14.10	96.59	104.68	17.95
B1-S2-Pd	112.72	108.47	111.27	108.79	111.87	110.24	108.91	111.98	105.42	108.65
Pd-Co*-Cp	122.89	102.58	114.46	97.45	119.80	125.11 116.58	102.40	118.66	103.57 150.54	109.06
Torsion angle	4.02	17.08	17.70	20.60	32.71	27.32	25.72	23.75	38.36	35.99
φ	93.53	/	82.34	/	87.41	95.56 84.56	/	86.93	70.84 121.80	/
φ'	/	57.09	/	54.14	/	/	58.64	/	/	65.75

Co1 and Co2: metal atom coordinated to the square planar arrangement of $[B_2S_2]$
Co*: metal atom coordinated to the square planar arrangement of $[B_2S_2]$

Table S3.AII HOMO/LUMO energy and Chemical potential (μ, eV), chemical hardness (η, eV) and electrophilicity index (ω, eV) of multi-decker sandwich cluster [(*CoCp)n {$B_2H_2S_2Pd(Cl)_2$}*], n=2 to 5

	E_{HOMO}	E_{LUMO}	μ	η	ω
MDS2	-7.865	-2.638	-5.2515	5.227	2.638
MDS'2	-7.033	-3.406	-5.2195	3.627	3.755
MDS3	-6.517	-2.586	-4.5515	3.931	2.634
MDS'3	-6.502	-3.641	-5.0719	2.861	4.494
MDS4	-5.357	-2.894	-4.1260	2.463	3.455
MDS4a	-6.120	-2.455	-4.2878	3.664	2.508
MDS'4	-5.603	-4.001	-4.8017	1.602	7.192
MDS5	-4.534	-3.270	-3.9022	1.263	6.023
MDS5a	-4.591	-3.465	-4.0285	1.126	7.201
MDS'5	-4.865	-4.301	-4.5833	0.563	18.638

Table S4.AII Molecular orbitals (MO) and electron density difference maps (EDDM) for the crucial excited states of MDSn , MDSna and MDS'n.

	S_n	$\Delta E_{0\rightarrow n}$	$\Delta\lambda_{0\rightarrow n}$	f	Excitation (% composition)	Character
MDS2	S_8	1.627	761.74	0.021	100 →101(HOMO→LUMO) **13 %** 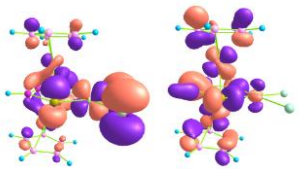	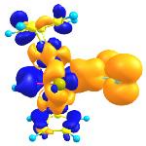
	S_{10}	2.074	597.64	0.001	97 →102(HOMO -3 →LUMO+1) **20 %** 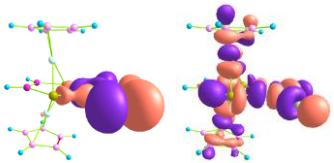	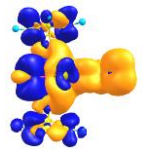
	S_{12}	2.23	556.24	<0.001	98→102 (HOMO-2 →LUMO+1) **23%** 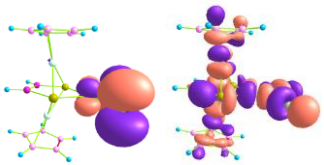	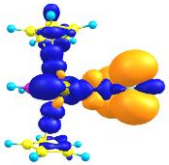
	S_{20}	3.076	403.01	0.137	100 →101 (HOMO →LUMO) **10%** 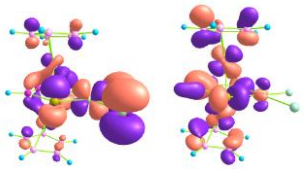	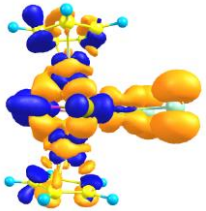

MDS'2	S_9	1.866	664.13	0.088	100 →101 (HOMO →LUMO) **23%** 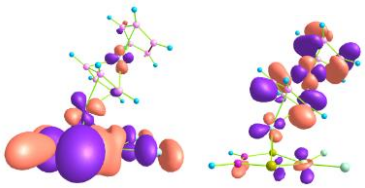	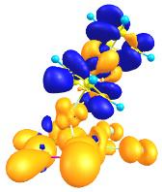
	S_{15}	2.26	546.70	0.018	98 →101 (HOMO-2 →LUMO) **30%** 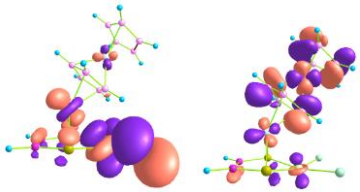	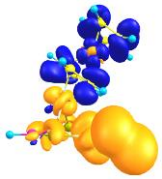
	S_{18}	2.611	474.84	0.051	93→101 (HOMO-7→LUMO) **12%** 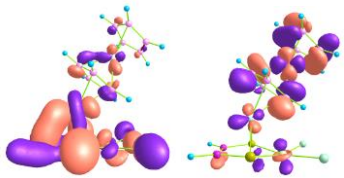 94→101(HOMO-6 →LUMO)**13%** 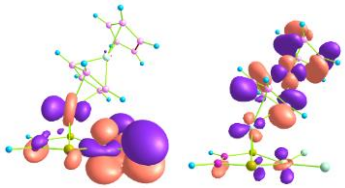	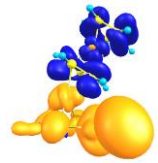
	S_{19}	2.626	472.08	<0.001	97 →101 (HOMO -3→LUMO) **40%** 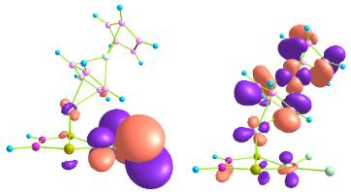	

MDS3	S_{12}	1.63	759.40	0.015	125 →128 (HOMO-1→LUMO+1) **10%** 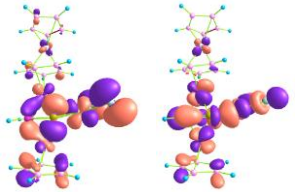	
	S_{14}	1.7157	722.66	0.261	126 →127 (HOMO →LUMO) **12%** 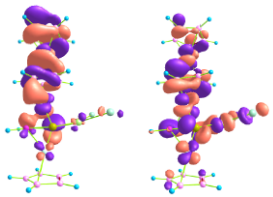	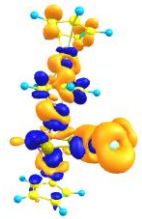
	S_{26}	2.9756	384.99	0.002	126 →129 (HOMO →LUMO+2)**10%** 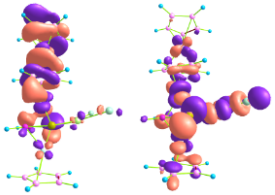	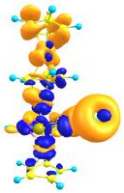
	S_{29}	3.2205	384.99	0.002	126 →129 (HOMO →LUMO+2) **18%** 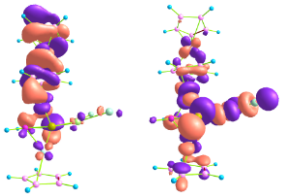	

MDS'3	S_5	0.661	1876.95	0.003	121 →128 (HOMO-5→LUMO+1) **10%** 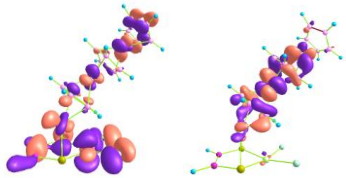	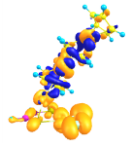
	S_{13}	1.451	854.55	0.426	126 →127 (HOMO →LUMO) **40%** 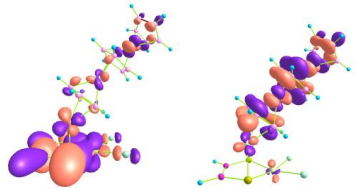	
	S_{14}	1.76	704.67	0.334	121 →127 (HOMO -5→LUMO) **11%** 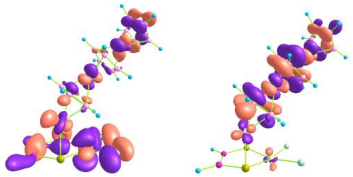	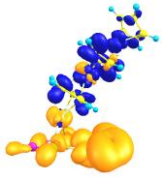
	S_{23}	2.28	541.94	<0.001	123 →127 (HOMO -3→LUMO) **41%** 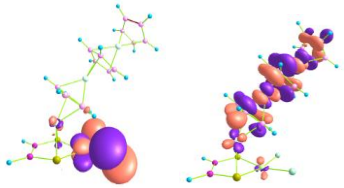	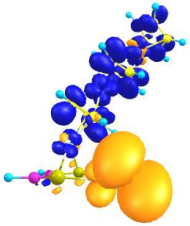

MDS4a	S_{14}	1.096	1130.64	0.007	152 →153 (HOMO →LUMO) **10%** 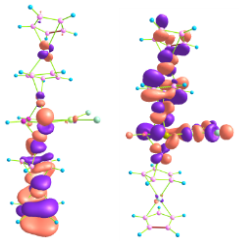	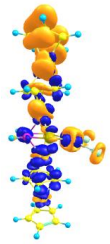
	S_{17}	1.59	779.73	0.384	150 →153 (HOMO -1→LUMO) **10%** 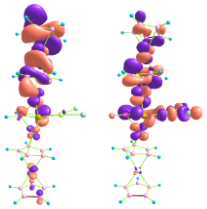	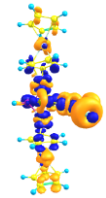
	S_{20}	1.75	705.13	0.408	151 →153 (HOMO -1→LUMO) **10%** 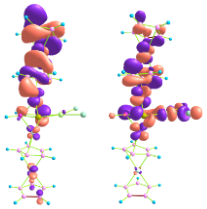	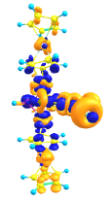
	S_{26}	2.18	566.82	0.05	152 →154 (HOMO →LUMO+1) **18%** 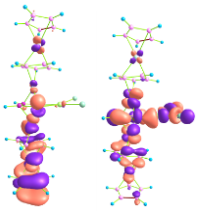	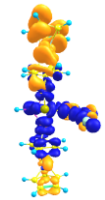

MDS4	S_{19}	1.5242	813.46	0.002	152 →153 (HOMO →LUMO) **36%** 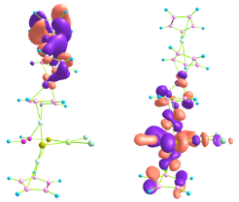	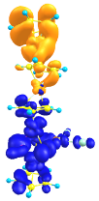
	S_{20}	1.58	780.98	<0.001	144 →154 (HOMO-8→LUMO+1) **12%** 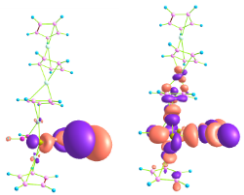	
	S_{25}	2.049	605.04	0.405	150 →153 (HOMO-2→LUMO) **10%** 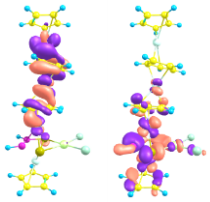	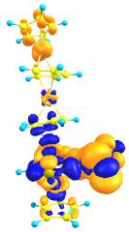
	S_{28}	2.30	539.05	0.003	152 →155 (HOMO →LUMO+2) **40%** 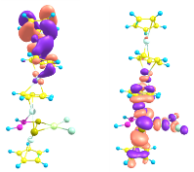	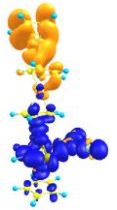

MDS'4	S_6	0.836	1380.64	0.098	152 →153 (HOMO →LUMO) **10%** 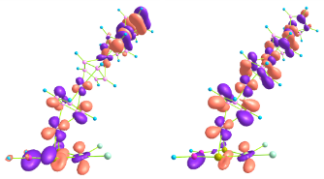	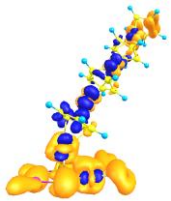
	S_{15}	1.147	1080.53	0.692	152 →153 (HOMO →LUMO) **33%** 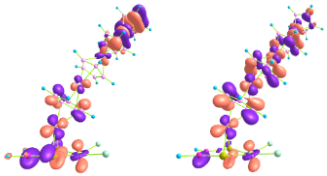	
	S_{18}	1.374	902.08	0.003	151 →153 (HOMO -1→LUMO) **46%** 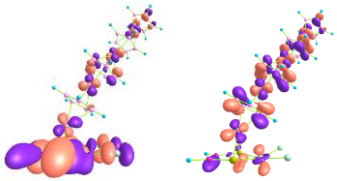	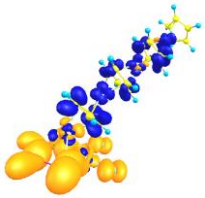
	S_{20}	1.701	728.95	0.003	150 →153 (HOMO-2 →LUMO) **43%** 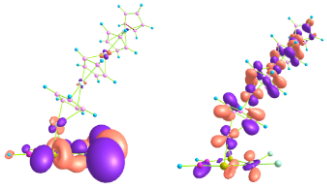	

MDS5	S_3	0.638	1942.02	0.001	178 →179 (HOMO →LUMO) **49%** 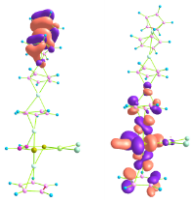	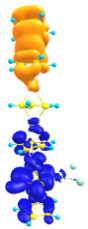
	S_{10}	0.901	1375.22	0.001	178 →180 (HOMO →LUMO+1) **47%** 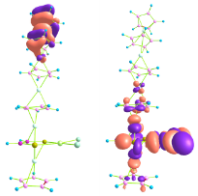	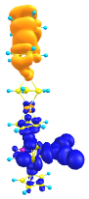
	S_{23}	1.516	817.67	0.002	178 →181 (HOMO →LUMO+2) **47%** 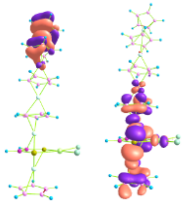	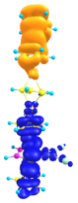
	S_{29}	1.845	671.82	0.017	177 →180 (HOMO-1 →LUMO+1) **39%** 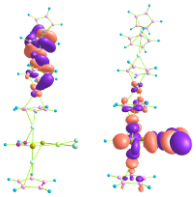	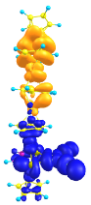

MDS'5	S_6	0.792	1566.12	<0.001	177 →179 (HOMO-1 →LUMO) **10%** 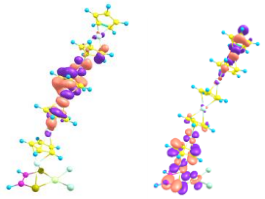	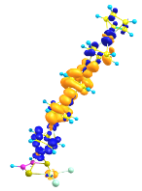
	S_{21}	1.228	1009.40	0.06	175 →179 (HOMO-3 →LUMO) **22%** 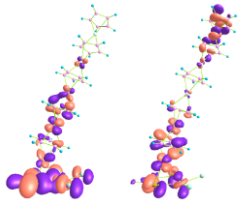	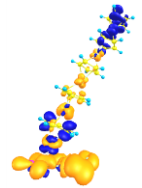
	S_{23}	1.397	912.70	<0.001	161 →179 (HOMO-17 →LUMO) **20%** 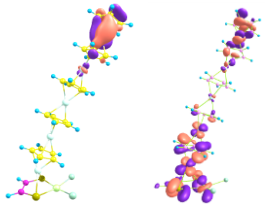	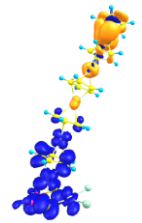
	S_{24}	1.397	887.04	0.22	175→179 (HOMO-3 →LUMO) **42%** 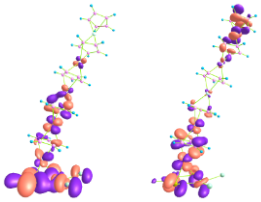	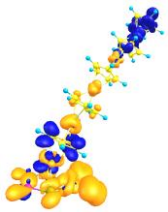

MDS5a	S_{10}	0.997	1243.56	<0.001	178→180(HOMO→LUMO+1) 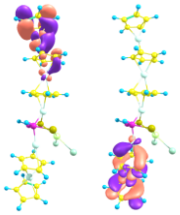	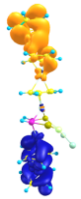
	S_{23}	1.629	761.12	0.0445	177 → 179 (HOMO-1→LUMO) 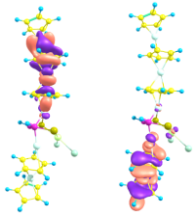	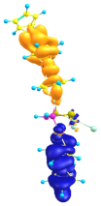
	S_{26}	1.907	650.09	0.0144	176 -> 179 (HOMO-2→LUMO) 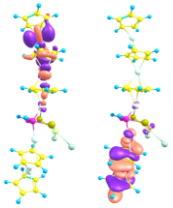	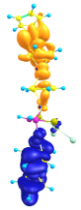
	S_{28}	2.013	615.89	0.0025	178 -> 181 (HOMO→LUMO+2) 40% 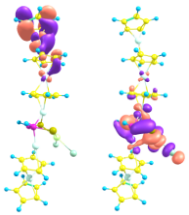	

Table S5.AII Excitation energy ($E_{0\rightarrow n}$, eV) and wavelength ($\lambda_{0\rightarrow n}$, nm), oscillator strengths ($f_{0\rightarrow n}$, dimensionless), variation in dipole moment between the ground and the excited states ($\Delta\mu_{CT}$, a.u), $S_r(r)$ overlap, charge transfer length (D_{CT}, Å), RMSD of hole and electron (Å), H and t indexes (Å) associated to the $S_0 \rightarrow S_n$ transition, as calculated at the M06-2X/ SDD/6-311G(d) of the studied compounds MDSn, MDSna and MDS'n.

	$S_{0\rightarrow n}$	$\Delta E_{0\rightarrow n}$	$\Delta\lambda_{0\rightarrow n}$	$f_{0\rightarrow n}$	Integral of hole	Integral of electron	$\Delta\mu_{CT}$	Sr	D_{CT}	RMSD hole	RMSD electron	H index	t index
MDS2	$S_{0\rightarrow 8}$	1.627	761.74	0.021	0.502	0.502	2.034	**0.643**	2.145	2.467	2.420	2.443	0.770
	$S_{0\rightarrow 10}$	2.074	597.64	0.001	0.947	0.956	3.436	**0.743**	1.923	2.788	2.354	2.571	0.475
	$S_{0\rightarrow 12}$	2.229	556.24	<0.001	0.604	0.609	3.293	**0.421**	2.884	2.454	2.125	2.289	1.712
	$S_{0\rightarrow 20}$	3.076	403.01	0.137	0.994	0.998	3.177	**0.537**	1.687	2.489	2.565	2.527	0.003
MDS'2	$S_{0\rightarrow 9}$	1.866	664.13	0.088	0.632	0.636	3.537	**0.712**	2.960	2.360	3.164	2.762	0.842
	$S_{0\rightarrow 15}$	2.267	546.70	0.018	0.800	0.803	6.855	**0.179**	4.534	2.090	2.330	2.210	3.262
	$S_{0\rightarrow 18}$	2.611	474.84	0.051	0.775	0.775	6.547	**0.171**	4.471	2.032	2.475	2.254	3.227
	$S_{0\rightarrow 19}$	2.626	472.08	<0.001	0.846	0.848	7.118	**0.233**	4.451	2.364	2.304	2.334	3.001
MDS3	$S_{0\rightarrow 12}$	1.632	759.40	0.015	0.423	0.424	1.096	**0.900**	1.373	2.842	3.248	3.045	-0.308
	$S_{0\rightarrow 14}$	1.715	722.66	0.261	0.359	0.359	0.863	**0.929**	1.273	2.999	3.092	3.046	-1.011
	$S_{0\rightarrow 26}$	3.220	384.99	0.002	0.420	0.421	1.952	**0.832**	2.459	2.799	3.717	3.258	0.054
	$S_{0\rightarrow 29}$	3.2205	384.99	0.002	0.438	0.440	2.876	**0.773**	3.476	3.029	3.434	3.232	0.870
MDS'3	$S_{0\rightarrow 5}$	0.661	1876.95	0.003	0.520	0.528	2.657	**0.722**	2.706	2.409	3.661	3.035	0.274
	$S_{0\rightarrow 13}$	1.451	854.55	0.426	0.597	0.598	6.605	**0.252**	5.858	2.539	2.461	2.500	4.032
	$S_{0\rightarrow 14}$	1.759	704.67	0.334	0.518	0.524	5.192	**0.304**	5.305	2.526	2.855	2.691	3.431
	$S_{0\rightarrow 23}$	2.287	541.94	<0.001	0.801	0.806	8.159	**0.179**	5.392	2.947	2.353	2.650	3.624
MDS4a	$S_{0\rightarrow 14}$	1.096	1130.64	0.007	0.458	0.458	3.643	**0.786**	4.207	3.799	3.943	3.871	0.840
	$S_{0\rightarrow 18}$	1.685	735.60	0.105	0.427	0.424	1.617	**0.807**	2.002	3.049	3.343	3.196	0.382
	$S_{0\rightarrow 20}$	1.758	705.13	0.408	0.403	0.400	1.021	**0.878**	1.341	2.904	4.224	3.564	-0.866

	$S_{0\to26}$	2.187	**566.82**	**0.05**	**0.544**	**0.539**	**4.044**	**0.710**	**3.937**	**2.764**	4.871	3.817	0.627
MDS4	$S_{0\to19}$	1.524	813.46	**0.002**	**0.844**	**0.843**	**14.926**	**0.051**	**9.359**	2.677	2.195	2.436	7.408
	$S_{0\to20}$	1.587	780.98	<0.001	0.633	0.637	3.563	**0.438**	2.981	2.800	2.288	2.544	1.696
	$S_{0\to25}$	2.049	605.04	0.405	0.493	0.494	2.007	**0.786**	2.153	2.769	4.852	3.810	-0.796
	$S_{0\to28}$	2.300	539.05	0.003	0.832	0.833	14.262	**0.06**	9.071	2.761	2.489	2.625	7.113
MDS'4	$S_{0\to6}$	0.898	1380.64	0.098	0.522	0.519	2.275	**0.884**	2.307	4.447	5.836	5.141	-2.027
	$S_{0\to15}$	1.147	1080.53	0.692	0.424	0.426	2.299	**0.822**	2.871	3.816	6.112	4.964	-1.440
	$S_{0\to18}$	1.374	902.08	0.003	0.501	0.504	5.716	**0.553**	6.041	3.987	3.563	3.775	2.867
	$S_{0\to20}$	1.701	728.95	0.003	0.848	0.851	10.374	**0.174**	6.475	4.255	2.404	3.329	4.180
MDS5	$S_{0\to3}$	0.638	1942.02	0.001	0.982	0.992	24.438	**0.002**	13.167	2.557	2.078	2.318	11.273
	$S_{0\to10}$	0.901	1375.22	0.001	0.957	0.961	23.220	**0.002**	12.845	2.953	2.217	2.585	10.952
	$S_{0\to23}$	1.516	817.67	0.002	0.951	0.961	23.187	**0.008**	12.908	2.848	2.170	2.509	10.825
	$S_{0\to29}$	1.845	671.82	0.017	0.947	0.974	18.024	**0.026**	10.074	2.780	2.358	2.569	8.144
MDS'5	$S_{0\to6}$	0.791	1566.12	<0.001	0.619	0.638	1.852	**0.499**	1.583	1.852	4.707	5.098	-3.054
	$S_{0\to21}$	1.228	1009.40	0.06	0.492	0.499	6.321	**0.746**	6.804	7.598	4.458	6.028	1.209
	$S_{0\to23}$	1.358	912.70	<0.001	0.748	0.784	16.414	**0.209**	11.608	5.867	2.036	3.951	7.887
	$S_{0\to24}$	1.397	887.04	0.22	0.514	0.523	6.634	**0.724**	6.826	7.724	4.552	6.138	1.134
MDS5a	$S_{0\to10}$	0.997	1243.56	<0.001	0.980	-0.985	27.388	**0.0001**	14.794	2.140	2.126	2.133	13.052
	$S_{0\to23}$	1.629	761.12	0.0445	0.863	-0.874	18.776	**0.0619**	11.508	2.395	3.311	2.853	**9.030**
	$S_{0\to26}$	1.907	650.09	0.0144	0.940	-0.951	22.778	**0.008**	12.818	2.249	2.535	2.392	10.728
	$S_{0\to28}$	2.013	615.89	0.0025	0.905	-0.897	17.194	**0.062**	10.058	3.070	2.634	2.852	7.858

Table S6.AII Static and dynamic of polarizability, anisotropy of polarizability and electro-optic Pockel's effect (EOPE, β_{EOPE}) of MDSn, MDSna and MDS'n.

		MDS2	MDS'2	MDS3	MDS'3	MDS4a	MDS4	MDS'4	MDS5	MDS'5	MDS5a
ω=0	α (0;0)	282	323	500	599	754	580	1245	1532	2154	648
	Δα (0;0)	96	201	585	879	1192	668	2640	3417	5190	732
ω= 0.0428	α (-ω;ω)	296	362	626	1094	1058	670	1301	1.14×10^{4}	841	734
	Δα (-ω;ω)	127	297	946	2337	2086	920	2579	1.77×10^{4}	1284	967
	β^{ω}_{EOPE}	1131	4.31×10^{4}	19879	5.43×10^{5}	1.99×10^{5}	1.76×10^{5}	2.61×10^{6}	9.48×10^{7}	1.56×10^{6}	2.13×10^{5}
ω= 0.034	α (-ω;ω)	289	343	562	769	914	631	8528	1263	795	692
	Δα (-ω;ω)	111	250	764	1375	1662	817	2.44×10^{4}	2640	1090	852
	β^{ω}_{EOPE}	1071	2.83×10^{4}	1.39×10^{4}	1.43×10^{5}	1.06×10^{5}	1.12×10^{5}	2.42×10^{7}	3.01×10^{7}	5.55×10^{4}	1.38×10^{5}
ω= 0.0239	α (-ω;ω)	276	331	526	660	812	590	1868	1891	703	664
	Δα (-ω;ω)	116	222	659	1057	1365	692	4500	4496	831	776
	β^{ω}_{EOPE}	2.15×10^{4}	2.08×10^{4}	1.13×10^{4}	7.21×10^{4}	5.57×10^{4}	8.91×10^{4}	4.01×10^{5}	1.46×10^{6}	4.99×10^{4}	1.15×10^{5}

Table S7.**AII** Static and dynamic of $\beta_{J=1}$ and $\beta_{J=3}$ of MDSn, MDSna and MDS'n.

		MDS2	MDS'2	MDS3	MDS'3	MDS4a	MDS4	MDS'4	MDS5	MDS'5	MDS5a
λ=∞	$\beta_{J=1}$	669	1.26×10^{4}	6959	3.49×10^{4}	3.23×10^{4}	5.37×10^{4}	5.58×10^{4}	2.75×10^{5}	1.88×10^{4}	6.71×10^{4}
	$\beta_{J=3}$	603	1.01×10^{4}	5404	2.97×10^{4}	2.71×10^{4}	4.33×10^{4}	4.65×10^{4}	2.25×10^{5}	1.93×10^{4}	5.28×10^{4}
λ=1064	$\beta_{J=1}$	1828	3.45×10^{4}	4.41×10^{4}	/	/	4.68×10^{4}	7.43×10^{5}	5.11×10^{8}	/	2.36×10^{4}
	$\beta_{J=3}$	2270	3.31×10^{4}	4.03×10^{4}	4.25×10^{5}	2.09×10^{5}	5.20×10^{4}	6.54×10^{5}	4.32×10^{8}	4.78×10^{5}	9.01×10^{4}
λ=1341	$\beta_{J=1}$	/	5.55×10^{6}	7.66×10^{4}	1.34×10^{5}	9.51×10^{4}	2.90×10^{5}	1.19×10^{8}	8.58×10^{6}	9.32×10^{4}	3.57×10^{6}
	$\beta_{J=3}$	3309	4.51×10^{6}	6.46×10^{4}	1.37×10^{5}	1.29×10^{5}	2.24×10^{5}	1.21×10^{8}	7.05×10^{6}	5.93×10^{4}	3.87×10^{6}
λ=1906	$\beta_{J=1}$	/	3.14×10^{4}	1.34×10^{4}	5.76×10^{5}	6.50×10^{4}	/	2.38×10^{6}	9.68×10^{5}	2.76×10^{5}	1.63×10^{5}
	$\beta_{J=3}$	1.03×10^{5}	2.44×10^{4}	9977	4.89×10^{5}	5.80×10^{4}	3.46×10^{5}	2.41×10^{6}	7.97×10^{5}	2.22×10^{5}	1.30×10^{5}

Table S8.AII Static and dynamic first hyperpolarizability (au) and depolarization ratio (DR) for MDSn, MDSna and MDS'n (n=2-5) calculated by the sum-over-states method.

	MDS2	MDS'2	MDS3	MDS'3	MDS4	MDS4a	MDS'4	MDS5	MDS5a	MDS'5
DR^{SOS}	6.10	5.48	4.89	4.84	5.01	4.83	4.70	5.00	5.23	4.98
β_{HRS}^{SOS}	860	1.17×10^{4}	1.03×10^{4}	3.07×10^{4}	2.93×10^{4}	7.97×10^{3}	2.12×10^{5}	4.81×10^{5}	3.83×10^{4}	5.83×10^{7}

Liste of figures

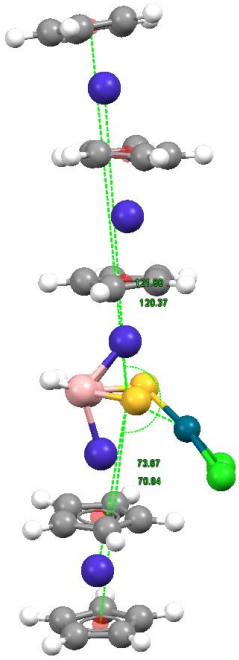

Figure. S1.AII The bond angles φ of MDS5a cluster

MDS5

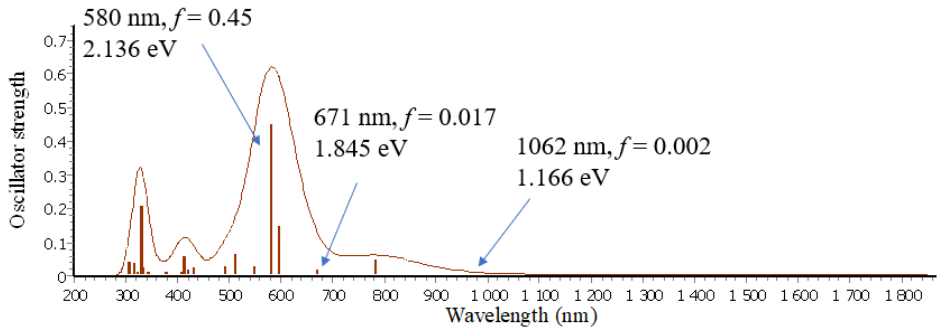

MDS'5

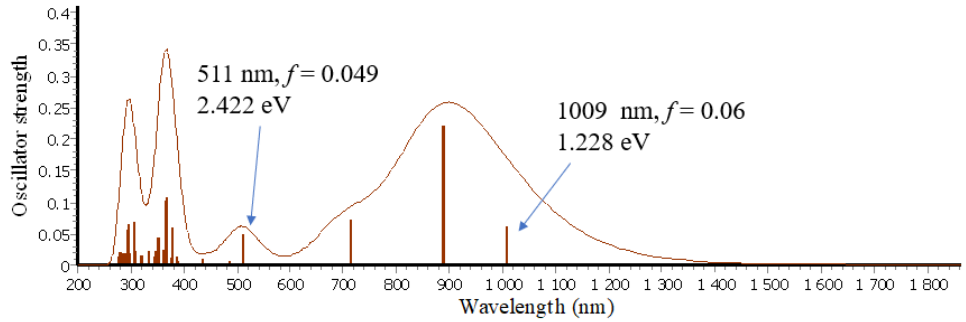

MDS4a

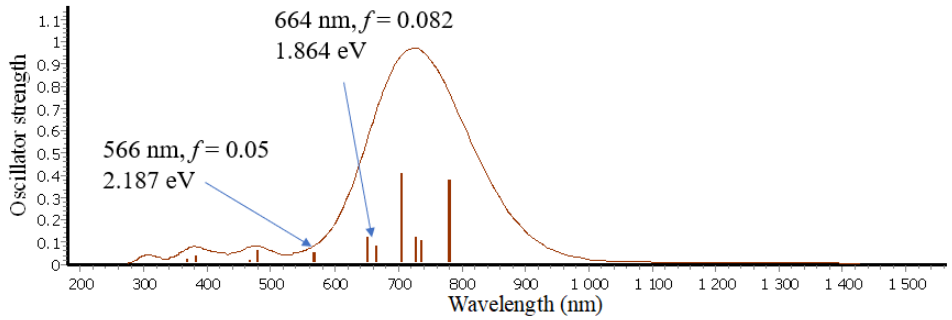

MDS5a

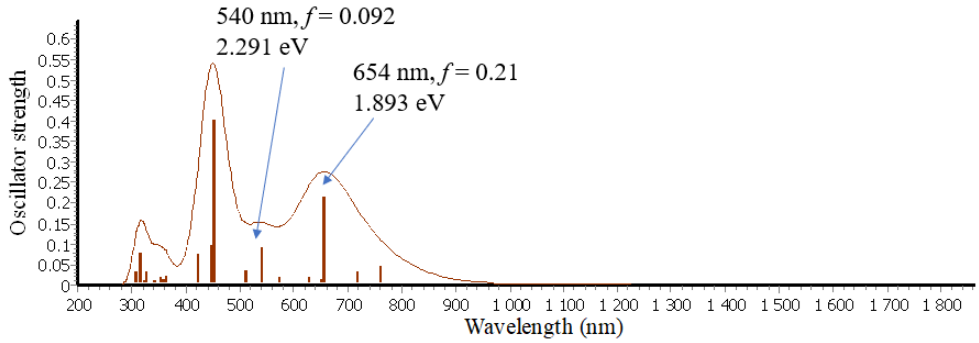

Figure S2.AII Simulated absorption spectrum of MDSn, MDSna and MDS'n (n= 4 and 5) .

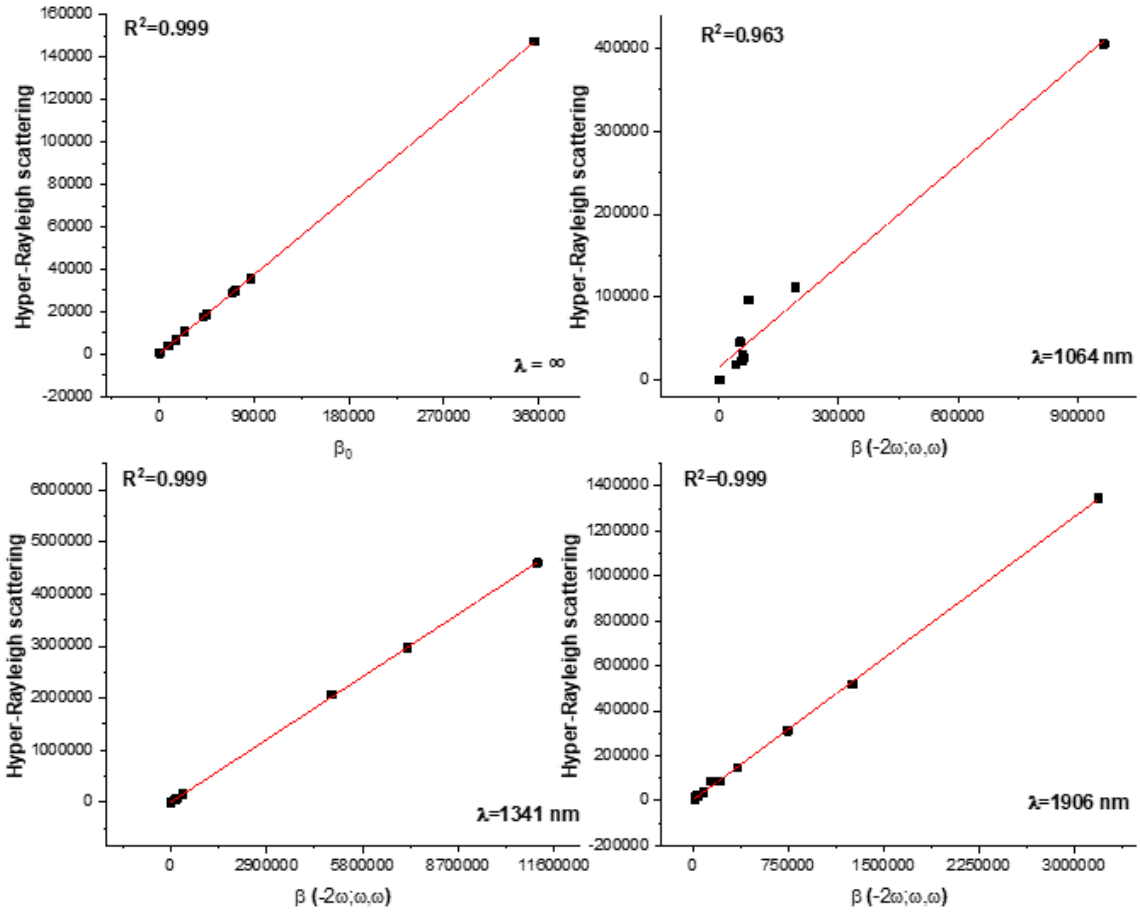

Figure S3.AII Correlation between the Hyper-Rayleigh scattering and dynamic second order NLO responses of MDSn, MDSna and MDS'n.

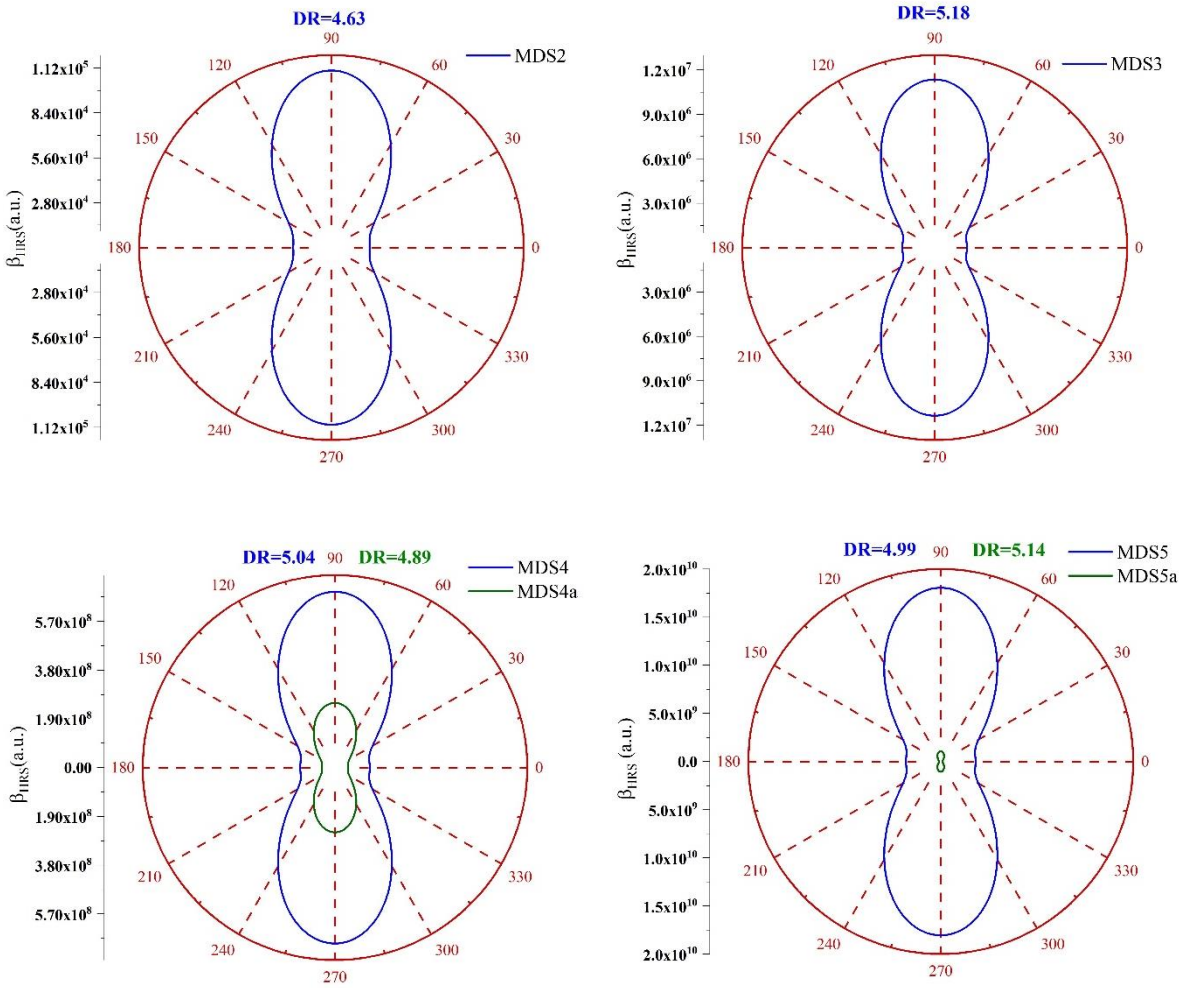

Figure S4.AII. Relationship between $I_{\Psi V}^{2w}$ and polarization angle Ψ of MDSn and MDSna complexes

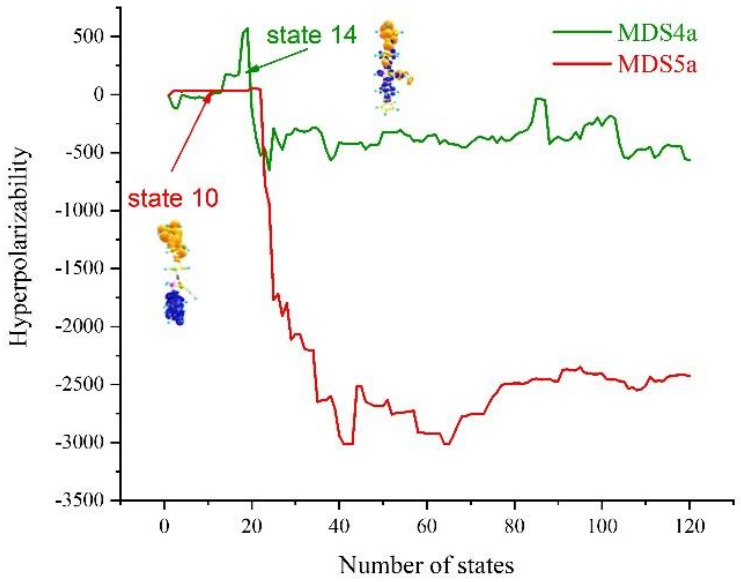

Figure. S5.AII Plots of static first hyperpolarizability values as computed in the SOS formalism as a function of the number of excited states for MDS4a and MDS5a, obtained at M06-2X/ SDD/6-311G(d) level.

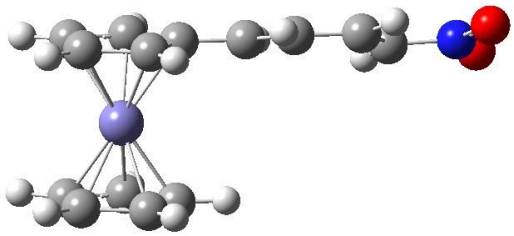

Figure. S6.AII The optimized geometry of $FeCp_2$-$(C_2H_2)_3$-NO_2

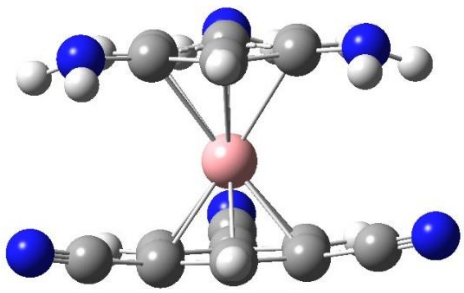

Figure. S7.AII The optimized geometry of $3NH_2$-VBz_2-3CN

NJC

ROYAL SOCIETY OF CHEMISTRY

PAPER

Cite this: *New J. Chem.*, 2024, **48**, 11812

Understanding the second and third order nonlinear optical responses of M@$b_{66/64}Al_{12}N_{12}$: a comprehensive DFT and TD-DFT study†

Meriem Zaidi, [ab] Douniazed Hannachi, *[cd] Nahla Chaoui[a] and Henry Chermette *[e]

Materials with significant first hyperpolarizability values are essential for application in second harmonic generation to achieve frequency doubling. Therefore, ideal NLO materials must not only exhibit a substantial NLO response but also maintain transparency when exposed to laser light. In this study, we investigate two series of nanoparticles, namely M@$b_{64}Al_{12}N_{12}$ and M@$b_{66}Al_{12}N_{12}$ (M ranges from Sc to Zn). The aim is to evaluate the second and third NLO responses through DFT and TD-DFT calculations. These evaluations are performed using the CAM-B3LYP/6-311+G(d) level of theory and the sum-over-states method in the static and dynamic regime ($\lambda = \infty$, 1906, 1341, and 1064 nm). These properties are further explained by considering factors such as molecular topology, delocalization indices, Waber–Cromer radius, excitation energy, oscillator strengths, variations of dipole moment of the excited state, and one/two-photon resonance effects. The results indicate that incorporating transition metals into $Al_{12}N_{12}$ substantially increases both the first and second hyperpolarizability. The delocalization index values reveal a higher degree of electron delocalization between the transition metal and nitrogen compared to that between the transition metal and aluminum. The QTAIM analysis displays that the presence of a closed quasi-ring structure between the metal and the nanocage, combined with electron delocalization, significantly enhances the first hyperpolarizability. TD-DFT calculations suggest potential application of these compounds in deep ultraviolet laser devices due to their transparency below 200 nm. The SOS approach reveals that the most critical excited states are local excitations, characterized by high S_r, small D, and negative t values. On the other hand, in the dynamic regime, our results indicated that the values of β_{HRS}, $\beta_{SHG}(-2\omega; \omega, \omega)$ and $\gamma_{ESHG}(-2\omega; \omega, \omega, 0)$ are larger than their static counterparts. Additionally, one/two photon resonance energy, along with substantial oscillator strength, plays a pivotal role in enhancing the dynamic hyperpolarizability of the investigated nanoparticles. Our findings suggest that the increase in β^{λ} is primarily linked to two-photon resonance rather than one-photon resonance. Based on our current understanding, this study provides novel evidence that, at $\lambda = \infty$, the first hyperpolarizability of M@$b_{64/66}Al_{12}N_{12}$ is correlated with the Waber–Cromer radius of the transition metal. Additionally, in the dynamic regime, the first hyperpolarizability is correlated with the second hyperpolarizability.

Received 22nd April 2024,
Accepted 29th May 2024

DOI: 10.1039/d4nj01849d

rsc.li/njc

Introduction

Nonlinear optics (NLO) is a branch of science that deals with the interaction of materials with strong oscillating electromagnetic fields, resulting in the generation of new electromagnetic fields with different phase, amplitude, frequency, and other optical properties from the incident ones.[1,2]

When light propagates through a molecule, the valence electrons create a charge transfer relative to the atoms in the compound under the action of the induced electric field, resulting in the polarization of matter (P). The integration of first-principles methodologies with the finite-field (FF) approach is extensively utilized in the exploration of nonlinear optical responses due to

[a] *Département de chimie, Faculté des Sciences, Université Ferhat Abbas, Setif-1, Algérie, Algeria*
[b] *Laboratoire de Chimie, Ingénierie Moléculaire et Nanostructures (LCIMN), Université Ferhat Abbas, Sétif 1, Sétif 19000, Algeria*
[c] *Laboratoire d'Électrochimie, d'Ingénierie Moléculaire et de Catalyse Redox (LEIMCR), Département d'Enseignement de Base en Technologie, Faculté de Technologie, Université Ferhat Abbas, Sétif-1, Algeria. E-mail: h_douniazed@yahoo.fr*
[d] *Département de Chimie, Faculté des Sciences de la Matière, Université de Batna-1, Algeria*
[e] *Université de Lyon, Université Claude Bernard Lyon 1, Institut des Sciences Analytiques, UMR CNRS 5280, 69622 Villeurbanne Cedex, France. E-mail: Henry.chermette@univ-lyon1.fr*

† Electronic supplementary information (ESI) available. See DOI: https://doi.org/10.1039/d4nj01849d

Journal of Photochemistry & Photobiology, A: Chemistry 469 (2025) 116523

Contents lists available at ScienceDirect

Journal of Photochemistry & Photobiology, A: Chemistry

journal homepage: www.elsevier.com/locate/jphotochem

Predicting and controlling the second-order NLO response in a new class of multi-decker sandwich clusters {μ-$B_2H_2S_2Pd(Cl)_2$}-$(CoCp)_n$, (n = 2 to 5)

Meriem Zaidi [a,b], Douniazed Hannachi [c,d,*], Djamila Samsar [e], Guillaume Hoffmann [f], Henry Chermette [f,*]

[a] Département de chimie, Faculté des Sciences, Université Ferhat Abbas, Setif-1, Algeria
[b] Laboratoire de Chimie, Ingénierie Moléculaire et Nanostructures (LCIMN), Université Ferhat Abbas Sétif 1, Sétif 19000, Algeria
[c] Laboratory of Electrochemistry, Molecular Engineering and Redox Catalysis, Faculty of Technology, Setif 1 University-Ferhat Abbas, Setif 19137, Algeria
[d] Département de Chimie, Faculté des Sciences de la Matière, Université de Batna-1, Algeria
[e] Institut D'Hygiène et Sécurité Industrielle, Département de Socle commun Hygiène et Sécurité Industrielle, Université de Batna-2, Algeria
[f] Université de Lyon, Université Claude Bernard Lyon 1, Institut des Sciences Analytiques, UMR CNRS 5280, 69622 Villeurbanne Cedex, France

ARTICLE INFO

Keywords:
Multi-decker
Cluster
NLO
Static
Dynamic

ABSTRACT

Using density functional theory calculations, we have conducted a systematic investigation of the nonlinear optical properties of a series of multi-decker sandwich clusters, [{$H_2B_2S_2Pd(Cl)_2$}-$(CoCp)_n$] (n = 2 to 5), which vary in structural configuration, shape and size namely MDSn, MDSna and MDS'n. The analysis encompassed polarizability, anisotropy of polarizability, and first-order hyperpolarizability, providing detailed insights into their geometric structure, stability, electronic properties, and absorption spectra. A comprehensive evaluation was performed to assess the impact of the {$H_2B_2S_2Pd(Cl)_2$} fragment's positioning, the number of (CoCp) units, and the incident frequency (ω = 0, 0.0428, 0.034, 0.0239 a.u.) on their first and second-order NLO responses. The results indicate that these clusters exhibit a significant NLO response, which is further amplified under an external electric field. Notably, the first hyperpolarizability (β) of the MDS'n series increases with the number of (CoCp) units (n = 2 to 4). However, a decrease in β is observed when the (CoCp) unit count reaches 5. Conversely, for MDSn (n = 2 to 5), first hyperpolarizability consistently rises with the number of (CoCp) units from n = 2 to 5, reflecting behavior akin to traditional push–pull π-systems. These findings underscore that the design of multi-decker sandwich clusters is a highly effective strategy for enhancing second-order NLO responses, primarily due to efficient charge transfer across the layered structure.

1. Introduction

Nonlinear optics is a subdiscipline of optics in which focuses on materials that can strongly interact with the electric field of incident laser radiation and generate nonlinear optical (NLO) responses which have grown significantly in scientific and technological domains [1–5]. The strength of light-matter interaction is much more intense than that typically encountered in linear optics. It provides fundamental theories and principles of devices for laser radiation in the visible, ultraviolet and infrared spectral ranges. The origins of modern nonlinear optics are often attributed to the experimental demonstration of second-harmonic generation (SHG) by Franken et al [6]. The pivotal advancement enabling this breakthrough was the invention of the first laser by Maiman and Collins in 1960 [7,8].

Nonlinear optical (NLO) materials are compounds that demonstrate NLO phenomena, such as second-harmonic generation (SHG) and third-harmonic generation (THG). These materials are indispensable in various applications, including optical communications, optical computing, optical memory and laser technology. Additionally, they are crucial in photopharmacology, photoactuators, controlled drug transport and release etc. In this context, numerous strategies and techniques have been proposed to enhance and tune the NLO response of materials. These include reinforcing [9] push–pull effects [10–14], designing octupolar compounds [15,16] and creating asymmetric coordination complexes [17,18]. Other promising approaches include introducing diffuse excess electrons [19], employing multi-decker sandwich clusters

* Corresponding authors at: Laboratory of Electrochemistry, Molecular Engineering and Redox Catalysis, Faculty of Technology, Setif 1 University-Ferhat Abbas, Setif 19137, Algeria.
E-mail addresses: h_douniazed@yahoo.fr (D. Hannachi), henry.chermette@univ-lyon1.fr (H. Chermette).

https://doi.org/10.1016/j.jphotochem.2025.116523
Received 4 March 2025; Received in revised form 17 May 2025; Accepted 25 May 2025
Available online 30 May 2025

NJC

ROYAL SOCIETY OF CHEMISTRY

PAPER

Cite this: *New J. Chem.*, 2023, **47**, 18359

The effect of resonance-assisted hydrogen bond on the second-order nonlinear optical properties of pyridine hydrazone photoswitches: a quantum chemistry investigation†

Douniazed Hannachi, *[ab] Noureddine Khelfaoui,[a] Meriem Zaidi, [ac] Diha Yahiaoui,[a] Salima Lakehal, [d] Christophe Morell [e] and Henry Chermette *[e]

The effect of hydrogen bonds on the NLO properties was not considered as essential, in particular in pyridine hydrazone systems. Yet, we show in the present study that a control of these photoswitches depends on the strength of hydrogen bonds. In this study, we investigate a selection of 18 *E*/*Z* pyridine hydrazone photoswitch molecules to explore the impact of resonance-assisted hydrogen bond (RAHB) on the NLO properties in the *E*/*Z* isomers. Using quantum calculations at the ωB97XD/6-311+g(d) level of theory, we determine various electronic parameters, reactivity descriptors, bond length alternation (BLA) values, nuclear independent chemical shift (NICS) aromaticity indices, QTAIM topology, energy of hydrogen bond (E_{HB}), RAHB, and linear and nonlinear optical properties for these molecules. The agreement between the quantum calculations and experimental spectra is illustrated through TD-DFT calculations, showing small deviations. Contrary to conventional expectations, our findings demonstrated that the delocalization strength of the electrons and NLO properties of the *Z* isomers are significantly enhanced by the presence of a resonance-assisted hydrogen bond. The *Z*-isomer exhibited a lower excited state energy, weaker energy gap, smaller BLA value, larger dipole moment variations for the first excited state, higher $\Phi_{E\rightarrow Z}$, and electron delocalization at the quasi-cycle closed (RAHB) compared to the *E*-isomer. Furthermore, we find that the hyperpolarizability value of the title photoswitches increases as the wavelength of the incident light decreases, *i.e.*, β(695) > β(1064) > β(1340) > β(∞), and the dispersion has less effect at λ = 1064 and 1340 nm. Additionally, we observe a strong relation between the photoisomerization quantum yield ($\Phi_{E\rightleftarrows Z}$) and static hyperpolarizability (β) of the first and second isomer, where $\Phi_{E\rightleftarrows Z}$ is proportional to β of the second isomer and inversely proportional to *b* of the first isomer. This inverse trend between static hyperpolarizability and photoisomerization quantum yields is attributed to the electron-withdrawing character of substituents on the Ar ring. Our research provides valuable insights into optimizing the 2nd-order NLO properties of pyridine hydrazone photoswitch molecules. By understanding the influence of hydrogen bonding on the delocalization strength of the electrons (RAHB) and the shape-dependent NLO performance, we gain the ability to design and synthesize novel photoswitch molecules with enhanced NLO characteristics.

Received 20th June 2023,
Accepted 4th September 2023

DOI: 10.1039/d3nj02848h

rsc.li/njc

[a] *Laboratoire d'Électrochimie, d'Ingénierie Moléculaire et de Catalyse Redox (LEIMCR), Département d'Enseignement de Base en Technologie, Faculté de Technologie, Université Ferhat Abbas, Sétif-1, Algeria. E-mail: douniazed_hannachi@univ-setif.dz*

[b] *Département de Chimie, Faculté des Sciences, Université Ferhat Abbas, Setif-1, Algeria*

[c] *Laboratoire de Chimie, Ingénierie Moléculaire et Nanostructures (LCIMN), Université Ferhat Abbas Sétif 1, Sétif 19000, Algeria*

[d] *Institut des Science de la Terre et de l'Univers, Université de Batna-2, Algeria*

[e] *Université de Lyon, Université Claude Bernard Lyon 1, Institut des Sciences Analytiques, UMR CNRS 5280, 69622 Villeurbanne Cedex, France. E-mail: henry.chermette@univ-lyon1.fr*

† Electronic supplementary information (ESI) available. See DOI: https://doi.org/10.1039/d3nj02848h

Introduction

Molecular photoswitches are defined as chemical compounds that can reversibly be transformed from one isomer into another one with light irradiation. The two isomers differ from each other in various chemical and physical properties, such as geometrical structure, absorption spectra, oxidation/reduction potentials, magnetic properties, dielectric constant, refractive index, and others.[1,2] This kind of molecules provides an invaluable tool for a large variety of applications, such as in information storage and processing,[3] photo-pharmacology,

Inorganic Chemistry

pubs.acs.org/IC

Article

Correlation between Second Ionization Potential and Nonlinear Optical Properties of Bivalent Transition-Metal Complexes: A Quantum Chemical Study

Meriem Zaidi, Douniazed Hannachi,* and Henry Chermette*

Cite This: https://doi.org/10.1021/acs.inorgchem.1c00412

Read Online

ACCESS | Metrics & More | Article Recommendations | Supporting Information

ABSTRACT: Discovering new materials with excellent nonlinear optical responses has recently become a very interesting research topic in the different domains of materials science. Currently, density functional theory (DFT) has been shown to be a powerful tool in the explanation and prediction of the performance of novel nonlinear optical (NLO) materials. Quantum chemical calculations using DFT/TD-DFT with the B3LYP exchange−correlation functional are reported to study the NLO properties of 26 bivalent transition-metal (TM) complexed by six acyclic hexadentate ligands providing pyridyl/pyrazine−amide-thioether/ether coordination and differing by the nature of the methylene dichalcogenate spacer between the rings. However, the geometry parameters and the theoretically predicted UV−vis absorption spectra of the optimized compounds M(II)L^{i} are in excellent agreement with the experiment, when available, the trends among the nature of the TM, the importance of the ligand spacer, and of the substituents of the pyridine/pyrazine amide ligand are discussed. To the best of our knowledge, our work evidences for the first time that the hyper-polarizability, second harmonic generation, and hyper-Rayleigh scattering response of TM coordination complexes can be correlated to the second ionization potential of metal and spin state of complexes.

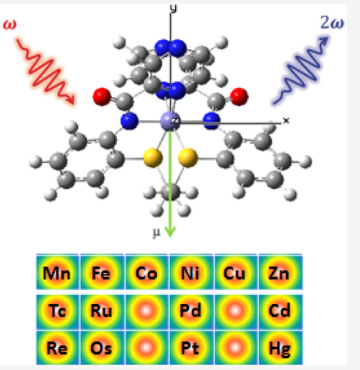

1. INTRODUCTION

Currently, the discovery of new nonlinear optical (NLO) materials has become one of the major challenging research fields because of its potential applications in various fields such as photonics, opto-electronics, optical communications, optical switching, optical computing, optical memory, dynamic holography photodynamic therapy, and biological imaging.[1−4]

Among systems, metal complexes with π-conjugated ligands have emerged and grown as a respectable class of NLO materials,[5−8] owing to their thermal stability, redox switching ability, and ultrafast response times.[9] Also, the metal complexes display a large variety of molecular geometry and electronic properties by virtue of the coordinated metal center. Furthermore, metal complexes have several additional electronic properties that distinguish them from organic compounds due to their low-energy charge-transfer transitions such as the ligand to metal charge transfer (LMCT), metal to ligand charge transfer (MLCT), and intra-metal charge transfer (IMCT) electronic transition. On the other hand, to provide a high NLO response, the coordination complex with the π-conjugated ligand should be asymmetric, and it should possess low-energy absorption with charge-transfer transitions, whereas the difference between the excited-state and the ground-state dipole moment should be large.[5]

The bonding model of transition-metal (TM) complexes can explain many important properties of the TM complexes including their magnetism, structures, stability, oxidation state, reactivity, and optical (linear and nonlinear) properties. It is to be noted that in the TM complexes, the energies of the five (n − 1) d orbitals of the TM ion are affected by the nature of the ligands (strong or weak field).

In the case of TM complexes in octahedral geometry, the $d_{x^2-y^2}$ and d_{z^2} orbitals interact very strongly with the ligands and form new σ bonding and antibonding molecular orbitals, called the "e_g" set of orbitals, in Oh symmetry. On the other hand, the d_{xy}, d_{xz}, and d_{yz} orbitals interact less strongly with the donor ligands and develop π orbitals (bonding and antibonding interactions), called the "t_{2g}" set of orbitals. The filling of these e_g and t_{2g} orbitals depends on the ligand field, leading to the spin state of the complex. For the weak field, we have the high spin (HS) state, with a filling of, successively, the t_{2g} (α spin), the e_g (α spin), the t_{2g} (β spin), and the e_g (β spin). For the strong field, we have low spin (LS) state with successively filling the t_{2g} (α spin), the t2g (β spin), the e_g (α spin), and the e_g (β spin). Therefore, in the case of $3d^4$−$3d^7$ configurations (Scheme 1), the occupation of the e_g orbital preferentially to a

Received: February 9, 2021

Abstract

This thesis presents a detailed theoretical investigation of the second- and third-order nonlinear optical (NLO) properties of two classes of materials: transition metal-doped nanocages ($M@Al_{12}N_{12}$, M = Sc to Zn) and multi-decker organometallic sandwich clusters [$\{H_2B_2S_2Pd(Cl)_2\}$–$(CoCp)_n$] (n = 2–5). Using DFT, TD-DFT, and the Sum-Over-States (SOS) approach at various frequencies (ω = 0.0428, 0.034, 0.0239 a.u.), we explored both static and dynamic NLO responses. Key parameters including oscillator strengths, excitation energies, and charge-transfer features were analyzed. In nanocages, strong NLO responses were linked to charge delocalization and closed ring topologies. The sandwich complexes MDSn, MDSna, and MDS'n showed structure-dependent polarizability and hyperpolarizability trends, with MDSn exhibiting a consistent increase in β and MDS'n peaking at n = 4. Both systems demonstrated significant frequency-dependent enhancement, particularly under two-photon resonance. Furthermore, MDSn/ MDS'n complexes show colossal γ responses that grow with deck number, peaking in MDS_5. Molecular length and topology govern these effects. These results offer important guidance for the rational design of high-performance NLO materials aimed at next-generation photonic and optoelectronic technologies.

Résumé

Cette thèse présente une étude théorique approfondie des propriétés optiques non linéaires (NLO) du second et du troisième ordre de deux classes de matériaux : les nanocages dopées aux métaux de transition ($M@Al_{12}N_{12}$, avec M = Sc à Zn) et les complexes sandwich organométalliques multi-couches [$\{H_2B_2S_2Pd(Cl)_2\}$–$(CoCp)_n$] (n = 2–5). En utilisant la théorie de la fonctionnelle de la densité (DFT), la DFT dépendante du temps (TD-DFT), ainsi que l'approche de la somme des états (SOS) à différentes fréquences (ω = 0.0428, 0.034, 0.0239 a.u.), nous avons exploré les réponses NLO statiques et dynamiques. Les paramètres clés tels que les forces d'oscillateur, les énergies d'excitation et les caractéristiques de transfert de charge ont été analysés. Dans les nanocages, les fortes réponses NLO sont attribuées à la délocalisation électronique et aux topologies en anneau fermé. Les complexes sandwich MDSn, MDSna et MDS'n ont montré des tendances dépendantes de la structure en polarisation et hyperpolarisation, avec une augmentation régulière de β pour MDSn et un pic pour MDS'n à n = 4. Les deux systèmes présentent un renforcement significatif dépendant de la fréquence, notamment en résonance à deux photons. De plus, les complexes MDSn/ MDS'n présentent des réponses γ colossales qui augmentent avec le nombre de ponts, atteignant un pic dans MDS_5. La longueur moléculaire et la topologie régissent ces effets. Ces résultats offrent des pistes prometteuses pour la conception de matériaux NLO performants destinés aux applications photoniques et optoélectroniques.

ملخص

تُقدم هذه الأطروحة دراسة نظرية مفصلة للخصائص البصرية غير الخطية من المرتبتين الثانية والثالثة (NLO) لفئتين من المواد: أقفاص نانوية مطعمة بالمعادن الانتقالية ($M@Al_{12}N_{12}$، حيث M من Sc إلى Zn)، ومجمعات عضوية معدنية متعددة الطبقات من نوع الساندويتش [$\{H_2B_2S_2Pd(Cl)_2\}$–$(CoCp)_n$] (n = 2–5). باستخدام DFT و TD-DFT بالإضافة إلى منهجية SOS عند ترددات مختلفة (ω = 0.0428, 0.034, 0.0239 a.u.)، تم استكشاف الاستجابات غير الخطية في كل من النظامين الساكن والديناميكي. تم تحليل معلمات رئيسية مثل شدة المتذبذب، طاقة الإثارة، وخصائص انتقال الشحنة. في أنظمة الأقفاص النانوية، ارتبطت الاستجابات القوية بانتشار الشحنة وتشكّل الحلقات المغلقة. أما المجمعات الساندويتشية من نوع MDSn وMDSna وMDS'n فقد أظهرت سلوكًا يعتمد على البنية في قيم الاستقطابية والاستقطابية الفائقة، حيث أظهرت MDSn زيادة منتظمة في β، في حين بلغت MDS'n ذروتها عند n =4. أظهرت كلا النظامين تحسنًا كبيرًا عند الرنين ثنائي الفوتون، علاوة على ذلك، أظهرت مجمعات MDSn / MDS'n استجابات γ ضخمة تنمو بزيادة عدد الطبقات وتبلغ ذروتها في MDS_5 تتحكم كل من طول الجزيء و طوبولوجيته ي هذه التاثيرات. وتوفر هذه النتائج توجيها مهما للتصميم المنهجي لمواد NLO عالية الأداء موجهة لتقنيات الفوتونيات و البصريات الالكترونات من الجيل القادم.